Study on High Breeding Reactors with Tightly Packed Fuel Assemblies Cooled by Light Water

燃料棒を隙間なく束ねた集合体を用いた高増殖軽水冷却炉の研究

July 2015

Rui　　GUO

郭　　鋭

Study on High Breeding Reactors with Tightly Packed FuelAssemblies Cooled by LightWater

燃料棒を隙間なく束ねた集合体を用いた高増殖軽水冷却炉の研究

July 2015

Waseda University Graduate School of Advanced Science and Engineering and Tokyo City University Graduate School of Engineering, Cooperative Major in Nuclear Energy, Research on Reactor Theory

Rui   GUO

郭   鋭

Abstract

Fast Breeder Reactors (FBRs) are of great interest owing to their great potential of enhanced utilization of the natural uranium resources. The breeder reactors by light water cooling (Pressurized Water Reactor (PWR) and Boiling Water Reactor (BWR) types) have been studied for decades but yet the high breeding has not been achieved. This thesis focuses on the studies regarding high breeding reactors cooled by light water with tightly packed fuel assemblies.

Chapter 1 provides the backgrounds and describes the necessities and objectives of the study. FBR is a nuclear reactor that generates more fissile material than it consumes. It can be an important potential source of energy. Most FBRs are fueled with ^{239}Pu, because ^{239}Pu gives rise to the highest value of neutron yield per neutron absorbed among the major fissile nuclides at fast neutron spectrum. At fast neutron spectrum the fertile ^{238}U can be converted to fissile ^{239}Pu more efficiently than that at thermal spectrum. Liquid metal coolant is used for most FBRs to avoid softening of neutron spectrum. Therefore, FBRs with light water cooling have been challenging for many years. The technology of light water cooling is more reliable and experienced, giving much less capital cost of construction, operation and maintenance. It is well known that the energy demand of a country is generally proportional to its Gross Domestic Product (GDP). For the G7 member countries, who are the members of the Organization for Economic Co-operation and Development (OECD), the recent average GDP growth rate is about 1.4%. It implies that the energy requirement is also growing at around 1.4% per year in these countries and the energy demand may double in 50 years. It is expected that operation of FBRs and reprocessing of the spent fuel will be utilized in advanced countries. Compound System Doubling Time (CSDT) indicates the time that is needed in a system of breeder reactors to double the reactor number as well as the energy output by using the excess fissile material generated in the system. In this study, CSDT of less than 50 years is determined as the target breeding performance of FBRs by referring to the expected energy demand growth in the G7 member countries.

Researchers have made continuous attempts to apply technology of light water cooling on FBR. Many concepts of high conversion PWR (HCPWR) were studied since 1970s, with tight fuel rod lattice arrangement to reduce moderation of neutron, achieving conversion ratio of close to 1.0 but not enough to breed. JAEA researchers proposed a BWR-type Reduced-Moderation Water Reactor (RMWR) with tight lattice configuration. RMWR is cooled by boiling water. Therefore large void fraction (70%) is created in the core to reduce moderation of neutron. As the result, conversion ratio of RMWR exceeded 1.0. However, this concept only

achieves a CSDT of 245 years which is still too far from achieving the high breeding of CSDT that is less than 50 years. Recently, concept of the tightly packed fuel assemblies was proposed by the researchers of Waseda University to substantially reduce the coolant volume fraction. With application of the assemblies, the concept of Supercritical pressure light water cooled Fast Breeder Reactor (Super FBR), which attained CSDT of 43 years was presented.

Although the reactor design of Super FBR is successful for high breeding, thermal hydraulics of the tightly packed fuel assembly has never been studied. Among all design parameters of this assembly, the channel geometry is the most important one, and its thermal hydraulic characteristics are needed to be analyzed. Compared with Super FBR, high breeding with the existing BWR technology is easier to implement. Hence, it is necessary to study the high breeding in the BWR-type fast breeder reactor by utilizing the tightly packed fuel assembly. Moreover, low average coolant density, which is comparable to that of Super FBR, can be created in a BWR-type core, which is favorable for high breeding. Another issue related to application of the tightly packed fuel assembly is the safety performance. Since the coolant channel area is very small, it is necessary to study the safety characteristics for reactors with tightly packed fuel assemblies.

Given above all, three objectives of this thesis are: (1) to study the thermal hydraulics of tightly packed fuel assembly in detail by Computational Fluid Dynamics (CFD) method; (2) to design a high breeding core (CSDT < 50 years) with tightly packed fuel assemblies working at BWR condition; (3) to clarify safety characteristics of Super FBR with the tightly packed fuel assemblies.

Chapter 2 is dedicated to thermal hydraulic analysis of different channel geometries in the tightly packed fuel assembly. As previously studied in core design of Super FBR, this assembly has the great potential of achieving high breeding by greatly reducing the coolant volume fraction, while the original circular coolant channel gives rise to high cladding temperature and high pressure drop. By ameliorating the channel geometry, it is expected to improve the performance on thermal hydraulics. Therefore, three types of coolant channel geometry are established and analyzed: geometry A is circular; geometry B is triangle-like shape with rounded-corner; geometry C is also triangle-like shape but with pointed corner. These geometries are selected based on the values of the ratio of hydraulic diameter to channel area, and represent the potential channel geometries. From geometry A to C, the channel area increases while the hydraulic diameter reaches peak around geometry B. The simulations are conducted at three pressure conditions, representing Super FBR pressure (30MPa), PWR

pressure (15.5MPa) and BWR pressure (7.2MPa), respectively.. A CFD code STAR-CCM+ v8.02 is used. For each pressure condition, validations against experiment data, related to heat transfer at supercritical pressure, critical heat flux (CHF) and distribution of void fraction, are performed at first. Then, assessment of thermal-hydraulic characteristics of each channel geometry was conducted with the boundary conditions established as to cover the design range of each corresponding reactor type. Assessments of the geometries are made based on thermal hydraulic parameters such as cladding temperature, pressure drop for all pressure conditions and with additional consideration of CHF at subcritical pressure. It is found that geometry B is superior to others at all operating pressures because of its broad design area in terms of power, cladding temperature and pressure drop, and it is able to meet the thermal hydraulic requirements in design of high breeding reactors.

Chapter 3 offers a conceptual core design of high breeding BWR with the tightly packed fuel assemblies. The goal of the high breeding BWR is to achieve CSDT < 50 years and negative reactivity simultaneously. Based on the experience of Super FBR core design, the neutronic design is conducted for the core in the way that: the seed and blanket assemblies are arranged in a radiating pattern; $ZrH_{1.7}$ pins are placed in a few blanket assemblies with the purpose of achieving negative void reactivity; the upper and lower blanket layers are placed in seed assemblies to improve the breeding. Sensitivities regarding the fuel enrichment, core average burnup, coolant channel geometry and water density distribution are studied to clarify the design area.

It is found that the breeding is better with lower plutonium enrichment and higher burnup. For attaining negative void reactivity, it is preferable to lower the enrichment and lower the burnup. In addition, the calculation results suggest that the coolant density change does not significantly affect the neutronics due to the small inventory of coolant. Therefore, the thermal hydraulic calculations were performed separately. It is found that the CSDT is mainly limited by a small Linear Heat Generation Rate (LHGR), while the LHGR is mainly limited by the CHF and power peaking factors. To increase the LHGR, CHF is increased by applying geometry B instead of geometry A in seed assemblies. It is also found that keeping geometry A in blanket assemblies to maintain the breeding ability is feasible, because the LHGRs of blanket assemblies are low. The power peaking factor is suppressed by enrichment zoning in both radial and axial directions. The pressure drop is higher than that of conventional BWRs due to application of narrow coolant channels. Resulting flow instability can be managed by applying orifices at the inlet in order to decrease the effect of the pressure drop change in the coolant

channel on the stability. The final breeding BWR core design achieves a CSDT of 41.6 years, while all the design criteria, with respect to Maximum Linear Heat Generation Rate (MLHGR), Minimum Critical Heat Flux Ratio (MCHFR) and negative void reactivity, are satisfied.

Chapter 4 clarifies the safety characteristics of Super FBR. Owing to application of the tightly packed fuel assembly, the coolant channel area is even smaller than that of the tight lattice fuel assembly in Super FRs. The main parts of the safety and plant system design of Super FBR are similar to that of Super FRs, while modifications are made to adapt to the higher system pressure of 30MPa compared with 25MPa of Super FR. The accident and transient scenarios are also selected from those of Super FRs owing to similarities in the plant systems. Events analyses are conducted by using the SPRAT code of Waseda University with a 2D heat transfer model that describes characteristics of the tightly packed fuel assembly in detail.

It is found that "control rod ejection" is the most important event, because both the highest values of the Maximum Cladding Temperature (MCT) and the peak pressure attained during this event are higher than those of other events. By contrast, "total loss of flow" is the most important event for Super FRs. This difference is due to one of the major safety characteristics of Super FBR caused by the small inventory of coolant in the core. Overall, the calculation results indicate that the designed safety system is capable to protect the reactor well at all accidents and abnormal transients.

Chapter 5 offers the general conclusions of the thesis. The thermal hydraulic characteristics of channel geometries in the tightly packed fuel assembly are understood for the first time by using the CFD method. The superiority of geometry B is demonstrated, owing to the broader design margin in terms of achievable power, cladding temperature and lower pressure drop. In practical applications, both geometry A and B are suitable for assembly design in high breeding Super FR, PWR and BWR, while geometry C is not suitable for high breeding PWR and BWR designs because it cannot satisfy the CHF criteria. Geometry B is adopted for seed fuel assemblies and geometry A is adopted for blanked assemblies to design a high breeding BWR core, which achieves a CSDT of 41.6 years meanwhile satisfying all the design criteria. Moreover, the safety characteristics of Super FBR with tightly packed fuel assemblies are clarified. The accident "control rod ejection" is found to be the most important event for the Super FBR because of the small volume fraction of coolant. All the safety criteria are satisfied for selected accidents and transients.

Acknowledgement

Contents

List of figures

List of tables

Chapter 1 Introduction

1.1 Nuclear energy and breeder reactors

Nuclear power development has been through over 70 years since the first reactor Chicago Pile-1 (ANL, 2013) was built in the year 1942. Although it was first driven by military purpose, the attention quickly turned to peaceful use with the ending of the World War II. Today, over 30 countries host about 430 commercial reactors and produce more than 11% of global electricity, seen in Table 1-1(WNA, 2014), and more countries without nuclear power plants yet use nuclear-generated electricity through regional grids such as Italy and Denmark. According to the World Nuclear Association (WNA), in ten countries, the nuclear power even contributes more than a third of their electricity production, such as Czech Republic, Finland and France. Nuclear power is characterized by low greenhouse gas emissions, high reliability, high efficiency and low-cost, and therefore it is increasingly recognized as the important source of electricity throughout the world. According to 2013 WNA Market Report (WNA, 2014), by the year 2030, 74 reactors will be retired while 272 new ones will come on line.

Table 1-1 Current status of global nuclear reactors (WNA, 2014)

Country	Nuclear electricity generation (2013)		Reactors operable (2015)		Reactors under construction (2015)		Reactors planned (2015)	
	10^9 kWh	% e	No.	MWe	No.	MWe	No.	MWe
Belgium	40.6	52.0	7	5943	0	0	0	0
Canada	94.3	16.0	19	13553	0	0	2	1500
China	104.8	2.1	22	19095	27	29548	64	71220
Czech Republic	29.0	35.9	6	3766	0	0	2	2400
France	405.9	73.3	58	63130	1	1720	1	1720
Finland	22.7	33.3	4	2741	1	1700	1	1200
Germany	92.1	15.4	9	12003	0	0	0	0
India	30.0	3.4	21	5302	6	4300	22	21300
Japan	13.9	1.7	48	42569	3	3036	9	12947
Korea RO (South)	132.5	27.6	23	20656	5	6870	8	11640
Russia	161.8	17.5	34	25264	9	7968	31	32780
Spain	54.3	19.7	7	7002	0	0	0	0
Sweden	63.7	42.7	10	9487	0	0	0	0
Switzerland	25.0	36.4	5	3252	0	0	0	0
Ukraine	78.2	43.6	15	13168	0	0	2	1900
United Kingdom	64.1	18.3	16	10038	0	0	4	6680
USA	790.2	19.4	99	98756	5	6018	5	6063
WORLD	2359	11	437	377,728	70	73,514	183	203,580

Worldwide, most reactors in operation are uranium-fueled with the thermal neutron spectrum, mainly consuming the fissile material ^{235}U which only takes a very small percentage (0.72%) of the natural uranium resources. The world's present measured resources of uranium is about 5.9 million tons while the global reactors require about 66,000 tons each year (WNA, 2014). Therefore, it is only able to supply for about 90 years. This number comes without considering the growing number and capacity of reactors owing to the growing demand for energy in the future. This number will also change if new uranium resources are identified or become practically available in the meantime. Just as expected for fossil energy resources, to the end, the fissile ^{235}U will eventually be exhausted.

Unlike thermal reactors, fast reactors with the hard neutron spectrum are able to use the major isotope of uranium (^{238}U) and other transuranics in the spent fuel from thermal reactors more efficiently. Isotopes such as ^{238}U, ^{234}U, ^{238}Pu and ^{240}Pu are known as "fertile" material which can be efficiently converted to fissile materials by fast neutrons. By using the fertile material (mainly is ^{238}U) in the blanket around the reactor core, the fast breeder reactor is capable of producing more fissile material than it consumes and is so called "breeder" (some thermal reactors also can breed but with thorium fuel cycle). Some other actinides (^{242}Pu, ^{241}Am, ^{236}U etc.) need to experience more complicated nuclear reactions to eventually become the isotopes that are fissile or stable enough to be readily handled.

1.2 GDP growth rate and goal of breeding

Many evidences (Soytas and Sari 2003; Richmond *et al.*, 2013) have shown that the demand for energy is more or less proportional to GDP. Figure 1-1 (Our finite world, 2011) shows example of the world's real GDP and total energy consumption from 1980 to 2010, which indicates that there is a roughly linear relationship between GDP and energy consumption.
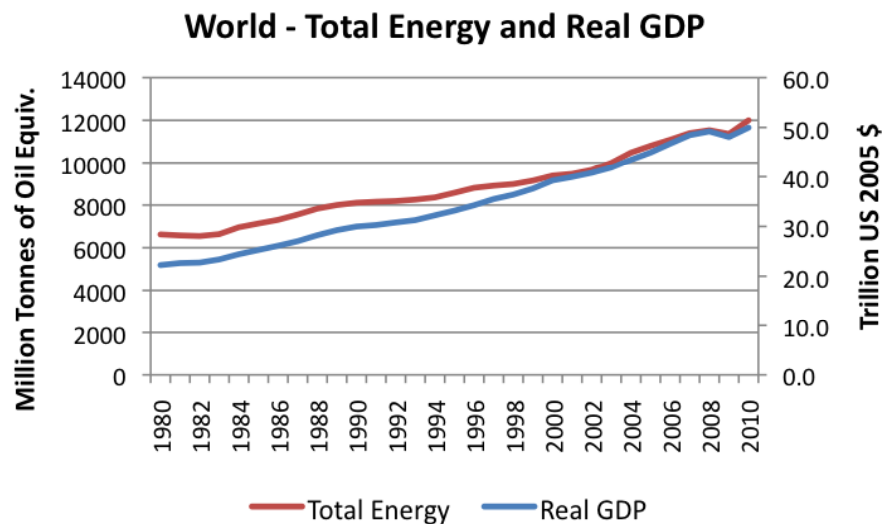
Fig. 1-1 Relationship between GDP and energy (Our finite world, 2011)

According to the Organization for Economic Co-operation and Development (OECD) economic outlook (Gurria and Padoan, 2012) , the recent average GDP growth rate in G7 member countries, which are also the members of OECD, is about 1.4 %, which implies that the energy

demand is also growing at around 1.4 % per year. Hence, the total energy requirement in these countries can be doubled in 50 years. Fast Breeder Reactors have the potential of meeting such growth in energy demand with sustainability, if they can be installed at a rate, which is comparable to the growth rate of the energy demand.

It is expected that operation of FBRs and reprocessing of the spent fuel will be utilized in advanced countries. Hence, for those countries, high breeding for a Fast Breeder Reactor system is able to satisfy the energy requirement, which is to double the energy output in 50 years. Compound System Doubling Time (CSDT, definitions are provided in Section 3.2) indicates the time that is needed in a system of breeder reactors to double the reactor number as well as the energy output by using the excess fissile material generated in the system. Based on above discussion, the high breeding goal in the current study is CSDT less than 50 years.

1.3 Current status of fast breeder reactors

Almost all the breeder reactors have been built are Liquid Metal cooled Fast Breeder Reactors (LMFBRs). The world's first electricity-generation reactor EBR-I (Experimental Breeder Reactor-1) was a fast breeder reactor that was built in 1950s in USA (ANL, 2013). It not just demonstrated that the nuclear power could generate clean and stable electricity but also proved that the breeding was technically possible. In the 1960s, EBR-II was built incorporated with a closed fuel cycle at Argonne National Laboratory (Sasahara *et al.*, 2004), with the fuel operations such as reprocessing and prefabrication all handled remotely. After then, the Americans had continually constructed several fast reactors such as Fermi-I, SEFOR and FFTF (USNRC, 2015). Russia (Soviet Union) had also built a series of fast reactors from earlier BR-10 to the latest BN-800 all cooled by sodium (USAEC, 1970). From 1957 to 1994, two fast reactors were constructed in UK, the 14MW DFR (Dounreay, 2015) and the 250MW PFR (Frank von Hippel *et al.*, 2010). The French first experimental 40MW fast reactor Rapsodie (Michaille, 2002) was first critical in 1960s, and then followed by the 233 MW Phénix (AtomInfo.ru., 2014) and the 1200MW Super-phénix (CEA, 2000). Both Germany and Japan started the research in 1970s, their first fast reactors KNK-II (ENS, 2003) and JOYO (Soga *et al.*, 2012) achieving criticality in 1977. In India, the FBTR first achieved criticality in 1985 (Srinivasan *et al.*, 2006), and China's CEFR attained criticality in 2010 (NEI, 2010), and now both are still in operation.

Basically, the development is carried out through three stages: the reactors in the first stage are usually aimed to demonstrate the technology and test the materials, operated at a small power, known as experimental reactors, such as EBR-I and BR-10; in the second stage, prototype

reactors are built to prepare for commercialization, generally operated at a higher power level (250-350 MW), for instance, Phénix and BN-600 (IAEA, 2012); With the construction and demonstration of commercial-sized reactors, the final goals of these fast reactor projects, commercialization, are eventually achieved in the third stage, currently, whereas only Russia's BN-800 is proceeded to construction.

In the year 2002, the Generation IV international Forum (GIF) proposed six types of innovative nuclear energy systems (Fig. 1-2) which are being developed to aim for commercial construction around 2030-2040 (WNA, 2014). Half of these reactors are known as fast reactors, including Gas cooled fast reactor (GFR), Sodium cooled Fast Reactor (SFR) and Lead cooled Fast Reactor (LFR). While some of the rest, such as Molten Salt Reactor (MSR) and Supercritical Water cooled Reactor (SCWR), also have fast versions, such as MFSR (Boussier, *et al.*, 2012) and Super FR (Liu and Oka, 2013). All these fast reactors can be designed as breeder reactors.
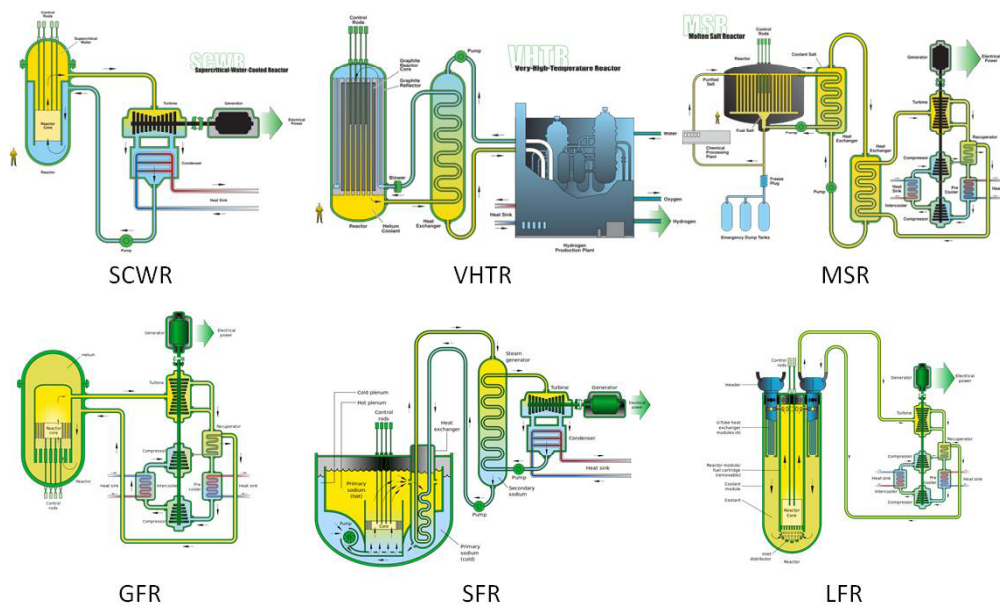
Fig. 1-2 Generation IV nuclear energy systems (Generation IV International Forum, 2014)

1.4 Basic physics of breeding

Breeding is basically the process that converts fertile material to fissile material via neutron reactions. Two distinct sets of reaction chains can fulfill the purpose as shown in Fig. 1-3, called U-Pu cycle and Th-U cycle respectively. In both cases, the fertile isotopes (^{238}U, ^{232}Th) capture a neutron, via twice successive beta emissions, converted to fissile isotopes (^{239}Pu, ^{233}U).
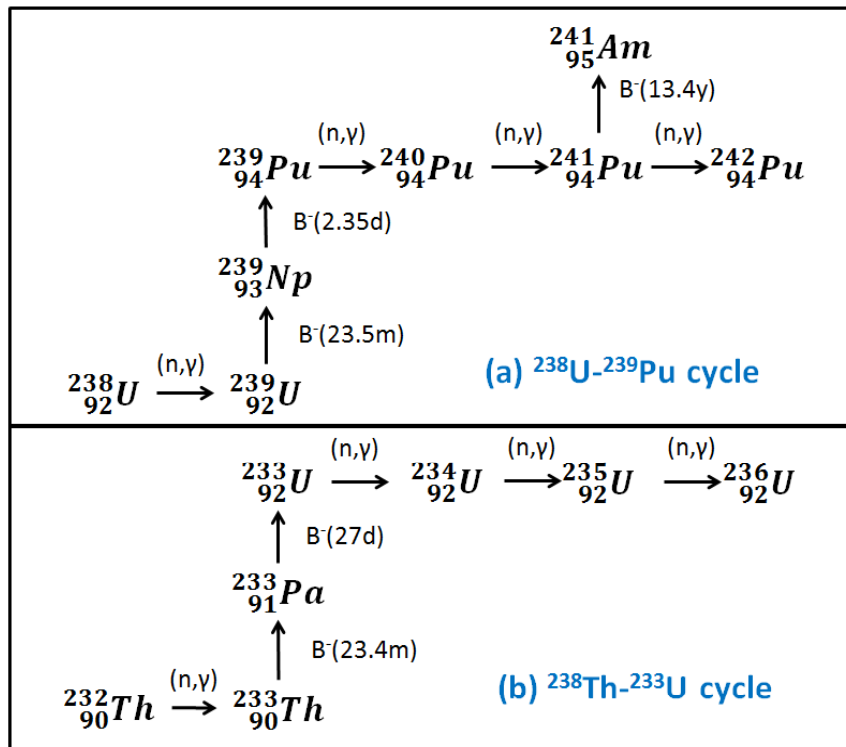
Fig. 1-3 Nuclear reactions chains of U-Pu cycle and Th-U cycle

Neutron yield per neutron absorbed (η) is a very important parameter in evaluation of breeding, and it can be denoted by:

$$\eta = v_f \frac{\sigma_f}{\sigma_a} = \frac{v_f}{1+\alpha} \tag{1-1}$$

where v_f is number of neutrons per fission, σ_f the cross-section of fission, σ_a the cross-section of absorption, α the capture to fission ratio (σ_c/σ_f).

In order to breed, it is known that the η theoretically should be greater than 2.0, which means that one neutron is used to sustain the critical reaction and the other to breed. Practically, by considering the leakage and the absorption by structural materials η should be at least 2.2 because it is very hard to reduce neutron loss to below 0.2. Figure 1-4 shows the η values of the typical fissile isotopes (Waltar *et al.*, 2012). It can be seen that all η values of the typical fissile isotopes are larger for neutron energy up to above 1MeV compared with those in smaller energy region, especially for ^{239}Pu (about 2.9 at 1MeV).
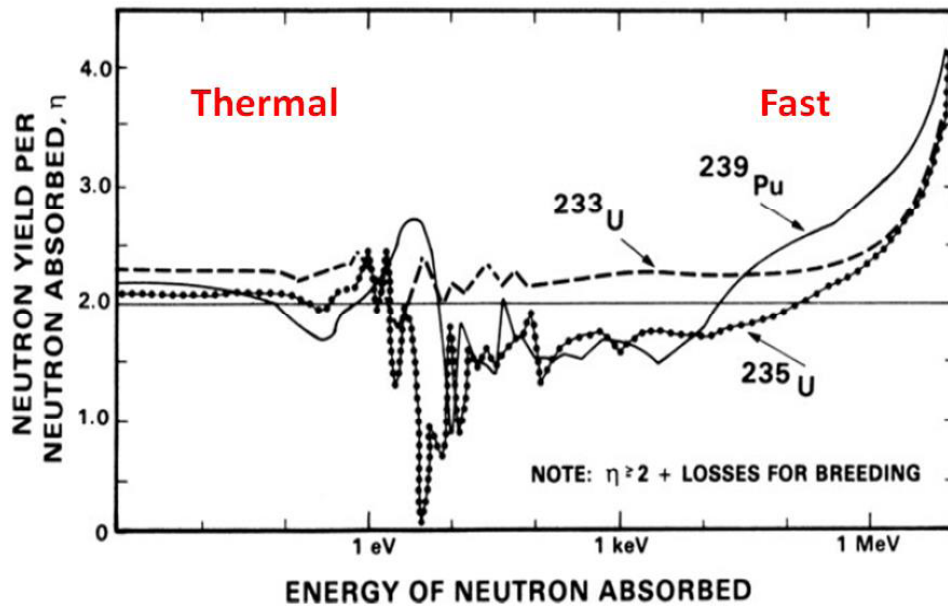
Fig. 1-4 η values of major fissile isotopes (Waltar, 2012)

The fission yield v_f is almost constant for each major fissile isotope in the neutron energy region form 10^{-5}eV to 10^5eV, as shown in Fig. 1-5, and then it greatly increase when the neutron energy is higher than 1MeV. This behavior indicates that in a fast neutron spectrum, more neutrons are remained for breeding. One of the reasons that typical fast reactors adopt ^{239}Pu as fuel is its significantly higher fission yield than those of ^{235}U and ^{233}U.
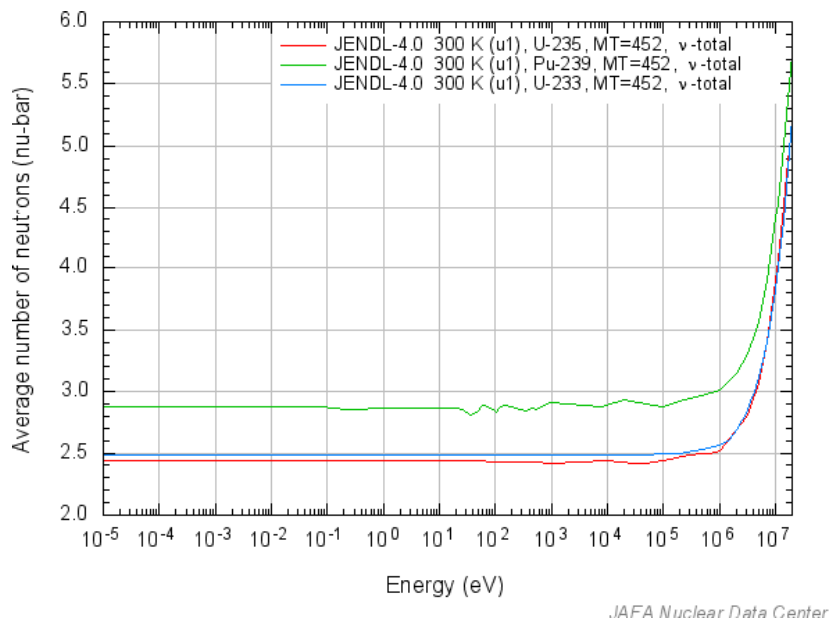
Fig. 1-5 Fission yield v_f of major fissile isotopes (JAEA, 2015)

Additionally, in a fast neutron spectrum, more ^{239}Pu generated from capture reaction of ^{238}U can be reserved from being used for fission than that in a thermal spectrum, despite the fact that the capture cross section of ^{238}U is higher at lower neutron energy. The reason for this is that fission reaction is in favor of thermal neutrons. In a thermal spectrum, the fission cross section of ^{239}Pu is also much higher so that most ^{239}Pu bred will fission as soon as generated. Fig. 1-6 indicates that the ratio of fission cross section of ^{239}Pu to capture cross section of ^{238}U is about 100 compared with that value of about 8 in a fast spectrum. Because both above cross sections (fission cross section of ^{239}Pu and capture cross section of ^{238}U) are smaller in a fast spectrum, higher enrichment is needed for fast reactors to maintain criticality than thermal reactors. Compared with a thermal reactor of the same power level, the fast reactor has higher neutron density due to removal of moderator.
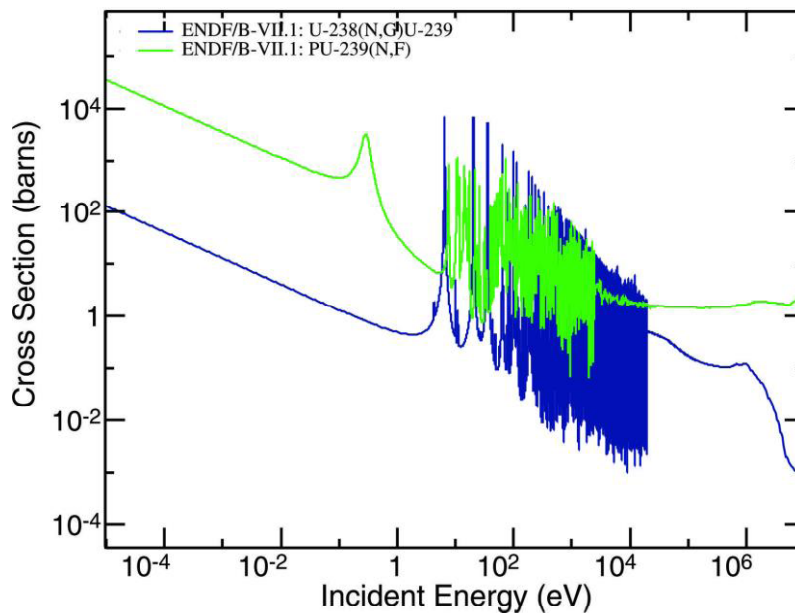
Fig. 1-6 Comparison of ^{238}U capture cross section and ^{239}Pu fission cross section (IAEA, 2015)

One of the indices of breeding is given by Fissile Plutonium Surviving Ratio (FPSR). FPSR over 1.0 indicates that the amount of fissile plutonium at the end of the equilibrium cycle (EOEC) is more than that at the beginning of the equilibrium cycle (BOEC). The details will be discussed in Chapter 3. CSDT also is an indicator parameter of breeding, more specifically, indicating the breeding efficiency as described in Section 1.2.

1.5 Fast reactors cooled by light water

Currently, all the fast reactors ever built are cooled by liquid metal and most of them are sodium cooled whereas most conventional power reactors are cooled by light water. Apart from the high efficiency of heat transfer by liquid metal, one more important reason is the fact that the light water used in conventional power reactors has good moderating property which softens the neutron spectrum and lowers the breeding performance of the reactor. On the other hand, light water cooling technology is well-established. The fast reactors based on LWRs technology are expected to be relatively cheaper compared to the liquid metal cooled reactors.

For assuring inherent safety of a reactor, it is important that the core possesses negative feedback characteristics to changes in the core status due to increase in the core power or heat up of the core. Among various relativities, void reactivity is a big safety concern for reactors cooled either by light water or liquid metal. Coolant voiding will harden the neutron spectrum so that the fast fission is built up while the neutron leakage increases. The reactivity may increase at void condition if the effect of fission buildup overs that of neutron leakage.

Many LMFBRs employ a short core or place some void channels in the core to achieve negative void reactivity by increasing the neutron leakage. Another approach is to place solid moderator, such as ZrH1.7, in the core to compensate for the neutron spectrum hardening at void, which is shown to be effective for light water cooled fast reactors (Jevremovic *et al.*, 1993; Oka and Jevremovic, 1996).

1.5.1 High Conversion Light Water Reactors

Researchers (Edlund, 1975; Oldekop *et al.*, 1982) started to study the High Conversion Light Water Reactors (HCLWRs) since 1970s in order to enhance the efficiency of fuel utilization, especially to utilize the large amount of plutonium generated in the conventional water reactors. The main characteristic of the HCLWRs is the similarity to the current LWRs, including the fuel cycle technologies and related infrastructures.

The main conceptual idea of these core types is to decrease the volume ratio of coolant to fuel by using a tight (triangular) lattice arrangement of fuel rods, thus hardening the neutron spectrum and increasing the conversion ratio. In the tight lattice, compared with the square lattice arrangement of the conventional LWRs, the gap between fuel rods becomes smaller as well as the coolant inventory and the fuel enrichment is also higher than conventional LWRs due to the hardening of the neutron spectrum. The conversion ratio of a homogeneous tight lattice core (all

assemblies are the same) with plutonium fuel is about 0.8~1.0 (Ronen, 1990), which is much higher than 0.4~0.6 in conventional LWRs, but breeding is not achieved.

One example, which shares various common design features of the high conversion light water reactors, is PWR-type Reduced-Moderation Water Reactor (RMWR) proposed by researchers from Japan Atomic Energy Agency (JAEA) (Hibi *et al.*, 2000). This core adopts the seed-blanket assemblies, as shown in Fig. 1-7. The seed fuel region, composed of Mixed Oxide (MOX) fuel pins of 9.5 mm in diameter, is surrounded by blanket region which consists of depleted uranium fuel pins of larger diameter (14.4mm). In both regions, the gaps between fuel pins are around 1mm. The fissile plutonium enrichment in seed pins is about 18 wt%. Several $ZrH_{1.7}$ pins are scattered in the blanket region in order to reduce the void reactivity. The core layout is shown in Fig. 1-8, with an out-in fuel shuffling pattern to minimize the power peaking. The PWR-type RMWR attains a conversion ratio of close to 1.0 and negative void reactivity coefficients with light water moderation. However, the conversion ratio does not exceed 1.0 and breeding is still not achieved.
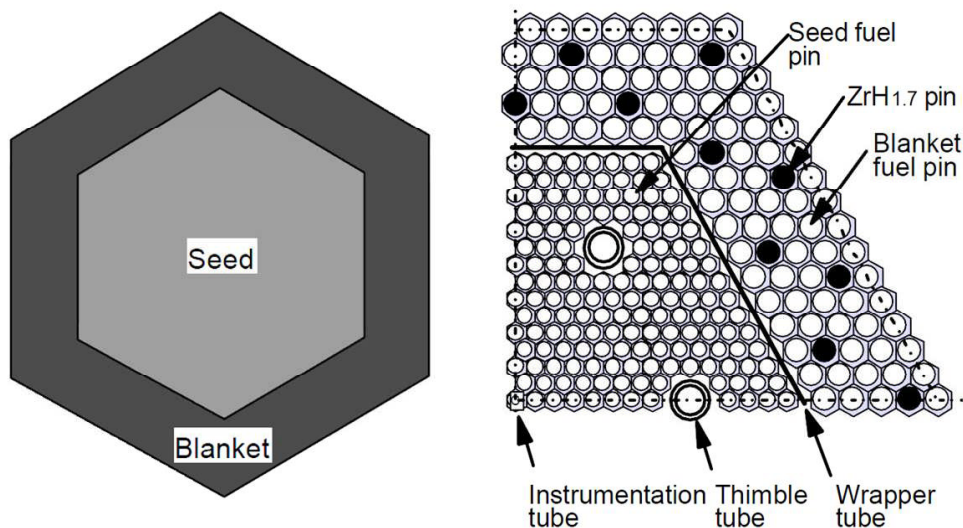
Fig. 1-7 Seed-blanket assembly in PWR-type RMWR (Hibi *et al.*, 2000)
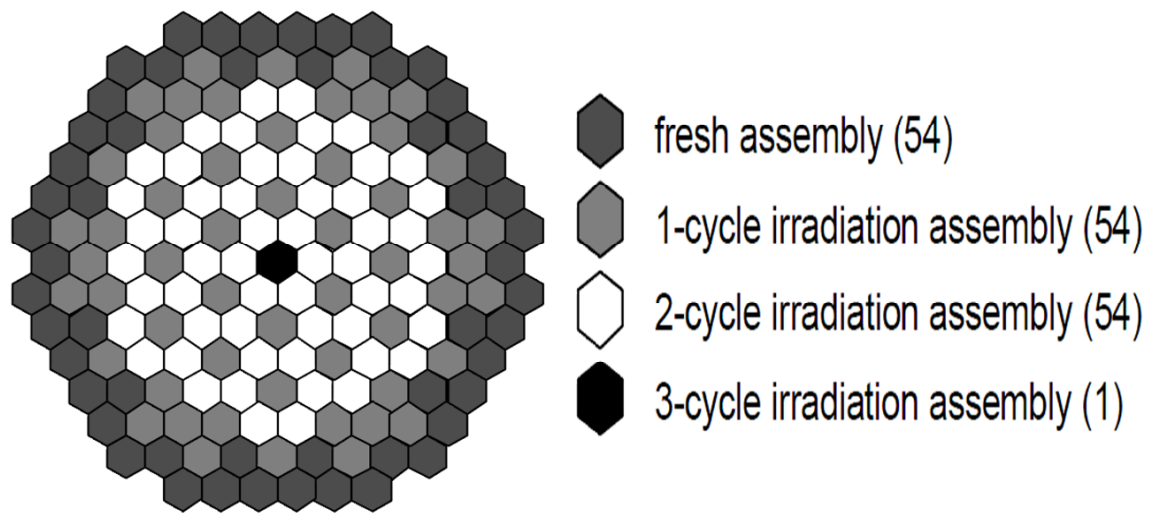
Fig. 1-8 Core layout of PWR-type RMWR (Hibi *et al.*, 2000)

1.5.2 Fast Breeder Reactors cooled by light water

The main approach to achieve breeding with light water cooling is to reduce the volume fraction of coolant so as to make the neutron spectrum harder and incorporate U-Pu fuel cycle.

BWR-type RMWR

Researchers from JAEA have proposed the BWR-type RMWR core concept (Okubo *et al.*, 2000), which can achieve breeding based on the LWR technologies. The tight-lattice fuel rod arrangement is adopted for assembly design as shown in Fig. 1-9 (Okubo *et al.*, 2000). The volume fraction of coolant to fuel is reduced to around 0.17, which is less than 1/4 of that of conventional BWR (0.82). Reduction of the moderator gives rise to a similar neutron spectrum to that of sodium cooled Fast Breeder Reactors (FBRs). To achieve negative void reactivity, the core has been designed as a "pie" shape with large aspect ratio to increase the neutron leakage. In the axial direction, the core is divided into five layers where the seed and blanket layers are alternately arranged as shown in Fig. 1-10 (Okubo *et al.*, 2000). This configuration also helps to improve the breeding, since the neutrons leaking out from the seed layer are effectively captured by ^{238}U in the neighboring blanket layer.
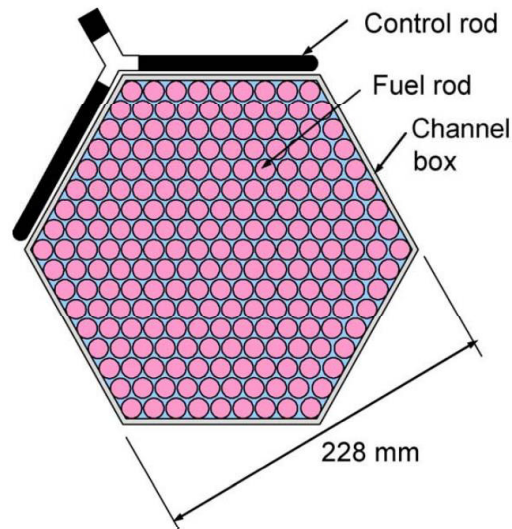
Fig. 1-9 The tight-lattice fuel rod arrangement in RMWR assembly (Okubo *et al.*, 2000)
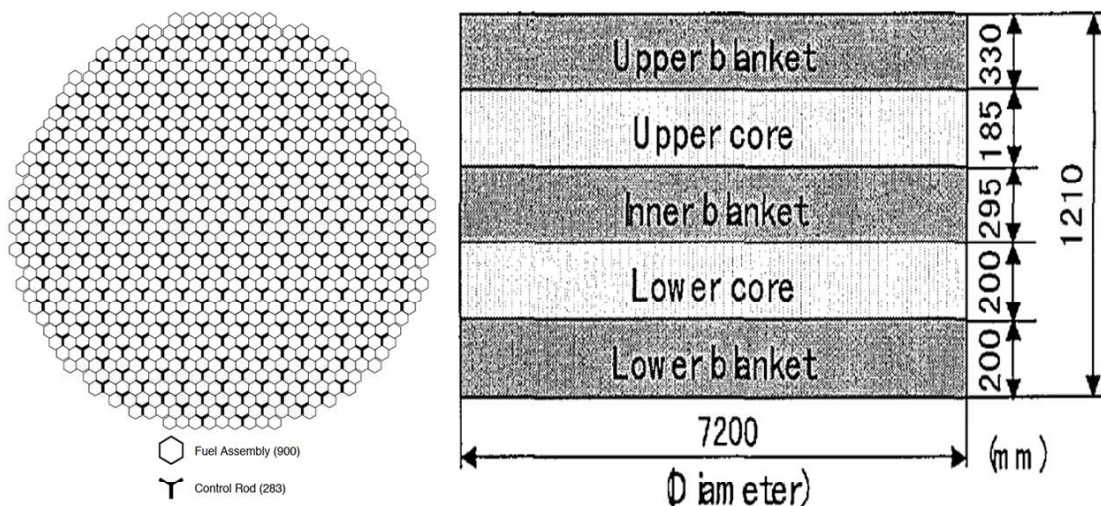
Fig. 1-10 Core geometry of RMWR (Okubo *et al.*, 2000)

Super FR with "briquet" assembly

Ishiwatari *et al.* (2001) proposed a core design concept which achieved high breeding, which is a kind of supercritical pressure light water cooled fast reactors (Super FRs). The core adopts an unique assembly design, called "briquet" assembly, as shown in Fig. 1-11 (Ishiwatari *et al.*, 2001), which is taken form the "tube-in-shell" assembly of liquid metal fast reactor (Hiraoka *et al.*, 1991). The coolant tubes are welded to the plates of the shell at the top and bottom. The coolant

volume fraction is reduced to 0.114. However, during operation, the different thermal expansion of these tubes may induce stress on the welding and may crack it. This raises concerns for fuel integrity.
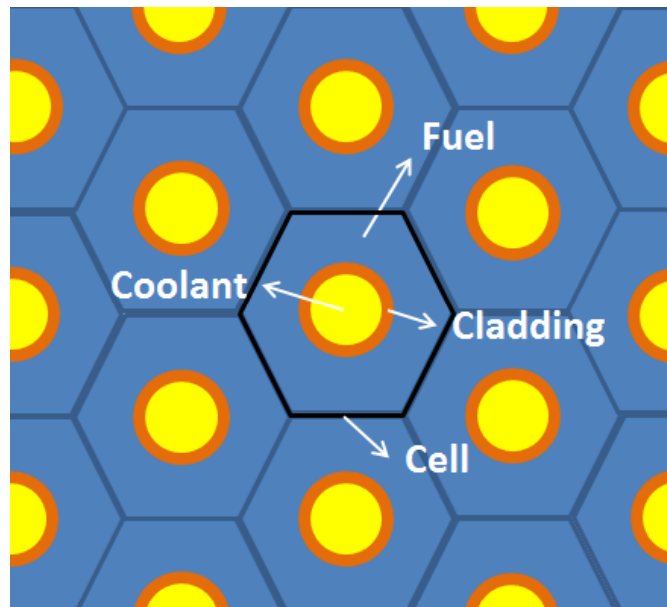
Fig. 1-11 Briquet assembly (Ishiwatari *et al.*, 2001)

Super FBR with tightly packed fuel assemblies

To overcome the issue of thermal stress of the Super FR design with the briquette assembly, as well as to maintain a small value of coolant volume fraction, Oka *et al.* (2013) devised a new "tightly packed fuel assembly" which is shown in Fig. 1-12. The fuel rods are just the same as conventional ones, with end plugs welded at the top and bottom. Therefore, no stress from thermal expansion is imposed on the welding during operation. The integrity of welding is kept, and the volume fraction of coolant is significantly decreased to 0.085.

The Supercritical-pressure light water cooled fast breeder reactor (Super FBR) with the tightly packed fuel assemblies has been designed by Yoshida and Oka (2013). Figure 1-13 shows the core geometry in both radial and axial directions. A comparison of major core parameters between Super FBR and BWR-type RMWR is shown in Table 1-2. It shows that, with the tightly packed fuel assemblies, the breeding performance of Super FBR (CSDT of 43years) substantially surpasses that of BWR-type RMWR (CSDT of 245years). To achieve the negative void reactivity,

unlike shortening the core in RMWR design, Super FBR core design applies $ZrH_{1.7}$ pins as solid moderator in some blanket assemblies as shown in Fig. 1-14 and described in Section 1.5.
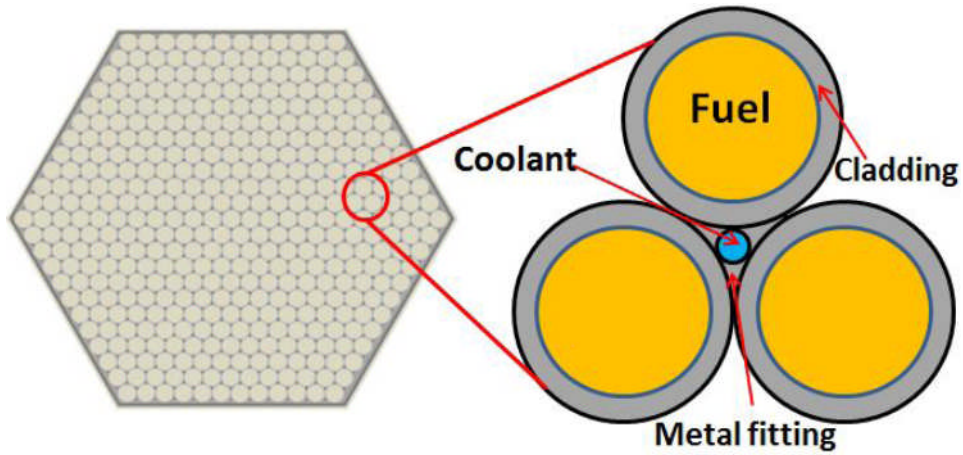
Fig. 1-12 Tightly packed fuel assembly (Oka *et al.*, 2013)
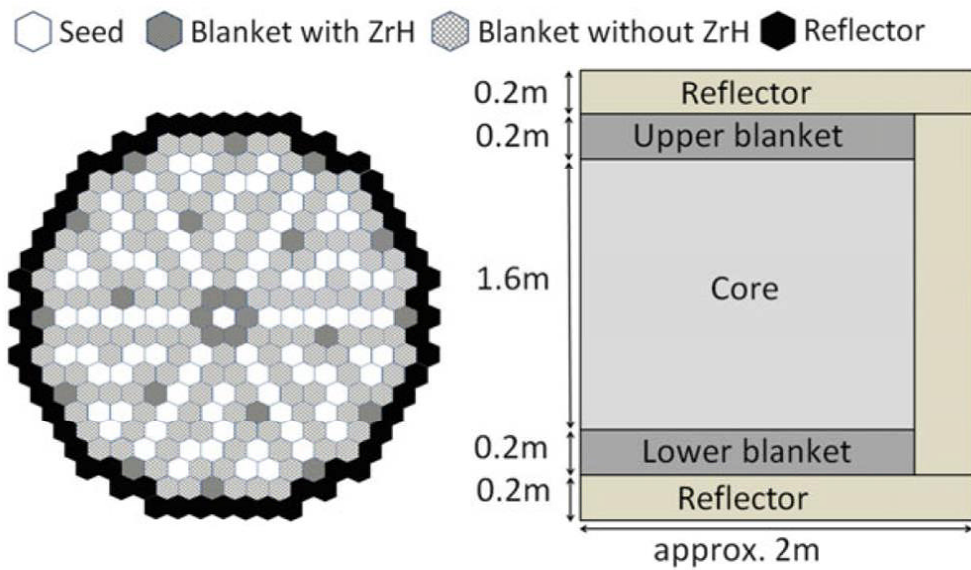
Fig. 1-13 Super FBR core layout (Yoshida and Oka, 2013)
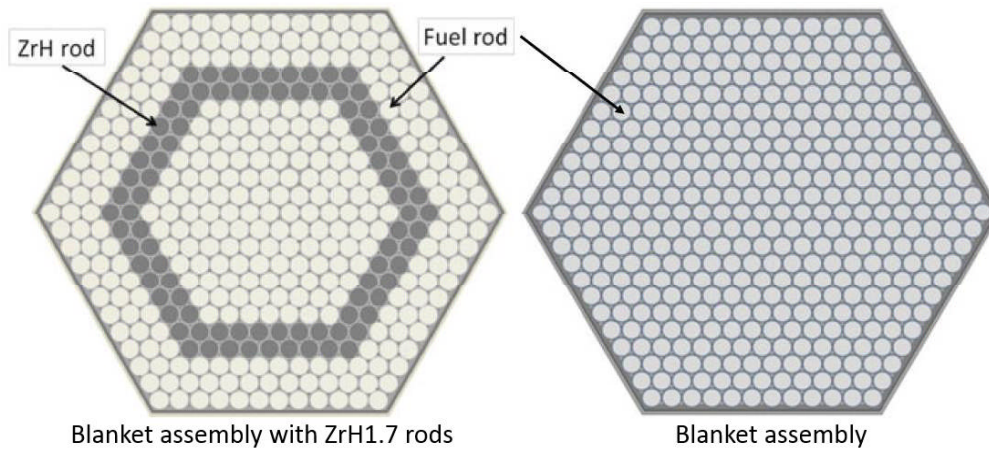
Fig. 1-14 Blanket assemblies (Oka *et al.*, 2013)

Table 1-2 Comparison of the core parameters between Super FBR and RMWR (Yoshida and Oka, 2013)

	Super FBR	BWR-type RMWR
Power (MW$_{th}$)	1,156	3,926
Core height(m)	2.0	1.255
Core equivalent diameter (m)	4.12	7.37
Operating cycle length (d)	550	456
Pu enrichment in seed (wt%)	29.2	31.3
Average coolant density (g/cc)	0.248	0.248
Core pressure (MPa)	30	8.2
Void reactivity (%) (BOEC/EOEC)	-0.70/-0.37	Negative
FPSR	1.026	1.006
CSDT (y)	43	245

1.6 Motivations and Objectives of the present study

As discussed in Section 1.2, the average energy demand is recently growing at around 1.4% in G7 member countries. In these advanced countries, operation of high breeding (CSDT < 50 years) FBRs and reprocessing of the spent fuel may be utilized. Hence, there is a potential of FBRs providing sustainable source of energy to meet the growth of the energy requirement in these countries.

In developing the FBRs, if the techniques based on light water cooling can be applied, it would be of more advantageous compared to the current liquid metal cooling technology, since the light water cooling is more reliable and experienced, being able to take advantage of the current infrastructures and human resources, giving much less capital cost of construction, operation and maintenance. In addition, LWRs regulatory procedures related to safety aspects are also well-established and widely accepted. The similarities of light water cooled FBRs to LWRs may, to some extent, simplify regulatory review. The core neutronics study on Super FBR with the tightly packed fuel assemblies showed the possibility of achieving high breeding by light water cooling (Oka *et al.*, 2013). However, the thermal hydraulic characteristics of the tightly packed fuel rods assembly have not been studied.

To further develop and improve the concept of breeding reactors with tightly packed fuel assemblies, the thermal hydraulic study for this kind of assembly is necessary. Studies not only under Super FBR condition, but also under typical BWR and PWR conditions are of great significance, considering the development of corresponding types of high breeding reactors with extension of the current LWR technologies. Among all the parameters of the tightly packed fuel assembly, the channel geometry is the most important one, because it greatly influence the thermal hydraulic characteristics, such as cladding temperature, pressure drop and Critical Heat Flux (CHF), and these impacts are needed to be analyzed both qualitatively and quantitatively to develop the core concept. In design of Super FBR the cladding temperature is the major limiting criterion, while in design of high breeding BWR and PWR, the pressure drop and Critical Heat Flux (CHF) are the most limiting factors.

Computational Fluid Dynamics (CFD) method is often used to study the thermal-hydraulic phenomena instead of experiment in cases, where physical properties and phenomena are well-known and modelled. It is able to accurately depict the complex 3-D geometry and simulate the phenomena with high reliability. Therefore, CFD method is well-fitted to analyze the thermal hydraulic characteristics of the coolant channel geometries, which is the first objective of the study.

The second study is to develop the high breeding BWR-type reactor with the tightly packed fuel assemblies. Compared with Super FBR, as well as other SCWRs which are still in stage of concept development and have not been built yet, existing LWR technology is much easier to implement. Among the two types of existing LWRs, PWR and BWR, the BWR-type core is of more advantages from the viewpoint of achieving high breeding, since the substantial core void fraction can be created in the core by boiling water. The low average coolant density would lead to

a comparatively hard neutron spectrum as in Super FBR. Moreover, high breeding with CSDT of less than 50 years has never been achieved in a BWR-type reactor. BWR-type RMWR achieves a CSDT of 245 years, but it is still far from the goal of high breeding. Compared with the assembly configuration in RMWR, the volume fraction of coolant to fuel in the tightly packed fuel assembly is much smaller, reduced from 0.17 to below 0.1, which is good for high breeding.

Safety is equally or even more important than economics in nuclear energy. The safety performance of Reactors with the tightly packed fuel assemblies are expected to be different from that with conventional assemblies, since the water inventory are much smaller. This effect might be more influential in Super FBR compared with BWR or PWR type reactor, giving greater challenges to core cooling system in case of abnormal events, because of its comparatively small coolant flow rate and once through coolant cycle (shown in Fig. 1-15) which are the same characteristics as Super LWR. Although the core design of Super FBR obtaining high breeding is shown, the safety system of that has not been shown yet. It is necessary to develop the safety system and clarify the safety characteristics of the Super FBR at accidents and abnormal transients.
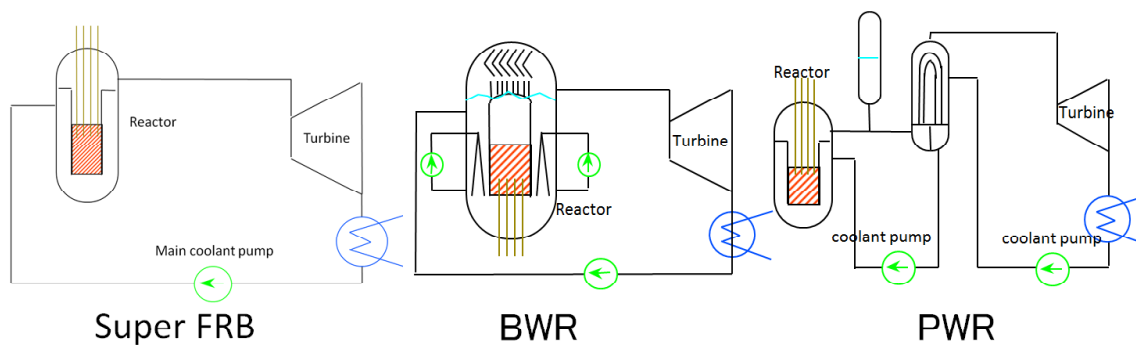
Fig. 1-15 Coolant cycles of Super FBR, BWR and PWR(Oka *et al.*, 2010)

Given above all, three objectives involved in this thesis are: (1) to study the thermal hydraulics of tightly packed fuel assembly in detail by CFD method; (2) to design the high breeding core (CSDT < 50 years) with tightly packed fuel assemblies working at BWR condition; (3) to clarify the safety characteristics of Super FBR with the tightly packed fuel assemblies.

1.7 Reference

ANL 2013. "Reactors Designed by Argonne National Laboratory: Chicago Pile 1". Retrieved. From: http://www.ne.anl.gov/About/reactors/frt.shtml

AtomInfo.ru., 2014. "Белоярская АЭС: начался выход БН-800 на минимальный уровень мощности". Retrieved 27 July 2014

Boussier, H. *et al.*, 2012. The Molten Salt Reactor (MSR) in Generation IV: Overview and Perspectives, GIF SYMPOSIUM PROCEEDINGS/2012 ANNUAL REPORT, NEA No. 7141, pp. 95

Bhabha Atomic Research Centre, 2013. Advanced Heavy Water Reactor (AHWR). Retrieved from IAEA.

CEA, 2000. CEA - Le CEA - Actualités - arrêt définitif du réacteur Phénix, Retrieved from CEA web.

Dounreay, 2015. DFR overview. Retrieved from:
http://www.dounreay.com/decommissioning/dounreay-fast-reactor/dfr-overview

Edlund, M. C. 1975. High conversion ratio plutonium recycle in pressurized water reactors. Ann. Nucl. Energy 2, 801-807.

Frank von Hippel *et al.*, 2010. Fast Breeder Reactor Programs: History and Status. International Panel on Fissile Materials, pp. 73–88

Gurria, A. and Padoan, P.C., 2012. "ECONOMIC OUTLOOK No. 92", Organization for Economic Co-operation and Development (OECD), pp.2, press conference in Paris.

Generation IV International Forum, 2014. Retrieved from:
https://www.gen-4.org/gif/jcms/c_59461/generation-iv-systems

Hiraoka T. *et al.*, 1991. "A high-breeding fast reactor with fission product gas purge/tube-in-shell metallic fuel assemblies", Nucl. Technol., 93, 305–329.

Hibi, K. *et al.*, 2000. Conceptual designing of reduced-moderation water reactors (2)―design for PWR-type reactors, Proceedings of ICONE 8, ICONE-8423, Baltimore, USA (2000)

Ishiwatari Yuki *et al.*, 2001. Breeding Ratio Analysis of a Fast Reactor Cooled by Supercritical Light Water, Journal of Nuclear Science and Technology, 38:9, 703-710

Ishiwatari, Y., Oka, Y., Koshizuka, S., Yamaji, A., Liu, J., 2005a, "Safety of super LWR, (I) safety system design," Journal of Nuclear Science and Technology, 42 (11), pp. 927-934.

Ishiwatari, Y., Oka, Y., Koshizuka, S., Yamaji, A., Liu J., 2005b, "Safety of Super LWR, (II) safety analysis at supercritical pressure," Journal of Nuclear Science and Technology, 42 (11), pp. 935-948.

Ikejiri, S., Ishiwatari, Y., Oka, Y., 2010. Safety analysis of supercritical-pressure water-cooled fast reactor under supercritical pressure. Nuclear Engineering and Design, 240, pp. 1218-1228.

Ikejiri, S., Han, C. Y., Ishiwatari, Y., Oka, Y., 2011. LOCA Analysis of Super Fast Reactor. Journal of Nuclear Science and Technology, 48(10), pp. 1289-1299

IAEA, 2012. Status of Fast Reactor Research and Technology Development. IAEA-TECDOC-1691, pp. 130

IAEA, 2015. Evaluated Nuclear Data File (ENDF) database Version of April 13, 2015. Retrieved from: https://www-nds.iaea.org/exfor/endf.htm

Jevremovic, T., Oka, Y., Koshizuka, S., 1993. Conceptual Design of an Indirect-Cycle, Supercritical-Steam-Cooled Fast Breeder Reactor with Negative Coolant Void Reactivity Characteristics, Annals of Nuclear Energy (20), pp. 305–313.

JAEA, 2015. Japan Charged-Particle Nuclear Reaction Data Group (JCPRG) PENDL：Plotter for Evaluated Nuclear Data Libraries. Retrieved from: http://www.jcprg.org/endf/

K., Hibi *et al.*, 2000. Conceptual designing of Reduced-Moderation Water Reactors (2) - Design for PWR-TYPE reactors. Proceedings of the 2000 21st International Conference on Nuclear Engineering, ICONE21-8423, Chengdu, China.

KNK-II, 2003. Info pool/Glossary, European Nuclear Society.

Li, H.P., Oka, Y., Ishiwatari, Y., 2013. Safety analysis of a supercritical water cooled fast reactor with all-upward two-pass flow, Annals of Nuclear Energy, 59, pp. 1-9.

Liu, Q. and Oka, Y., 2013. Core design for super fast reactor with all upward flow core cooling. J. Ann. Nucl. Energy 57, pp. 221-229.

Michaille, P. *et al.*, 2002. "operational & decommissioning experience with fast reactors", IAEA Technical Meeting, Cadarache

Nuclear Engineering International, 2010. "Criticality for China's first fast reactor". Retrieved 2010-07-23.

Oldekop, W., Berger, H. D., Zeggel, W. 1982. General features of advanced pressurized water reactors with improved fuel utilization. Nucl. Technol. 59, 212-227.

Oka, Y. and Jevremovic, T., 1996. Negative Coolant Void Reactivity in Large Fast Breeder Reactors with Hydrogenous Moderator Layer, Annals of Nuclear Energy (23), pp. 1105–1115.

Okubo, T. *et al.*, 2000. Conceptual designing of reduced-moderation water reactors (1)— design for BWR-type reactors Proceedings of ICONE 8, ICONE-8422, Baltimore, USA

Olson, G. L., McCardell, R. K., Illum, D. B., 2002. Fuel Summary Report: Shippingport Light Water Breeder Reactor. Idaho National Engineering and Environmental Laboratory Idaho Falls, Idaho 83415, INEEL/EXT-98-00799 Rev. 2.

Our finite world, 2011. "Is it really possible to decouple GDP Growth from Energy Growth?" Retrieved from: http://ourfiniteworld.com /2011/11/15

Oka, Y., Inoue, T., Yoshida, T., 2013. Plutonium breeding of light water cooled fast reactors. Journal of Nuclear Science and Technology, 50(1), pp. 15-20.

Oka, Y., Koshizuka, S., Ishiwatari, Y., Yamaji, A., 2010, Super Light Water Reactors and Super Fast Reactors. Springer. Chap. 6.

Ronen, Y., 1990. High Converting Water Reactors, Boca Raton, Florida, US. pp. 132

Richmond，P., Mimkes，J., Hutzler S., 2013. Econophysics and Physical Economics, Oxford, UK, pp. 174-175

Soga, T. *et al.*, 2012. Endeavor to improve in-pile testing techniques in the experimental fast reactor Joyo. Proceedings of a technical meeting, Halden, Norway

Sasahara, Akihiro; Matsumura, Tetsuo; Nicolaou, Giorgos; Papaioannou, Dimitri (April 2004). "Neutron and Gamma Ray Source Evaluation of LWR High Burn-up UO2 and MOX Spent Fuels".Journal of Nuclear Science and Technology 41 (4): 448–456.

Srinivasan, G; Sureshkumar, K; Rajendran, B; Ramalingam, P (2006). "The Fast Breeder Test Reactor—Design and operating experiences". Nuclear Engineering and Design 236 (7–8): 796–811

Sutanto, Oka, Y., 2014. Accidents and transients analyses of a super fast reactor with single flow pass core, Nuclear Engineering and Design, Volume 273, Pages 165-174,

Sutanto, Oka, Y., 2015. Analysis of anticipated transient without scram of a Super Fast Reactor with single flow pass core, Annals of Nuclear Energy, Volume 75, Pages 54-63

Soytas, U. and Sari, R. Energy consumption and GDP: causality relationship in G-7 countries and emerging markets, Energy Economics, Volume 25, Issue 1, January 2003, Pages 33-37,

Tabuchi, H., 2011. "Japan Strains to Fix a Reactor Damaged Before Quake". The New York Times.

USAEC Division of Technical Information, 1970. ANL-175 - Nuclear Reactors Built, Being Built, or Planned in the United States as of June 30, 1970 TID-8200 (22nd Rev.),

USNRC, 2015. Sites Undergoing Decommissioning (by Location or Name). Retrieved from: http://www.nrc.gov/info-finder/decommissioning/power-reactor/

Waltar, A.E., Todd, D.R., Tsvetkov, P.V., 2012. Fast Spectrum Reactors. Springer, pp. 11.

WNA, 2014. Uranium and Depleted Uranium. Retrieved from: http://www.world-nuclear.org/info/Nuclear-Fuel-Cycle/Uranium-Resources

WNA, 2014. Global Nuclear Fuel Market report Sept 2013 (reference scenario 2014) – for U. Retrieved from: http://www.world-nuclear.org

WNA, 2014. Generation IV Nuclear Reactors. Retrieved from: http://www.world-nuclear.org/info/Nuclear-Fuel-Cycle/Power-Reactors/Generation-IV-Nuclear-Reactors/

Yang, W. *et al.*, 2004. Long-lived fission product transmutation studies. Nucl. Sci. Eng. (146), pp. 291–318

Yoshida, T. and Oka, Y., 2013. High breeding core of a supercritical-pressure light water Cooled fast reactor. Proceedings of the 2013 21st International Conference on Nuclear Engineering, ICONE21-15753, Chengdu, China.

Chapter 2 CFD analysis of channel geometry in tightly packed fuel assembly

2.1 Introduction

High breeding achieved by the supercritical pressure light water cooled fast breeder reactor (Super FBR) shows great potential of the tightly packed fuel assembly. The cross section geometry of this assembly with magnified coolant channel region is shown in Fig. 1-12. The coolant channel is tangent to three fuel rods, and the space among them is filled with the metal fitting. In addition to application to Super FBR, this kind of assembly is also promising for PWRs and BWRs for obtaining high breeding. Therefore, detailed analyses of this assembly are needed to clarify the key design parameters and expected design ranges of high breeding BWR, PWR, and Super FBR from the thermal-hydraulic viewpoint. It is expected that the small flow area and the nonexistence of cross flows among adjacent channels may be challenging for attaining high heat transfer, while amelioration of the channel geometry may improve the thermal-hydraulic performance. The original channel cross-sectional geometry for Super FBR is circular (Yoshida and Oka, 2013), by contrast, two other noncircular geometries (geometry B and C) are considered from the thermal hydraulic features as shown in Fig. 2-1. The three geometries represent the typical channels that could be established in the new assembly. To perform the analyses, a commercial computational fluid-dynamic (CFD) software STAR-CCM+ v8.02 is used (CD-Adapco, 2013).
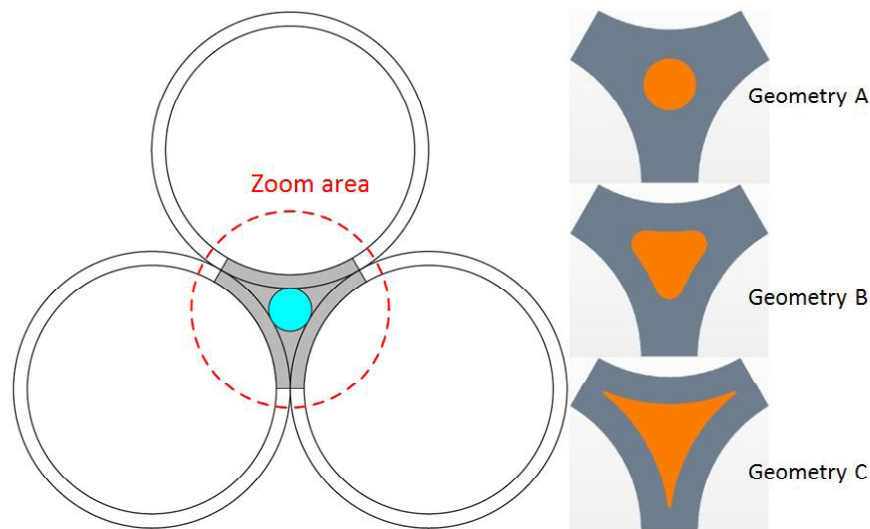
Fig. 2-1 Three channel geometries for analysis

The aim of this chapter is to clarify the channel thermal hydraulic characteristics of the tightly packed fuel assembly, mainly focusing on the channel geometry effect. The three cross-sectional channel geometries are respectively evaluated at Super FBR pressure (30MPa), PWR pressure (15.5MPa) and BWR pressure (7.17MPa). To study the characteristics of heat transfer is normally to conduct the related experiments, while the experiments give rise to a lot of capital as well as time costs. CFD technology is an alternative to experiment for fluid mechanics study and widely used for thermal hydraulic design to save the expensive experimental costs. The empirical methods, such as empirical correlations derived from experiments, also can be used for the study, but the parameter ranges and using conditions are usually restricted by conducted experiments (e.g. some CHF correlations are involved with boiling length). While CFD method is much more flexible and can describe complex geometries and apply various boundary conditions.

The numerical methods are introduced in Section 2.2, and the main prediction results at supercritical pressure and subcritical pressures are discussed in Section 2.3 and Section 2.4, respectively.

2.2 Numerical methods

CFD method is able to accurately depict the complex 3-D geometry and simulate the phenomena with high reliability. The accuracy of simulating supercritical fluids, single-phase and two-phase flow by CFD codes has been extensively tested. Many researchers (Kim *et al.*, 2004;

Koshizuka *et al.*, 1995; Yang *et al.*, 2006; Gu *et al.*, 2007; Gou *et al.*, 2010) achieved good agreements with the experimental data in modeling Super Critical Water (SCW) flows. In simulations of the subcritical flows, CFD codes also have been extensively verified regarding turbulence flow (Horvath and Dressel, 2012), heat transfer and void fraction of subcooled and saturated boiling (Krepper *et al.*, 2007; Petrov *et al.*, 2012) and even for more complicated phenomena such as boiling crisis (Habib *et al.*, 2014). In applications to assembly design, a lot of articles are available related to studies on the grid spacer in SCWRs (Zhu *et al.*, 2014) and PWRs (Cinosi *et al.*, 2014), as well as the safety aspects (Zhao *et al.*, 2013; Boyd and Skarda, 2014). Physical phenomena of the current study, such as two phase flow, wall boiling and conjugate heat transfer, can be captured in detail by CFD method.

The characteristics of the flows under the three different pressure conditions significantly differ from each other. In this study, the SCW flow is treated as single phase flow, while the flows at the both subcritical pressures are treated as two-phase flows. In a PWR core, bulk boiling as observed in a BWR core is not observed, but there exists some subcooled boiling and therefore, the coolant flow in a PWR core should be regarded as two phase flow. Hence, two sets of computational approach with different models are adopted. The water and steam properties are determined according to IAPWS-IF 97 database (Wagner and Kruse, 1998) and expressed as the polynomial functions of temperature at each operating pressure.

2.2.1 Conservation equations

For all the kinds of flow conditions mentioned above, the governing conservation equations are solved for mass and momentum by using the steady-state segregated flow model, which combines the pressure-velocity coupling with a SIMPLE-type algorithm. For the two-phase flow, each phase has its own set of the mass, momentum and energy conservation equations. Additional transport equations are also solved for turbulent flows.

2.2.1.1 The mass conservation equation

The equation for conservation of mass, also known as continuity equation, can be written as follows:

$$\frac{\partial \rho}{\partial t} + \nabla \cdot \left(\rho \, \boldsymbol{u} \right) = S_m$$

(2-1)

which is the general form for the mass conservation equation and is valid for both incompressible and compressible flows. ρ and u are the density and velocity respectively. The source term (S_m) is the mass transferred from one phase to another.

2.2.1.2 The energy conservation equations

The energy conservation equation is written in integral form is:

$$\frac{d}{dt}\int_V \rho E dV + \oint_A [\rho H(\mathbf{v} - \mathbf{v}_g) + \mathbf{v}_g p] \cdot d\mathbf{a} =$$
$$-\oint \dot{\mathbf{q}}'' \cdot d\mathbf{a} + \oint \mathbf{T} \cdot \mathbf{v} d\mathbf{a} + \int \mathbf{f} \cdot \mathbf{v} dV + \int s_u dV \tag{2-2}$$

where E is the total energy, H is the total enthalpy, q'' is the heat flux vector, T is the viscous stress tensor, v is the velocity vector, and v_g is the grid velocity vector. f is the body force vector representing the combined body forces of rotation and gravity. s contributes additional energy source terms, such as the heat generation rate in fuel pellet.

Total energy correlates with the total enthalpy H by:

$$E = H - p/\rho \tag{2-3}$$

where:

$$H = h + |\mathbf{v}|^2/2 \tag{2-4}$$

and

$$h = C_p T \tag{2-5}$$

2.2.1.3 The momentum conservation equations

The momentum equation in steady state can be expressed as：

$$\rho(\vec{u} \cdot \vec{\nabla})\vec{u} = -\vec{\nabla}p - \vec{\nabla} \cdot \vec{\vec{\tau}} + \rho\vec{f} \tag{2-6}$$

where f is the volumetric force vector accounting for the gravity force in the current study, and the viscous stress tensor can be described by Newton's law of viscosity:

$$\vec{\vec{\tau}} = -\mu(\vec{\nabla}\vec{u} + (\vec{\nabla}\vec{u})^T) + \frac{2}{3}\mu(\vec{\nabla} \cdot \vec{u})\vec{\vec{\delta}}. \tag{2-7}$$

2.2.2 Modeling the turbulence

2.2.2.1 Turbulence models

The turbulence models provide closure for Reynolds Averaged Navier-Stokes (RANS) equations. They are particularly important for the accuracy of modeling SCW flow, since the water properties at supercritical pressure experience large variations near the pseudo-critical point. In the recent years, many researchers have carried out comprehensive studies on the turbulence model selection for SCW flow.

Kim *et al.* (2004) pointed out that the RNG k-ε model with the enhanced wall treatment gives the most accurate prediction after studies of more than 10 first-order turbulent models, and Roelof *et al.* (2004) confirmed this finding. Yang *et al.* (2007) revealed that the two-layer model (Hassid and Poreh) is able to predict accurately and the Standard high *Re* model with wall function gives acceptable results; Gou *et al.* (2011) found that the Speziale non-linear quadratic high Re k-ε two layer model and the Standard high Re k-ε two layer model give the results which best describe the measurements; Cheng *et al.* (2007) performed the similar study by using CFX-5.6 and concluded that the tested 4 ε-type turbulence models (including Standard k-ε model and RNG k-ε model) agreed well with the experimental data, whereas the two ω-type models (SST and RSO) in CFX-5.6 were not recommended. Both Kim *et al.* and Yang *et al.* reported that the Low-Re number *k-ε* models result in higher temperature than the experiment data especially when the heat flux is high. Sharabi and Ambrosini (2009) tested six different Low-Re number *k-ε* models, and the same conclusion was given that the wall temperature was excessively overestimated, but the Low-Re number *k-ε* models could qualitatively depict the Heat Transfer Deterioration (HTD) phenomena.

In the current study, three turbulence models are selected for SCW flows as the candidates by referring to experience of previous researchers. They are Standard *k-ε*, Standard Two Layer *k-ε* and Realizable *k-ε* turbulence models. While for the two phase flows, the default Standard *k-ε* is used, which gives rise to the good results in simulating the PSBT international benchmark exercise (Lo and Osman, 2012).

The Standard *k-ε* model is one of the Eddy viscosity models based on the framework of RANS, in which Navier-Stokes equations for the instantaneous velocity and pressure fields are treated as the combination of a mean value and a fluctuating component. The Reynolds stress tensor T_t is treated as a function of the turbulent viscosity μ_t, indicated by following equation, also known as the Boussinesq approximation:

$$T_t = 2\mu_t \mathbf{S} - \frac{2}{3}(\mu_t \nabla \cdot \mathbf{v} + \rho k)\mathbf{I} \tag{2-8}$$

where *S* is the strain tensor:

$$\mathbf{S} = \frac{1}{2}(\nabla \mathbf{v} + \nabla \mathbf{v}^T) \tag{2-9}$$

where, *k* is the turbulent kinetic energy, *v* the velocity, ρ the fluid density and $\mathbf{I}$ the turbulence intensity. Additional transport equations are solved for scalar quantities μ_t that enable the turbulent viscosity to be derived. The standard *k-ε* model was firstly proposed by Launder and

Spalding (1972). It is robust, economical in terms of calculation cost, and reasonable accuracy is expected for a wide range of turbulent flows.

The Standard Two-Layer *k-ε* model combines the Standard *k-ε* model with the two-layer approach that allows the *k-ε* model to be applied in the viscous sublayer. The coefficients of the two models are identical, but the Standard Two-Layer k-ε model is more flexible for the treatment near the wall and has a better adaptability over a wide range of mesh size.

The Realizable *k-ε* model is developed relatively recently (Shih *et al.*, 1994). The turbulent dissipation rate ε is solved from a new transport equation (CD-Adapco, 2013) that is incorporated in this model. In addition, a key coefficient of the model, Cμ, can be expressed as the function of mean flow and turbulence properties, while that in the standard model is treated to be a constant. Therefore, the model satisfies certain mathematical constraints on the normal stresses which is consistent with the physics of turbulence, known as the realizability.

2.2.2.2 Near-wall treatments

The near-wall modeling has significant impacts on the accuracy of numerical solutions, because the mean vorticity and turbulence are mainly influenced by the walls. In the near-wall region, major variables have large gradients, such as temperature and velocity, leading to intense transports of the momentum and other scalar. Thus, for a flow problem that is strongly bounded with wall, accurate simulation of the flow in the near wall region plays a determining role for a successful prediction. A non-dimensional wall distance y+ is closely bounded with the near wall treatment, which is expressed as:

$$y^+ \equiv \frac{u_* y}{\nu}$$

(2-10)

where u_* is the friction velocity at the nearest wall, y the distance from near-wall cell center to the wall and ν is the local kinematic viscosity of the fluid.

Three types of wall treatment are provided in STAR-CCM+: 1) The high- y+ wall treatment, which assumes that the first node of the near-wall cell lies within the logarithmic region of the boundary layer and allows use of the wall-function; 2) The low-y+ wall treatment assumes that the viscous sublayer is adequately resolved and is only suitable for low-Reynolds number turbulence models; 3) The all- y+ wall treatment is a kind of a hybrid treatment that is relatively independent to mesh dividing of the near wall region: for coarse meshes, the solution is close to that of the high-y+ wall treatment, and for fine meshes it gives solution, which is close to that of the low-y+ wall treatment. It also gives good adaptability because it produces reasonable answers for meshes of intermediate resolution. In most high-Reynolds-number flows, the high y+ or all y+ approach saves computational resources substantially, because in the viscosity-affected near-wall

region, variables that vary dramatically do not need to be resolved by using a very fine mesh. These characteristics make the wall function method popular in account of its calculation cost, robustness, and reasonable accuracy and it is commonly used in industries.

This study focuses on the high y+ and two layer all y+ near-wall treatment in order to avoid creating meshes with large cell aspect ratio and as well as to save computational resource. Validations are provided in Sections 2.3.1. The standard wall function are used with the high y+ wall treatment, whereas the damping function with blended wall laws are used with the two layer all y+ wall treatment. Other parameters related to turbulence models are the default values in STAR-CCM+ (CD-Adapco, 2013).

2.2.3 Modeling the two phase flow

In modeling two-phase flow, phase interaction models are one of the key factors because they define how pairs of phases interact with each other across the interfacial area between them and to closure the conservation equations.

2.2.3.1 Interfacial momentum transfer

The momentum transfer between two phases is modeled in terms of drag force and non-drag force, as expressed in Eq. 2-11.

$$\vec{M}_i = \Sigma(\vec{F}_{ij}^D + \vec{F}_{ij}^{VM} + \vec{F}_{ij}^L + \vec{F}_{ij}^{TD})$$
$$\vec{F}_{ij} = -\vec{F}_{ji}^D$$

(2-11)

The drag force ($\vec{F}_{ij}^D$) plays the most important role and dominate the influence on the flow direction, whereas the no-drag force, namely the lift ($\vec{F}_{ij}^L$), the turbulent dispersion ($\vec{F}_{ij}^{TD}$) and the virtual mass forces ($\vec{F}_{ij}^{VM}$), act in crosswise direction (perpendicular to flow direction) with smaller magnitudes. Pierre and Bankoff (1966) and Roy *et al.* (2002) pointed out the application of the wall lubrication force may be questionable at high-pressure wall boiling conditions. It is also pointed out that this force is mainly considered for adiabatic two-phase flows, therefore it is not included in the current study. The accuracy of predicting the phase distribution is the resultant of the combined effects of all these above mentioned forces.

The drag force can be represented as:

$$\vec{F}_{ij}^D = \frac{1}{2}C_{ij}^D\rho_c|\vec{v}_j - \vec{v}_i|(\vec{v}_j - \vec{v}_i)A_p$$

(2-12)

where the ρ_c is the density of the continuous phase, A_p the projected area of the particle, C_{ij}^D the drag coefficient which takes the bubble size and shape into consideration and can be written as:

$$C_{ij}^D = C_{ij\infty}^D f_{ij}^D \tag{2-13}$$

in which the $C_{ij\infty}^D$ is the single-particle drag coefficient，f_{ij}^D the drag correction factor which covers physical effects of multiple particles such as hindering, swarming or coalescence. Because those characteristics of bubble change with change of concentration, it is important to apply the appropriate method to the drag coefficient at specific flow conditions. In this study, Tomiyama Drag Coefficient (Tomiyama, 1998) as the recommendation of STAR-CCM+ user guide (CD-Adapco, 2013) is used for all computational cases due to its applicability for a wide range of bubble size.

In addition, two drag correction methods are used in simulation to reproduce the terminal velocities as functions of bubble concentration. Depending on the approximate bubble size, they are Lockett Kirkpatrick (Lockett and Kirkpatrick, 1975) correction and Volume Fraction Exponent correction for small and relatively large channels, respectively.

The applied lift force is based on the theory of Auton *et al.* (1988) and represented as:

$$\vec{F}_L = C_l \alpha_d \rho_c [\vec{v}_r \times (\nabla \times \vec{v}_r)] \tag{2-14}$$

The Tomiyama (Tomiyama *et al.*, 2002) correlation is used to calculate the lift force coefficient.

The virtual mass force helps to improve the accuracy of modeling the acceleration of bubbles, and it is calculated by correlation from Auton *et al.* (1988) for two-phase flow:

$$\vec{F}_{ij}^{VM} = C_L^{VM} \alpha_d \rho_c [\vec{a}_j - \vec{a}_i] \tag{2-15}$$

The surrounding turbulent eddies interacting with dispersed bubbles results in the turbulent dispersion force, and it can be modeled as:

$$\vec{F}_{ij}^{TD} = A_{ij}^D \frac{v_c^t}{\sigma_\alpha} \left(\frac{\nabla \alpha_j}{\alpha_j} - \frac{\nabla \alpha_i}{\alpha_i} \right) \tag{2-16}$$

where v_c^t is the kinematic viscosity of liquid, σ_α is the turbulent Prandtl number.

2.2.3.2 Interfacial energy and mass transfer

To model the rate of bulk boiling and condensation between phases, which are due to the non-equilibrium state of two phases except at the interface where both phases are equal to the saturation temperature, Ranz-Marshall correlation (Ranz and Marshall, 1952) is used to compute the Nusselt number of continuous phase (liquid), while that of dispersed phase (vapor) is assumed to be at constant.

2.2.3.3 Wall heat transfer

To simulate the subcooled boiling, the heat balance at the wall can be generally expressed as three components:

$$q_w'' = q_{conv}'' + q_{evap}'' + q_{quen}'' \tag{2-17}$$

where q_{conv}'', q_{evap}'' and q_{quen}'' are the heat flux due to single-phase turbulent convection, quenching and evaporation, respectively. This model follows the approach of Kurul and Podowski (1990) which has been widely used and validated by several researchers (e.g. Krepper *et al.*, 2007 and 2011 and In *et al.*, 2013). These heat transfer mechanisms are modeled as functions of local thermal-dynamic conditions, namely the nucleation site density, the bubble departure diameter, the bubble departure frequency and the waiting time (the time interval between two bubbles formation at the same site). The relevant formulations can be referred to the user guide of STAR-CCM+ (CD-Adapco, 2013).

When approaching the CHF condition, the vapor contribution to heat flux is taken into account, thus, Eq. 2-17 can be represented as:

$$q_w'' = \left(q_{conv}'' + q_{evap}'' + q_{quen}''\right)\left(1 - K_{dry}\right) + K_{dry}q_{dry}'' \tag{2-18}$$

where q_{conv}'' indicates the vapor contribution to convective heat flux which is based on the single-phase turbulent convection by the vapor, and K_{dry} is vapor contact area fraction. It should be noted that K_{dry} is zero when the fluid is under non-CHF conditions where the heat transfer is fully depended on the liquid. In STAR-CCM+, the trigger mechanism of CHF is that, when the vapor volume fraction of the near wall cell exceeds a specified value, the local wall begins to dryout and heat transfer from the wall to the vapor begins, as an consequence, which declines the heat transfer of liquid convection and evaporation. The layer averaged vapor volume fraction α_δ is defined as:

$$\alpha_\delta = \frac{1}{\delta} \int_0^\delta dy \left[\alpha_g(y_c) + \frac{\partial \alpha_g}{\partial y_c}(y_c)(y - y_c) \right] = \alpha_g(y_c) + \frac{\partial \alpha_g}{\partial y_c}(y_c)\left(\delta/2 - y_c\right) \tag{2-19}$$

where $\alpha_g(y)$ is the bubble volume fraction as the function of distance y from wall, y_c is the distance at cell center from the wall, and δ is the near wall layer thickness defined as the distance from the first cell center to the wall. Based on above definitions, K_{dry} can be expressed as:

$$K_{dry} = \begin{cases} 0 & \alpha_\delta \leq \alpha_{dry} \\ f(\beta) & \alpha_\delta > \alpha_{dry} \end{cases} \tag{2-20}$$

where the α_{dry} is the critical vapor volume fraction at which heat transfer to vapor begins, $f(\beta)$ is the function:

$$f(\beta) = \beta^2(3 - 2\beta)$$
$$\beta = \frac{\alpha_\delta - \alpha_{dry}}{1 - \alpha_{dry}} \tag{2-21}$$

According to the critical heat flux model derived by Weisman and Pei(1983), $\alpha_{dry} = 0.82$ is used in current study when approaches to Departure from Nucleate Boiling (DNB) conditions, in other words, DNB can be identified by either near wall void fraction $\alpha_{dry} > 0.82$ (Weisman and Pei, 1983) or $K_{dry} > 0$. From Eq. 2-18, it should be note that K_{dry} value of slightly above zero does not cause q_w'' to decrease dramatically but is the start point of the sharp decrease of q_w'', and the DNB here is defined as the point just before the q_w'' sharply decreases(OECD, 2010).

2.3 Channel geometry analysis at supercritical pressure

2.3.1 Validation at supercritical pressure

To validate the capability of STAR-CCM+ for simulating supercritical flow by selecting the appropriate turbulence models as well as the meshing conditions, a comparison has been done against Yamagata's experimental data (Yamagata, 1972). The supercritical water has characteristics of large and continuous variation of properties at pseudo-critical point as shown in Fig. 2-2. Therefore, the turbulence model is vital for the accurate simulation. By referring to experience from previous researchers as explained in Section 2.2.2.1, three turbulence models as well as the near-wall treatment are selected and summarized in Table 2-1.
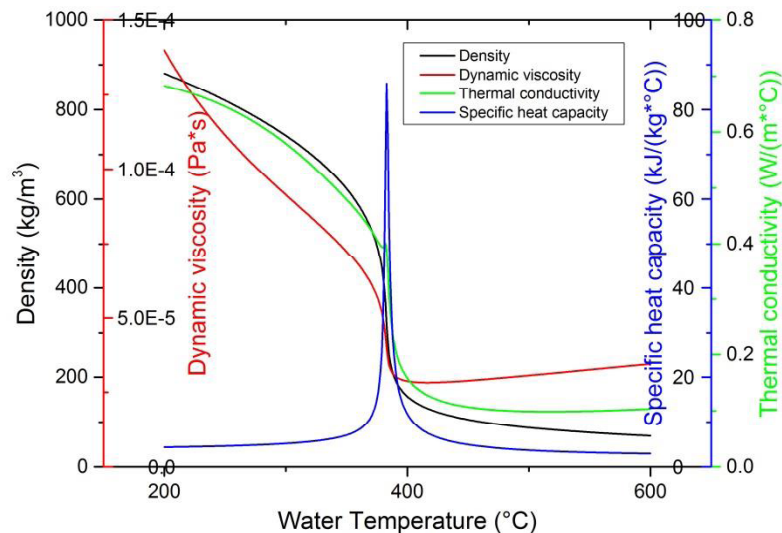
Fig. 2-2 Supercritical Water thermal properties at 24.5MPa

Table 2-1 Turbulence models and corresponding mesh conditions selected in this study

Turbulence model	Near-wall treatment	Cell number (N1, N2, N3)	Average y+ (y_1^+, y_2^+, y_3^+)
Standard k-ε Two Layer (Wolfstein)	Two layer all y+	451526, 306967, 143105,	34.2, 37.8, 42.8
Standard k-ε	High y+	428473, 293618, 140281	36.6, 40.2, 44.1
Realizable k-ε	High y+	431554, 291181, 144557	36.4, 39.1, 43.5

The computational conditions for validation are based on Yamagata's experiment: the reference pressure is 24.5 MPa, and a circular tube with diameter of 7.5 mm is vertically oriented. The inlet mass flux is 1260 kg/m^{2}s, and a uniform heat flux of 698 kW/m^2 is applied on the tube wall. All the boundary conditions are schematically illustrated in Fig. 2-3. The simulations were conducted by using the 3-D geometrical model, which is 1/12 of the integrated tube by considering the symmetry. The supercritical water properties used in the numerical simulation were according to IAPWS-IF 97 database (Wagner and Kruse, 1998), which is wildly applied and acknowledged. Because the axial and radial pressure differences are very small compared with the system pressure, they were ignored and assumed not to affect the water properties.
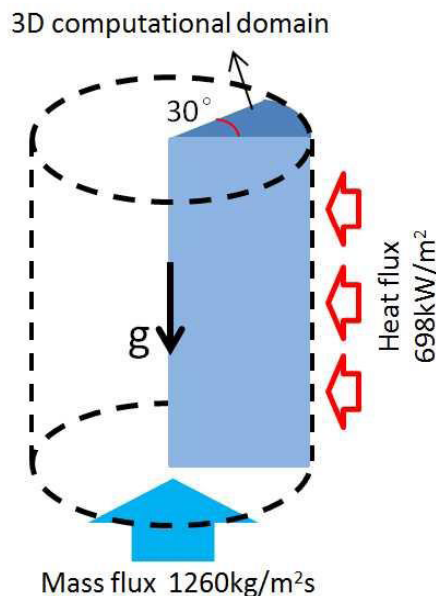
Fig. 2-3 Computational model for Yamagata's experiment

The reliability of numerical simulations strongly depends on the meshing methods for the selected turbulence models. To obtain results with sufficiently fine meshes, which provide converged results with respect to the mesh number, for each turbulence model, three levels of mesh are established by using the polyhedral mesh technology (a group of sample meshes are shown in Fig. 2-4), and the cell number and y+ characteristics of each mesh are summarized in Table 2-1. As the cell number increases, the resolution of boundary layer is also refined, but the y+ values larger than 30 are confirmed (high y+ wall treatment normally requires y+ > 30) for simulations with either the high y+ or the two layer all y+ near-wall treatment. The y+ values in this study refer to the average values along the channel.
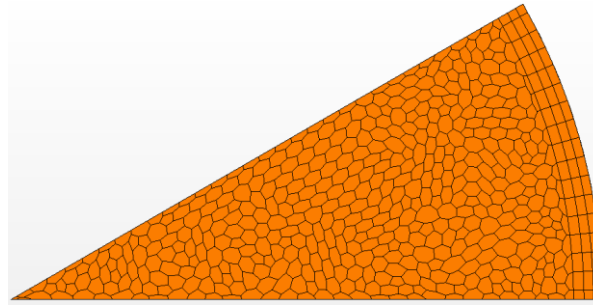
Fine mesh
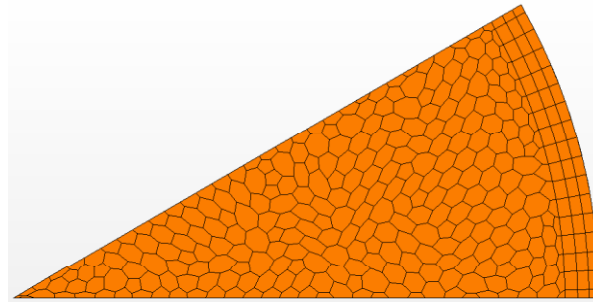
Middle mesh
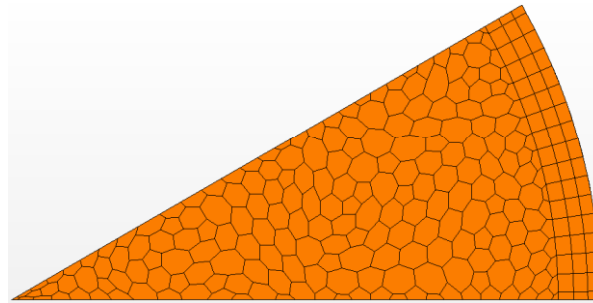
Coarse mesh

Fig. 2-4 Meshes with different refinements at cross-sections

Figure 2-5 shows the evaluated wall temperatures using the selected turbulence models compared with experimental data. Figure 2-5 shows that the evaluated wall temperatures given by the Standard k-ε two-layer model agrees the best with the experimental data among the three models, though small deviations appear near the pseudo-critical point. In the cases of using the standard k-ε model, the evaluated wall temperature is relatively lower than the experimental data until near the pseudo-critical point. This is consistent with the results reported by Kim *et al.* (2004) and Gou *et al.* (2010). On the contrary, in the cases of using the realizable k-ε model, the

evaluated wall temperatures are higher than the experimental data especially near the pseudo-critical point.

The average relative errors due to mesh number and the average relative errors of the results with finest mesh from the experimental data are summarized in Table 2-2. In calculations of the relative errors caused by mesh, the finest meshes are taken as the reference meshes, and the e_m and e_s in Table 2-2 indicate the relative errors of the coarse mesh and the middle number mesh respectively. It is seen that the deviations of the three curves in each sub-figure of Fig. 2-5 are small, and the relative errors shown in Table 2-2 are negligible for the purpose of conceptual design.
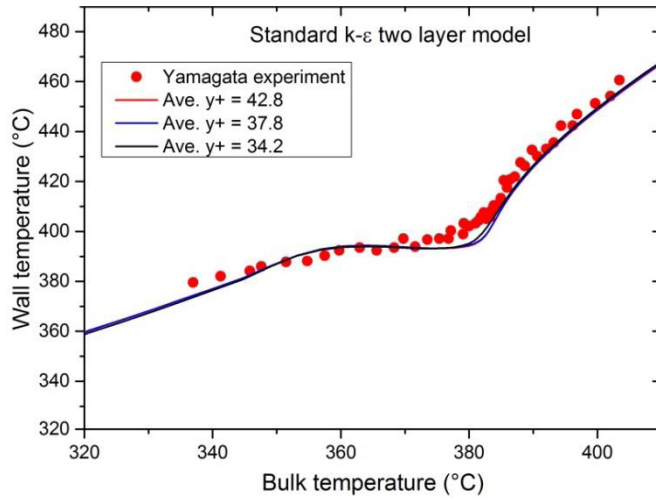
(a) Standard k-ε two layer model
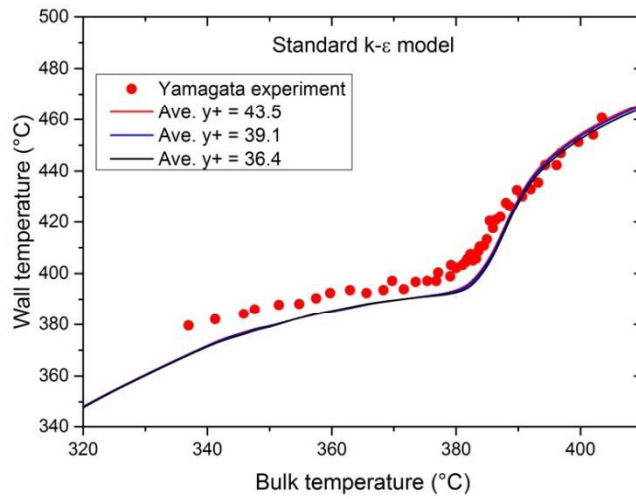
(b)Standard k-ε model
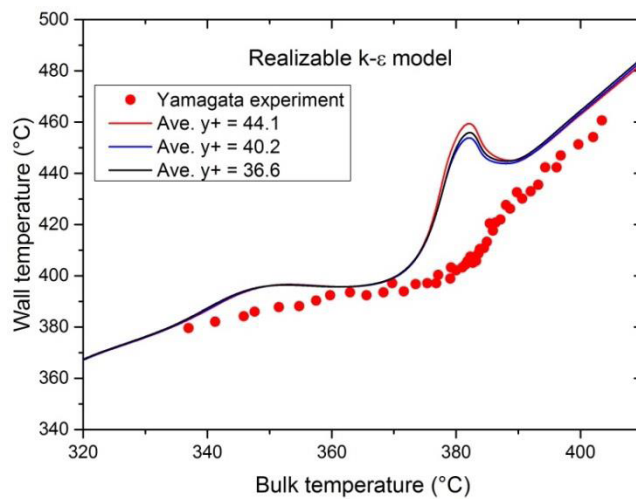
(c)Realizable k-ε model

Fig. 2-5 Wall temperature distribution with different turbulence models

Table 2-2 Relative errors of turbulence models

Turbulence model	Average errors of mid and fine mesh results relative to the finest mesh results (e_m, e_s)	Average error of the finest mesh result relative to the experimental data
Standard k-ε two-layer (Wolfstein)	0.21%, 0.25%	0.93%
Standard k-ε	0.12%, 0.19%	1.72%
Realizable k-ε	0.21%, 0.24%	3.40%

Based on above results, the subsequent simulations adopt the Standard k-ε two-layer model with all y+ near-wall treatment and keep the average y+ value greater than 30. This turbulence model gives rise to the most accurate results among all selected models

2.3.2 Geometrical models and mesh generation

Different cross-sectional geometries of the coolant channel in tightly packed fuel assembly are established with the purpose of understanding the geometrical effect on the thermal hydraulic performance. The constructing method is shown in Fig. 2-6. The potential fluid region is the space that is surrounded by three tangentially contacted fuel rods, and it appears as a triangle-like shape where the coolant channel is confined. The boundary of coolant channel can be smoothly extended from a circular shape towards vertices of this triangle. The rest of the space between claddings and channel is occupied by stainless steel which is the same material as cladding.

A character number named sharp degree (SD) is proposed in this study to quantitatively depict the continuous variation of these shapes. Eq. 2-22 defines the SD value, where L is the largest dimension of geometry (from geometric center towards the tangency point of fuel rods) and R is the radius of the equivalent circle with the area being equal to the channel. Geometrically, it can be inferred that SD ranges from 1 to 2.537, and as this value increases, the area of coolant channel increases as well, however, the hydraulic diameter continuously increases until SD is around 1.25 then turns to decrease. Figure 2-7 shows hydraulic diameter versus the channel area. Three representative geometries are selected to perform the study, namely the geometry A, B and C, with SD values of 1, 1.25 and 2 respectively. The cross-sections have been shown in Fig. 1-12 and here lists the detail geometrical parameters in Table 2-3.

$$SD = L/R \qquad (2\text{-}22)$$
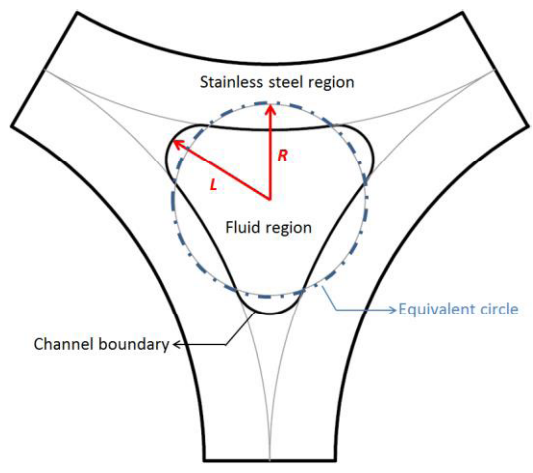
Fig. 2-6 Geometry construction method
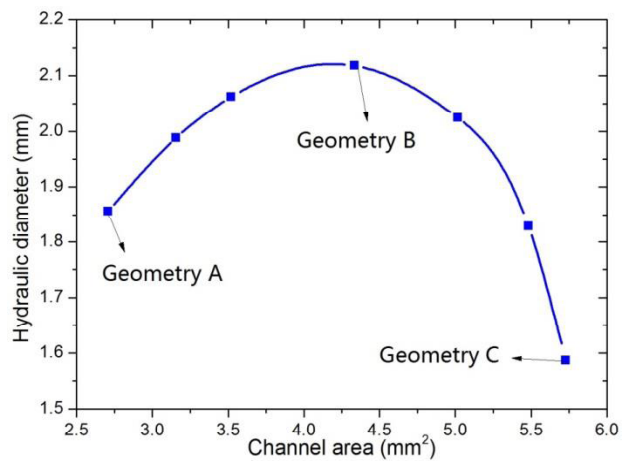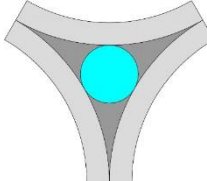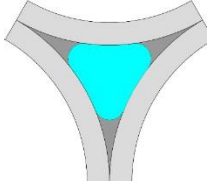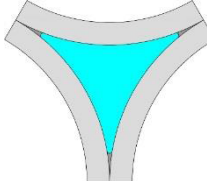
Fig. 2-7 Hydraulic diameter vs. channel area

Table 2-3 Geometric images and parameters

Geometry	A	B	C
Image			
SD	1	1.25	2
Fluid area(mm^2)	2.7066	4.3339	5.7279
Hydraulic diameter(mm)	1.8564	2.1183	1.5863

Coolant · Cladding · Metal fitting

These geometries are confined by metal fitting and three representative geometries are selected: Geometry A (circular) represents the reference geometry, which has the smallest channel area among the three; geometry C (triangle with pointed corner) represents the largest channel area among the three; geometry B (triangle with round corner) represents the intermediate shape between A and C, characterized by the largest hydraulic diameter among the three.

By taking advantage of the symmetry, 1/6 of the intact channel and related cladding are taken as the CFD computational domains as shown in Fig. 2-8(a), and the mirror boundaries are adopted on the cutting edges due to the symmetry in physics. All the models were created by using commercial computer aided design (CAD) software AutoCAD 2012 (Kevin and Alan, 2011). The mesh generation was performed by polyhedral mesh technology from STAR-CCM+, which has a unique superiority on dealing with complex geometry. In regions where spatial gradient are high, such as the corner of geometry C, and regions where strong shear layers are present, relatively higher resolution was applied with the purpose of improving the accuracy and convergence. The generated computational meshes for three geometries are shown in Fig. 2-8(b).
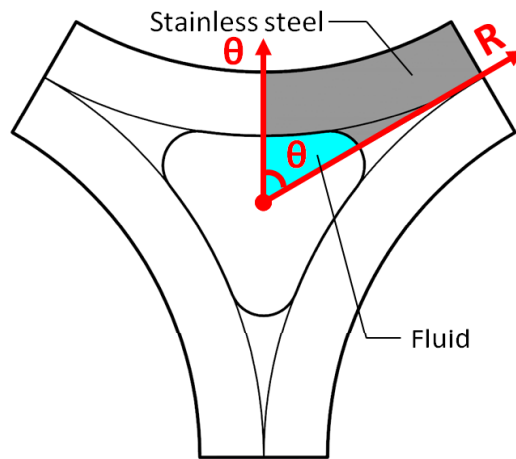
(a) Schematic diagram of computational domain in cylindrical coordinate
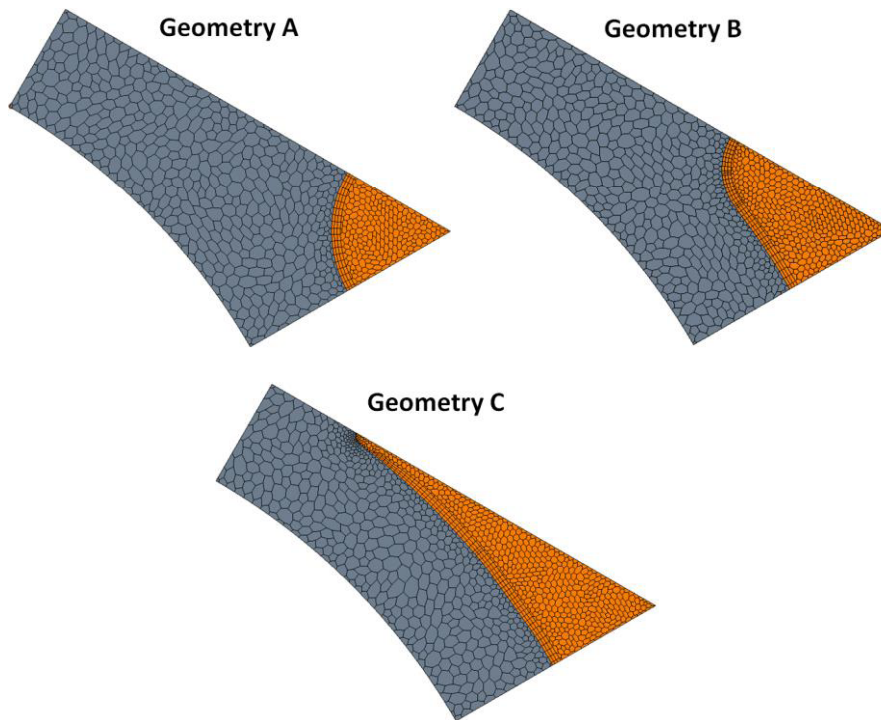
(b) Meshing of computational models

Fig. 2-8 Computational domain and meshing of the CFD analyses

2.3.3 Boundary conditions and assessment criteria

The boundary conditions of the following simulations are shown in Fig. 2-9 in terms of inlet temperature, outlet temperature, system pressure and the power, which are governed by the energy conservation equation:

$$h_{out} - h_{in} = \frac{P_h}{G_m A} \int_{z_{in}}^{z_{out}} q''(z) dz \qquad (2\text{-}23)$$

where,

h, bulk enthalpy

P_h, Perimeter of channel

G_m, mass flux

A, area of channel

q'', heat flux

z, axial height of channel

   The mass flux is considered as a dependent variable determined by power and outlet temperature. Except the mass flux, power and channel geometry, all other computational conditions, such as system pressure, fuel rod diameter, cladding thickness, inlet temperature and axial height, are based on the design presented by Oka *et al.* (2013) and listed in Table 2-4.
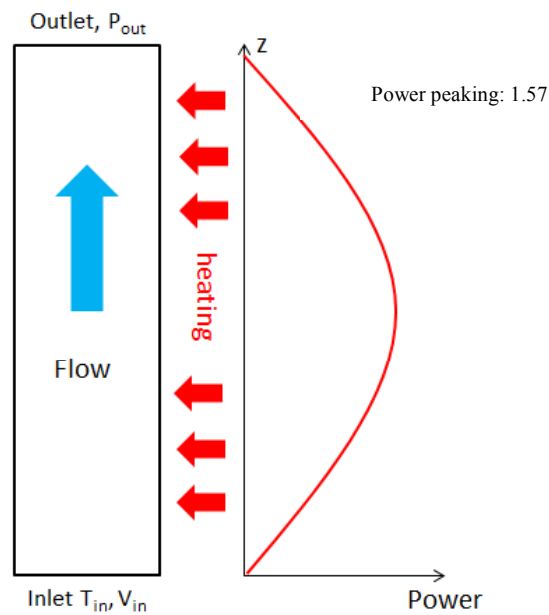
Fig. 2-9 Boundary conditions for the CFD analyses

Table 2-4 Specification of computational conditions

Parameter	Value
Core operating pressure (Mpa)	30
Inlet temperature (°C)	385
Core height (m)	2.0
Outer diameter of fuel rods (cm)	1.2
Cladding thickness (cm)	0.0873
Pellet diameter (cm)	1.0124
Gap between clad and pellet (cm)	0.0065
Fuel rod pitch (cm)	1.2
Gap between fuel rods (cm)	0

In the earlier numerical analysis for assembly design for Super FRs, researchers such as Yang *et al.* (2007) and Cheng *et al.* (2007) applied a uniform heat flux on the wall and the non-uniformity of axil power distribution in reactors was neglected. In the present study, a typical cosine axil power profile, with power peaking of 1.57, is applied for all the cases with the purpose of approaching the realistic power distribution of a typical nuclear reactor.

The so-called computational variables are selected from the boundary conditions including the channel cross-sectional geometry, average power level and outlet temperature. The purpose of these computational variables is to cover the potential design range of Super FBRs as well as to obtain a consistent assessment over a range of boundary conditions. For each geometry, 9 cases were calculated (3 power levels Multiplied by 3 outlet temperatures); respectively, the average power levels are selected as 10kW/m, 15 kW/m and 20 kW/m and outlet temperatures are 500°C, 550°C and 600°C. These parameters generally cover the design range of Super FBR (Yoshida and Oka, 2013).

In the earlier study of SCWRs, Dobashi *et al.* (1998) proposed the criterion of MDHFR to avoid HTD (where the heat transfer coefficient substantially drops) at supercritical pressure, but lately, it was found that the cladding surface temperature (CST) is predictable even HTD occurs, and Kitoh *et al.* (1997) calculated the heat transfer coefficient at various mass flow rates and heat fluxes which enabled to replace the design criterion of MDHFR > 1.3 to the new design criterion of maximum cladding surface temperature (MCST) < 650°C (Oka *et al.*, 2010) to maintain the integrity of cladding under transients. In the present study, the surface of cladding is defined as the interface between the fluid and stainless steel, and the previous MCST criterion is retained

preliminarily. Additionally, the maximum temperature of cladding (MAXT) is taken into account due to the anisotropy of the heat transfer, and 700°C is tentatively adopted for MAXT from the view point of thermodynamics (P. MacDonald, *et al.*, 2005), so that the thermal stress can be limited. Pressure drop is another concern of this study. As reported by Yoshida and Oka (2014), it should be limited under 2MPa with high head pumps. Given above all, the assessment parameters are determined to be MCST, MAXT and pressure drop.

2.3.4 CFD results at Super FBR pressure

One of the major purposes of this study is to evaluate the geometrical effect of the coolant channel on the thermal hydraulic characteristics of the tightly packed fuel assembly at different outlet temperatures and power levels. Three geometries are compared in terms of MCST, MAXT and pressure drop.

2.3.4.1 Mesh sensitivity analysis

The mesh sensitivity analyses are conducted for three meshes of varying cell number for each geometry. The computational conditions are the same as listed in Table 2-4 while the power and outlet temperature are set to be representative constant values, and they are 15kW/m and 550°C respectively. The critical variables (represented by Greek letter Φ with a subscript to indicate the mesh) in terms of MCST, MAXT, pressure drop (ΔP) and outlet temperature (T_{out}) are evaluated based on analysis of the relative errors. The values of the finest meshes are used as the reference to calculate the errors. The results as well as the cell numbers for each geometry are summarized in Table 2-5. It can be seen that the relative errors generally decrease with the mesh refinement, and all are within 2%. In the cases of geometry C, the relative errors associated with the cladding temperatures (MCST and MAXT) are relatively larger (>1.3%) compared with the cases of geometry A and B (both less than 0.6%), whereas the errors of pressure drop are smaller (< 0.2%). All the errors of outlet temperature are small (<0.3%). The results suggest that the solution has converged and mesh independence has been achieved. Hence, the meshes with middle cell number are used for the following simulations.

Table 2-5 Sensitivity analysis results at supercritical pressure with different meshing for geometry A, B and C

		Φ=MCST(°C)	Φ=MAXT(°C)	Φ=ΔP(MPa)	Φ=Tout(°C)
Geometry A	Mesh number N1, N2, N3	987022,471588 ,189781	987022,471588 ,189781	987022,471588 ,189781	987022,471588 ,189781
	Average y+ (y_1^+, y_2^+, y_3^+)	34.9,38.1,41.7	34.9,38.1,41.7	34.9,38.1,41.7	34.9,38.1,41.7
	Φ1, Φ2, Φ3	571.87,572.40, 573.10	693.15,693.31, 692.70	0.761,0.757, 0.751	552.00,552.37, 553.23
	e_m, e_s	0.092%, 0.215%	0.023%, 0.065%	0.525%, 1.314%	0.067%, 0.223%
Geometry B	Mesh number N1, N2, N3	1111781,55482 9,217016	1111781,55482 9,217016	1111781,55482 9,217016	1111781,55482 9,217016
	Average y+ (y_1^+, y_2^+, y_3^+)	35.9,37.4,42.1	35.9,37.4,42.1	35.9,37.4,42.1	35.9,37.4,42.1
	Φ1, Φ2, Φ3	587.66,587.38, 585.51	675.72,674.48, 672.21	0.300,0.298, 0.296	551.47,551.53, 552.17
	e_m, e_s	0.047%, 0.366%	0.184%, 0.520%	0.702%, 1.334%	0.011%, 0.127%
Geometry C	Mesh number N1, N2, N3	1612021,68359 8,307172	1612021,68359 8,307172	1612021,68359 8,307172	1612021,68359 8,307172
	Average y+ (y_1^+, y_2^+, y_3^+)	34.1,37.1,41.5	34.1,37.1,41.5	34.1,37.1,41.5	34.1,37.1,41.5
	Φ1, Φ2, Φ3	634.06,638.70, 642.68	663.48,666.54, 672.47	0.203,0.203, 0.204	550.12,550.38, 550.98
	e_m, e_s	0.732%, 1.360%	0.461%, 1.354%	0.153%, 0.400%	0.046%, 0.155%

2.3.4.2 Cladding temperatures and pressure drop

Figure 2-10 shows the results of simulations with 500°C outlet temperature. It can be seen that the MCST and the MAXT almost linearly increase with the power. Figure 2-10 (a) indicates that MCST of geometry A is the highest and followed by geometry B and C. In addition, it is shown that MCST difference between geometry B and C is relatively small, while that between geometry

A and B is much larger. It is also revealed that the MCST increase with power of geometry A is more than that of geometry B and C. For MAXT, as shown in Fig. 2-10 (b), the line of geometry B still lies in the middle, whereas that of geometry C shifts to the top. It should be noted that the outlet temperature is fixed, so that increase of power leads to an increase of mass flux, seen from heat balance Eq. 2-23 and the boundary conditions summarized in Table 2-4, therefore, a higher pressure loss in higher power cases can be seen from Fig. 2-10 (c) due to the greater flow acceleration and the heavier friction between the wall and fluid. The channel area can be regarded as an intrinsic characteristic of geometry, smaller area leads to a higher fluid velocity at the same mass flow rate, and therefore, geometry A gives a higher pressure drop than that of B and C.
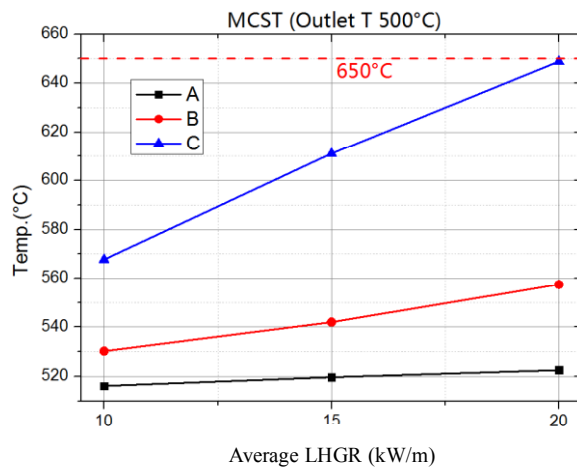
(a) MCST
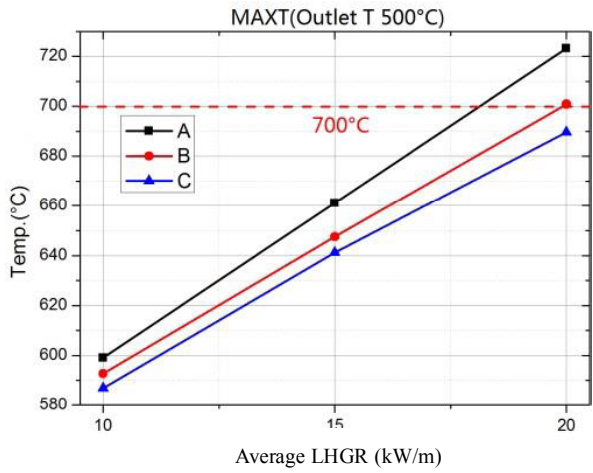
(b) MAXT
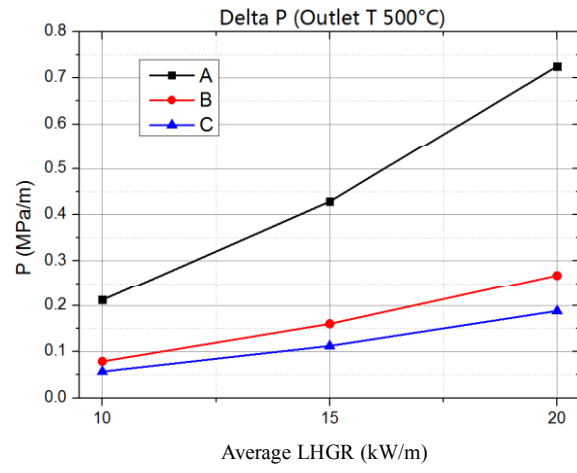
(c) Pressure drop

Fig. 2-10 MCST, MAXT and pressure drop dependence on average LHGR at outlet temperature of 500°C

Figure 2-11 and Fig. 2-12 show the results of simulations with 550°C and 600°C outlet temperature, respectively. Generally, the variation trends of all assessment parameters are consistent with above discussions. From the viewpoint of magnitude, the MCSTs and MAXTs increase with the increase of outlet temperature. However, under a fixed power, the increase of outlet temperature leads to a decrease of mass flux (seen from Eq. 2-23 and Table 2-4), thus the pressure drops decrease slightly. From all the above figures, it can be noted that the assessment parameters of geometry B are always inclined to approach the lowest values (e.g. MCST of geometry A, MAXT and pressure drop of geometry C) among the three geometries, the overall characteristics of geometry B is better than the other two from the viewpoint of attaining broader design ranges under the given design criteria of MCST, MAXT and pressure drop.
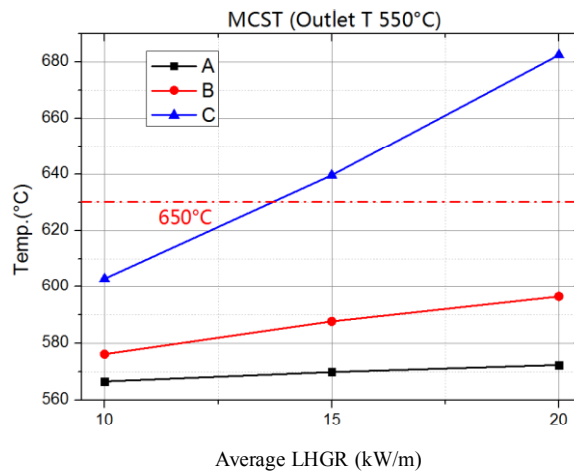
(a) MCST
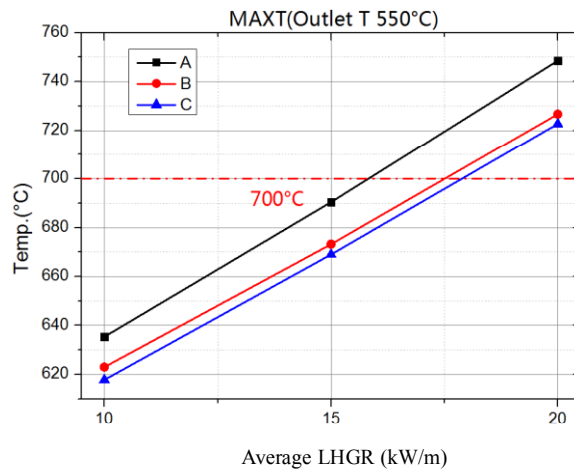
(b) MAXT
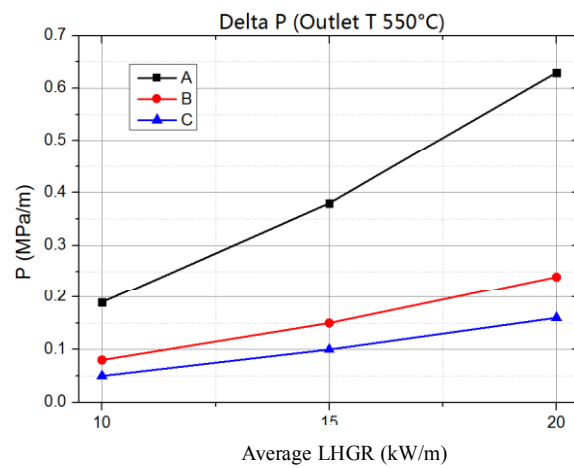
(c) Pressure drop

Fig. 2-11 MCST, MAXT and pressure drop dependence on average LHGR at outlet temperature of 550℃
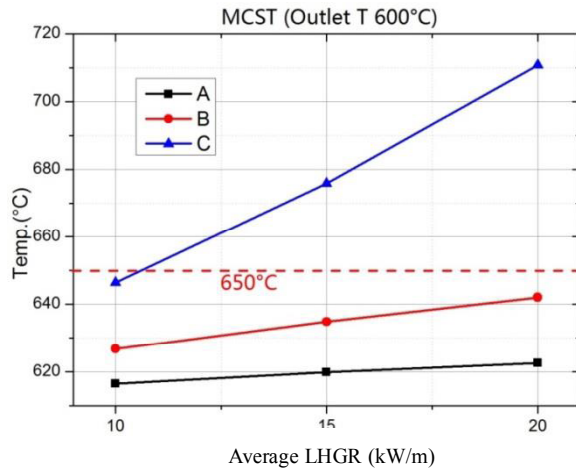
(a) MCST
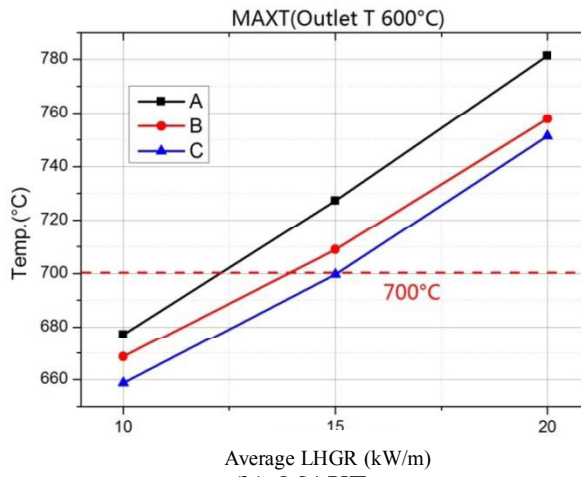
(b) MAXT
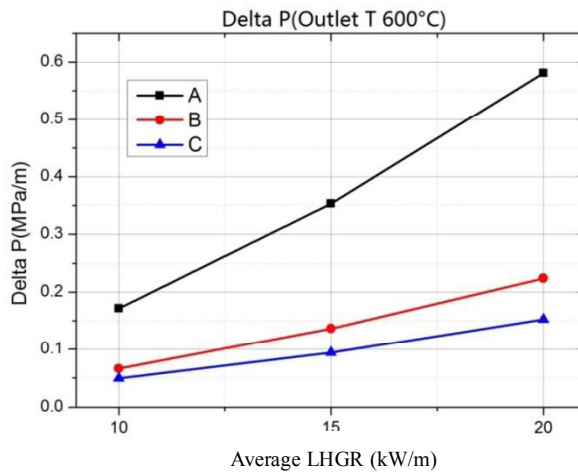
(c) Pressure drop

Fig. 2-12 MCST, MAXT and pressure drop dependence on average LHGR at outlet temperature of 600°C

2.3.4.3 Pressure drop consideration

Generally, the total pressure drop $\Delta p_{tot.}$ is composed of three main parts and can be expressed as:

$$\Delta p_{tot.} = \Delta p_{fri.} + \Delta p_{acc.} + \Delta p_{grav.} \tag{2-24}$$

where $\Delta p_{fri.}$ is the friction pressure drop, $\Delta p_{acc.}$ is the acceleration pressure drop, and $\Delta p_{grav.}$ is the pressure drop caused by elevation. Respectively, they can be represented as:

$$p_{fri.} = \frac{G^2}{2\rho} \cdot \frac{L}{D} \cdot f \tag{2-25}$$

$$p_{acc.} = G^2 \left(\frac{1}{\rho_{out}} - \frac{1}{\rho_{in}} \right) \tag{2-26}$$

$$p_{grav.} = g \left(\frac{\rho_{out} + \rho_{in}}{2} \right) \cdot L \tag{2-27}$$

where G is mass flux (kg/m²s), L the channel length (m), f the friction factor, g the gravity (9.81 m/s²), ρ the coolant density (kg/m³) and D the hydraulic diameter (m).

In the current computational models, all the cases have the same channel length, and thus for the cases with the same outlet temperature, $\Delta p_{grav.}$ are the same. From Eq. 2-25 and Eq. 2-26, it can be seen that both $\Delta p_{fri.}$ and $\Delta p_{acc.}$ are proportional to the mass flux squared. By subtracting the $\Delta p_{grav.}$ in Eq. 2-24 and moving the G^2 to the left hand side in Eq. 2-25 and Eq. 2-26 then combining the three equations, the rest part at the right hand side of Eq. 2-24 $\left(\Delta p_{tot.} - \Delta p_{grav.} \right)/G^2$ would be dependent on the channel geometry and independent from the mass flux, and this term has the same dimension as specific volume (the unit is m³/kg). Figure 2-13 shows the variation of $\left(\Delta p_{tot.} - \Delta p_{grav.} \right)/G^2$ with respect to average LHGR. It shows that pressure drop in geometry B is lower than those of geometry A and C under the given average LHGR condition. It is also seen that as the outlet temperature increase, this advantage of geometry B over geometry A becomes smaller, but over geometry C becomes larger.
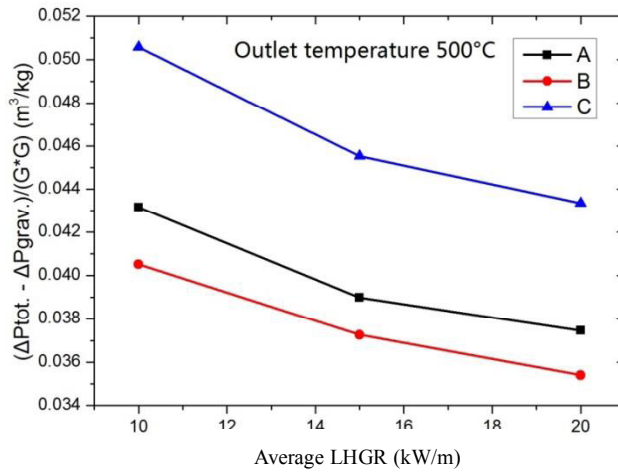
(a) Tout = 500°C
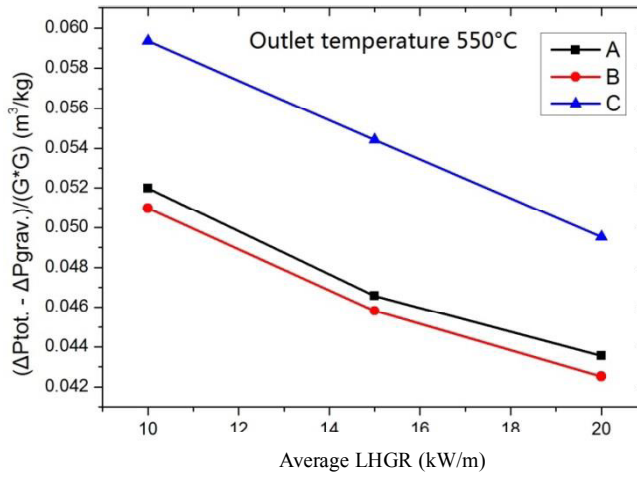
(b) Tout = 550°C
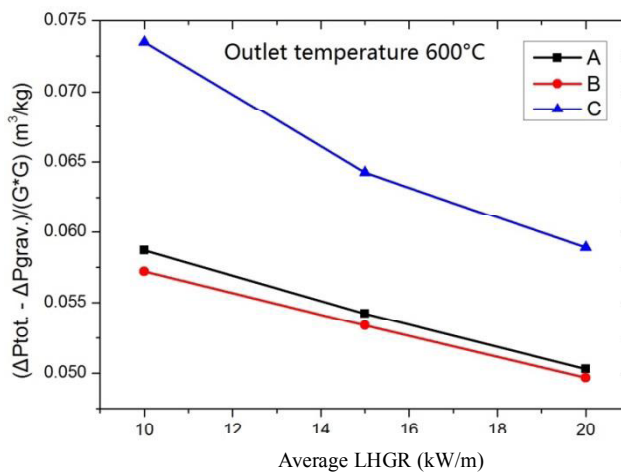
(c) Tout = 600°C

Fig. 2-13 Results of $\left(\Delta \mathrm{p_{tot.}} - \Delta \mathrm{p_{grav.}}\right)/\mathrm{G}^2$ vs. average power at different outlet temperatures

2.3.4.4 Determination of design area for Super FBR

From Fig. 2-9 to Fig. 2-12, it is seen the all the assessment parameters have the approximate linear relations with power. By linear interpolation, the design area of a Super FBR with the tightly packed fuel rod assembly can be determined in terms of average LHGR and outlet temperature. The calculations show that MCST and MAXT are the limiting parameters, while the pressure drop is within the allowance of criterion even under the most limiting condition (geometry A, 20kW/m, 500°C). The specific design areas for the three geometries with different power levels and outlet temperatures are summarized in Table 2-6 and Table 2-7, respectively, from which it is seen that, in most situations, geometry B is superior to the other two especially for high power level and high outlet temperature.

Table 2-6 Maximum applicable power at different outlet temperatures

Target outlet temperature	Maximum applicable average linear power(kW/m) for each geometry		
	A	B	C
500°C	16	20	20
550°C	16	17.5	13.8
600°C	12.5	13.8	11

Table 2-7 Maximum achievable outlet temperature at different average power level

Average power level	Maximum achievable outlet temperature(°C) for each geometry		
	A	B	C
10kW/m	629	628	600
15kW/m	567.5	587.5	567.5
20kW/m	461	500	500

2.3.4.5 Temperature distribution and heat transfer characteristics

Temperature distribution

In the current study, the non-uniform heat conduction is considered throughout all the simulations in both the axial and radial directions. The most important impact of this non-uniformity is on the temperature distribution as well as the heat transfer coefficient (HTC) distribution. Figure 2-14 shows the typical cross-sectional temperature color maps at 400°C bulk coolant temperature. It is seen that point A is the position where the highest cladding temperature appears.
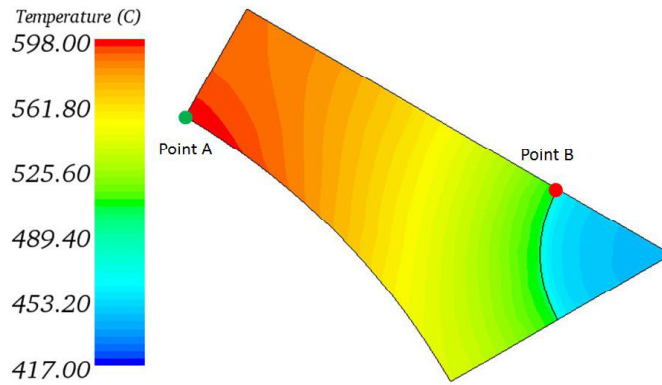
Geometry A
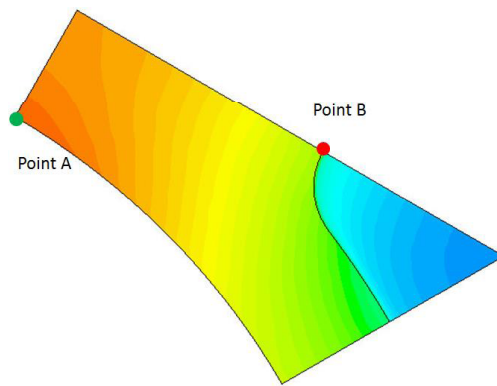
(b) Geometry B
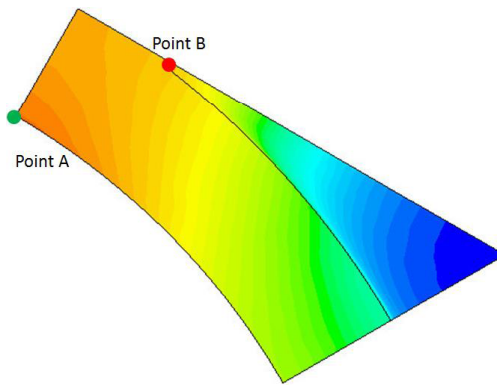
(c) Geometry C

Fig. 2-14 Radial temperature color maps at average power = 10KW/m, T_{out} = 500°C, T_{bulk} = 400°C

Figure 2-15 shows the typical cladding surface temperature distribution in a cylindrical coordinate. The temperature difference across the angle 0° to 60° varies from less than

5°C in geometry A to around 50°C in geometry C, and it also indicates that the MCST radially occurs at point B (0°). It can be explained that the heat from point A is conducted through the longest distance (the largest heat resistance) to be transferred to the fluid. Thus, there is the highest cladding temperature; at point B, the highest temperature of cladding surface occurs due to the poor heat transfer that is limited by spatial effect. Figure 2-16 indicates that the temperature difference increases from 0° to 60°with the power or mass flux in geometry B and C.
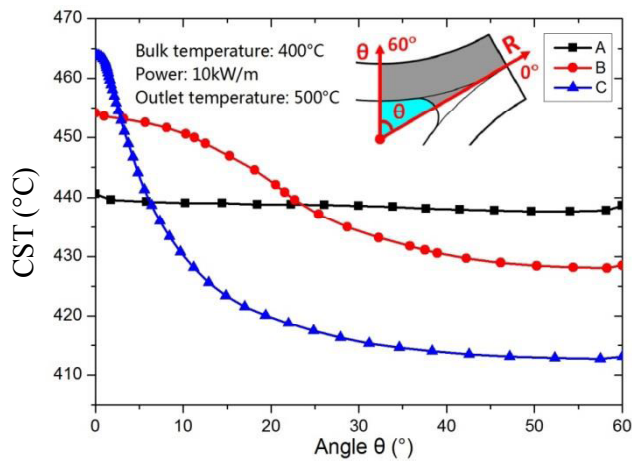
Fig. 2-15 Circumferential cladding surface temperature distribution for the three geometries
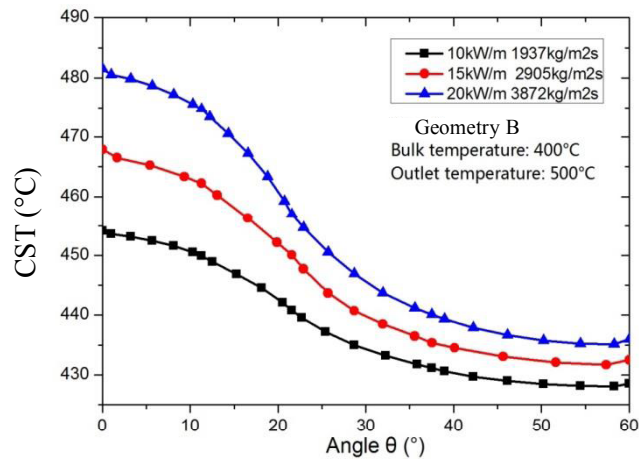
(a) Geometry B
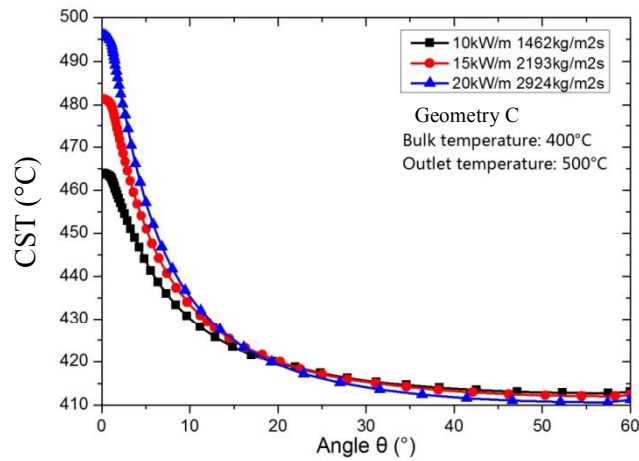
(b) Geometry C

Fig. 2-16 Circumferential cladding surface temperature distribution with different power

In the axial direction, the temperature distribution is characterized by the power profile as presented in Fig. 2-17. In each sub-figure, two solid curves show the axil temperatures of point A and B respectively. It is clearly seen that, the difference between the MAXT and the MCST becomes smaller from geometry A to geometry C, which has been discussed in Section 4.1. Figure 2-17 also indicates that the power profile affects the axial temperature distribution heavier one by one from geometry A to geometry C, because both the locations of MAXT and MCST are axially moving toward the power peak (H = 1.0m).
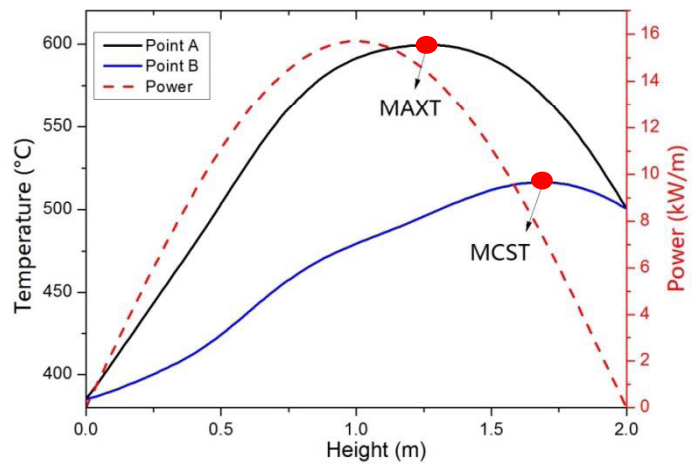
(a)Geometry A
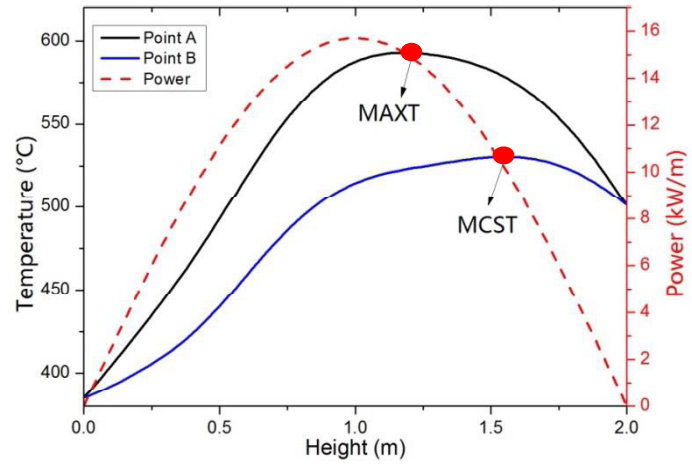
(b)Geometry B
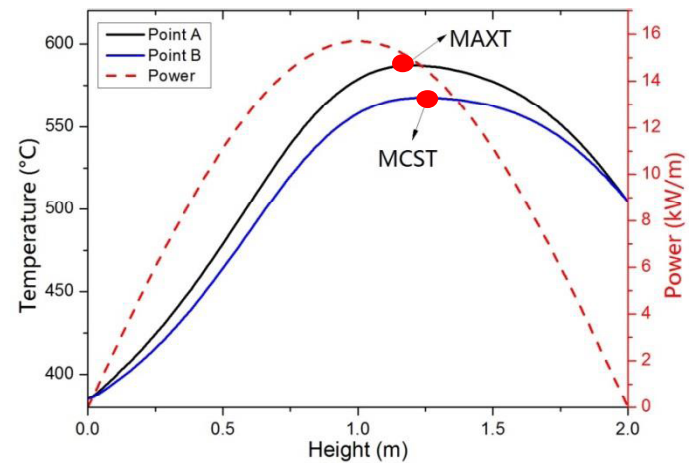
(c) Geometry C

Fig. 2-17 Axial temperature distribution of point A and B at average power = 10kW/m, Outlet T = 500°C

Local heat transfer coefficient (HTC) distribution

Figure 2-18 shows the circumferential local HTC distributions in the cross-sectional interface at different bulk coolant temperatures, which present the fact that the poor heat transfer results in the highest surface temperature at 0° of geometry B and C. Especially in geometry C, the HTC at 0° is almost 0. HTCs are evaluated to be significantly greater when the coolant bulk temperature is at 400 °C compared with the cases with different coolant bulk temperatures. It is due to the properties of supercritical water. Equation 7 (Liang *et al.*, 2004) denotes that the pseudo-critical temperature of water at 30MPa is around 400°C.It is well known that HTC peaks at around pseudo-critical temperature as the coolant's specific heat takes the peak value.

$$T_{cri} = 558.12118 + 4.61398p - 0.02407p^2 - 273.15 \tag{7}$$
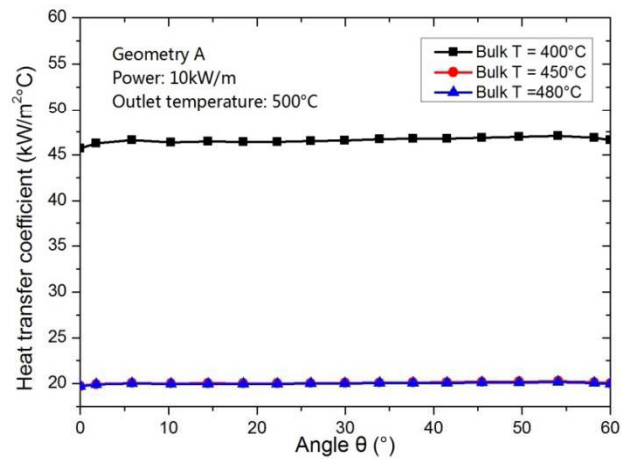
(a) Geometry A
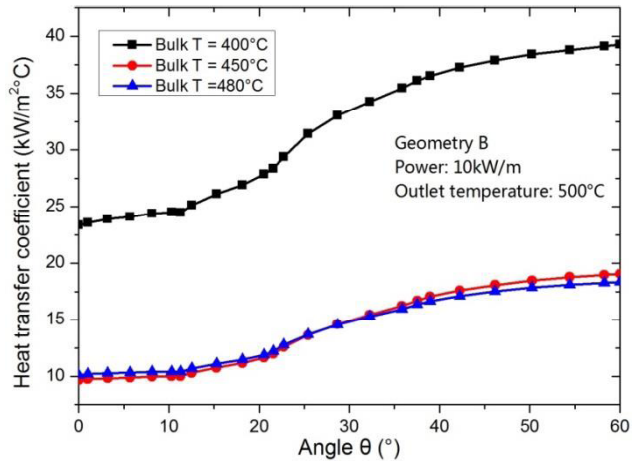
(b) Geometry B
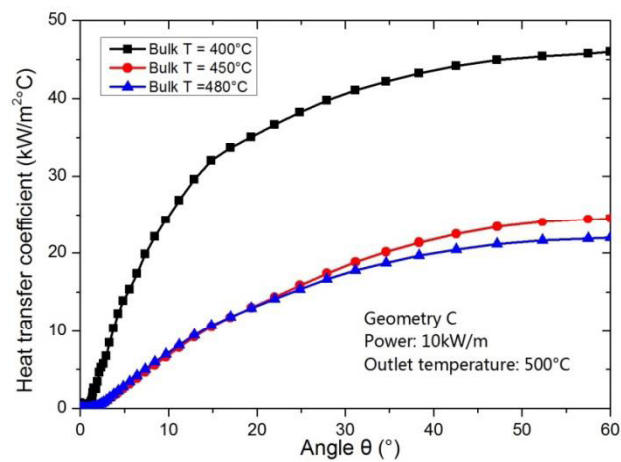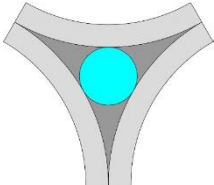
(c) Geometry C

Fig. 2-18 Circumferential HTC distribution
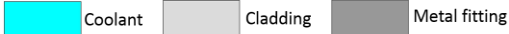
2.4 Channel geometry analysis at subcritical pressures

2.4.1 Channel geometry and mesh generation

The channel geometries analyzed at subcritical pressure conditions are the same as that at supercritical pressure, but the fuel rod diameters are changed to the representative sizes in a typical PWR and BWR. The related geometrical parameters are listed in Table 2-8, and the samples of generated computational meshes for the three geometries are shown in Fig. 2-19.

Table 2-8 Geometric images and geometrical parameters

Geometry	A	B	C
image			
SD	1	1.25	2
Fluid area(mm2)	5.43	8.7	11.5
Hydraulic diameter(mm)	2.63	3.0	2.25

Coolant   Cladding   Metal fitting
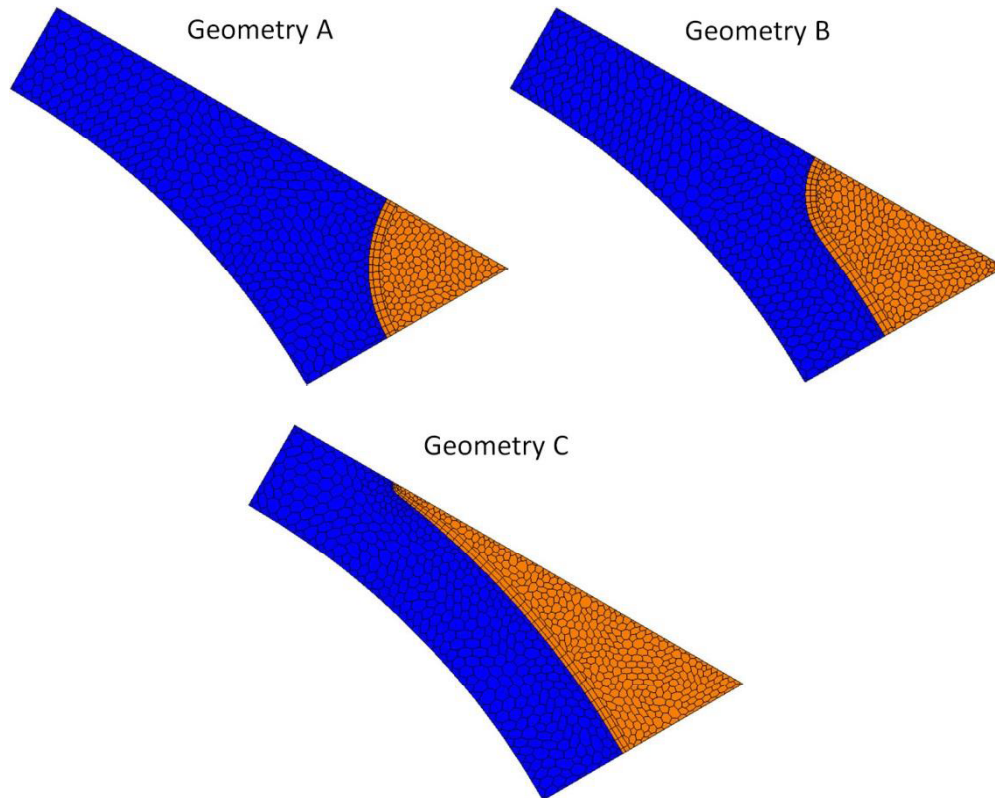
Fig. 2-19 Meshing of the CFD analyses

2.4.2 Boundary conditions and study method

Generally, the thermal-hydraulic boundary conditions are similar among the cases at different pressures (BWR and PWR), except the outlet conditions, which are significantly different. BWRs usually aim to achieve a certain exit quality, whereas PWRs are designed to reach a certain outlet coolant temperature. Figure 2-20 is a simple schematic diagram that shows the boundary conditions in terms of inlet temperature, outlet condition, system pressure and the power, which are all governed by the energy conservation equation:

$$h_{out} - h_{in} = \frac{P_h}{G_m A} \int_{z_{in}}^{z_{out}} q''(z) dz \qquad (2\text{-}28)$$

where:

h, bulk enthalpy

P_h, Perimeter of channel

G_m, mass flux

A, area of channel

q'', heat flux

z, axial height of channel

and for cases at BWR condition, the outlet enthalpy can be represented by:

$$h_{out} = h_{fs} + x \cdot h_{fg} \tag{2-29}$$

where, the h_{fs}, h_{fg} and x are the enthalpy of saturated liquid, latent heat and exit quality, respectively. The overall boundary conditions are listed in Table 2-9. Most parameters are selected from the current BWR (Amselem，2011) and PWR (Glasstone and Sesonske, 1994) design with minor differences, except the mass flux and channel length. The channel area of tightly packed fuel assembly is much smaller than that of conventional ones, it is necessary to apply a high mass flux to achieve a relatively large average LHGR, since it can be seen from Eq. 2-28 that mass flux is proportional to heat flux. Also because of the small channel areas and the small hydraulic diameters, CHF in a tightly packed fuel assembly is expected to be small, thus the selected channel lengths are shorter than that of conventional ones with the purpose of increasing the CHF. For all simulations, the heat flux is applied on the inner side of cladding; it is assumed that the metal fitting is firmly contacted with claddings and heat resistance between them can be ignored; For the purpose of evaluating thermal-hydraulic characteristics of the three representative channel geometries, axial power distribution is assumed to be uniform.
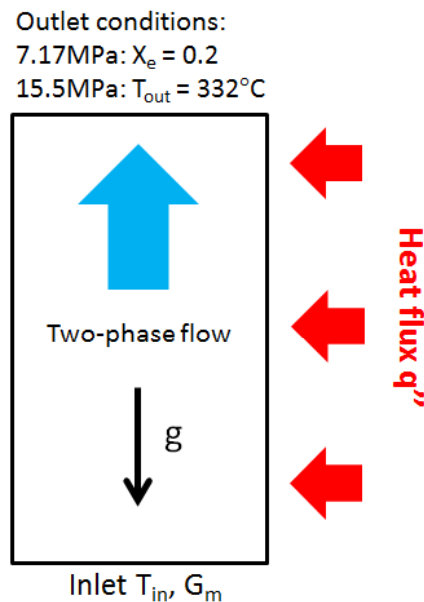
Fig. 2-20 Thermal-hydraulic boundary conditions

Table 2-9 Specification of computational conditions

Parameter	PWR condition	BWR condition
Core operating pressure (MPa)	15.5	7.17
Inlet temperature (°C)	260	283
Outlet temperature (°C)	332	287.5
Inlet mass flux (kg/m2s)	4500, 6000, 7500	5000, 6500, 8000
Equilibrium exit quality	-0.51	0.2
Core height (m)	2.0, 2.5, 3.0	1.5, 2.0, 2.5
Outer diameter of fuel rods (cm)	1.7	1.7
Cladding thickness (cm)	0.0873	0.0873
Pellet diameter (cm)	1.5124	1.5124
Gap between clad and pellet (cm)	0.0065	0.0065
Fuel rod pitch (cm)	1.7	1.7
Gap between fuel rods (cm)	0	0

It could be noted from Table 2-9 that parameters of inlet mass flux and channel length vary at both pressure conditions. There are three Mass fluxes ranged from 4500 kg/m^{2}s to 7500 kg/m^{2}s for PWR condition and from 5000 kg/m^{2}s to 8000 kg/m^{2}s for BWR condition; three channel lengths range from 2 m to 3 m for PWR condition and from 1.5 m to 2.5 m for BWR condition. Including these two parameters and the channel cross-sectional geometry, there are three varying parameters while other boundary conditions in Table 2-9 are always being held constants. For each geometry, simulations are conducted on three channel lengths and three mass fluxes, thus, there are totally 27 cases (3 geometries multiplied by 3 mass flux levels multiplied by 3 channel lengths). Consequently, three comparisons can be made: 1) geometry comparison, where characteristics of different geometries are compared at the same mass flux and channel length; 2) mass flux comparison, where characteristics with different mass fluxes are compared for the same geometry and channel length; 3) channel length comparison, where characteristics with different channel lengths are compared for the same geometry and mass flux. This study focuses on the first one. The variation of mass flux and channel length are in order to cover the potential design range in terms of inlet mass flux and core height, as well as to check the consistence of assessment under these different boundary conditions.

2.4.3 Assessment criteria

Assessments of all cross-sectional channel geometries are based on the thermal hydraulic criteria related to LWRs design at normal operation (OECD, 2012). These design criteria are in terms of cladding temperature, critical heat flux, maximum linear heat generation rate (MLHGR) and pressure drop in the current study. The cladding material is stainless steel, and its temperature is evaluated by two characteristic temperatures in terms of MCST and MAXT with the same related criteria as the cases at supercritical pressure. DNB and CHF criteria are referred to the values typically adopted in PWR and BWR designs respectively. They are the Minimum Departure from Nucleate Boiling Ratio (MDNBR) > 1.3 (at 115% normal power) for PWR condition and Maximum Critical Heat Flux Ratio (MCHFR) > 1.9 for BWR condition. To prevent the fuel from melting, the limit of MLHGR is typically set to be about 43kW/m for both pressure conditions.

Pressure drop is another important item. Due to application of the tightly packed fuel assembly, the pressure drop will be much higher than that of conventional LWRs, by considering the pumping power, for BWR condition, the upper limit is taken to be 1.5MPa, and for PWR condition, it is 1.0MPa. They are substantially higher than that of conventional BWR and PWR (both less than 0.2 MPa). For high breeding BWR and PWR with tightly packed fuel assemblies, the high pressure drop possibly leads to a high pumping power requirement and flow instability issue. The high pumping power will be addressed in the future study with detailed design of the plant system. The flow instability can be managed by applying the inlet orifice to increase the pressure drop at inlet. Given above all, the assessment parameters are cladding temperatures (MCST and MAXT), CHF, MLHGR and pressure drop.

2.4.4 CFD Results at subcritical pressure

This section introduces the simulation results of cases at PWR and BWR conditions, respectively. At each condition, the related CHF estimation is performed at first to determine the power range that satisfies the CHF criteria. Then, the calculations at normal operation conditions are conducted.

Before the calculation, the capability of the CFD software for modeling the two-phase flow needs to be validated. The validity related to applied boiling models can be referred to the user guide (CD-Adapco, 2013), and in present study, the capability of STAR-CCM approaching DNB condition is validated by comparing with the 2006 look-up table (Groeneveld *et al.*, 2007) based on experimental data.

2.4.4.1 Calculation at PWR condition

Validation of DNB condition in a single tube

The calculations were performed with a single round tube at a pressure of 15.5 MPa. The tube length is 2.4 m with 2 m long heated length and 0.2 m long inlet and outlet adiabatic sections. The tube inner diameter is selected as 8 mm which is the same as reference value in the look-up table. Therefore, direct comparison of the simulated results with CHF data in the look-up table is possible without any approximations. CHF here indicates the conditions at which the heat transfer coefficient of two phase flow deteriorates dramatically. CHF condition at low quality is known as Departure from Nucleate Boiling (DNB), while at high quality is known as dryout.

The tube was modeled by 2-dimensional axisymmetric geometry with 25 cells in radial and 500 cells in axial direction. The numerical models, such as turbulence model and boiling models, are the same as described in Section 2.2. For drag force correction, volume fraction exponent method (CD-Adapco, 2013) is used to suit the flow conditions.

The inlet temperature was set to 260°C, the mass flux of water varies from 1500 kg/m^{2}s to 8000 kg/m^{2}s. The calculations were started with an estimated wall heat flux, which was slightly lower than the CHF from the look-up table. If the computational residuals were stable while CHF is not reached, then the heat flux is slightly increased until the DNB occurs at the end of heated length which can be indicated by parameters α_{dry} or K_{dry} in steady-state.

Figure 2-21 shows the typical case (G_m= 4500kg/m^{2}s) of the CHF calculation procedure. The power gradually increases by fine steps of 50kW/m^2. At the first few steps, the maximum wall temperature increases with the increase of heat flux by a small value, and then it jumps dramatically which indicates the occurrence of DNB and the heat flux reaches CHF (the CHF is defined as the heat flux before the jump of maximum wall temperature).
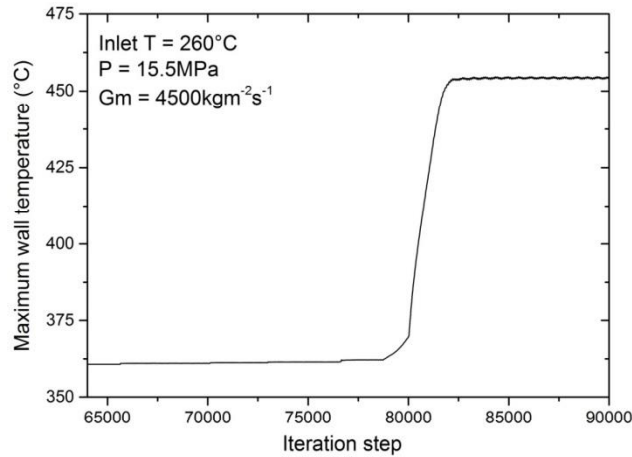
Fig. 2-21 Increase of maximum wall temperature with heat flux increase

The mesh convergence study for this problem is conducted on the medium mass flux of 4500 kg/m^{2}s and heat flux of 2.450 MW/m^2. The relative errors for exit quality (x_{exit}), maximum wall temperature (T_{max}) and maximum K_{dry} are calculated for three selected meshes illustrated in Table 2-10. It is seen that all the relative errors are below 1.5%. Based on these uncertainties, the simulations for this problem are conducted on the smallest mesh to save the computational resource meanwhile guarantee the accuracy.

Table 2-10 Mesh independence study results for validations of DNB evaluated by STAR-CCM+

	$\Phi = x_{exit}$	$\Phi = T_{max}$	$\Phi = \text{maximum} K_{dry}$
Mesh number N1, N2, N3	81250, 31250, 12500	81250, 31250, 12500	81250, 31250, 12500
Φ_1, Φ_2, Φ_3	0.0552, 0.0547, 0.0542	362.73,360.67,360.65	0.03087,0.03063,0.03015
e^{21}, e^{32}	0.852%,0.999%	0.568%,0.007%	1.100%,1.245%

Figure 2-22 shows the calculated critical quality with corresponding CHF compared with the data from the look-up table. It is seen that the two curves generally agree well with each other, and the CHF calculated from CFD is slightly lower in most cases. Therefore, STAR-CCM+ is capable of predicting the DNB phenomenon for the design range of this study. Figure 2-23, Fig. 2-24 and Fig. 2-25 show the examples of void fraction and K_{dry} at the wall and void fraction map at longitudinal section, respectively. From Fig. 2-23 and Fig. 2-24, it can be concluded that the CHF

is reached, because at the end of heated length the near wall void fraction exceeds 82% and K_{dry} is larger than zero.
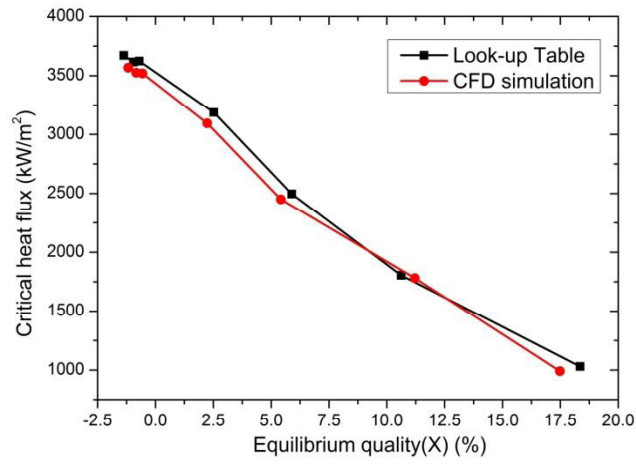
Fig. 2-22 Comparison of CHF evaluated by STAR-CCM+ and the look-up table
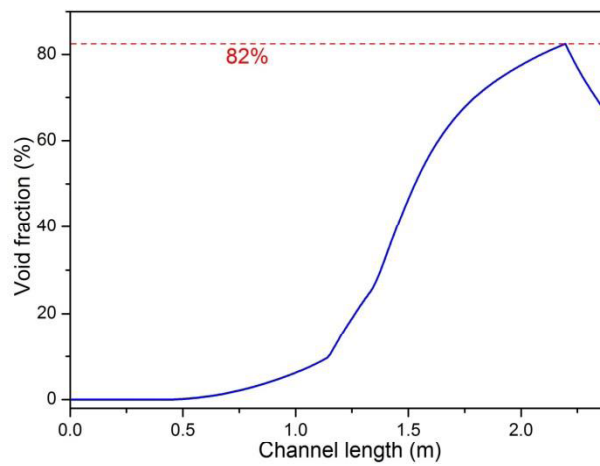
Fig. 2-23 α_δ along the channel
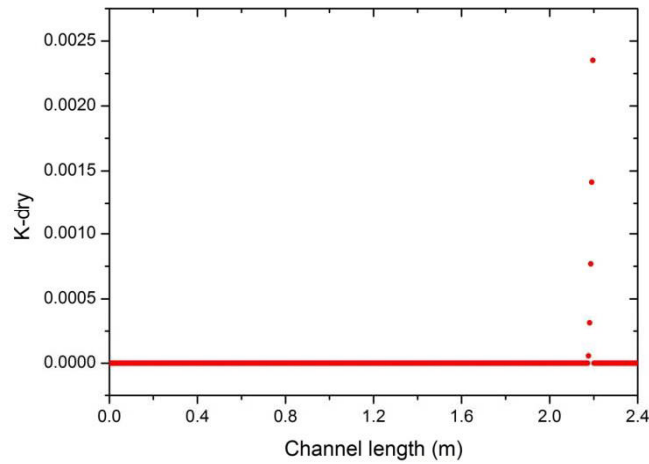
Fig. 2-24 K_{dry} along the channel
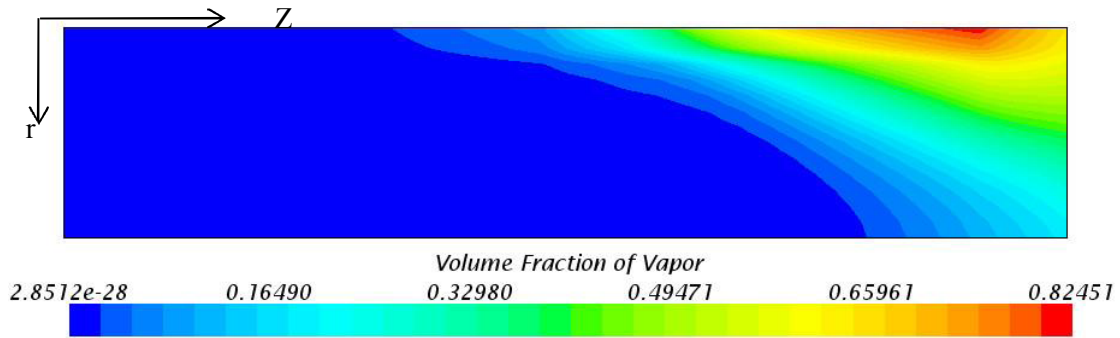
Fig. 2-25 Distribution of void fraction in the channel

Mesh independence for channel geometries

For simulations of selected geometries, the channels are narrower (hydraulic diameter ranges from 2mm-3mm) and the bubble size is restrained by the channel wall in the transverse direction. For these small bubbles, the Lockett Kirkpatrick method is a more appropriate drag force correction than the volume fraction exponent method and used in the following simulations. The detail of this method can be referred to the user guide (CD-Adapco, 2013).

The estimation for numerical uncertainty is conducted on representative cases (G_m= 6000 kg/m^{2}s, LHGR = 10.35 kW/m for geometry A, LHGR = 16.58kW/m for geometry B, LHGR = 17.03kW/m for geometry C, inlet temperature T_{in}= 260°C, channel length L = 2.5m) for all three geometries. Uncertainties of the four critical variables (MCST, MAXT, pressure drop and outlet temperature) are analyzed. Three meshes with refinement ratios around 1.3 are established. The

detail parameters and results are summarized in Table 2-11. It is seen that all the relative errors are smaller than 1%, and for the critical variables, the differences due to differences of the meshes are negligible. Therefore, the following simulations at PWR condition adopt the mesh with the smallest number of cells.

Table 2-11 Mesh independence study results for cases at PWR pressure

		$\Phi = MCST$	$\Phi = MAXT$	$\Phi = \Delta P$	$\Phi = T_{out}$
Geometry A	Mesh number N1, N2, N3	263531,151280, 82948	263531,151280, 82948	263531,151280, 82948	263531,151280, 82948
	$\Phi_1, \Phi_2, \Phi_3,$	342.89,342.90, 341.36	422.59,422.17, 419.18,	0.3835,0.3824, 0.3828	332.48,332.48, 331.13
	e^{21}, e^{32}	0.004%,0.451%	0.098%,0.708%	0.294%,0.094%	9.02e-4%,0.408%
Geometry B	Mesh number N1, N2, N3	331820,179765, 90247	331820,179765, 90247	331820,179765, 90247	331820,179765, 90247
	Φ_1, Φ_2, Φ_3	350.03,350.07, 349.27	441.95,441.54, 438.76	0.3203,0.3200, 0.3197	331.13,332.27, 332.28
	e^{21}, e^{32}	0.010%,0.227%	0.093%,0.629%	0.081%,0.106%	0.002%,0.383%,
Geometry C	Mesh number N1, N2, N3	521932,300745, 169773	521932,300745, 169773	521932,300745, 169773	521932,300745, 169773
	Φ_1, Φ_2, Φ_3	349.40,349.38, 349.21	361.33,361.11, 360.82	0.1017,0.1016, 0.1016	318.31,318.31, 318.27
	e^{21}, e^{32}	0.008%,0.048%	0.060%,0.079%	0.059%,0.031%	0.002%,0.012%

CHF estimation

Following the above mentioned validations, the CHFs of all geometries were calculated by CFD method. Calculations were performed at conditions of a fixed inlet temperature of 260°C, mass fluxes ranged from 3000 kg/m²s to 9000 kg/m²s and channel lengths from 2 m to 3 m. The results are shown in Fig. 2-26. It should be noted that, for convenience, the CHF on the channel surface has been converted to the linear heat generation rate (LHGR) of a single fuel rod (note that one coolant channel is heated by half a fuel rod seen in Fig. 2-1), which corresponds to the calculation domain. It can be seen that the CHF of geometry B is the highest for all channel lengths, followed by geometry A, and geometry C, which is much smaller compared with the former two especially when the mass flux is large. The results also show that decrease of the channel length can improve the CHF to some extent for geometry A and B, while it is not effective for geometry C.
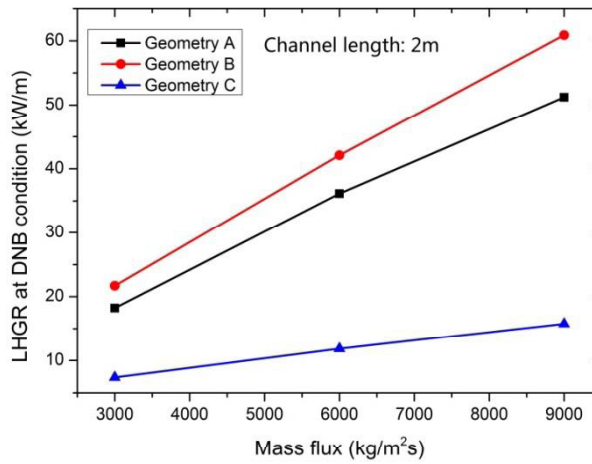
(a) Channel length: 2.0 m
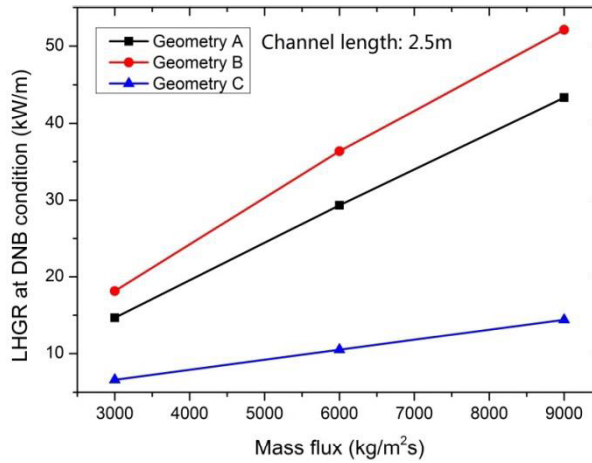
(b) Channel length: 2.5 m
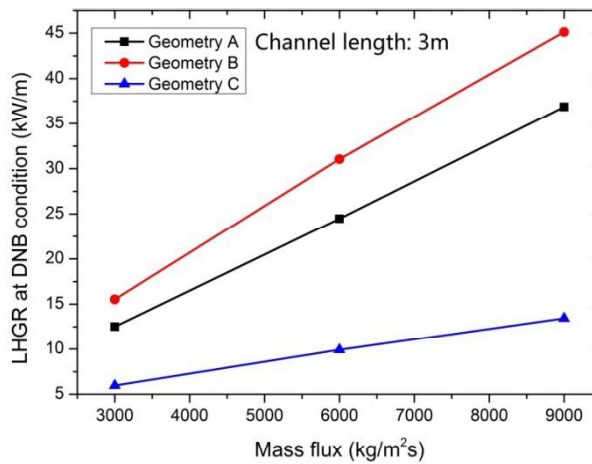
(c) Channel length: 3.0 m

Fig. 2-26 LHGR at DNB condition vs. mass flux with different channel lengths

By considering the DNB criterion in Section 2.4.3, the maximum applicable power for all geometries at different mass flux can be determined. On the other hand, the required power at normal operation to attain the target outlet temperature (332 °C) can be calculated from the heat balance (Eq. 2-23). By comparing the two, the whether the CHF criteria are satisfied can be clearly understood: to satisfy the CHF criteria, required power should be lower than corresponding limit power.   Figure 2-27 shows the mass flux dependences of the limit power (the "limit power" means the maximum applicable average LHGR limited by DNB criterion) by solid lines and that of the required power by dashed lines. The design ranges can be identified from the results of geometry A and B where the limited power is greater than the required power. However, the design range cannot be identified for geometry C. Hence, it is excluded from the candidates of the channel geometries.

From Table 2-9, it can be calculated that the flow area of geometry B is about 1.6 times that of geometry A. According to the heat balance Eq. 2-23, the applied power on geometry B also will be 1.6 times that on geometry A in case of fixed outlet condition. In practical application, it means geometry B can allow a higher reactor power density.
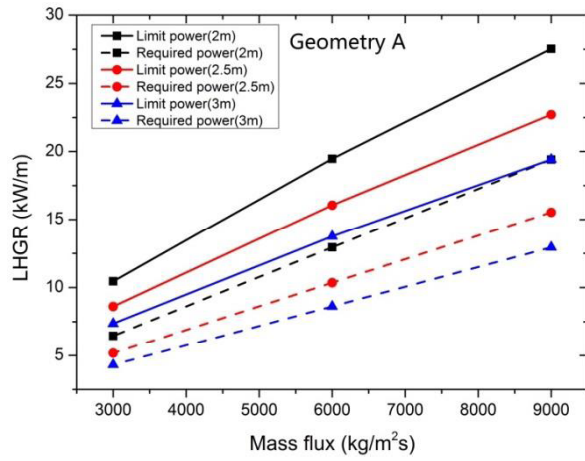
(a) Geometry A
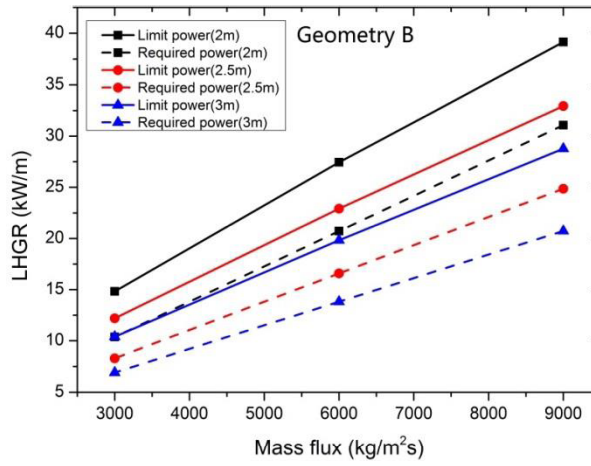
(b) Geometry B
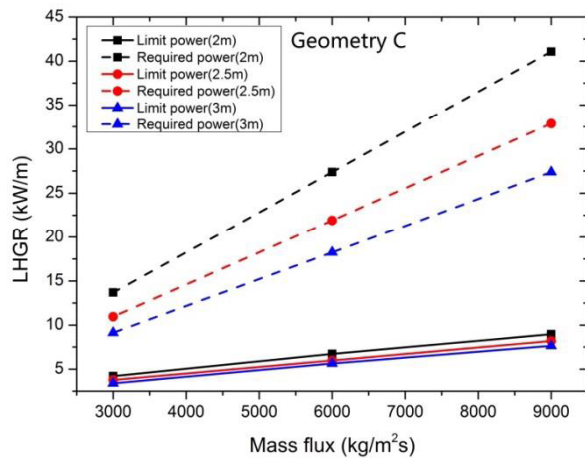
(c) Geometry C

Fig. 2-27 LHGR limited by DNB criterion and required for 332°C outlet temperature for different channel geometries

Cladding temperatures, pressure drop and CHF at normal operation condition

Figure 2-28 shows the comparison of MCSTs and MAXTs for geometry A and B at various mass fluxes and channel lengths. They indicate that the both MCST and MAXT of all cases are far below the related criteria (650 °C for MCST, 700 °C for MAXT). MCST and MAXT of geometry B are slightly higher than those of geometry A. The difference of MCST between geometry A and B is less than 10°C, and that of MAXT it is less than 20°C. It is understood from the heat balance Eq. 2-23 that, for the same outlet temperature, geometry B needs a higher heat flux due to the larger mass flow rate.

In the other computational approach, where the applied power and mass flow rate (in kg/s) are the same for both geometry A and B, while mass fluxes (in kg/m^2s) are different. The results are shown in Fig. 2-29. It is the case of 2 m channel length and indicates that the MAXT of geometry B is lower than that of geometry A for the same LHGR. MCST of geometry B is only several degrees of Celsius higher than that of geometry A, and it indicates that the cladding temperature distribution in geometry B is more uniform than that in geometry A. The results of other cases with different channel lengths show the same characteristics.
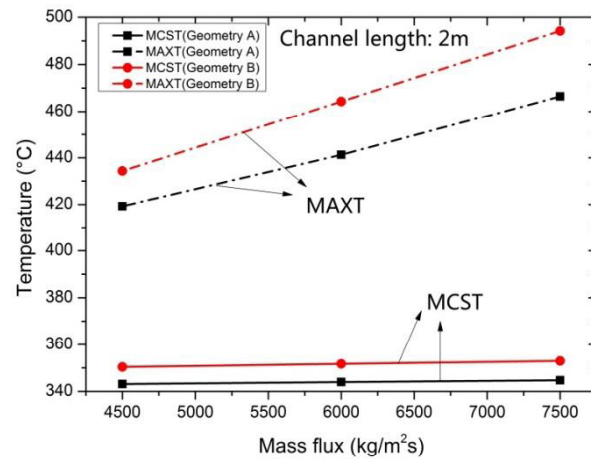
(a) Channel length: 2.0 m
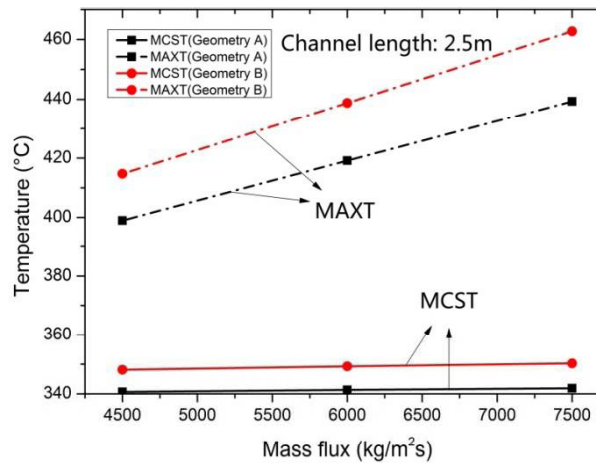
(b) Channel length: 2.5 m
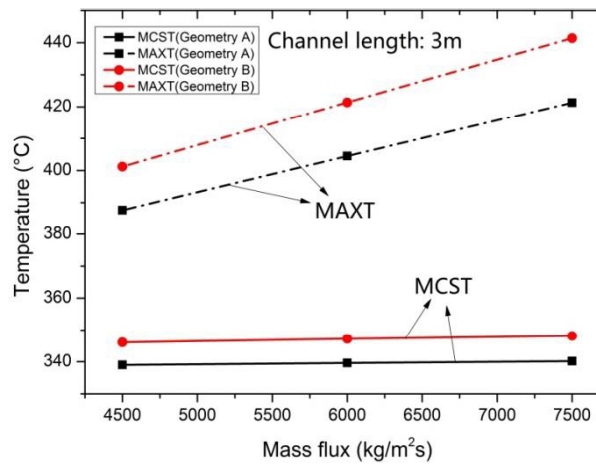
(c) Channel length 3.0 m

Fig. 2-28 Coolant mass flux dependences of MAXT and MCST of geometry A and B with different channel lengths

Fig. 2-29 LHGR dependences of MAXT and MCST of geometry A and B

In Fig. 2-30, the pressure drop characteristics of geometry A and B are presented. In all cases, geometry B gives pressure drop by around 0.05 MPa less than that given by geometry A. For both geometries, the pressure drop increases with channel length.
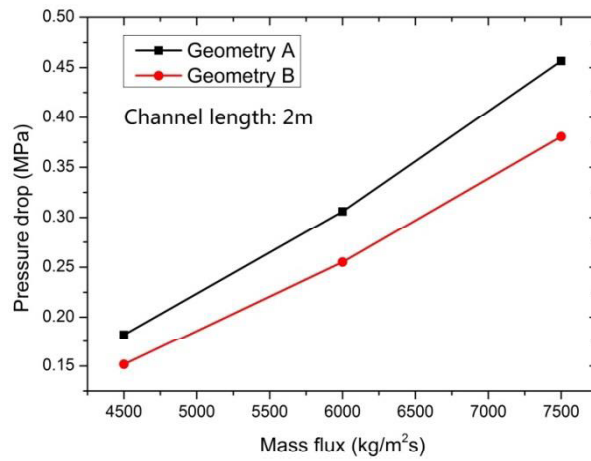
(a) Channel length: 2.0 m

(b) Channel length 2.5 m

(c) Channel length 3.0 m

Fig. 2-30 Coolant mass flux dependences of pressure drop of geometries A and B with different channel lengths

Maximum LHGR

LHGR and the correlated channel length are important parameters for reactor design, since both determine the total core power. A larger core power implies a shorter CSDT, which can be seen from Eq. 3-2 to Eq. 3-4. From Fig. 2-27, Fig. 2-28 and Fig. 2-30, it is seen that the dependences of the required power, MCST, MAXT and pressure drop are all approximately linear with the coolant mass flux. By using the linear extrapolation on lines in these figures, it is possible to estimate the maximum LHGR for geometries at each channel length, taking into account of the design criteria of MCST, MAXT, and pressure drop. During the extrapolation, the mass flux and power increase together at a constant ratio to maintain the heat balance and the constant boundaries in Table 2-9 are maintained as well. This approach is to extrapolate the lines of required power, cladding temperatures and pressure drop versus mass flux until one of them reaches its limit value, and at this critical mass flux, the corresponding extrapolated required LHGR is determined to be the maximum LHGR.

For instance, considering geometry A with 2.0 m channel length, firstly, linearly extrapolate the black dash line in Fig. 2-27(a) (i.e., required power) until LHGR reaches to 43kW/m (MLHGR criterion), and the corresponding mass flux at this LHGR will be about 20000 kg/m^{2}s; Secondly, extrapolate the black dash line in Fig. 2-28(a) (i.e. MAXT) until the it reaches 700°C (compared with MCST, MAXT is more limiting), and the corresponding mass flux is about 22200 kg/m^{2}s; thirdly, extrapolate the black line in Fig. 2-30(a) (i.e., pressure drop) until it reaches to 1.0 MPa (pressure drop criterion), and the corresponding mass flux is about 13600 kg/m^{2}s; fourthly, extrapolate the black dash line in Fig. 2-27(a) until mass flux reaches to the smallest value (13600 kg/m^{2}s) among above three. Thus, the maximum LHGR is calculated to be 29.5kW/m, and the limiting criterion is pressure drop.

Generally, to increase the power, the mass flux needs to be increased. When mass flux and outlet condition (outlet temperature for cases at PWR pressure) are fixed, increase of the channel length will not increase the total power, because the average LHGR thus is being decreased. Table 2-12 summarizes the Maximum LHGR, total power of a single rod and limiting criterion for geometry A and B with different channel lengths. In cases of geometry A, the power is limited by the pressure drop criterion, and the shorter channel length could achieve both larger LHGR and total power; in cases of geometry B, when channel length is as short as 2.0 m, power is limited by MLHGR criterion, while as the channel length increases, the total power can be increased as well and the limiting criterion changes to be the pressure drop criterion. Both total power and LHGR decrease for 3.0 m channel length. By contrast, the cladding temperature and DNB criteria have

larger margins and are not limiting at PWR condition. From the view point of maximum LHGR, geometry B has advantages over geometry A at PWR condition.

Table 2-12 Design range of power and limiting criterion for geometry A and B at different channel lengths

	Geometry A			Geometry B		
Channel length(m)	Maximum LHGR (KW/m)	Total Power of a single fuel rod(kW)	Limiting criterion	Maximum LHGR (KW/m)	Total Power of a single fuel rod(kW)	Limiting criterion
2.0	29.5	59	$\Delta P < 1MPa$	43	86	MLHGR < 43kW/m
2.5	20	50	$\Delta P < 1MPa$	36.2	90.5	$\Delta P < 1MPa$
3	14.5	43.5	$\Delta P < 1MPa$	26.3	78.9	$\Delta P < 1MPa$

2.4.4.2 Calculation at BWR condition

Mesh independence

The mesh convergence study at BWR condition is conducted for geometry A and B at representative conditions of 283 °C inlet temperature, 6500 kg/m^{2}s mass fluxes, 20 kW/m LHGR and 2.0 m channel length. Three meshes are constructed for evaluating the numerical uncertainty. Variables of MCST, MAXT, pressure drop and exit quality are evaluated by the Grid-Convergence Index (GCI) method. Table 2-13 shows mesh numbers and the corresponding results. It indicates that the maximum relative error is below 2%, so that the meshing with the smallest number of cells is able to give stable solutions.

Table 2-13 Mesh independence study results for cases at BWR pressure

		$\Phi = MCST$	$\Phi = MAXT$	$\Phi = \Delta P$	$\Phi = X_{exit}$
Geometry A	Mesh number N1, N2, N3	571974,279576, 128516	571974,279576, 128516	571974,279576, 128516	571974,279576, 128516
	Φ_1, Φ_2, Φ_3	295.44,295.44, 295.45	384.53,384.40, 383.93	0.8498,0.8483, 0.8462	0.1978,0.1985, 0.2013
	e^{21}, e^{32}	<1e-3%,0.005%	0.035%,0.121%	0.174%,0.242%	0.373%,1.373%
Geometry B	Mesh number N1, N2, N3	694869,320762, 168345	694869,320762, 168345	694869,320762, 168345	694869,320762, 168345
	Φ_1, Φ_2, Φ_3	297.54,297.56, 297.55	401.99,401.78, 401.90	0.7276,0.7285, 0.7186	0.2018,0.2038, 0.2013
	e^{21}, e^{32}	0.006%,0.004%	0.053%,0.032%	0.120%,1.361%	0.981%,1.197%

Validation of axial void fraction distribution

Void fraction calculated by STAR-CCM+ was validated by Krepper *et al.* (2011) and Petrov *et al.* (2012) against the DEBORA experiment. Since the axil void fraction may affect the breeding performance of tightly packed fuel assemblies, it is necessary to validate it for conditions at which the tightly packed fuel assemblies operate. The computational condition is as following: coolant with 5000 kg/m2s mass flux flows through a 2 m long vertical channel, heated by 10 kW/m uniform LHGR. Because currently there is no experimental data for this condition, empirical methods are used for validation, including the Homogeneous Equilibrium Model (HEM), slip ratio model (Smith, 1969), EPRI model (Lellouche, 1982) and Chexal-lellouche model (Chexal and lellouche, 1991). Figure 2-31 shows the results comparison between STAR-CCM+ and empirical methods. It is seen that STAR-CCM+ generally has a good agreement with empirical methods.
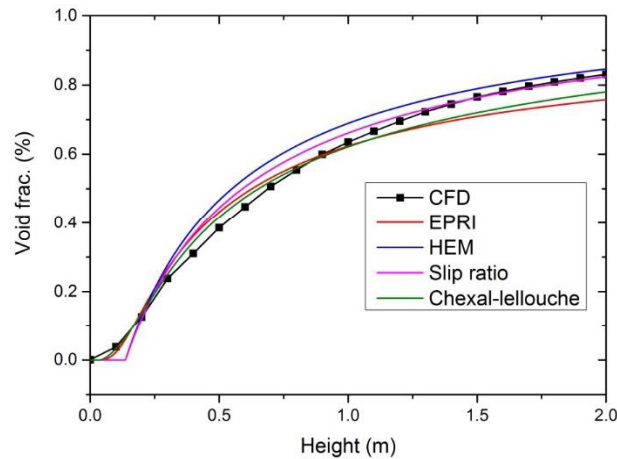
Fig. 2-31 Validation of axial void fraction profile

CHF estimation

The mechanism of the CHF model described in Section 2.2 is according to the near wall bubble crowding theory, however, at BWR condition, boiling crisis is usually triggered by the dryout of liquid film in an annular flow. In this condition, the Shah's correlation (Shah, M.M, 1987) was used to estimate the CHF values due to its wide applicable parameter range, especially for the small diameter tubes. A good agreement with experimental data of narrow channels is shown in study of Zhang *et al.* (2006). This correlation was originally developed for round tubes, but in case of geometry other than round but close to, the geometrical effect is approximately accounted by using equivalent hydraulic diameter.

It is reasonable to infer that geometry C has a very small CHF due to the poor heat transfer at the sharp corner, and this has been shown at the DNB condition, therefore the CHF estimations as well as followed comparisons at normal operation condition are preliminarily performed only on geometry A and B. The calculations approaching CHF condition were performed at conditions of 283°C inlet temperature, mass fluxes varied from 3500 kg/m^2s to 9500 kg/m^2s and channel lengths from 1.5m to 2.5m.

It turns out that geometry B has a relatively larger CHF compared with geometry A as shown in Fig. 2-32. To some extent, geometry B has advantages over A owing to its larger hydraulic diameter. Based on these results and the CHF criterion, the limit powers can be evaluated. At normal operation condition, 0.2 exit quality is the outlet condition, the required powers for all cases are shown in Fig. 2-33 compared with the limit power. It is seen that both geometry A and B can satisfy the CHF criterion in most cases except geometry B in case of channel length longer

than 1.5m and mass flux larger than 9500 kg/m2s. The design margin of average LHGR to limited power decreases as the mass flux increases but slightly increases with the increase of channel length. It also can be seen that geometry B can accommodate a larger power especially in case of high mass flux, which is resulted from its larger cross-sectional area.
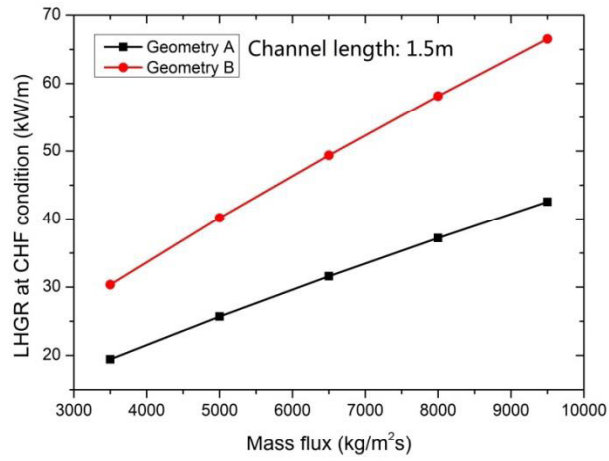
(a) Channel length: 1.5 m
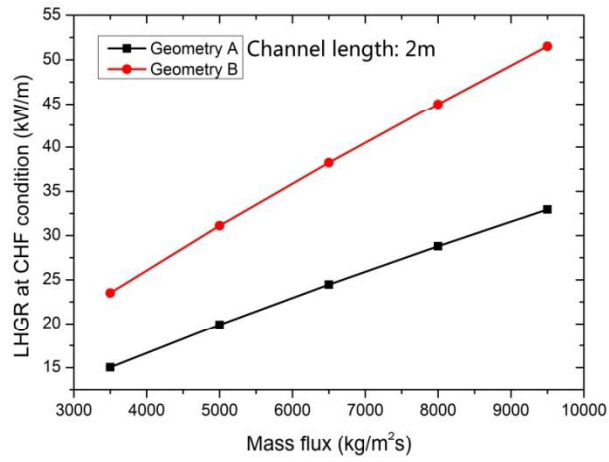
(b) Channel length: 2.0 m
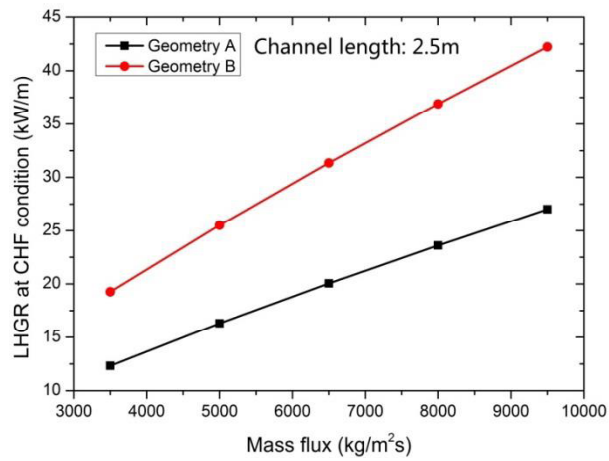
(c) Channel length 2.5 m

Fig. 2-32 LHGR at CHF condition vs. mass flux for different channel lengths
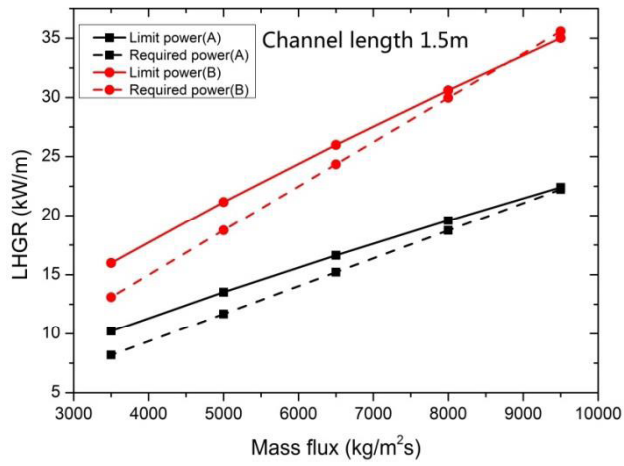
(a) Channel length: 1.5 m
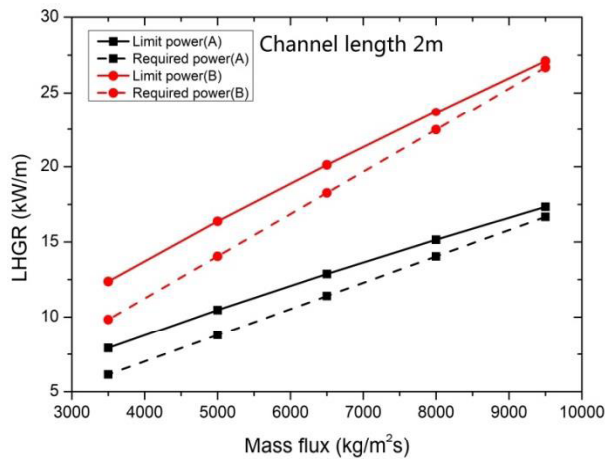
(b) Channel length 2.0 m
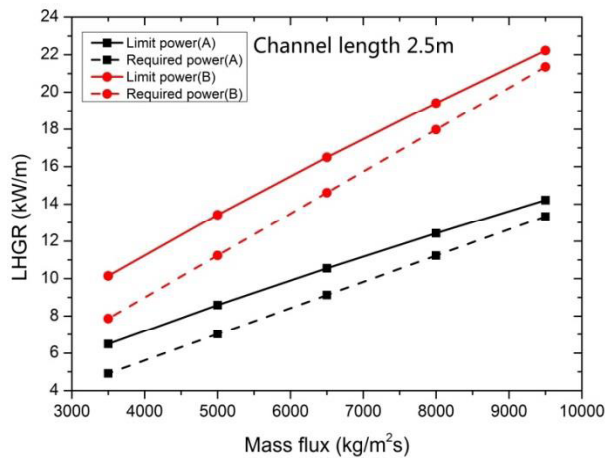
(c) Channel length 2.5 m

Fig. 2-33 LHGR limited by CHF criterion and required for 0.2 exit quality for different channel lengths

Cladding temperatures, pressure drop and CHF at normal operation condition

Figure 2-34 shows the comparison of cladding temperatures of geometries A and B. The results show the similar characteristics as those at PWR conditions. MAXT and MCST of geometry B are slightly higher than those of geometry A by less than 25 °C and 5 °C, respectively. The higher MAXT of geometry B is mainly resulted from the higher applied power. Figure 2-35 shows the example that at the same power levels, the MAXT of geometry A is higher than that of geometry B. Compared to the PWR condition, the MCST difference between the geometry A and B is much smaller due to the highly efficient heat transfer of boiling convection at the BWR condition.
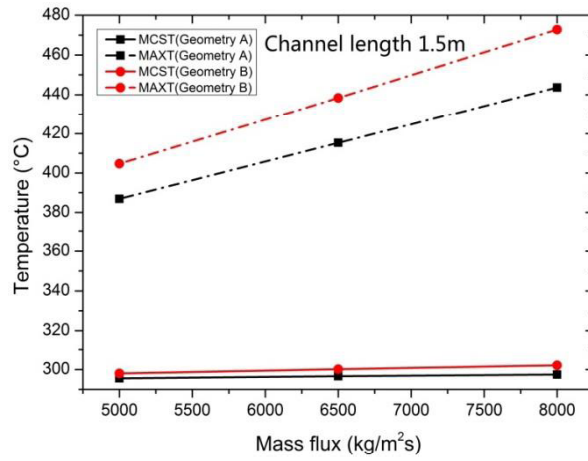
(a) Channel length 1.5 m
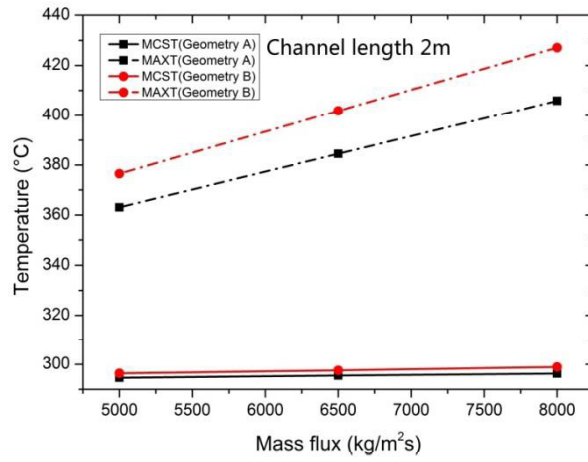
(b) Channel length 2.0 m
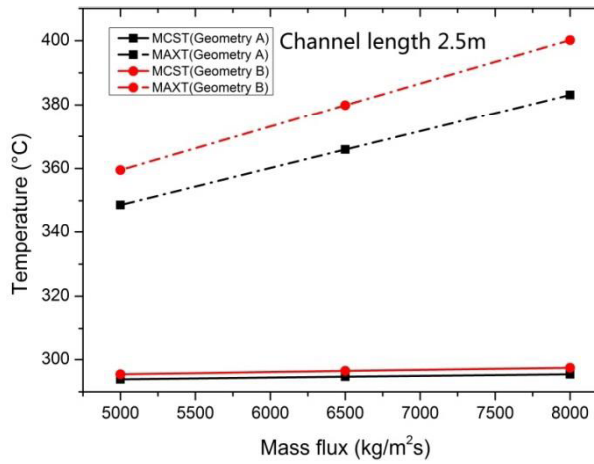
(c) Channel length 2.5 m

Fig. 2-34 MAXT and MCST of geometry A and B with different channel lengths
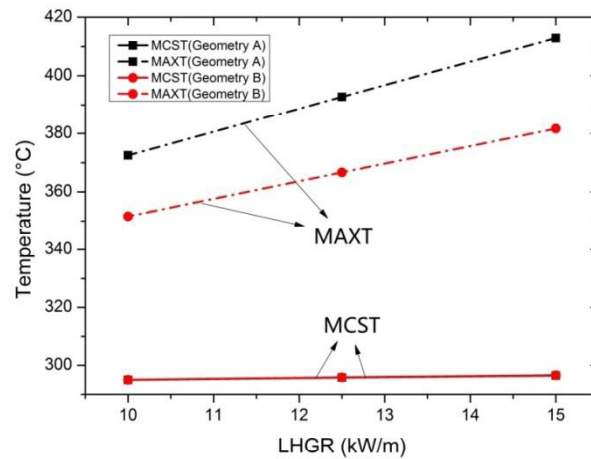
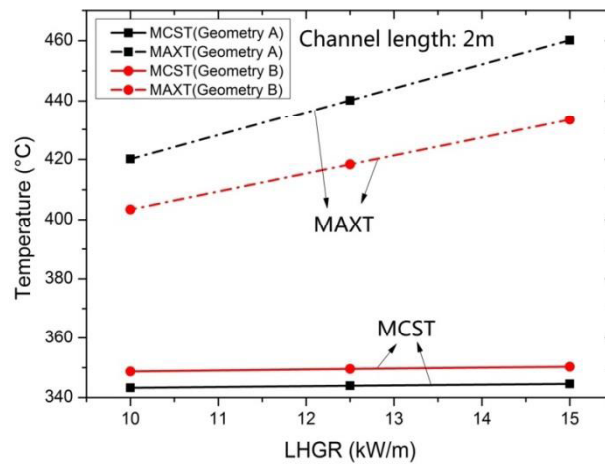Fig. 2-35 LHGR dependences of MAXT and MCST of geometries A and B (2 m channel)

Figure 2-36 illustrates the pressure drop of geometries A and B. As is the case for PWR condition, the pressure drop of geometry A is higher than that of geometry B, and for both geometries it increases with the increase of the channel length and coolant mass flux. However, compared to PWR condition, the pressure drop is about 75% higher, because friction caused by two-phase flow is larger and dominates at BWR condition.
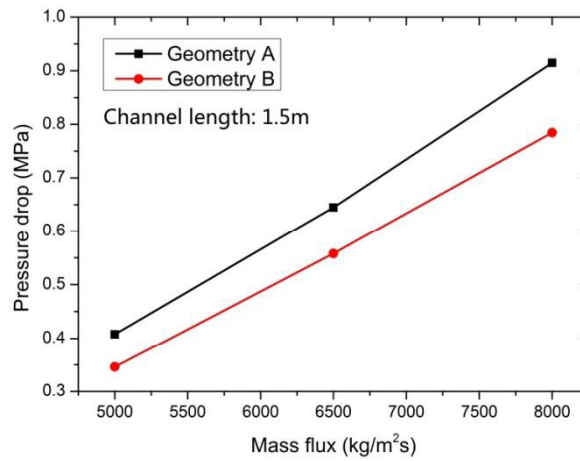
(a) Channel length 1.5 m
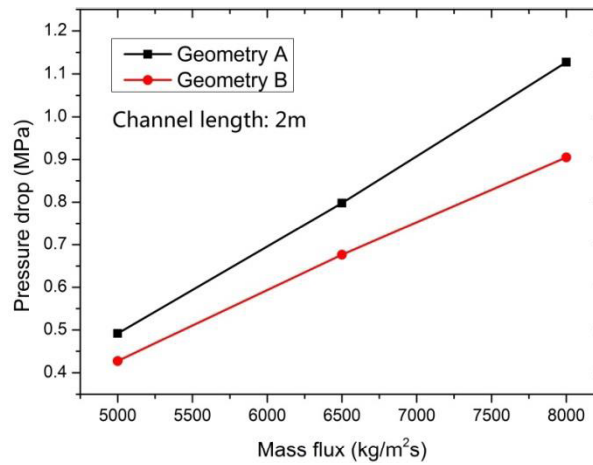
(b) Channel length 2.0 m
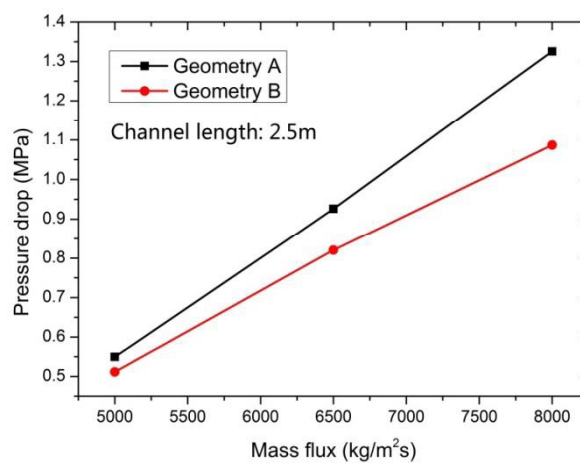
(c) Channel length 2.5 m

Fig. 2-36 Coolant mass flux dependences of pressure drop of geometries A and B with different channel lengths
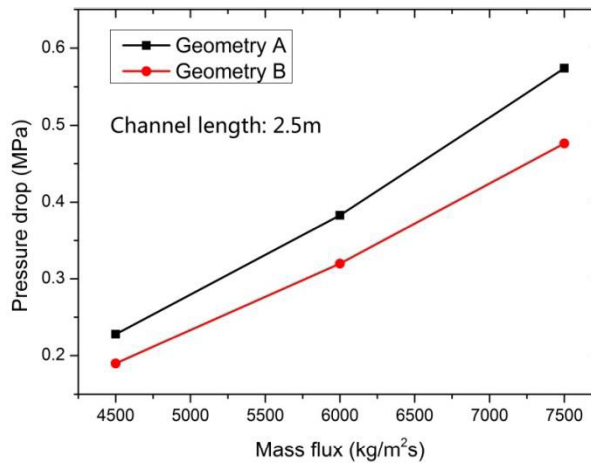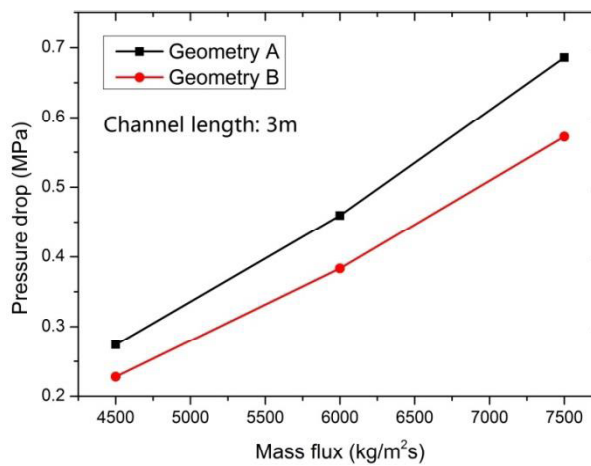
Maximum LHGR

Determination of the maximum LHGR is similar to that of PWR condition in Section 2.4.4.1. Table 2-14 shows that the maximum LHGR decreases with the increase of channel length. In cases of short channel, which is less than1.5 m for geometry A and less than 2.5 m for geometry B, the increases of LHGR and total power are limited by MCHFR criterion. With the increase of channel length, the limiting criterion switches to pressure drop and the total power reaches to maximum at the switch point. Geometry B is superior to A due to the larger maximum LHGR.

Table 2-14 Design range of power and limiting criterion for geometry A and B at different channel length

	Geometry A			Geometry B		
Channel length(m)	Maximum LHGR (KW/m)	Total Power of a single fuel rod(kW)	Limiting criterion	Maximum LHGR (KW/m)	Total Power of a single fuel rod(kW)	Limiting criterion
1.5	22.5	33.75	MCHFR > 1.9	33.3	49.95	MCHFR > 1.9
2	17.3	34.6	ΔP < 1.5MPa	28.7	57.4	MCHFR > 1.9
2.5	12.1	30.25	ΔP < 1.5MPa	22.5	56.25	ΔP < 1.5MPa

2.4.4.3 Heat transfer characteristics at subcritical pressures

Radial temperature distribution

In the radial direction, the heat transfer is not uniform due to the asymmetry of geometries, even in cases of geometry A. Although this channel is circular, the heat source (three fuel rods) is not uniformly distributed around the channel. The non-uniformity influences the temperature distribution of cladding and fluid. Figure 2-37 shows the cross-sectional temperature color map of examples where the bulk coolant temperature is 295°C at PWR condition. It can be seen that point A of each geometry is the place where the highest cladding temperature appears. Figure 2-38 shows that the temperature difference between angle positions of 0° and 60° becomes larger from 2 °C in geometry A to 30 °C in geometry C, and the highest radial cladding surface temperature occurs at point B.
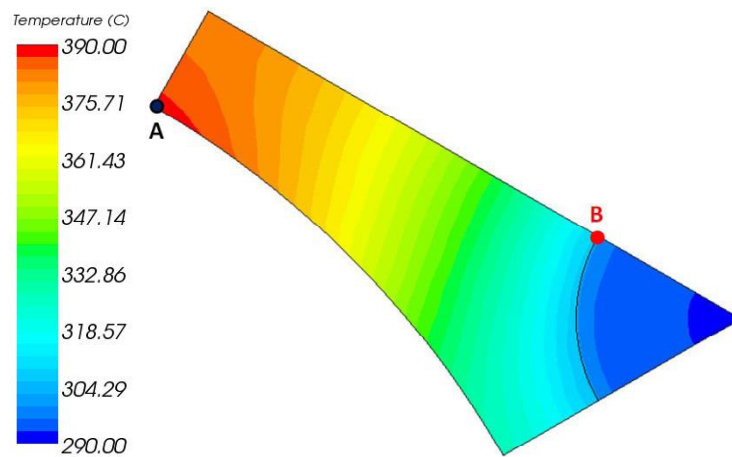
(a) Geometry A
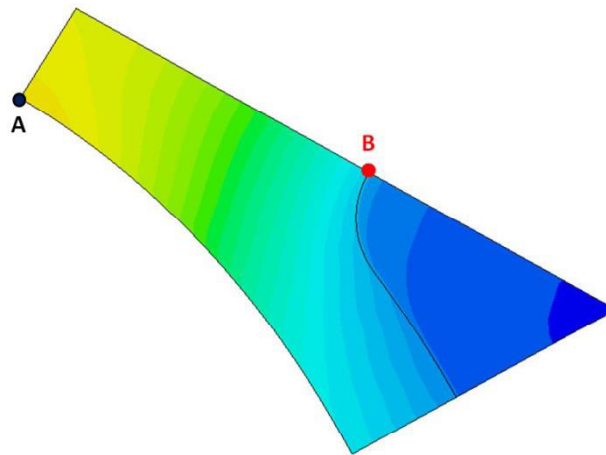
(b) Geometry B
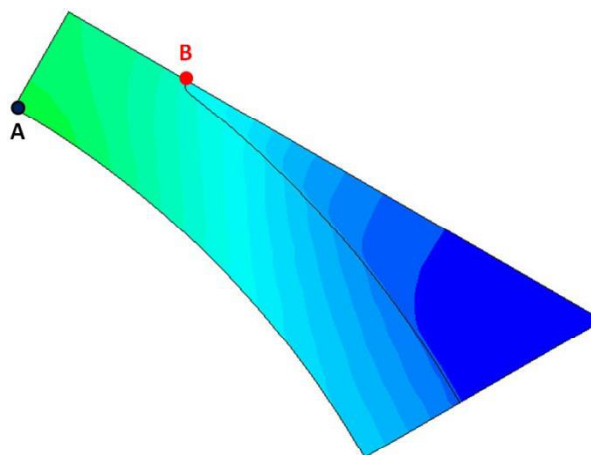
(c) Geometry C

Fig. 2-37 Cross-sectional temperature distribution (295°C bulk temperature, PWR condition) of different geometries
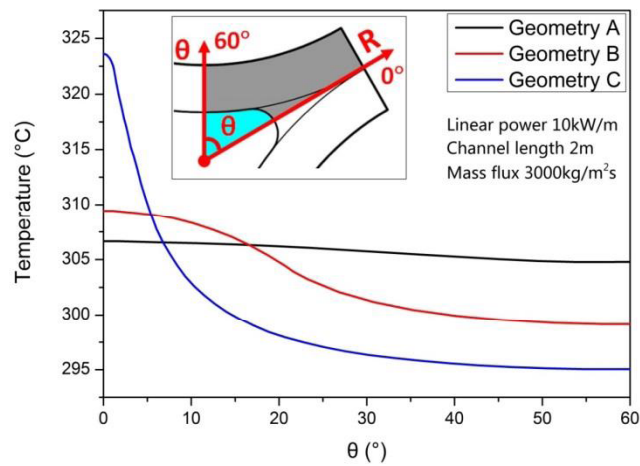
Fig. 2-38 Circumferential temperature distribution of cladding surface.

Above features can be explained by that the heat from point A is conducted through the longest distance (larger heat resistance) to transfer to the fluid, thus there is the highest cladding temperature. At point B, the highest temperature of cladding surface occurs due to the poor heat transfer that is limited by spatial effect, which is seen in Fig. 2-39 that the turbulence around point B (red dots) is weaker especially in geometry B and C.
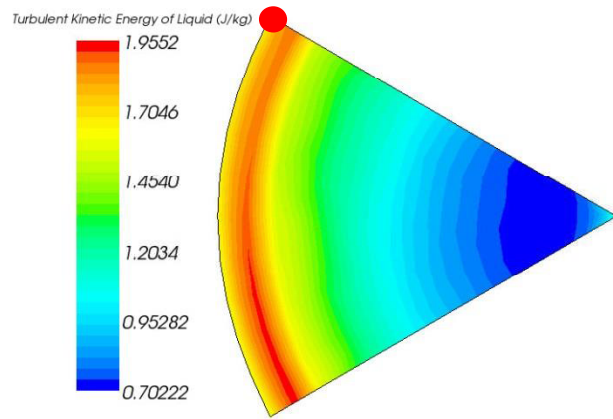
(a) Geometry A
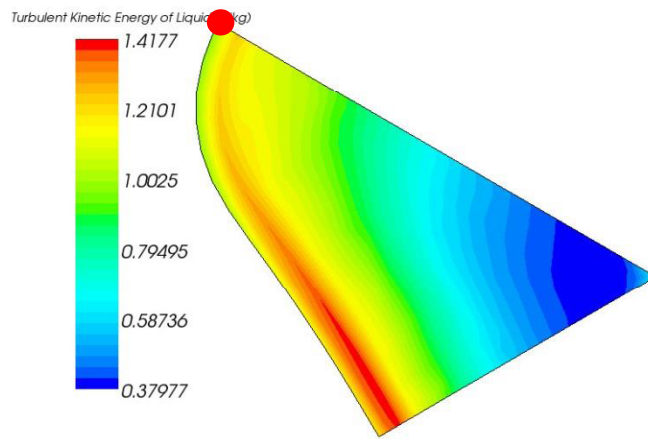
(b) Geometry B
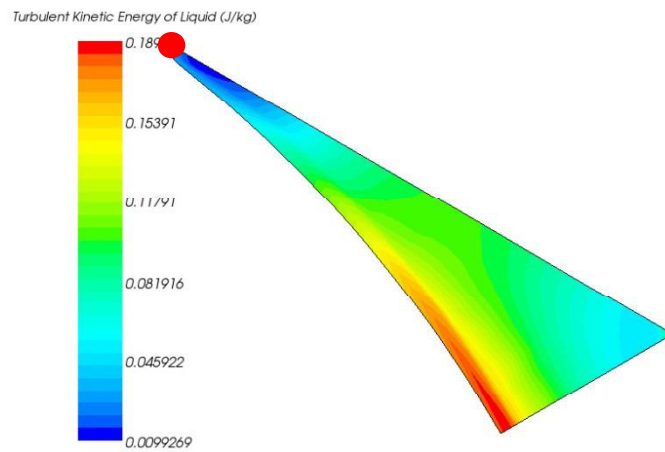
(c) Geometry C

Fig. 2-39 Cross-sectional liquid turbulent kinetic energy distribution (295°C bulk temperature, PWR condition) of the different geometries

Radial void distribution

Void distribution is also influenced by the asymmetry characteristic, and it then determines the occurrence position and magnitude of CHF. Figure 2-40 illustrates the void distribution of cases at PWR DNB condition (the outlet of the channel where the DNB firstly occurs). It can be seen that the highest void fraction emerges near the point B (red dots in Fig 2-40), and is slightly away from the wall due to the pull of lift force. The results also indicate that the point B is the first dryout position where CHF occurs. From geometry A to C, the void fraction is more and more unevenly distributed. Especially in geometry C, the quality of bulk fluid is still low while that of the corner (near the point B) already reaches to the critical limit (0.82), and it is the main reason that geometry C has a low CHF.
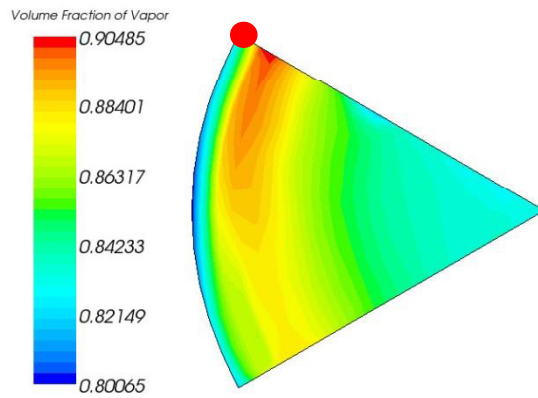
(a) Geometry A
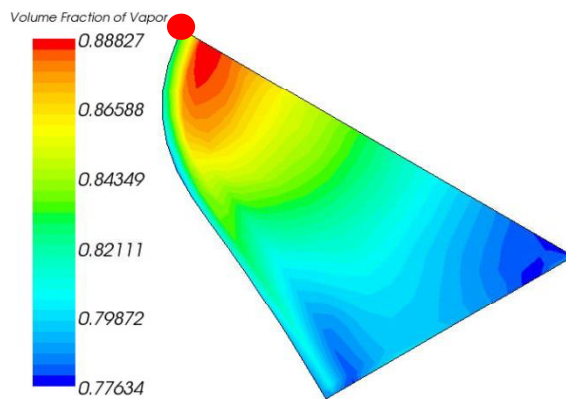
(b) Geometry B
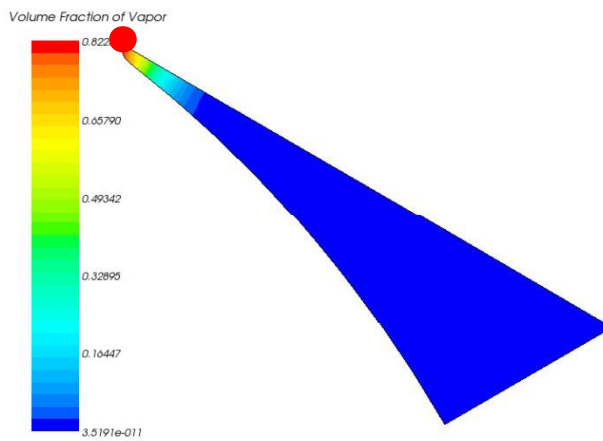
(c) Geometry C

Fig. 2-40 Cross-sectional void distribution (295°C bulk temperature, PWR condition) of the different geometries

2.5 Summary

Compared with conventional assemblies in LWRs, the tightly packed fuel rods assembly has much smaller coolant channel area. While it is expected to bring the benefit of high breeding, the thermal hydraulic issues become more challenging, such as cladding temperature, pressure drop and CHF. From above investigations, the following conclusions can be drawn:

At the supercritical pressure, geometry B is characteristic of moderated performance in terms of cladding temperature (MCST or MAXT) and the pressure drop: these assessment parameters of geometry B are always inclined to approach the lowest values (e.g. MCST of geometry A, MAXT and pressure drop of geometry C) among the three geometries, the overall characteristics of geometry B is better than the other two from the viewpoint of attaining broader design ranges under the given design criteria of MCST, MAXT and pressure drop. At the subcritical pressures, geometry C is not applicable due to the small CHF that could not satisfy the CHF criterion. Geometry B is superior to geometry A due to the broader design margins in terms of power, cladding temperature, CHF and pressure drop.

Although geometry B shows better thermal hydraulic characteristics than the other two geometries, this study is not intended to show that geometry B is the optimum among all potential geometries. The optimization of the channel geometry based on B is remained for the further study. CFD analyses show that the coolant channel geometries should be designed with considerations of CHF (DNB), pressure drop, MLHGR, MCST, MAXT. This methodology is applicable for high breeding reactors with tightly packed fuel assemblies at the operating pressures of Super FBR, PWR and BWR.

2.6 Reference

Auton, T.R., Hunt, J.C.R., and Prud'homme, M. 1988. The force exerted on a body in inviscid unsteady non-uniform rotational flow. Journal of Fluid Mechanics, 197, pp. 241-257.

Ampomah-Amoako, E., Akaho, E.H.K., Nyarko, B.J.B., Ambrosini, W., 2013. CFD analysis of the dynamic behavior of a fuel rod subchannel in a supercritical water reactor with point kinetics. Annals of Nuclear Energy, 59, pp. 211-223

Amselem, E., 2011. Analysis of boiling water reactor design and operating conditions effect on stability behavior. M. Sc. thesis, Royal Institute of Technology School of Engineering Sciences.

Chexal, B. and Lellouche, G., 1991. Void fraction correlation for generalized applications, Nuclear Safety Analysis Centre of the Electric Power Research Institute, Report NSAC/139.

Cui, X.Z., Kim, K.Y., 2003. Three-dimensional analysis of turbulent heat transfer and flow through mixing vane in a subchannel of nuclear reactor. Journal of Nuclear Science and Technology, 40, 719–724.

Cheng, X., Kuang, B., Yang, Y.H., 2007. Numerical analysis of heat transfer in supercritical water cooled flow channels. Nuclear Engineering and Design, 237(3), pp. 240-252.

Conner, M.E., Baglietto, E., Elmahdi, A.M., 2010. CFD methodology and validation for single-phase flow in PWR fuel assemblies. Nuclear Engineering and Design, 240(9), pp. 2088-2095.

Dobashi, K., Kimura, A., Oka, Y., Koshizuka, S., 1998. Conceptual design of a high temperature power reactor cooled and moderated by supercritical light water, Annals of Nuclear Energy, 25(8), pp. 487-505.

CD-Adapco, 2013. STAR-CCM+ Version 8.02 USER GUIDE.

Glasstone, S. and Sesonske, A. (1994) " Nuclear reactor engineering" 4th edition, Chapman and Hall, New York, NY, USA. ISBN 0-412-98521-7.

Groeneveld, D.C., Shan, J.Q., Vasić, A.Z., Leung, L.K.H. Durmayaz, A., Yang, J., Cheng, S.C., Tanase, A., 2007. The 2006 CHF look-up table, Nuclear Engineering and Design, 237(15–17), pp. 1909-1922

Guo, R. and Oka, Y., Unpublished results. CFD analysis of coolant channel geometries for a tightly packed fuel rods assembly of Super FBR. Submitted to Nuclear Engineering and Design.

Gu, H.Y., Cheng, X., Yang, Y.H., 2010. CFD analysis of thermal–hydraulic behavior of supercritical water in sub-channels, Nuclear Engineering and Design, 240(2), pp. 364-374.

Gou, J., Ishiwarari, Y., Oka, Y., Yamakawa, M., 2011. CFD analyses in tight-lattice subchannels and seven-rod bundle geometries of a Super Fast Reactor, Nuclear Engineering and Design, 241(5), pp. 1656-1666.

Horvath, A., Dressel, B., 2012. Numerical simulations of square arrayed rod bundles. Nuclear Engineering and Design, 247, pp. 1168–182.

Habib, M.A., Nemitallah, M.A., El-Nakla, M., 2014. Current status of CHF predictions using CFD modeling technique and review of other techniques especially for non-uniform axial and circumferential heating profiles. Annals of Nuclear Energy, 70, pp. 188-207.

Ismail, C., Karatekin, O., 1997. Numerical experiments on application of Richardson extrapolation with nonuniform grids, ASME J. Fluids Eng. 119, pp. 584–590.

In, W.K., Hwang, D.H., Jeong, J.J., 2013. A subchannel and CFD analysis of void distribution for the BWR fuel bundle test benchmark, Nuclear Engineering and Design, 258, pp. 211-225.

Kurul, N. and Podowski, M.Z. 1990. Multidimensional effects in sub-cooled boiling. Proceedings of the Ninth Heat Transfer Conference, Jerusalem.

Koshizuka, S., Takano, N., Oka, Y., 1995. Numerical analysis of deterioration phenomena in heat transfer to supercritical water, International Journal of Heat and Mass Transfer, 38(16), pp. 3077-3084.

Kitoh, K., *et al.*, 1997. Improvement on transient criteria of a supercritical water cooled reactor based on numerical simulation. Proceedings of 5th International Conference of Nuclear Engineering, ICONE5-2341, Nice, France.

Kim, S.H., Kim, Y.I., Bae, Y.Y., Cho, B.H., 2004. Numerical simulation of the vertical upward flow of water in a heated tube at supercritical pressure. In: Proc. of ICAPP04, Pittsburgh, PA, USA, June 13–17 (Paper 4047).

Krepper, E., Koncar, B., Egorov, Y., 2007.CFD Modelling of subcooled boiling—concept, validation and application to fuel assembly design. Nuclear Engineering and Design, 237, pp. 716–731.

Krepper, E., Rzehak, R., 2011. CFD for subcooled flow boiling: Simulation of DEBORA experiments. Nuclear Engineering and Design, 241(9), pp. 3851-3866.

Kevin L. and Alan J. K. 2011. AutoCAD 2012 Tutor for Engineering Graphics (1st ed.). Autodesk Press/Thomson Learning.

Lockett, M.J. and Kirkpatrick R.D., 1975. Ideal Bubbly Flow and Actual Flow in Bubble Columns. Transactions of the Institution of Chemical Engineers, 53, pp. 267-273.

Lellouche, G.S. and Zolotar, L.A., 1982. "Mechanistic Model for Predicting Two-Phase Void Fraction for Water in Vertical Tubes, Channels and Rod BundIes", Electric Power Research Institute, NP-2246-SR.

Liu, B., Dzodzo, M.B., Smith III, L.D., Conner, M.E., Young, M.Y., 2004. Application of CFD in the design process for PWR spacer grid mixing vanes. In: Proceedings of 2004 International Meeting on LWR Fuel Performance, Paper, 1065, pp. 127–138.

Liang, F.C., Wang, D., Lin, Z.H., 2004. Determination of the pseudo-critical temperature of water in the supercritical pressure region, Power Eng., 24(6), pp. 869–892.

Lo, S., Osman, J., 2012. CFD modeling of boiling flow in PSBT 5 × 5 bundle. Science and Technology of Nuclear Installations 2012, pp. 1–8.

Mokry, S., Pioro, I., Kirillov, P., Gospodinov, Y., 2010. Supercritical-water heat transfer in a vertical bare tube. Nuclear Engineering and Design, 240(3), pp. 568-576.

OECD, 2010. OECD/NRC benchmark based on NUPEC PWR subchannel and bundle tests (PSBT), Chapter 2 TEST FACILITIES, pp. 24.

OECD, 2012. Nuclear Fuel Safety Criteria Technical Review, Chapter 3: Review of fuel criteria, pp. 21-61.

Oka, Y., Inoue, T., Yoshida, T., 2013. Plutonium breeding of light water cooled fast reactors. Journal of Nuclear Science and Technology, 50(1), pp. 15-20.

Pierre, C.C., Bankoff, S.G., 1966. Vapor volume profiles in developing two-phase flow. International Journal of Heat and Mass Transfer, 10, pp. 237–249.

Petrov, V., *et al* 2012. Validation of STAR-CD and STAR-CCM+ boiling models against PSBT and DEBORA experimental data. CASL repot: CASL-U-2012-0163-000

Ranz, W.E., and Marshall, W.R. 1952. Evaporation from drops--Part I and II, Chemical Engineering Progress, 48(3), pp. 141

Roache, P. J., 1994. "Perspective: A method for uniform reporting of grid refinement studies." Journal of Fluids Engineering, 116(3), pp. 405-41

Roy, R.P., Kang, S., Zarate, J.A., Laporta, A., 2002. Turbulent subcooled boiling flow—experiments and simulations. International Journal of Heat and Mass Transfer, 124, 73–93.

Reinders, R., Odras, F., Keheley, T., 2003. Thermal hydraulic fuel assembly optimization with CFD programs. In: Proceedings of ENS Top Fuel 2003, Paper 420.

Palko, D., and Anglart, H., 2008. Theoretical and Numerical Study of Heat Transfer Deterioration in High Performance Light Water Reactor, Sci. Tech. Nuclear Installations, (2008), pp. 1–5.

Roelofs, F., 2004. CFD Analyses of heat transfer to supercritical water flowing vertically upward in a tube. Under the contract of the Netherlands Ministry of Economic Affairs.

Smith, S. L., 1969. Void fractions in two-phase flow. A correlation based on an equal velocity head model. Proc. Inst. Mech. Engng., 184(36), 647-664.

Shah, M.M., 1987. Improved general correlation for critical heat flux during upflow in uniformly heated vertical tubes. International Journal of Heat and Fluid Flow, 8(4), pp. 326-335.

Shih, T.-H., Liou, W.W., Shabbir, A., Yang, Z. and Zhu, J. 1994. "A New k- Eddy Viscosity Model for High Reynolds Number Turbulent Flows --Model Development and Validation", NASA TM 106721.

Sharabi, M., Ambrosini, W., 2009. Discussion of heat transfer phenomena in fluids at supercritical pressure with the aid of CFD models. Annals of Nuclear Energy, 36(1), pp. 60-71

Tomiyama, A., Kataoka, I., Zun, I., and Sakaguchi, T. 1998. Drag Coefficients of single bubbles under normal and micro gravity conditions. JSME International Journal, Series B, 41(2), pp. 472-479.

Tomiyama, A., Tamai, H., Zun, I., and Hosokawa, S. 2002. "Transverse migration of single bubbles in simple shear flows". Chemical Engineering Science, 57, pp. 1849–1858.

Weisman, J. and Pei, B.S., 1983. Prediction of critical heat flux in flow boiling at low qualities, Int. J. Heat Mass Transfer 26, pp. 1463 - 1477.

Wagner, W., Kruse, A., 1998. Properties of Water and Steam: The Industrial Standard IAPWS-IF97 for the Thermodynamic Properties and Supplementary Equations for Other Properties: Tables Based on These Equations, Springer-Verlag.

Yamagata, K., Nishikawa, K., Hasegawa, S., Fujii, T., Yoshida, S., 1972. Forced convective heat transfer to supercritical water flowing in tubes, International Journal of Heat and Mass Transfer, 15(12), pp. 2575-2593.

Yang, S.-G., Jeong, Y.-S., Kim, H.-J., Kim, K.-H., Park, E.-J., Hwang, S.-T., Kim, Y.-K., 2005. Heat transfer performance analysis of a 5 × 5 rod bundle spacer grid by CFD Simulations. Proceedings of ICAPP'05, Paper 5124.

Yoshida, T. and Oka, Y., 2013. High breeding core of a supercritical-pressure light water Cooled fast reactor. Proceedings of the 2013 21st International Conference on Nuclear Engineering, ICONE21-15753, Chengdu, China.

Zhang, W., Hibiki T., Mishima K., Mi Y., 2006. Correlation of critical heat flux for flow boiling of water in mini-channels, Int. J. Heat Mass Transfer 49 1058–1072

Chapter 3 Core design of breeding BWR with tightly packed fuel assemblies

3.1 Introduction

High breeding with light water cooling is not easy to be achieved. The main obstacle is the moderating effect of light water, which softens the neutron spectrum. Decreasing the volume ratio of coolant to fuel is normally introduced as a way to harden the neutron spectrum and achieve breeding with light water cooling. Therefore, the tight-lattice assembly was proposed to design reactors cooled by light water with hard neutron spectrum. However, most of them were HCLWRs and none achieved high breeding to meet the growth rate of energy demand in advanced countries as explained in Section 1.2.

With tightly packed fuel assemblies, the number ratio of hydrogen atoms to heavy metal atoms (H/HM) is significantly reduced to less than 0.1 which is about 1/6 of that of Reduced-Moderation Water Reactor (RMWR) (HIBI *et al.*, 2001). Super FBR adopts these assemblies, obtaining high breeding of CSDT, which is less than 50 years (Yoshida *et al.*, 2014).

The high breeding performance of Super FBR indicates that, application of the tightly packed fuel assembly on conventional LWR-type reactors, such as BWR-type or PWR-type reactor, may also be effective in achieving high breeding. Compared with Super FBR, the conventional LWR-type reactors with technologies which are currently in use are expected to be easier to implement. When comparing the two main LWR types, BWR-type and PWR-type, BWR-type gains more advantages on breeding, since the coolant is boiling water that generates larger amount of void in the reactor core, leading to a harder neutron spectrum. Meanwhile, from the viewpoint of safety, the negative void reactivity should be satisfied, which is consistent with conventional LWRs. From the viewpoint of neutron economy, high enrichment should be avoided as well.

Hence, this study aims to design the BWR-type reactor with the tightly packed fuel assemblies, which attains both high breeding and negative reactivity.

3.2 Core design methods

3.2.1 Design goals and criteria

3.2.1.1 Design goals for breeding BWR

The design goals of the breeding BWR core mainly focus on the breeding performance, which is evaluated by two most important parameters, Fissile Plutonium Surviving Ratio (FPSR) and Compound System Doubling Time (CSDT). Both the two parameters here are evaluated with an equilibrium core.

FPSR is usually used for MOX fuel, when the fissile materials mainly consist of ^{239}Pu and ^{241}Pu, other isotopes such as ^{235}U are negligible. The definition of FPSR is given as follows:

$$\text{FPSR} = \frac{FP(EOEC)}{FP(BOEC)} \tag{3-1}$$

where the FP(BOEC) is the Fissile Plutonium (FP) inventory at the Beginning Of the Equilibrium Cycle (BOEC), the FP(EOEC) is the FP inventory at the End Of the Equilibrium Cycle (EOEC).

CSDT is different from FPSR, this parameter involves multiple breeder reactors in a system. It takes into account the process that the breeder reactors in the system produce excess fissile materials and use them to start up a new breeder reactor via reprocessing and fabrication. The time required for the system to generate equivalent quantity of fissile materials to double the capacity of the installed breeder reactors is the definition of CSDT. It assumes that all the produced fissile materials are utilized to build new reactors as soon as enough excess fuel from each cycle is accumulated and hence the reactor number is growing. The CSDT can be calculated by the following equation:

$$\text{CSDT} = \frac{\text{Reactor doubling time}}{\text{Operating ratio}} \times \frac{\text{Ex-core factor}}{\text{1-ex-core fissile Pu loss rate}} \times ln2 \tag{3-2}$$

where the Reactor Doubling Time (RDT) is defined as:

$$\text{RDT} = \frac{\text{Loaded fissile Pu inventory} \times \text{Refueling batch}}{\text{Fissile Pu inventory at EOEC-Fissile Pu Inventory at BOEC}}$$

$$\times \frac{\text{Cycle length}}{365} \tag{3-3}$$

and the Ex-core Factor (EF) and operating ratio are given by Eq. 3-4 and Eq. 3-5 respectively:

$$\text{Ex-core factor} = 1 + \frac{\text{Ex-core period}}{\text{In-core period}} \tag{3-4}$$

$$\text{operating ratio} = \frac{\text{cycle length}}{\text{cycle length+reactor downtime}} \tag{3-5}$$

where the reactor downtime is preliminarily set to be 30 days which is the same as Super FBR (Yoshida *et al.*, 2013).

From the above equations, it can be seen that the fissile material lost in fabrication and reprocessing operations is taken into account. In the current study, to estimate the ex-core fissile plutonium loss, the half-life of ^{241}Pu, is given as 14.4 years and the ex-core period for fuel reprocessing and fabrication is considered as 5 years, which is the same as that of RMWR (Hibi *et al.*, 2001).

To achieve breeding, FPSR should be at least larger than 1.0. As discussed in Section 1.2, to meet the energy demand of advanced countries, such as G7 member countries, CSDT should be shorter than 50 years.

Thus, specifically, the design goals are:

1).   FPSR is larger than 1.0

2).   CSDT is less than 50 years.

3.2.1.2 Design criteria for breeding BWR

It is expected that the high breeding BWR core can be incorporated in the current BWR plant system, utilizing as much established technologies as possible for the sake of obtaining high reliability as well as saving the capital cost. Therefore, developing the design criteria basically follows the track of that for conventional BWRs. Generally, these design criteria include:

Negative coolant void reactivity during cycle

Coolant void reactivity has been a big concern for fast reactor design for a long time. For light water cooled reactors, the negative void reactivity is especially required since the loss of coolant accident (LOCA) is a design basis accident (DBA). In fast reactors, coolant voiding hardens the neutron spectrum and enhances the fast fission, meanwhile increasing the neutron leakage. The void reactivity depends on which effect is more dominant.

By understanding the above mechanism of void reactivity, several methods have been proposed to decrease the void reactivity. An effective approach is to reduce the active core height, which is widely adopted in liquid metal cooled fast breeder reactors (LMFBRs). Short core is in favor of neutron leakage. Placing void channels in the core is another approach which also enhances the neutron leakage at void condition. The other method is to apply heterogeneous blanket layers in the axial direction. The blanket layers absorb the neutrons transporting out from the seed region rather than letting them leak out of the core. This approach is shown to be effective in design studies of RMWR (Hibi *et al.*, 2001).

Placing a solid moderator, such as $ZrH_{1.7}$, in the core is known as another effective way to reduce the coolant void reactivity (Jevremovic *et al.*, 1993; Oka and Jevremovic, 1996). By applying $ZrH_{1.7}$ in blanket assemblies, neutron spectrum hardening at void condition can be mitigated, neutrons coming out from voided seed assemblies being slowed down by $ZrH_{1.7}$ and then absorbed in the blanket assemblies. However, the solid moderator softens the neutron spectrum at normal operation condition as well. From the viewpoint of neutronics, it is not in favor of breeding, thus, the amount of solid moderator should be limited in design of breeder reactors.

Maximum linear heat generation rate below 44kW/m

As the burnup increase, the fuel pellet will gradually swell and pose stress on cladding, in extreme conditions, cracking the cladding. Moreover, the stress increases at abnormal conditions with a temperature rise owing to the different expansion rate of cladding and fuel pellet. This phenomenon is known as pellet-clad mechanical interaction (PCMI). In the conventional BWR design, the plastic circumferential deformation of cladding due to PCMI is limited to be less than 1% at abnormal transients. Correspondingly, the maximum linear heat generation rate (MLHGR) is restricted to be less than 44kW/m at normal operating condition. It is also taken as the limitation for the current study.

Minimum critical heat flux ratio over 1.9

At BWR operating condition, the void fraction is normally high and the heat transfer between cladding surface and coolant depends on liquid film. Critical heat flux (CHF) phenomenon leads to a sudden decrease of heat transfer coefficient in the two-phase flow owing to the liquid film dryout, leading to the cladding overheat. Normally, the measure to increase the CHF is to increase the mass flux, while this measure leads to reduction of the exit quality under a certain power. From the CFD study in Chapter 2, it is found that coolant channel geometry also significantly influences the CHF, applying geometry B can increase the CHF from that of geometry A (Guo and Oka, 2015). Critical condition limit is established in terms of minimum critical heat flux ratio (MCHFR), as shown in Eq. 3-6:

$$\text{MCHFR} = \min\left(\frac{Critical\ heat\ flux}{Heat\ flux\ at\ normal\ operating\ condition}\right) \qquad (3\text{-}6)$$

For development of new fuel assembly (FA) designs, FA specific Critical Power Ratio (CPR) correlations are not available, since most of them are for bundle geometry. For current channel geometry, CHFR criterion is used. Taken from the conventional BWR design, MCHFR in the current study is preliminarily set to be larger than 1.9 (GE, 1973; Todreas and Kazimi, 1999;

Ishigai, 1999) at normal operating condition so as to prevent the boiling transition condition at the most adverse transient situations.

Core pressure drop and stability considerations

Narrow coolant channels in tightly packed fuel assembly lead to high pressure drop, resulting in high pumping power and potential flow instability problem. To adapt this characteristic, different plant systems from that of conventional BWRs are needed. Pressure drop is not strict design limit for the high breeding BWR core design, because the high pumping power requirement can be managed by engineering techniques and the flow instability is able to be eliminated by applying inlet orifice to increase the pressure drop at the inlet. In addition, high mass flux also compensates for the flow instability.

3.2.2 Calculation scheme for core design

The flowchart of core calculation scheme is shown as Fig. 3-1. Neutronic calculation is conducted at first for achieving an equilibrium core, and then thermal-hydraulic calculation is conducted based on the power distribution from the neutronic calculation. Normally, in light water cooled thermal reactor designs, the core neutronic calculation is coupled with that of thermal-hydraulics. But in the current design, the coupling is weak (void reactivity close to 0) due to small inventory of coolant in the core, the coupling calculation is not is not necessary. More details can be found in Section 3.4.5. Hence, a two-step calculation procedure is adopted: at the first step, the coolant density distribution applied in the nuclear calculation is evaluated by assuming a uniform core power distribution; at the second step, the evaluated power distribution from the first step is used to recalculate the coolant density distribution. Then, this distribution is applied to conduct the second time nuclear calculation. It was found that, the above two coolant distributions do not significantly differ from each other.
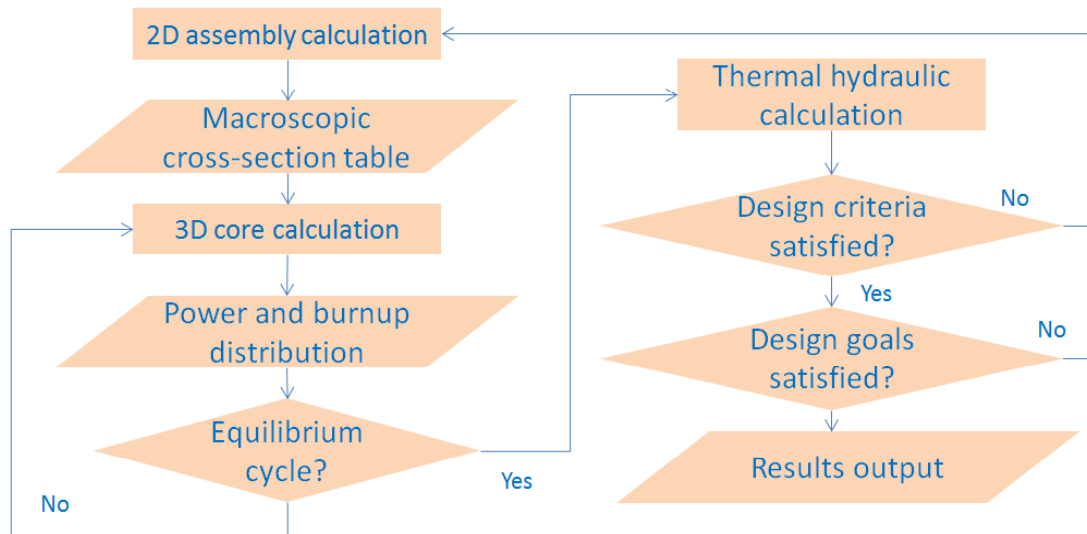
Fig. 3-1 Flowchart of calculation for core design

3.2.3 Neutronic calculation method

The nuclear design is conducted with SRAC code system (Okumura *et al.*, 2007) developed by Japan Atomic Energy Agency (JAEA), which consists of several modules to perform the nuetronic calculations. In the current study, PIJ module is used to calculate the cell depletion and ASMBURN is used for assembly burnup calculations. The above two calculations are the staged homogenized procedure for preparation of homogenized macroscopic cross-sections for fuel assembly. Then, these cross-sections are used in CORBN to conduct the 3-D core burnup calculations. The overall calculation procedure is shown in Fig. 3-2 (Han, 2010): first, the cross-sections of the basic fuel cells are calculated by using PIJ (collision probability method) module in SRAC for a range of burnup steps; then, by using ASMBURN, assembly-wise cross-sections are prepared based on cell cross-sections from the first step; at last, core calculation is conducted by using COREBN (Finite Difference Method) on the basis of assembly cross-sections.

Rod pitch

White or reflective boundary condition

Assembly depletion calculation (ASMBURN, CPM)
- Intra-assembly heterogeneity
- Guild tube
- Wrapper tube and assembly gap
- For given coolant density and burnup

Rotational boundary condition

Reflective boundary

Rotational boundary condition

C L

1/6 symmetry of fuel assembly

Unit cell depletion calculation (PIJ CPM)
- Resonance integral (PEACO)
- Spatial selfshielding
- For given coolant density and burnup state

Rotational boundary condition

C L

Rotational boundary condition

Core depletion calculation (COREBN, FDM)
- Tri-Z model
- Thermal hydraulic coupling
- Core heterogeneity
- Fuel management scheme
- Interpolation of macro. XS with respect to coolant density and burnup

Fig. 3-2 The calculation procedure of nuclear design (Han, 2010)

Currently, the SRAC 2006 is used for core design with the neutron data libraries JENDL-3.3 (Shibata, 2003), which consists of 107 group neutron cross-sections for more than 300 nuclides. Above staged calculation procedure has the convenience of describing complicated core geometries, and this method as well as the code system are wildly used for conceptual design of various core types.

3.2.3.1 Cell depletion calculation

A cell in the nuclear design of the current study represents a single fuel rod and the surrounding coolant (or surrounding coolant channels and metal fitting for tightly packed fuel assembly, as shown in Fig. 3-3), also known as "unit cell", which is the representative and repetitive structure in the fuel assembly. The spatial and energy distribution of neutron flux within the unit cell can be calculated by the cell depletion calculation. White or reflective boundary condition is used to model "representative" unit cell.

In the current study, PIJ module is used to perform the cell depletion, which is based on the Collision Probability Method (CPM) that solves the neutron transport equations (Okumura *et al.*, 2007). The original 62 fast energy groups and 45 thermal energy groups in SRAC are collapsed to 15 groups for each energy ranges in the output homogenized macroscopic cross-sections of cells. The effective resonance cross-sections are directly calculated with hyper-fine neutron energy group by PEACO routine (Okumura *et al.*, 2007).
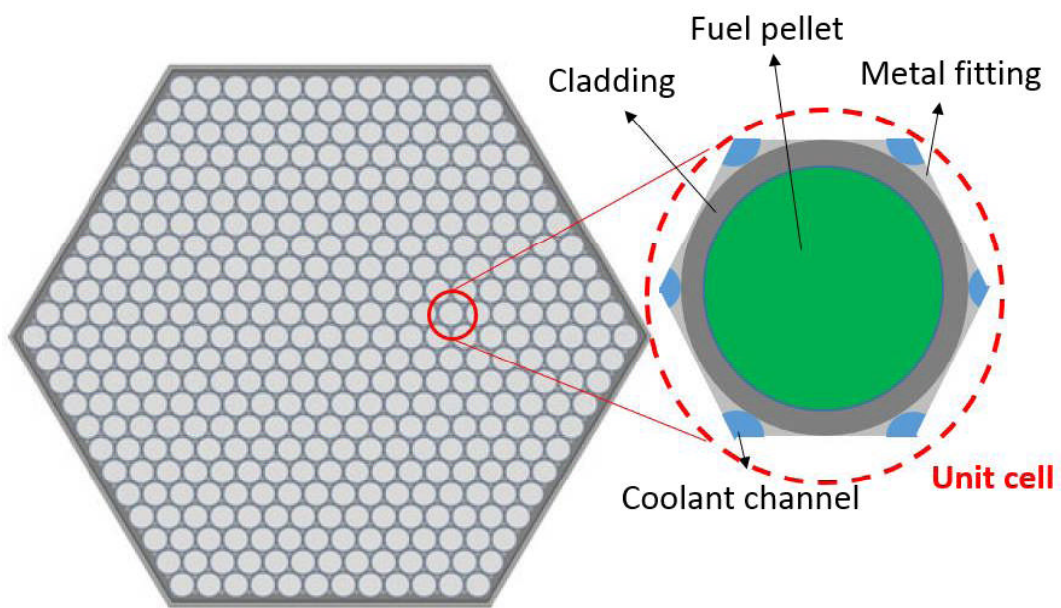
Fig. 3-3 Unit cell in tightly packed fuel assembly cell depletion calculation

To prepare the macroscopic cross-sections corresponding to different coolant densities (or coolant temperatures) as well as different fuel temperatures, the branch-off calculations are performed, in which the macroscopic cross-sections are obtained by using a linear interpolation of depletion data of the reference case instead of neutronic calculations.

Two depletion methods are used in PIJ module: for seed fuel pins, the constant Linear Heat Generation Rate (LHGR) is assumed; while for blanket fuel rods, the constant neutron flux is assumed on account of the considerable change of the LHGR with the increase of burn up, owing to the buildup of fissile Pu.

3.2.3.2 Assembly depletion calculation

The calculation procedure for assembly depletion is similar to that of cell depletion. The calculations produce the homogenized macroscopic cross-sections over fuel assembly geometry

for core depletion calculation, reflecting the heterogeneity caused by different fuel regions, existence of control rods or other non-fuel materials, and duct wall etc. inside the assembly. The calculations are performed by ASMBURN module, which is also based on CPM, with input cross-sections of 30 energy groups from the cell depletion calculations. The output cross-sections are further collapsed to 10 energy groups, as shown in Table 3-1. Similarly to cell depletion calculations, branch-off calculations are performed for different coolant densities.

Table 3-1 Neutron energy group structure for core diffusion calculations

Upper energy (eV)	Lower energy (eV)	Group number
1.00E+07	8.21E+05	1
8.21E+05	8.65E+04	2
8.65E+04	9.12E+03	3
9.12E+03	9.61E+02	4
9.61E+02	1.01E+02	5
1.01E+02	1.07E+01	6
1.07E+01	3.93E+00	7
3.93E+00	1.86E+00	8
1.86E+00	3.42E-01	9
3.42E-01	9.99E-06	10

For one assembly, one set or multiple sets of cross-sections can be prepared for succeeding core calculation. Each set of cross-sections, known as X-region in SRAC system, depends on the degree of heterogeneity within the assembly, for instance, the existence of different enrichments or materials. For example, Fig. 3-4 shows the blanket assembly with $ZrH_{1.7}$ layers, the cross-sections of fuel pins adjacent to $ZrH_{1.7}$ layer would be very different from that of fuel pins away from that layer, thus they are treated as different X-region (fuel region as indicated in Fig. 3-4), where cross-section set for each being prepared separately.
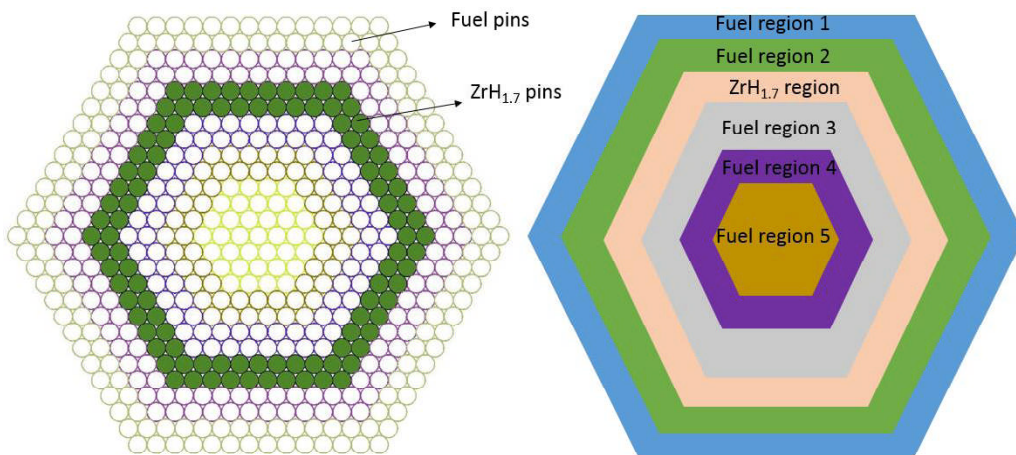
Fig. 3-4 Multiple X-regions in one assembly

3.2.3.3 Core depletion calculation

With cross-sections prepared by assembly depletion calculations, the core depletion calculation is conducted by using the COREBN module, which is based on three-dimensional diffusion calculation in triangular mesh geometry of CITATION code (Mclane, 1996) using Finite Difference Method (FDM). One sixth symmetric geometry of the core with rotational boundary condition is described in the calculation, an example given in Fig. 3-5.
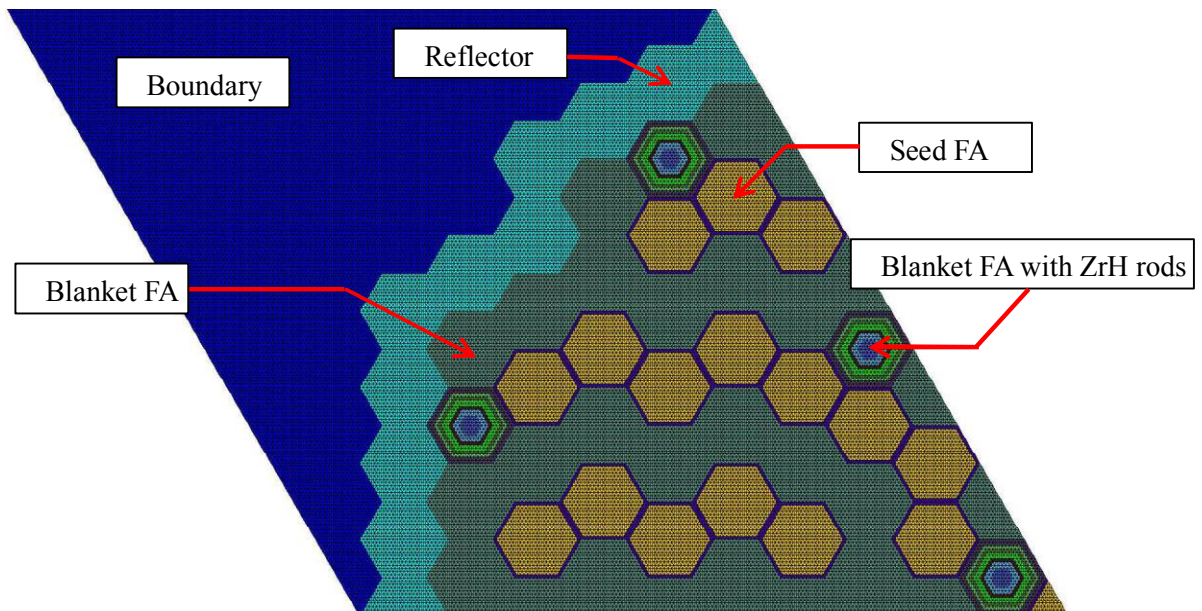
Fig. 3-5 Example of core geometry described in triangular mesh for 1/6 symmetric core

In the radial direction, each assembly or reflector is constructed of hundreds of triangle meshes, while tens of that in the axial direction, because of the large heterogeneity of the core in the radial direction compared with the relatively small heterogeneity in the axial direction. The tabulated cross-sections from assembly depletion calculations are used in COREBN module to calculate the cross-sections at each mesh by using a linearly interpolation method with respect to the burnup, fuel temperature and coolant density of its belonging fuel element.

Location change of fuel assemblies due to the fuel shuffling is also taken into account. Neutron flux distribution at each mesh is obtained by solving the neutron diffusion equation of finite difference scheme and then used to evaluate the power density for each mesh and derive the three-dimensional core power distribution. However, the fuel-pin wise power density as well as the power distribution cannot be obtained directly from the mesh power.

3.2.3.4 Pin power calculation

The power distribution obtained from core depletion calculation is based on a homogeneous cross-section of each X-region (for most cases, one assembly is treated as one X-region), and cannot take into account the influence of the heterogeneity within the X-region. However, the local neutron flux and power distribution for each fuel pin within an X-region may differ significantly from others when the heterogeneity within the X-region is considered.

Hence, the heterogeneity is evaluated by a local Heterogeneous Form Factor (HFF) obtained from assembly calculation of ASMBURN. Combined with the Homogeneous Power Distribution (HPD) and Average Power (AP) for each X-region obtained from core calculation, the pin power can be reconstructed as follows:

$$P_{pin} = HPD \cdot AP \cdot HFF \tag{3-7}$$

Because the triangle mesh and fuel rod do not correspond one-to-one in position, the triangular interpolation method is used to reconstruct the pin power by correlating the powers of neighboring three meshes, as shown in Fig. 3-6. Power of each rod is obtained by using equation:

$$P_{rod} = \frac{P_1 L_1 + P_2 L_2 + P_3 L_3}{L}$$
$$L = L_1 + L_2 + L_3 \tag{3-8}$$

where L is the distance form rod center to mesh center, P is the power.
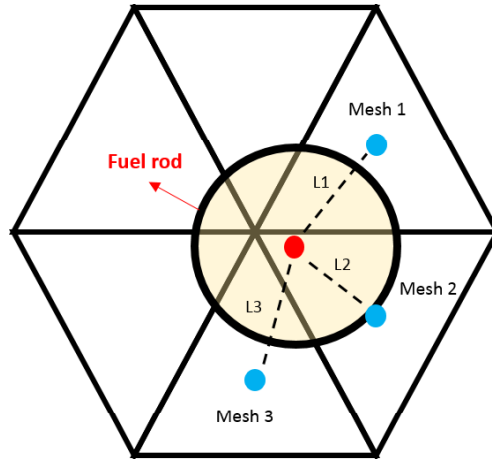
Fig. 3-6 Pin power reconstruction

3.2.4 Thermal hydraulic calculation

Coolant channels of the tightly packed fuel assemblies take a small area fraction, below 0.1 as introduced in chapter 2. From the viewpoint of neutronics, the feedback effect from thermal-hydraulics is much weaker than that of conventional LWRs. However, the thermal-hydraulic calculations are still required to evaluate the thermal-hydraulic performances of the core and to evaluate the satisfaction of design criteria.

The single channel model is employed to conduct the calculations, considering its efficiency and sufficient accuracy for conceptual design. Several fundamental parameters are evaluated by the thermal-hydraulic calculations, such as coolant density, exit quality, pressure drop, critical heat flux ratio (CHFR), mass flux and cladding temperature. A home-made code based on MATLAB language (Mathworks, 2015) is developed for this purpose. In this chapter, only steady-state condition is considered.

3.2.4.1 General relations

The single channel model assumes smooth cylindrical tubes. Channel geometry other than circular is accommodated by using the equivalent diameters.

Some commonly-used relations are shown as following:

mass flux:

$$G = \frac{4\dot{m}}{A} \tag{3-9}$$

equilibrium quality:

$$x_e = \frac{h - h_l^{sat}}{h_l^{sat} + h_v^{sat}} \tag{3-10}$$

114

real vapor quality:

$$x = \frac{\dot{m}_v}{\dot{m}_v + \dot{m}_l} \qquad (3\text{-}11)$$

where the G is the mass flux (in kg/m2s), $\dot{m}$ the mass flow (in kg/s), A the (cross-sectional) area (in m^2), h the specific enthalpy (in kJ/kg), h^{sat} the saturated enthalpy, the subscript v and l indicate the vapor and liquid respectively.

3.2.4.2 Axial enthalpy, equilibrium quality and density fields

Either average channel or hot channel is divided into several nodes $\varDelta z$ (m) in the axial direction, and for each node the enthalpy $h_{f,m}(z)$ is calculated by using the energy balance:

$$h_{f,m}(z) = h_{f,m}(z - \Delta z) + \frac{q\prime(z) \cdot \Delta z}{G \cdot A} \qquad (3\text{-}12)$$

where the $q'(z)$ is the linear heat flux (in kW/m) which is function of channel length and gained from core neutronic calculation.

After the enthalpy field is calculated, the coolant temperature field $T(z)$ is obtained from the water steam table (Wagner, 1998), and the equilibrium quality field $x_e(z)$ can be calculated by using Eq. 3-10.

The density field $\rho(z)$ is calculated by:

$$\rho(z) = \begin{cases} \rho_l(z), & x_e < 0 \\ \rho_m(z), & x_e \geq 0 \end{cases} \qquad (3\text{-}13)$$

$$\rho_m(z) = \frac{1}{\left[\frac{1-x(z)}{\rho_l(z)} + \frac{x(z)}{\rho_g}\right]} \qquad (3\text{-}14)$$

3.2.4.3 Subcooling models

Subcooling models are used for computing the real vapor quality where the local boiling occurs at the heated surface, while the mean enthalpy of coolant is still less than saturation. The subcooling is characteristic of existence of non-thermal-equilibrium.

The true quality $x(z)$ is defined according to the EPRI model (Lellouche, 1982) expressed by hyperbolic functions:

$$x = \begin{cases} \dfrac{x_e - x_d\left[1 - tanh\left(1 - \frac{x_e}{x_d}\right)\right]}{1 - x_d\left[1 - tanh\left(1 - \frac{x_e}{x_d}\right)\right]}, & x_e \geq x_d \\ \qquad\qquad 0, & x_d \leq x_d \end{cases} \qquad (3\text{-}15)$$

where x_d is the bubble departure quality. The location of the void departure point is determined by using the criteria from the empirical method (Saha and Zuber, 1974):
if $Pe < 70{,}000$:

$$\left[h_f - (h_l)_d\right] = 0.0022 \frac{q\prime\prime D_h C_{pl}}{k_l} \qquad (3\text{-}16)$$

115

if $Pe > 70,000$:

$$[h_f - (h_l)_d] = 154q''/G \qquad (3\text{-}17)$$

where the Pe is Péclet number, D_h the hydraulic diameter, C_{pl} the liquid heat capacity.

3.2.4.4 Void fraction models

The vapor volume fraction is computed based on the true quality obtained by method from above section. Several methods are provided here to correlate the void fraction and true quality. When no slip between the vapor and liquid phases is assumed, the void fraction can be represent as following:

$$\alpha = \frac{xv_g}{(1-x)v_f + xv_g} \qquad (3\text{-}18)$$

known as homogeneous equilibrium model (HEM).

A simple way accounting for the effect of phase slip is to incorporate a slip ratio S in the HEM model as:

$$\alpha = \frac{xv_g}{(1-x)v_f S + xv_g} \qquad (3\text{-}19)$$

The slip ratio S is defined as the velocity ratio of vapor to liquid phase. In the current study, the Smith correlation (Smith, 1969) is used to compute the S, described as:

$$S = 0.4 + 0.6 \left[\frac{0.4 + x(\frac{v_g}{v_f} - 0.4)}{0.4 + 0.6x} \right]^{1/2} \qquad (3\text{-}20)$$

Another void model developed by EPRI (Lellouche, 1982) includes the drift velocity Vgi, the vapor velocity relative to mean velocity of the mixture, and can be correlated with the subcooled boiling models. The correlation is:

$$\alpha = \frac{xv_g}{C_0 \left[x + \frac{\rho_g}{\rho_f}(1-x) \right] + \frac{\rho_g v_{gj}}{G}} \qquad (3\text{-}21)$$

and the drift velocity V_{gi}, is expressed as:

$$v_{gj} = 1.41 \left[\frac{\sigma g g_c (\rho_f - \rho_g)}{\rho_f^2} \right]^{1/4} \frac{(1-\alpha)^{1/2}}{1+\alpha} \qquad (3\text{-}22)$$

where the g is gravitational acceleration, $g_c = 32.2$ is the conversion factor of unit, and σ the water surface tension. C_0 is a function of pressure and void fraction itself, described as:

$$C_0 = \frac{L(\alpha, P)}{K_0 + (1 - K_0)\alpha^r} \qquad (3\text{-}23)$$

$$L(\alpha, P) = \frac{1 - e^{-C_1 \alpha}}{1 - e^{-C_1}} \qquad (3\text{-}24)$$

$$K_0 = K_1 + (1 - K_1)(\frac{\rho_g}{\rho_f})^{1/4} \qquad (3\text{-}25)$$

$$r = \frac{1 + 1.57\frac{\rho_g}{\rho_f}}{1 - K_1} \tag{3-26}$$

$$C_0 = \frac{4}{\frac{P}{P_c}(1 - \frac{P}{P_c})} \tag{3-27}$$

$$K_1 = \min(0.8, K_1^F) \tag{3-28}$$

Iteration is necessary to compute the C_0.

3.2.4.5 Pressure drop

The total pressure drop in a two-phase flow channel is comprised of three components due to acceleration, friction and gravity:

$$\Delta P_{tot} = \Delta P_{acc} + \Delta P_{fric} + \Delta P_{grav} \tag{3-29}$$

where:

$$\Delta P_{acc} = \left(\frac{G^2}{\rho_m}\right)_{out} - \left(\frac{G^2}{\rho_m}\right)_{in} \tag{3-30}$$

$$\Delta P_{grav} = \int_{z_{in}}^{z_{out}} \rho_m g \, dz \tag{3-31}$$

It should be noted that if the drift flux model is used, the velocities of vapor and liquid are different, resulting in a different ΔP_{acc} from that of HEM model.

For single-phase flow, the friction pressure drop ΔP_{fric} can be expressed in a general form:

$$\Delta P_{fric} = \frac{G^2}{2\rho_m} \cdot \frac{L}{D} \cdot f_{lo} \tag{3-32}$$

where f_{lo} is the single-phase friction factor, which is usually expressed by:

$$f_{lo} = a \cdot Re^b + c \tag{3-33}$$

For Re < 30,000, the turbulent friction factor for smooth tubes is given by Blasius relation, where a=0.316, b=-0.25; for 30,000 < Re < 1,000,000, the McAdams relation is used, where a=0.184, b=-0.2.

For two-phase flow, a general approach to obtain the two-phase friction factor is to define a multiplier $\emptyset_{lo}^2$ for single phase (liquid phase in this study) which flows at the same mass flux as the total two-phase flow. Thus, the friction pressure drop for two-phase flow is given by:

$$\Delta P_{fric}^{TP} = \Delta P_{fric}^{lo} \cdot \emptyset_{lo}^2 \tag{3-34}$$

The EPRI correlation (Reddy, 1982) is used to compute the two-phase multiplier, where $\emptyset_{lo}^2$ is given by a function of the flowing quality, mass flux and pressure as:

$$\emptyset^2 = 1.0 + (\frac{v_g}{v_f} - 1)xC_F \tag{3-35}$$

if P $\geq$ 600 psi,

$$C_F = 1.02x^{-0.175}(0.0036G)^{-0.45} \tag{3-36}$$

if P < 600 psi,

$$C_F = 0.357x^{-0.175}(0.0036G)^{-0.45}(1 + 10P/P_c) \tag{3-37}$$

where Pc is the critical pressure, v_g is the specific volume of saturated vapor, and v_f is the specific volume of saturated liquid.

3.2.4.6 Radial heat transfer models

The overall radial heat transfer models include the fuel rod heat conduction model and the heat transfer model from cladding wall to coolant. Fuel rod heat conduction model includes heat conduction in pellet, gap conductance between the pellet surface and the cladding inner surface, and heat conduction from inner surface to outer surface of the cladding. The calculation is conducted on the two-dimensional geometry, as shown in Fig. 3-7. The computational domain is comprised of 1/12 fuel rod and 1/6 coolant channel boundary. Adiabatic boundary condition is applied on the cutting edges, and the convection boundary condition is applied on the edge of coolant channel. The fuel pellet, cladding and the gap between the former two are divided into several meshes (triangle meshes for fuel and cladding, rectangle meshes for gap).
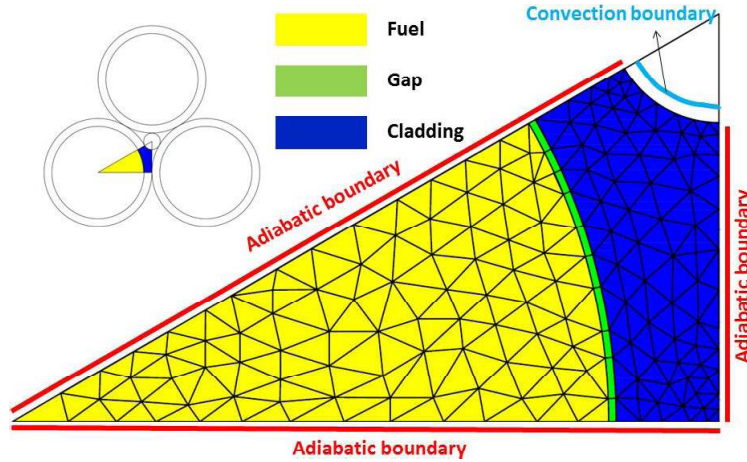
Fig. 3-7 Radial heat transfer model of fuel rod

The heat balance at steady-state for fuel meshes is given as a form of Poisson equation:

$$\nabla^2 T + \frac{q_v}{\kappa_f} = 0 \tag{3-38}$$

where q_v is volumetric heat generation rate, κ_f the thermal conductivity of fuel. The thermal conductivity is expressed as function of temperature (Ishiwatari, 2006):

$$K_f(\text{T}) = \frac{3824}{T+129.4} + 6.13 \times 10^{-11} T^3 \tag{3-39}$$

For meshes of gap and cladding, the heat balance is given by:

$$\nabla(\kappa_{c,g} \cdot \nabla T) = 0 \tag{3-40}$$

The gap conductance and thermal conductivity of the cladding are 0.44 W/m·K and 15.67 W/m·K, respectively in this study.

For adiabatic boundaries, the boundary condition is given by:

$$\nabla T = 0 \tag{3-41}$$

while for the convection boundary, the boundary condition is given by:

$$-\kappa_c \cdot \nabla T = h_f(T_c - T_{bulk}) \tag{3-42}$$

where h_f is the heat transfer coefficient on the cladding surface, T_c is the cladding surface temperature and T_{bulk} is the bulk temperature of coolant.

For the coolant flow in the BWR core, the heat transfer from cladding wall to coolant is related to both single-phase and two-phase flows. In the single phase region, the Dittus-Boelter correlations are the most commonly used for turbulent flows:

$$\text{Nu} = 0.023 Re_l^{0.8} Pr^{0.4} \tag{3-43}$$

where *Nu* is the Nusselt number, the *Re$_l$* is the single-phase Reynolds number and *Pr* is the Prandtl number. All fluid properties are obtained at the mean bulk temperature.

For two-phase flow region, the heat transfer coefficient ($h_{2\emptyset}$) is commonly expressed as the sum of contributions from nucleate boiling (h_{NB}) and convection (h_c):

$$h_{2\emptyset} = h_{NB} + h_c \tag{3-44}$$

A wildly used correlation of this form is from Chen (1966), which has a modified Dittus-Boelter correlation as the convection part h_c:

$$h_c = 0.023 \left(\frac{G(1-x)D_e}{\mu_f}\right)^{0.8} Pr_f^{0.4} \frac{k_f}{D_e} F \tag{3-45}$$

The F factor is given by:

$$\begin{aligned} F &= 1 & for\ \frac{1}{X_{tt}} < 0.1 \\ F &= 2.35\left(0.213 + \frac{1}{X_{tt}}\right)^{0.736} & for\ \frac{1}{X_{tt}} > 0.1 \end{aligned} \tag{3-46}$$

where $\frac{1}{X_{tt}}$ is given by:

$$\frac{1}{X_{tt}} = \left(\frac{x}{1-x}\right)^{0.9} \left(\frac{\rho_f}{\rho_g}\right)^{0.5} \left(\frac{\mu_g}{\mu_f}\right)^{0.1} \tag{3-47}$$

The nucleate part h_{NB} is given by:

$$h_{NB} = S(0.00122) \left[\frac{(k^{0.79} c_p^{0.45} \rho^{0.49})_f}{\sigma^{0.5} \mu_f^{0.29} h_{fg}^{0.24} \rho_g^{0.24}} \right] \Delta T_{sat}^{0.24} \Delta p^{0.75} \tag{3-48}$$

where:

$$\Delta T_{sat} = T_w - T_{sat} \tag{3-49}$$

$$\Delta p = p(T_w) - p(T_{sat}) \tag{3-50}$$

S is the suppression factor expressed as a function of the total Reynolds number:

$$S = \frac{1}{1 + 2.53 \times 10^{-6} Re^{1.17}} \tag{3-51}$$

where $Re = Re_l F^{1.25}$.

Chen's correlation covers the entire range of saturated boiling region and also can be extended to subcooled boiling region with x substituted for x_e.

3.2.4.7 Critical heat flux

Critical heat flux (CHF) is the phenomenon that the heat transfer of two-phase flow significantly deteriorates, resulting in a drastic increase of temperature on the cladding surface and possibly leading to a failure of cladding. At BWR working condition (high quality), CHF occurs as the form of "dryout", which indicates that the liquid film disappear at the end of annual flow due to evaporation, as shown in Fig. 3-8.

WALL AND FLUID
TEMPERATURE
VARIATION

Fluid
Temperature   H

$x_e = 1$

Vapor Core
Temperature   G

Wall
Temperature

"Dryout"

F

Fluid
Temperature   E

Wall
Temperature   D

Liquid Core
Temperature   C

$x_e = 0$

B

Saturation
Temperature   A
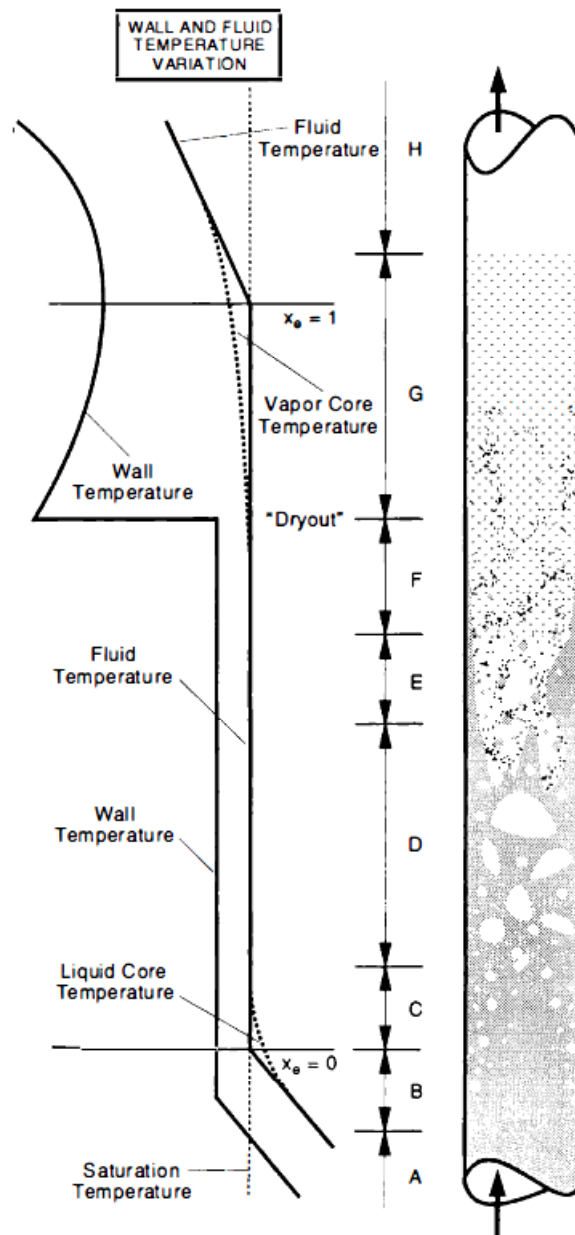
Fig. 3-8 Dryout in two-phase flow (Todreas and Kazimi, 1999)

In the current study, the Shah's correlation (Shah, M.M, 1987) was used to estimate the CHF (q_{crit}) values due to its wide applicable range, especially for small diameter tubes. Zhang *et al.* (2006) investigated several CHF correlations for application on small-diameter tubes (0.33< D_h <6.22mm) at various boundary conditions, and concluded that Shah's correlation showed good

agreements against experimental data. For conceptual design, it is expected that Shah's correlation could provide adequate accuracy. The equations are given by:

$$\frac{q_{crit}}{\dot{m}h_{fg}} = 0.124 \left(\frac{L}{z}\right)^{-0.89} \left(\frac{10^4}{Y_{shah}}\right)^n (1 - x_{in})$$

(3-52)

where L is the channel length, Y_{shah} is the parameter:

$$Y_{shah} = \dot{m}^{1.8} z^{0.6} \left(\frac{c_{pl}}{k_l \rho_l^{0.8} g^{0.4}}\right) \left(\frac{\mu_l}{\mu_g}\right)^{0.6}$$

(3-53)

while $Y_{shah} \leq 10^4$, n = 0,

if $Y_{shah} \geq 10^4$:

$$\begin{aligned} Y_{shah} \leq 10^6 \quad & n = \left(\frac{z}{L}\right)^{0.54} \\ Y_{shah} > 10^6 \quad & n = \frac{0.12}{(1-x_{in})^{0.5}} \end{aligned}$$

(3-54)

This correlation was originally developed for round tubes, but in case of geometry other than round but close to, the geometrical effect is approximately accounted by equivalent hydraulic diameter.

3.3 Fuel assembly design

Unlike with thermal LWRs, the tight fuel lattice is commonly used in assembly design of fast breeder reactors. The triangular lattice arrangement intrinsically gives rise to the higher fuel volume fraction than a square lattice with the same fuel pin pitch. In fast reactors cooled by light water, this lattice arrangement is adopted to minimize the fissile inventory by reducing the neutron leakage and maximize the fuel volume fraction to harden the spectrum.

In conventional triangular lattice, the fuel pins are separated by a spiral wire wrap or grid spacers. By contrast, the tightly packed fuel assembly is even "tighter" with zero gap between fuel pins. Metal fitting is used to interlink the fuel pins, axially penetrated by coolant channels in the center. The configuration of the tightly packed fuel assembly is used for both seed and blanket assemblies.

3.3.1 Seed assembly

Seed assembly is comprised of MOX fuel pins with rod diameter of 11 mm. The MOX fuel is made of spent LWR fuel, assuming the isotope composition of ^{238}Pu / ^{239}Pu / ^{240}Pu / ^{241}Pu / ^{242}Pu = 0.4 % / 51.3 % / 37.8 % / 6.5 % / 4.0 %. The isotopes of fissile plutonium take the weight fraction of 57.8 % among all the plutonium. The density of MOX pellet is assumed to be 95 % of the theoretical density. The cross and radial sectional views of seed assembly are shown in Fig. 3-9.

The detail design parameters are summarized in Table 3-2, which are based on the design of Super FBR (Yoshida *et al.*, 2013).
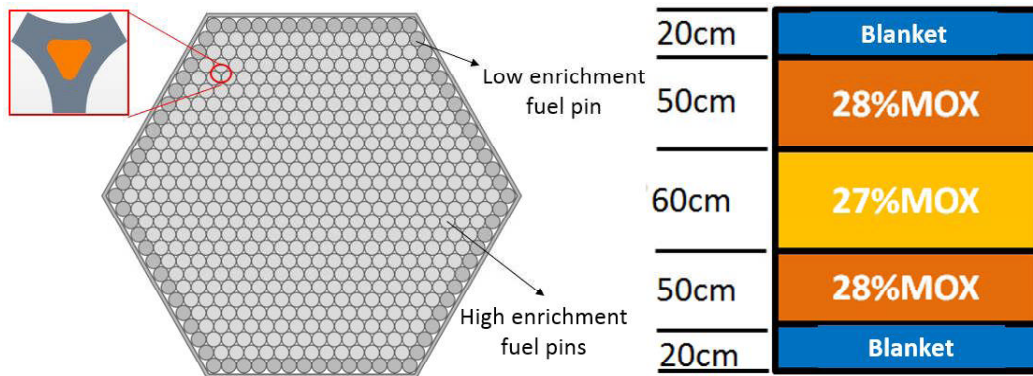
Fig. 3-9 Configuration of the seed assembly

Table 3-2 Design parameters of the seed assembly

Assembly type	Seed
Number of fuel rods per assembly	547
Outer diameter of fuel rods (cm)	1.1
Cladding thickness (cm)	0.08
Pellet diameter (cm)	0.928
Gap between clad and pellet (cm)	0.006
Gap between fuel rods (cm)	0.0
Fuel assembly pitch (cm)	26.1
Gap between fuel assemblies (cm)	0.1
Channel box thickness (cm)	0.2
Number of coolant channels per assembly	1092
Coolant to fuel volume ratio (Vm/Vf)	0.136
Coolant channel geometry	B
Cladding material	Zircaloy-4 Alloy

Enrichment zoning is applied in both radial and axial directions with the purpose of power peaking suppression. The radial power peaking usually appears at peripheral fuel pins when three

seed assemblies are neighboring with each other or when faced to $ZrH_{1.7}$ pins of the blanket assembly. Thus, enrichment of peripheral pins is reduced to suppress the peaking. In the axial direction, the power peaking occurs in the middle if the enrichment distribution is uniform. By decreasing the enrichment of the middle region fuel, the peaking can be effectively suppressed. Blanket layers fueled with depleted UO_2 are placed at the top and bottom of the MOX fuel region, aiming to absorb the neutrons leaking out from MOX fuel region so as to improve the breeding.

Learned from CFD analysis, geometry B (explained in Chapter 2) is taken as the channel geometry, which is beneficial to cope with the thermal hydraulic challenges, such as high cladding temperature, high pressure drop and low CHF, which are usually faced in seed assemblies. Unlike in Super FBR, the cladding material is made of Zr alloy. Compared with Super FBR, the cladding temperature in BWR-type reactor is lower, owing to the lower coolant temperature, so that the Zr alloy can be applied with the purpose to improve the neutron economy.

3.3.2 Blanket assembly

Two kinds of blanket assemblies are utilized in the current study, and both are fueled with depleted UO_2. They are with and without $ZrH_{1.7}$ rods respectively, as shown in Fig. 3-10 (left side). $ZrH_{1.7}$ rods have the same diameter as UO_2 fuel rods, two layers of $ZrH_{1.7}$ being nested in the blanket assembly, providing moderation at void condition. The cross-sectional views of blanket assemblies are shown in Fig. 3-10 (right side). The design parameters are summarized in Table 3-3, which are also based on design of Super FBR (Yoshida *et al.*, 2013).

By referring to the CFD analysis results (Section 2.4.4.2), geometry A is taken as the coolant channel, because the thermal hydraulics in blanket channels are not as challenging as those in seed assemblies. Meanwhile, volume fraction of coolant with geometry A is smaller than that with geometry B, which is in favor of breeding.
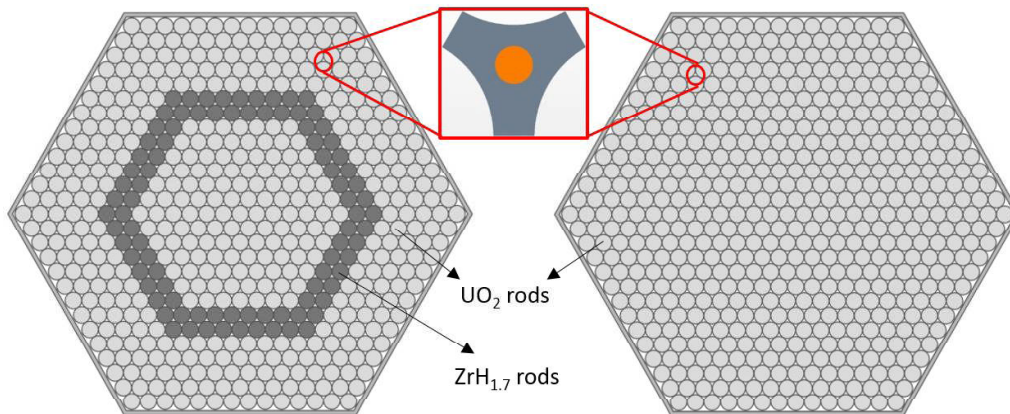
Fig. 3-10 Configuration of blanket assemblies

Table 3-3 Design parameters of blanket assemblies

Assembly type	Blanket with $ZrH_{1.7}$	Blanket without $ZrH_{1.7}$
Number of depleted UO_2 fuel rods per assembly	457	547
Outer diameter of fuel rods (cm)	1.1	1.1
Cladding thickness (cm)	0.08	0.08
Pellet diameter (cm)	0.928	0.928
Gap between clad and pellet (cm)	0.006	0.006
Gap between fuel rods (cm)	0	0
Fuel assembly pitch (cm)	26.1	26.1
Gap between fuel assemblies (cm)	0.1	0.1
Channel box thickness (cm)	0.2	0.2
Number of coolant holes per assembly	1092	1092
Coolant to fuel volume ratio (Vm/Vf)	0.085	0.085
Coolant channel geometry	A	A
Cladding material	Zircaloy-4 Alloy	Zircaloy-4 Alloy
Number of $ZrH_{1.7}$ rods	90	0

3.4 Core design parameters survey

The design of breeding BWR core is developed based on Super FBR core design, since there are many characteristics in common from the viewpoint of neutronics. To achieve the design

goals of breeding, dependency of core characteristics on the performance of breeding and negative reactivity is investigated. The investigations are based on the design experience of Super FBR. For the following studies, neurotic calculation is not coupled with thermal hydraulic calculation on account of the small coolant volume in tightly packed fuel assembly, and the core power is assumed to be the same as Super FBR without considering the thermal-hydraulic limits for the purpose of qualitative comparison.

3.4.1 Core loading pattern

The core loading pattern has significant impacts on breeding and negative void reactivity, which have been studied in detail by Yoshida and Oka (2014) in designing Super FBR. In their study, three types of core loading patterns were investigated, as depicted in Fig. 3-11. The seed assemblies were arranged in scattered, annular and radiating patterns with uniform enrichment zoning. All the blanket assemblies contain two layers of $ZrH_{1.7}$ rods (as shown in Fig. 3-10). The active core height is 4.4 meters with 40 cm axial blankets at both ends. The results are summarized in Table 3-4, which indicates that the radiating core has the best performance on FPSR among the three, while that of negative void reactivity is not as good as the other two. The highest breeding of the radiating core is mainly resulted from its relatively smaller number of seed assemblies compared with annular core and lower enrichment of plutonium compared with the scattered core.
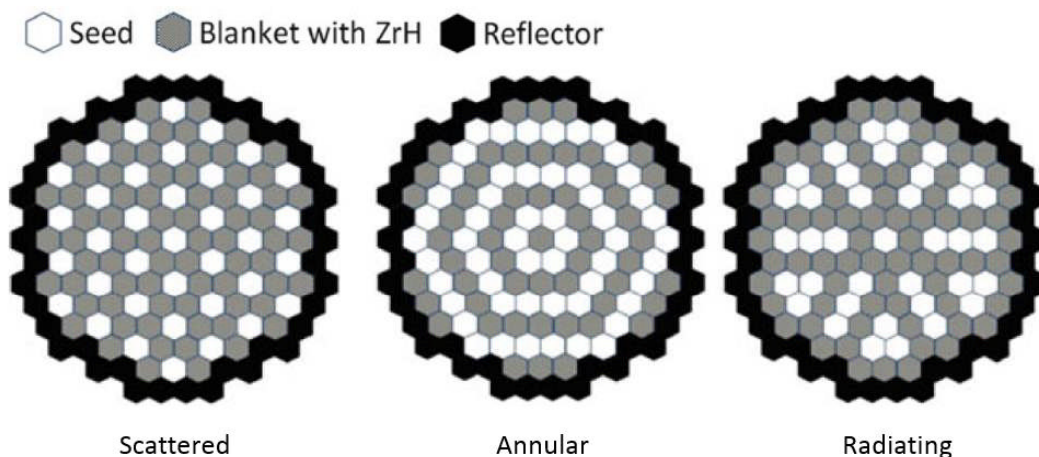
Fig. 3-11 Three types of core loading patterns studied for Super FBR (Yoshida and Oka, 2013)

Table 3-4 Core design parameters and characteristics of Super FBR (Yoshida and Oka, 2013)

	Scattered	Annular	Radiating
Number of seed assemblies	36	54	37
Number of blanket assemblies with ZrH	73	55	72
Operating cycle length (d)	400	400	400
Pu enrichment (seed) (wt%)	45.7	28.9	29.5
Void reactivity (BOEC) (%$\triangle$k/k)	-1.43	-1.90	-1.29
Void reactivity (EOEC) (%$\triangle$k/k)	-1.49	-1.89	-1.01
FPSR	0.983	0.988	0.990

All the above cores achieved negative void reactivity by applying large number of blanket assemblies with ZrH, which, however, was not favorable for improving breeding, because it softened neutron spectrum.

In this study, based on the radiating core, the dependency of FPSR on the number of blanket assemblies containing $ZrH_{1.7}$ was investigated. Cores with different number fractions of blanket assemblies with $ZrH_{1.7}$ rods to seed assemblies (72/72, 60/72, 24/72) are analyzed, as shown in Fig. 3-12. The results are summarized in Table 3-5. It is seen that, compared with the Super FBR, the void reactivity of breeding BWR design of this study becomes worse, especially at the EOEC, while the breeding is improved due to hardening of the neutron spectrum by reducing amount of $ZrH_{1.7}$.
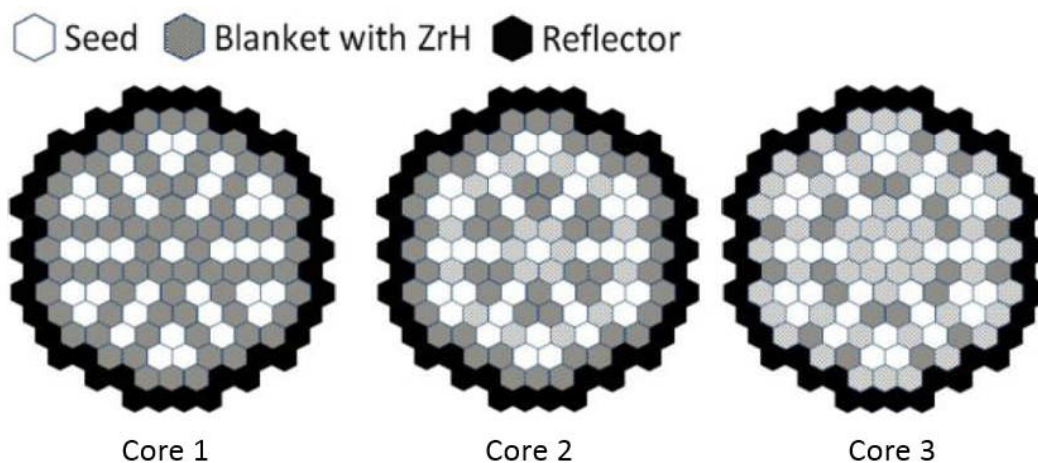
Fig. 3-12 Core loading patterns of breeding BWR with different number of assemblies with $ZrH_{1.7}$

Table 3-5 Core design parameters and evaluated characteristics of breeding BWR

	Core 1	Core 2	Core 3
Number of seed assemblies	37	37	37
Number of blanket assemblies with ZrH	72	60	24
Number of blanket assemblies without ZrH	0	12	48
Operating cycle length (d)	400	400	400
Pu enrichment (Seed) (wt%)	29.5	28.1	27.6
Void reactivity (BOEC) (%$\triangle$k/k)	-1.29	-1.23	-1.14
Void reactivity (EOEC) (%$\triangle$k/k)	-1.01	-0.95	-0.84
FPSR	0.99	1.002	1.010

3.4.2 Number of $ZrH_{1.7}$ layers

$ZrH_{1.7}$ rods play a key role in achieving negative void reactivity. Hence, the sensitivity related to the amount of $ZrH_{1.7}$ is investigated. $ZrH_{1.7}$ rods are arranged in circular layer form in the blanket assemblies, surrounded by UO_2 pins to avoid high power peaking in the neighboring seed assembly.

The tentative cores used to conduct this sensitivity study are based on deign of the Super FBR, denoted as CORE A to CORE D. Figure 3-13 shows the blanket assemblies with different number of $ZrH_{1.7}$ layers adopted by these cores. The major core design parameters are summarized in Table 3-6. The core loading pattern is shown in Fig. 1-13, which contains 162 assemblies with seed assemblies radially arranged. Geometry A (described in Chapter 2) is applied as the coolant channel geometry for all assemblies. All claddings are made of stainless steel. An average coolant density of 0.248 g/cc, which equals to that of Super FBR, is assumed uniformly distributed throughout all the channels.

2 layers

3 layers

ZrH1.7 rods
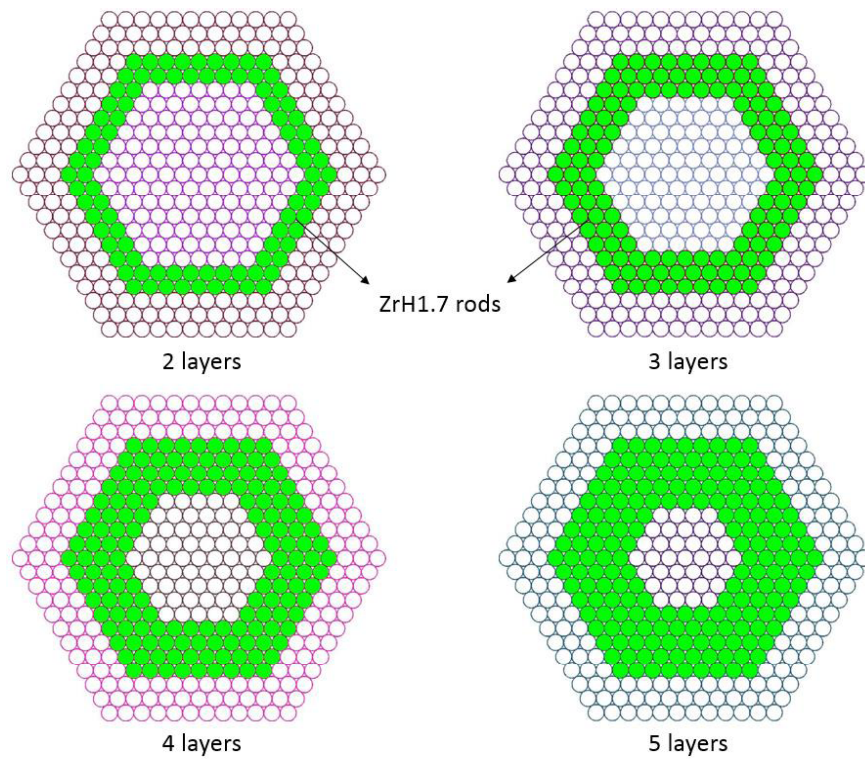
4 layers

5 layers

Fig. 3-13 Blanket assemblies with different number of $ZrH_{1.7}$ layers

Table 3-6 Design parameters of CORE A, B, C and D

Core	CORE A	CORE B	CORE C	CORE D
Number of seed assemblies		97		
Number of blanket assemblies (without $ZrH_{1.7}$ / with ZrH)		162 (144 / 18)		
Total number of rods in an assembly		397		
Number of $ZrH_{1.7}$ rods per assembly (number of layers)	90(2)	236(3)	156(4)	180(5)
Assembly pitch (cm)		34.4		
Fuel rod diameter (mm)		17		
Assembly wall thickness (mm)		2		
Assembly gap (mm)		2		
Power(th) (MW)		1310		
Average coolant density (g/cc)		0.248		
EFPD* (day)		550		

* EFPD: effective full power days

Figure 3-14 and Fig. 3-15 show the influence of the amount of $ZrH_{1.7}$ on breeding (FPSR) and void reactivity, respectively. The result indicates that the FPSR decreases with the increase of amount of $ZrH_{1.7}$ owing to the softening of neutron spectrum. The void reactivity is not greatly improved by increasing the $ZrH_{1.7}$. Therefore, by considering both above factors, it is not necessary to apply $ZrH_{1.7}$ more than two layers.
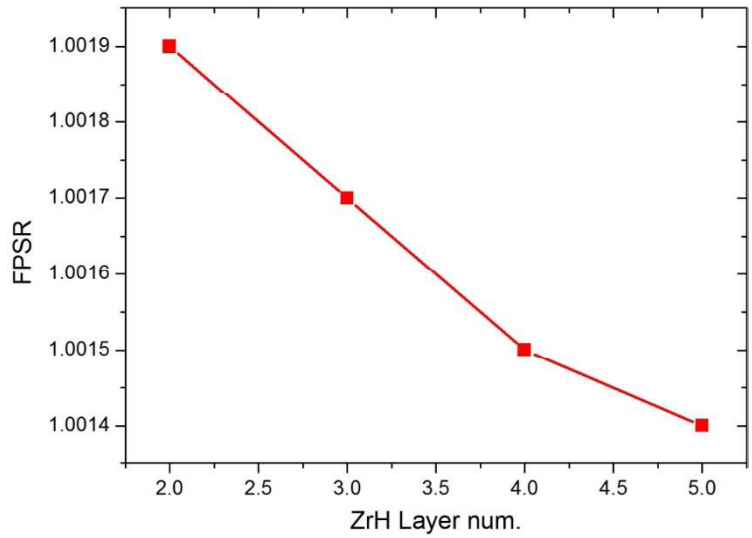
Fig. 3-14 Dependence of FPSR on ZrH layer number
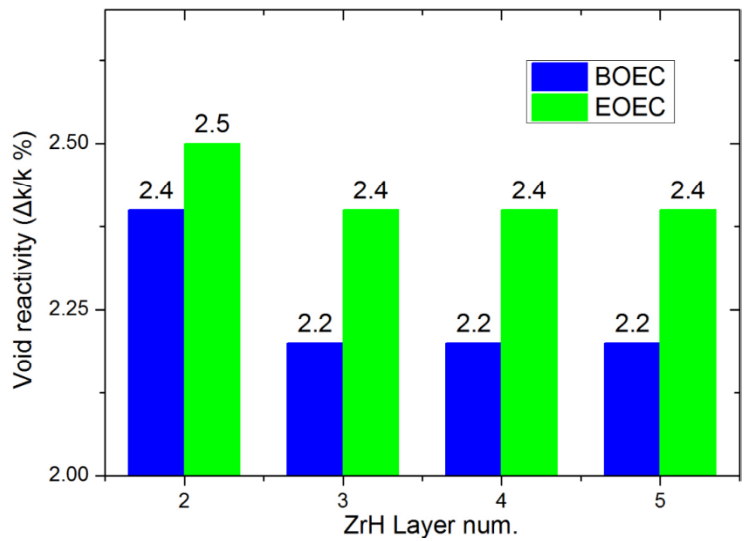
Fig. 3-15 Dependence of void reactivity on ZrH layer number

3.4.3 Plutonium enrichment in seed assembly

Plutonium enrichment is one of the most important parameters of reactor design with MOX fuel. It not just concerns the fuel inventory of the core, but also significantly affects the breeding performance of a breeder reactor, as indicated by the definition of CSDT. The influence of plutonium enrichment on void reactivity is also necessary to be investigated on account of safety.

The reference core basically is the same as CORE A but with smaller fuel rod diameter as well as the assembly size to achieve better void reactivity, denoted as CORE E. The average plutonium enrichment in seed assembly is gradually increased form 27.5% to 30.5%. Other major parameters of the core are summarized in Table 3-7. The core loading patterns is the same as CORE A, which is shown in Fig. 1-13.

Table 3-7 Design parameters of the reference core (CORE E)

Number of SD*	97
Number of blanket assemblies (without ZrH1.7/with ZrH)	162(144/18)
Number of fuel rods in SD / BL1 / BL2*	397/307/397
Assembly pitch (cm)	24.7
Fuel rod diameter (mm)	12
Assembly wall thickness (mm)	2
Assembly gap (mm)	2
Power(th) (MW)	1310
Average coolant density (g/cc)	0.248
EFPD (d)	550

*SD = seed assembly

BL1 = Blanket assembly with ZrH1.7 rods

BL2 = Blanket assembly without ZrH1.7 rods

The dependency of breeding and void reactivity on plutonium enrichment are shown in Fig. 3-16 and Fig. 3-17 respectively. It is seen that both the breeding performance (FPSR and CSDT) and void reactivity become worse with the increase of plutonium enrichment. Meanwhile, from the viewpoint of economy, plutonium enrichment should be minimized on the premise of maintaining criticality, which is consistent with the requirement of improving breeding and void reactivity.
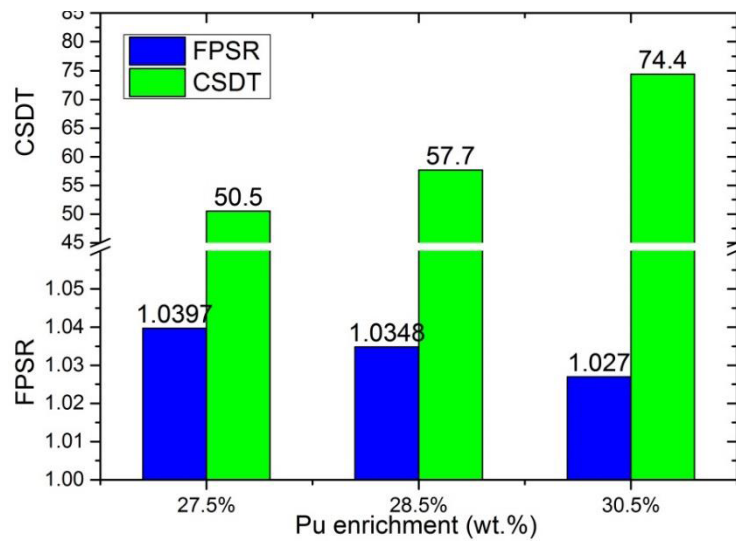
Fig. 3-16 Dependency of breeding on Pu enrichment
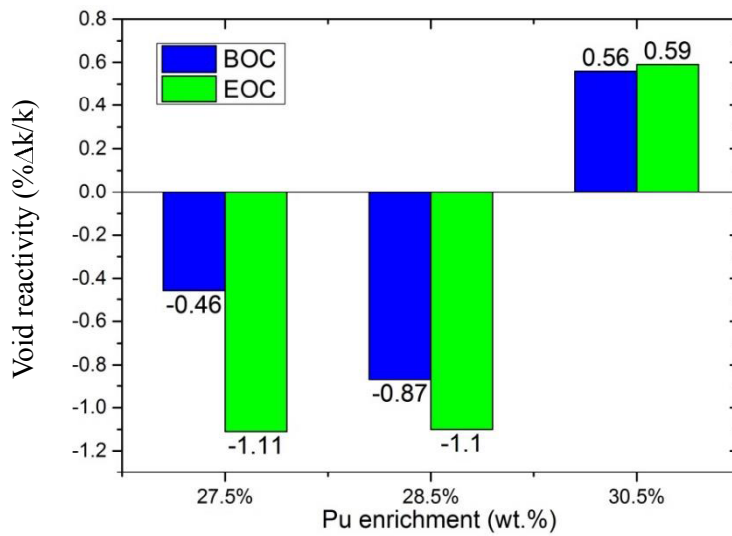
Fig. 3-17 Dependency of void reactivity on Pu enrichment

3.4.4 Average burnup of seed assembly

Average burnup of seed assembly is another major concern of reactor design. For breeder reactors at constant power, higher burnup leads to a longer operating cycle length, which is an influential parameter in definition of CSDT. Its dependency on breeding and void reactivity are investigated based on CORE E by increasing the average burnup from 39.8 MWd/tHM to 53.1 MWd/tHM. The results are shown in Fig. 3-18 and Fig. 3-19. It is shown that the breeding

performances are enhanced with the increase of burnup, while void reactivity becomes worse owing to the fissile plutonium built up with a larger burnup. Appropriate burnup should be determined with the purpose of obtaining high breeding under the negative void reactivity criterion.
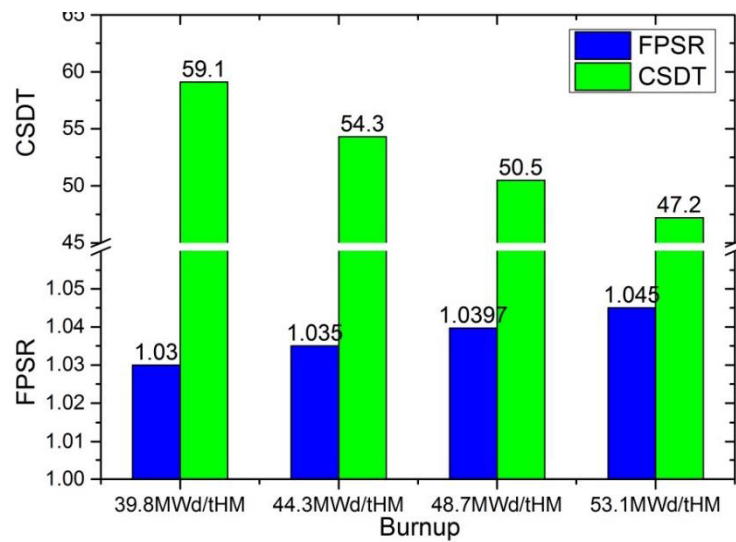
Fig. 3-18 Dependency of breeding on burnup
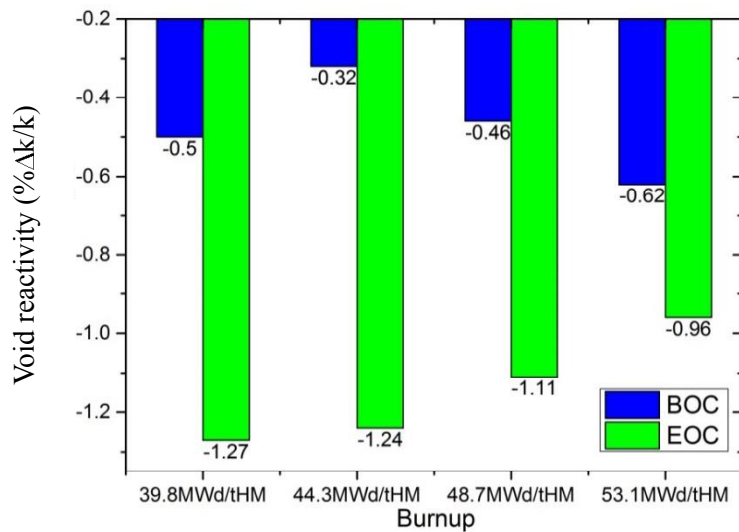
Fig. 3-19 Dependency of void reactivity on burnup

3.4.5 Influence of coolant density

In the current study, the neutronic performance and characteristics of the core is not expected to be significantly affected by the coolant density, since the coolant volume is very small compared with conventional LWRs. However, quantitative evidence is necessary to support this expectation.

Hence, in order to investigate the influence of coolant density, thermal hydraulic calculations are conducted separately to provide three coolant density distributions corresponding to different mass fluxes in average channel with the same power. The coolant density distributions are shown in Fig. 3-20. It is seen that the differences among different mass fluxes are not so large, and the average coolant densities are 0.318 g/cc, 0.413 g/cc and 0.479 g/cc. Based on these distributions, core calculations are then conducted. The results of FPSR, void reactivity and criticality are shown in Fig. 3-21, Fig. 3-22 and Fig. 3-23, respectively, where the reference core is CORE E with uniform coolant density distribution with average density of 0.248 g/cc. It is seen that the different coolant average densities as well as distributions cause little impact on all above parameters. Hence, the coupling calculation between the neutronics and thermal hydraulics is not so necessary.
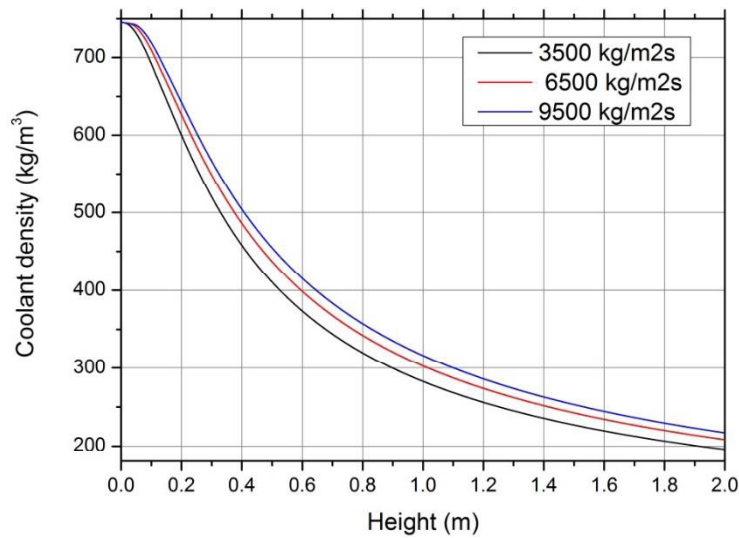
Fig. 3-20 Coolant density distributions with different mass fluxes
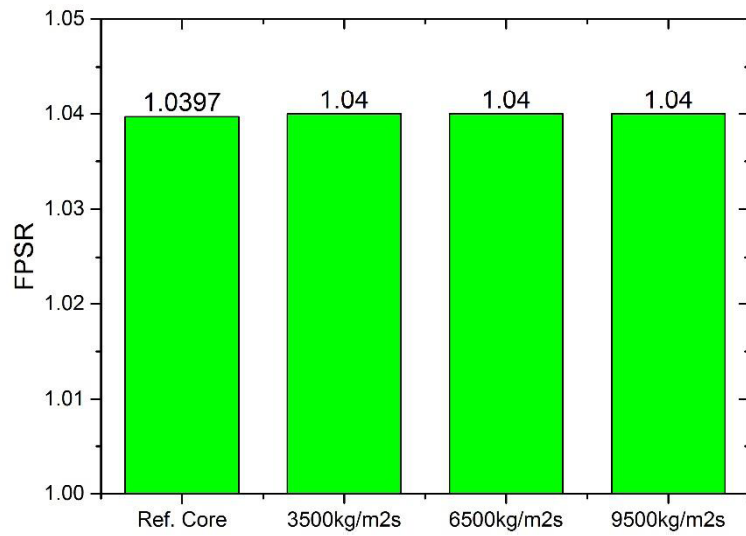
Fig. 3-21 FPSRs with different coolant density distributions arising from different mass fluxes
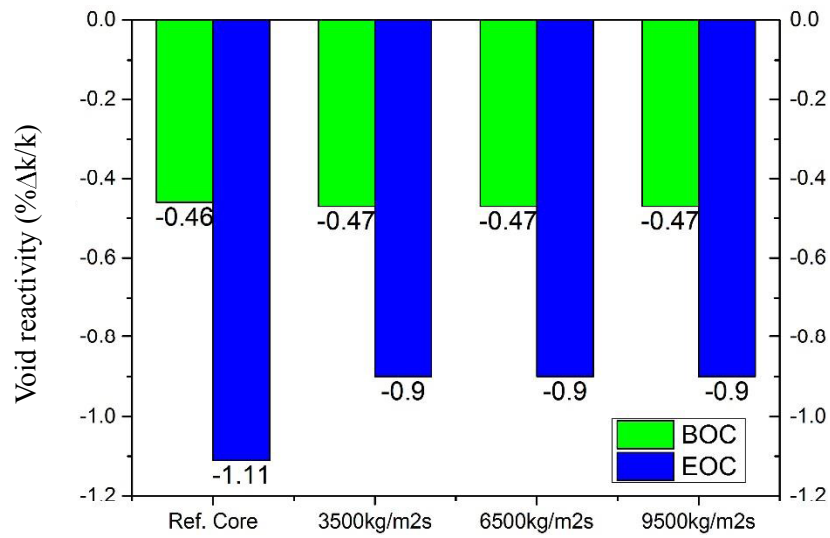
Fig. 3-22 Void reactivity with different coolant density distributions arising from different mass fluxes
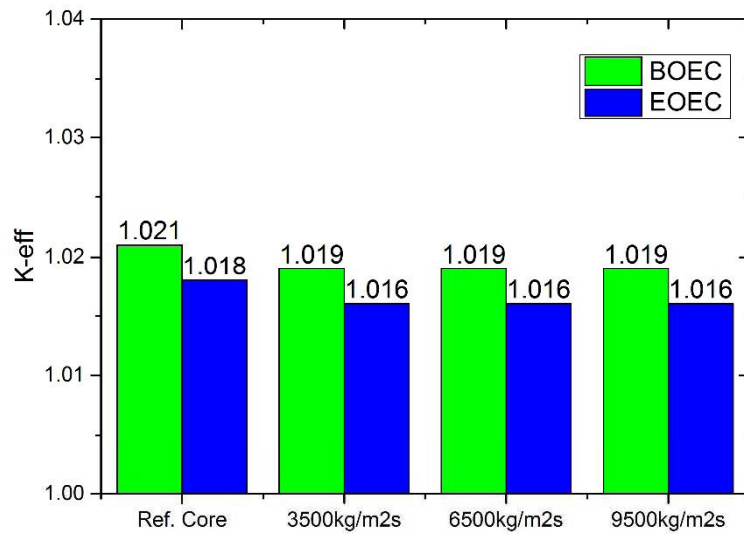
Fig. 3-23 Criticality with different coolant density distributions arising from different mass fluxes

3.5 Breeding BWR core design

The breeding BWR core design is developed from the reference core (CORE E) by understanding the characteristics revealed from Section 3.4. The major core design parameters are summarized in Table 3-7. The core loading pattern as well as the shuffling scheme of seed assemblies are shown in Fig. 3-24. Several aspects of improvement are made in order to achieve the design goals.
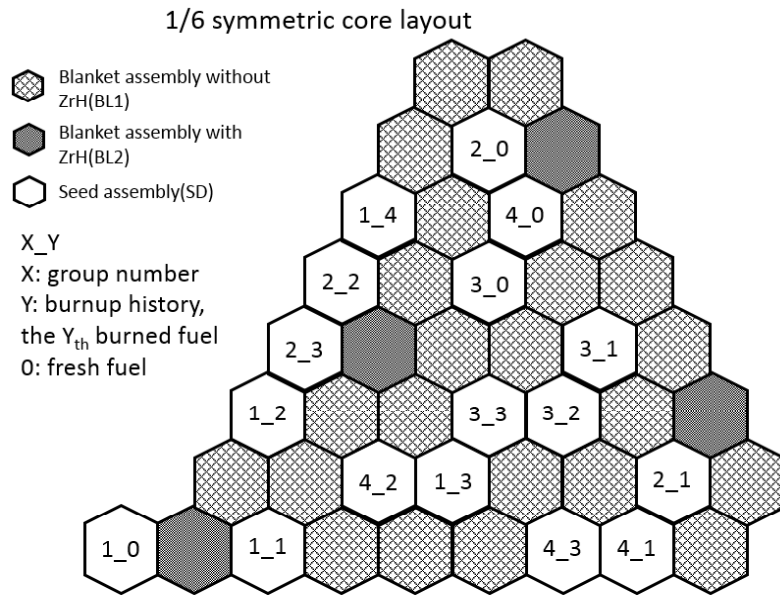
Fig. 3-24 Core loading pattern and shuffling scheme of breeding BWR core design (1/6 core)

Under the BWR operating condition, the cladding temperature is much lower compared with that of Super FBR owing to the relatively low coolant temperature. Thus, the stainless steel cladding previously used in Super FBR is not necessary. From the viewpoint of neutron economy, the zirconium alloy is much better on account of a smaller neutron absorption cross-section. By using Zr-4 alloy cladding, the average Pu enrichment in seed assemblies reduce by 2% (from 29.5% to 27.5%).

Compared with Super FBR, the LHGR of BWR is relatively lower owing to the CHF limitation. The breeding performance, especially the CSDT, strongly depends on the core power, as shown in Fig. 3-25, which is obtained based on design of CORE E with fixed burnup of 65.1 MWd/tHM. It is seen that the CSDT decreases with the increase of core power. To achieve the CSDT less than 50 years, the core thermal power should at least be larger than 1000 MW for CORE E. However, by considering the CHF criterion, for coolant channel in assemblies with 12 mm diameter fuel rods, the core power is limited to less than 600 MW.
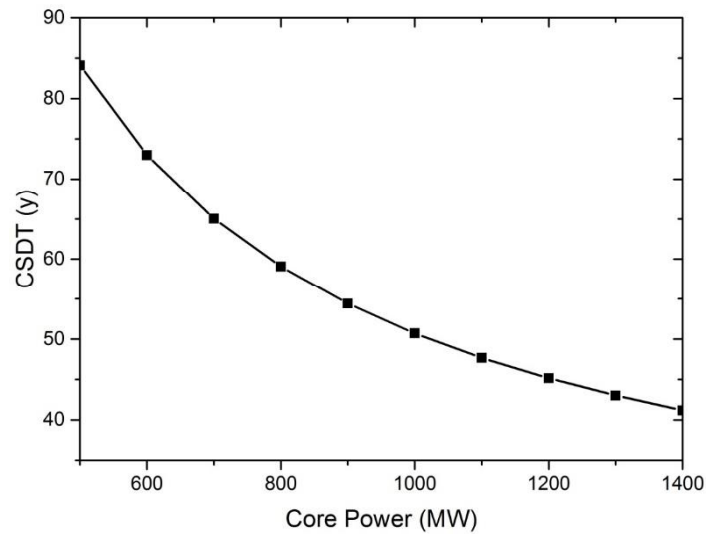
Fig. 3-25 CSDT vs. core power for CORE E

Learned from CFD analysis results in Chapter 2, compared with original coolant channel geometry, which is geometry A, geometry B has lager CHF and leads to lower pressure drop and cladding temperature. Three cores with different design scheme of coolant channel geometry are proposed: one is the reference core with geometry A adopted for all coolant channels, which is CORE E; CORE F is the core with geometry B adopted for all coolant channels; CORE M is the core with mixed use of the channel geometries, using geometry A for channels of blanket assemblies and geometry B for that of seed assemblies.

The evaluated breeding, void reactivity and criticality are shown in Fig. 3-26, Fig. 3-27 and Fig. 3-28, respectively. It can be seen that CORE M is greatly superior to the others in terms of lower void reactivity, comparable breeding and higher k-eff, which implies that a smaller plutonium inventory is required.
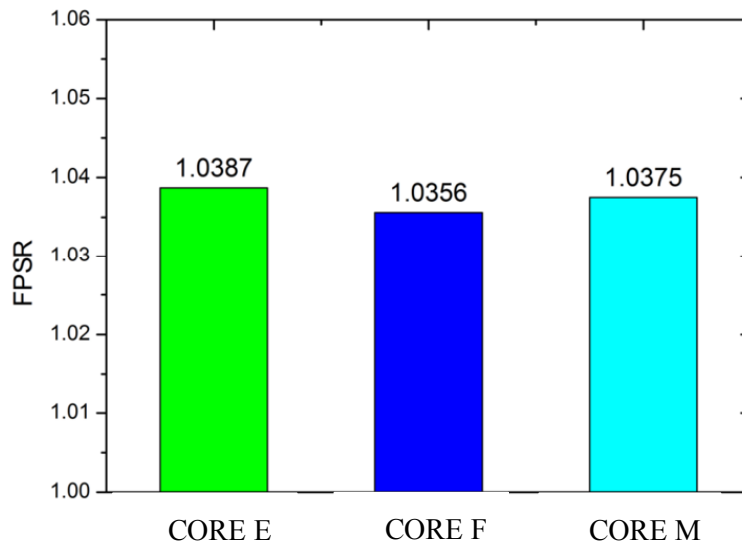
Fig. 3-26 FPSRs of cores with different design scheme of coolant channels
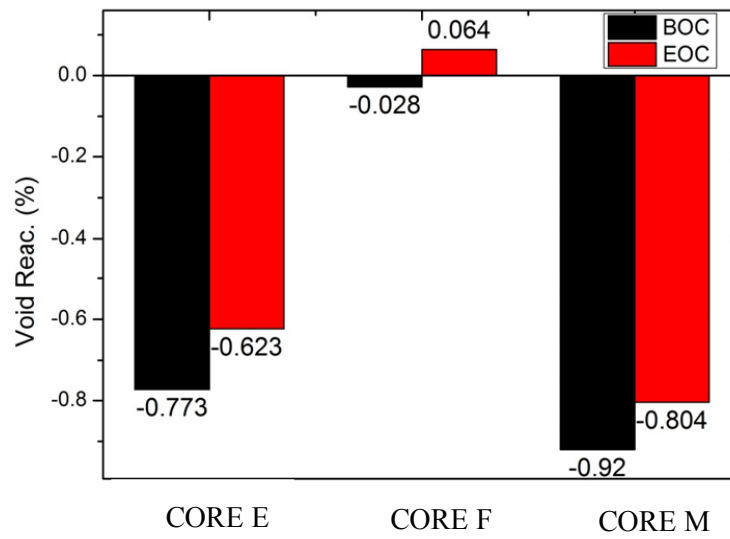
Fig. 3-27 Void reactivity of cores with different design scheme of coolant channels
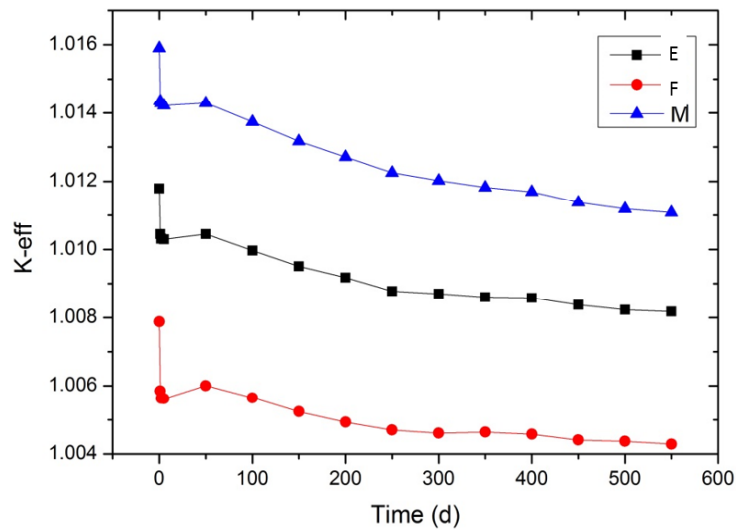
Fig. 3-28 K-eff at EOEC of cores with different design scheme of coolant channels

One approach to increase the core power is to reduce the fuel rods diameter and increase the number of fuel rods while keeping the core size fixed. Hence, the dependency of core power on the fuel rods diameter is investigated. Super FBR is regarded as the reference core. By keeping the assembly size the same as much as the Super FBR, the fuel diameter is reduced while the number of fuel rods is increased. Figure 3-29 shows the relationship of the fuel rods diameter, the number of fuel rods for an assembly and the assembly heated perimeter D_{heated} (defined as the product of rods number and rod perimeter). Based on the principle of maintaining the assembly size, it is seen that the number of fuel rods and assembly heated perimeter generally increase with the decrease of rod diameter. With the decrease of fuel rod diameter, the channel size also becomes smaller due to geometric similarity, leading to smaller CHF and higher pressure drop. Figure 3-30 shows the average LHGR in seed assembly and pressure drop (when G = 10000 kg/m²s) at different rod diameters. The total core power depends on the average LHGR in seed assembly and the number of fuel rods per assembly. Figure 3-31 shows the core power versus rod diameter. It can be seen that core power tends to increase with the decrease of fuel rod diameter, but not monotonously. This is because the number of fuel rods does not increase monotonously since size of the assembly is fixed. The 11mm diameter of fuel rod is relativity good to increase the core power meanwhile maintain a comparable size as Super FBR. Thereby, the core power is increased to be around 826 MW form core E(< 600MW).
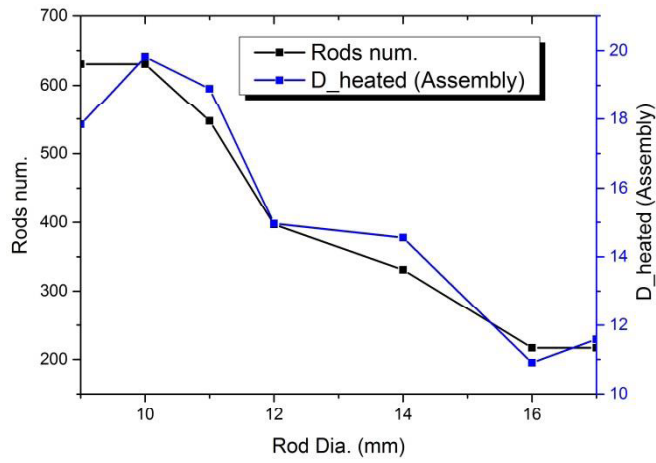
Fig. 3-29 Fuel rod diameter vs. rods number and assembly heated perimeter
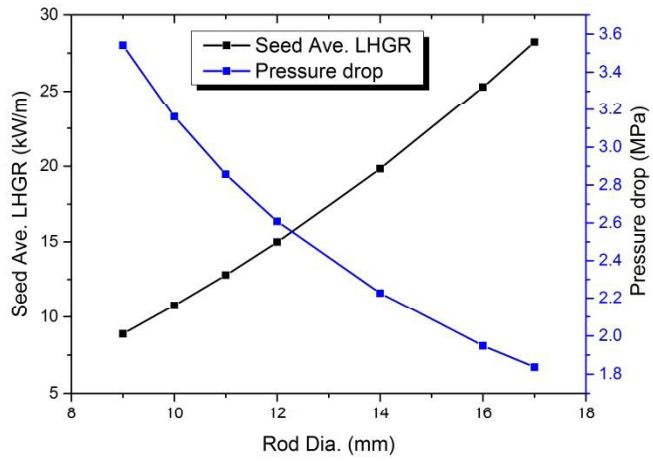
Fig. 3-30 Fuel rod diameter vs. average LHGR in seed assembly and core pressure drop
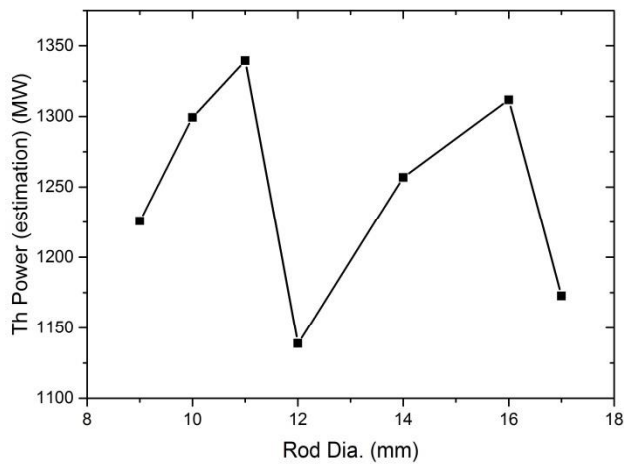
Fig. 3-31 Core power vs. fuel rod diameter

In addition, it is found that the local power peaking is another restriction to power increase. For a core with blanket and seed assemblies radially arranged, the power peaking usually appears at the peripheral rods in seed assemblies facing blanket assemblies, where the local spectrum is softer. Enrichment zoning by placing lower enrichment fuel rods in the periphery of seed assemblies can effectively manage the local power peaking. A comparison of local power peaking between before and after enrichment zoning is shown in Fig. 3-32, which indicates that the power peaking is greatly reduced by enrichment zoning so that the core thermal power can be further increased from 826MW to 1010MW.
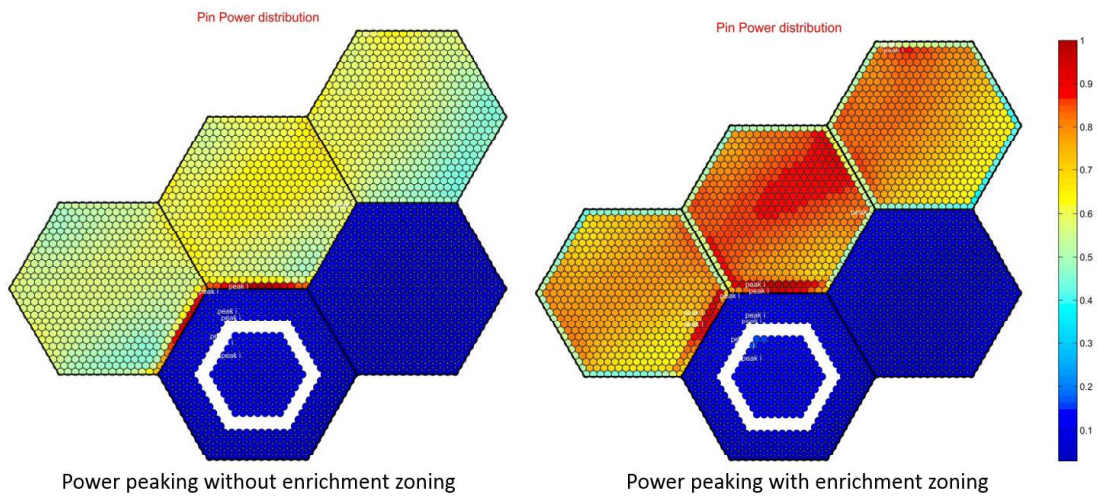
Fig. 3-32 Local power peaking comparison between before and after enrichment zoning

Overall, the core performance is summarized in Table 3-8. It indicates that the design goals are accomplished, meanwhile satisfying all the design criteria.

Table 3-8 The core design parameters and characteristics of the high breeding BWR

Core parameters	
Number of Seed assemblies	97
Number of blanket assemblies (without ZrH/with ZrH)	162(144/18)
Number of fuel rod in a SD*/BL2*(ZrH)/BL1*	547 / 457 /547
Core height (m)	2
Core equivalent diameter (m)	4.3
ZrH volume fraction in a BL2(ZrH) assembly (%)	3.6%
Assembly pitch (cm)	26 .1
Fuel rod diameter (mm)	11
Cladding material	Zr Alloy
Coolant channel geometry	B(SD), A(BL)
Ave. Pu enrichment (wt%)	27.5
Operating cycle length (d)	700
Ave. discharge burnup (seed) (GWd/tHM)	48.25
Fuel batch (Seed/Blanket)	4/1
Mass flux in hottest channel (kg/m^{2}s)	9,950
Power(th) (MW)	1,017
Average exit quality (%)	0.226
Maximum cladding temperature in Seed (BOEC/EOEC) (°C)	307.2 /306.1
Maximum cladding temperature in Blanket (BOEC/EOEC) (°C)	293.4/296.2
Void reactivity (BOEC/EOEC) (%dk/k)	-0.29/-0.49
MCHFR (BOEC/EOEC)	1.9/1.9
FPSR	1.061
CSDT (y)	41.6

*SD = seed assembly

BL1 = Blanket assembly with ZrH1.7 rods

BL2 = Blanket assembly without ZrH1.7 rods

3.6 Consideration of stability

Although the current core design is for a BWR-type reactor, it mainly serves the purpose of achieving high breeding, which means that this reactor core will not be completely compatible

with the current BWR system. However, engineering issues should also be addressed in order to further develop the concept in future. One of the major concerns of the current design concept is the high core pressure drop, which may introduce stability issues.

Various instabilities may exist in a reactor system. Generally, there are five types of major instabilities in a BWR system (Ikeda *et al.*, 2007): channel instability, regional instability, core instability, Xenon instability and plant instability.

The channel instability mainly indicates the oscillation of coolant density wave in a boiling channel, and excitation of the channel instability can be suppressed by increasing the inlet pressure drop with inlet offices. In addition, the high mass flux in the current core design also helps to suppress this instability.

Core instability and regional instability are kind of coupled neutronic-thermal-hydraulic instabilities. Due to the application of tightly packed fuel assembly, there is a weak coupling between thermal hydraulics and netronics in the current core design, which is shown in Section 3.4.5. The neutronic feedback is small (void reactivity < 1 %dk/k) compared with conventional BWRs. Therefore, these instabilities are not expected to be limiting the design concept. It has been shown in RMWR (Hu, 2007), which is another BWR-type reactor with tight lattice fuel assembly, that the decay ratio for both coupled out-of-phase and in-phase stabilities are well below the criterion.

Xenon instability mainly exists in large-size thermal reactors, but in fast reactors Xenon effect is not important, and it is not necessary to be considered in the current core.

Plant stability strongly depends on the plant control systems, and can be managed with appropriate control system design.

3.7 Summary

The high breeding BWR core with tightly packed fuel assemblies is proposed in this chapter. The core design is accomplished step by step by conducting the parameter sensitivity study, such as adjusting the core loading patterns and analyzing the influence of coolant density distributions with thermal hydraulics calculations. Although the similarity exists between the high breeding BWR core and Super FBR core, difference in the thermal hydraulic characteristics give rise to different criteria, such as CHF, MLHGR and pressure drop, and increasing core power becomes the major design consideration for improving the CSDT.

From the sensitivity study, it is found that the breeding performance is better with lower plutonium enrichment and higher burnup. For attaining negative void reactivity, it is preferable

to lower the enrichment and the lower the burnup. In addition, the calculation results indicate that the coolant density change does not significantly affect the neutronics due to the small inventory of coolant.

It is found that the CSDT is mainly limited by the Linear Heat Generation Rate (LHGR), while the LHGR is mainly limited by the CHF and power peaking factors. To increase the LHGR, CHF is increased by applying geometry B (triangular with round corners) instead of geometry A (circular) in seed assemblies. It is also found that keeping the geometry A in blanket assemblies to maintain the breeding ability is feasible, because the LHGRs of blanket assemblies are low. The power peaking factor is suppressed by enrichment zoning in both radial and axial directions. The pressure drop is higher than that of conventional BWRs due to application of narrow coolant channels. Resulting flow instability may be managed by applying orifices at the inlet in order to decrease the effect of the pressure drop change in the coolant channel on the stability.

The final breeding BWR core design achieves a CSDT of 41.6 years, while all the design criteria, with respect to Maximum Linear Heat Generation Rate (MLHGR), Minimum Critical Heat Flux Ratio (MCHFR) and negative void reactivity, are satisfied. For the first time, the breeder reactor concept with light water cooling has been shown to achieve high breeding. The role of nuclear power may be greatly enhanced for countries with advanced nuclear technologies and infrastructures, such as some of the G7 members, if high breeding with light water cooling can be achieved.

Stability analysis of the current design will be remained for future study, and it may be worth further developing the concept to high breeding BWR with larger power and lower pressure drop.

3.8 Reference

Chen, J . C. 1966. "Correlation for Boiling Heat Transfer to Saturated Liquids in Convective Flow." Int. Eng. Chem. Process Design and Development, 5,322.

General Electric Co., 1973. General Electric BWR thermal analysis basis (GETAB): Data, correlation and design application, NEDO-0958.

Han, C.Y., 2010. Code System for Core Design of Supercritical Water-Cooled Fast Reactor - SRAC/ASMBURN/CORERN, Technical report, The University of Tokyo, Tokyo.

Hibi, K. *et al.*, 2001. Conceptual Designing of Reduced-Moderation Water Reactor with Heavy Water Coolant, Nuclear Engineering and Design (210), pp. 9–19.

Hu, R., 2007. Stability analysis of the boiling water reactor : methods and advanced designs, Doctoral thesis, Massachusetts Institute of Technology

Ishigai, S., 1999. Steam power engineering: thermal and hydraulic design principles., Cambridge University Press, Cambridge, pp. 306.

Ishiwatari, Y., 2006. Safety of supercritical light water cooled reactors. Doctoral thesis, the University of Tokyo.

Jevremovic, T., Oka, Y., Koshizuka, S., 1993. Conceptual Design of an Indirect-Cycle, Supercritical-Steam-Cooled Fast Breeder Reactor with Negative Coolant Void Reactivity Characteristics, Annals of Nuclear Energy (20), pp. 305–313.

Lellouche, G.S. and Zolotar, L.A., 1982. "Mechanistic Model for Predicting Two-Phase Void Fraction for Water in Vertical Tubes, Channels and Rod BundIes", Electric Power Research Institute, NP-2246-SR.

Mclane, V., 1996. Citation guidelines for nuclear data retrieved from databases resident at the nuclear data centers network. Informal Report BNL-NCS-63381.

MathWorks, 2015. Getting started with MATLAB. Retrieved from: http://uk.mathworks.com/help/pdf_doc/matlab/getstart.pdf

Okumura, K., *et al.*, 2007. SRAC2006: a Comprehensive Neutronics Calculation Code System, Technical report, Japan Atomic Energy Research Institute (JAERI), Ibaraki-Ken.

Oka, Y. and Jevremovic, T., 1996. Negative Coolant Void Reactivity in Large Fast Breeder Reactors with Hydrogenous Moderator Layer, Annals of Nuclear Energy (23), pp. 1105−1115.

Reddy, D.G., Sreepada, S.R., Nahavandi, A.N., 1982. "Two-Phase Friction Multiplier Correlation for High-Pressure Steam-Water Flow", Electric Power Research Institute, NP-2522

Smith, S. L., 1969. Void fractions in two-phase flow. A correlation based on an equal velocity head model. Proc. Inst. Mech. Engng., 184(36), 647-664.

Saha, P., and Zuber, N., 1974. "Point of Net Vapor Generation and Vapor Void Fraction in Subcooled BOiling," Proc. Fifth Int. Heat Transfer Conf. , Vol . IV.

Shah, M.M., 1987. Improved general correlation for critical heat flux during upflow in uniformly heated vertical tubes. International Journal of Heat and Fluid Flow, 8(4), pp. 326-335.

Shibata, K., 2003. Descriptive Data of JENDL-3.3 (Part I and II), JAERI-Data/Code 2002-026, Part I, Part II.

Todreas, N.E., Kazimi, M.S., 1999. Nuclear Systems I: Thermal Hydrulic Fundamentals. Hemisphere Publishing, New York, pp. 24.

Wagner, W., Kruse, A., 1998. Properties of Water and Steam: The Industrial Standard IAPWS-IF97 for the Thermodynamic Properties and Supplementary Equations for Other Properties: Tables Based on These Equations, Springer-Verlag.

Yoshida, T. and Oka, Y., 2013. High breeding core of a supercritical-pressure light water Cooled fast reactor. Proceedings of the 2013 21st International Conference on Nuclear Engineering, ICONE21-15753, Chengdu, China.

Chapter 4 Safety analysis of Super FBR

4.1 Introduction

Supercritical pressure light water cooled Fast Breeder Reactor (Super FBR) is the first reactor that adopts the tightly packed fuel assembly for high breeding. Essentially, it is a type of supercritical pressure water cooled reactor (SCWR) with once-through direct cycle (there is no recirculation of the coolant in the core and the entire coolant is fed to the turbine). The cross-section of this assembly is shown in Fig. 2-1. It is characterized by the special configuration of fuel rods and coolant channels: the fuel rods are closely packed without gap and the coolant channel is tangent to the surrounding fuel rods, the space among them being filled with the metal fitting that is the same material as cladding. The coolant to fuel volume fraction is dramatically reduced to 0.085 compared with 0.82 of the conventional BWR and 0.17 of RMWR as described in Section 1.5.2. This fuel assembly enables designing of a high breeding water cooled reactor with hard neutron energy spectrum.

Super FBR adopts the once-through direct cycle just as Super LWRs and Super FRs, and the plant system is almost the same. However, the volume fraction of the coolant is smaller than that of the Super FR. It makes the pressure be more sensitive to the core heat up. The coolant channels are physically separated from each other and cross flow cannot be formed. The special layout of coolant channels and fuel rods gives rise to different cladding temperature distribution from that of conventional fuel assembly. The above mentioned characteristics would influence the safety performance, especially for Super FBR on account of its small flow rate and once through direct cycle (Yoshida and Oka, 2013). Therefore, it is necessary to clarify the safety characteristics of Super FBR at accidents and abnormal transients.

4.2 Core characteristics of Super FBR

Although the neutron energy spectrum is hardened by adopting the tightly packed fuel assembly, the negative coolant void reactivity is ensured by applying ZrH rods in part of the blanket assemblies and elaborately arranging the core loading pattern. This is extremely important for inherent safety. The major parameters of the assembly and the core designs are summarized in Table 4-1 and Table 4-2, respectively. Three kinds of assemblies are heterogeneously arranged in the core, and they are seed assembly, blanket assembly and blanket assembly with $ZrH_{1.7}$ rods. The assembly and core geometry are shown in Fig. 1-12 and Fig. 1-13,

respectively. The enrichment zoning is applied on seed assemblies in order to suppress the axil power peaking, and the axial power profiles are shown in Fig. 4-1.
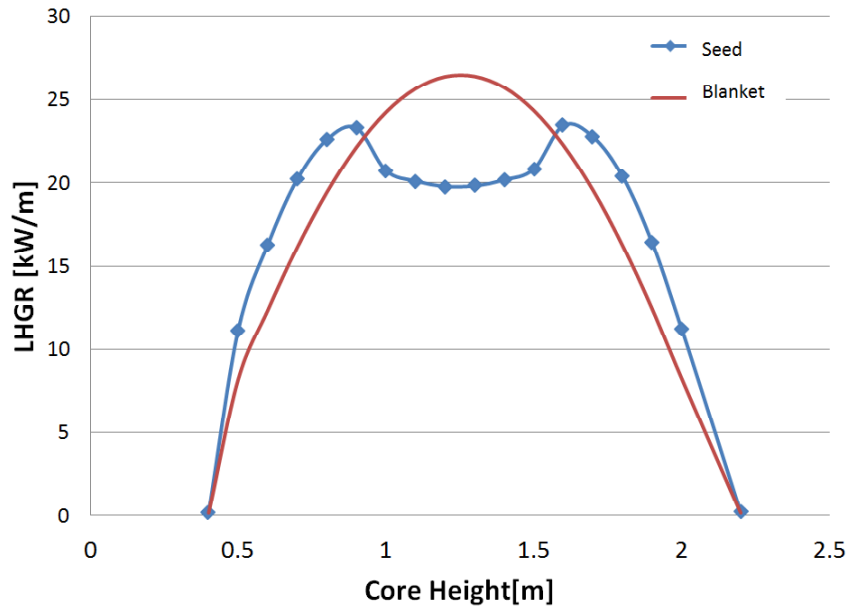
Fig. 4-1 Axial power profile of seed and blanket assembly in Super FBR at BOEC

Table 4-1 Design specification of the tightly packed fuel rods assembly (Yoshida *et al.*, 2013)

Channel box thickness [cm]	0.2
Gap between fuel assemblies [cm]	0.1
Fuel assembly pitch [cm]	24.66
Outer diameter of fuel rods [cm]	1.2
Cladding thickness [cm]	0.0873
Pellet diameter [cm]	1.0124
Gap between clad and pellet [cm]	0.0065
Fuel rod pitch [cm]	1.2
Gap between fuel rods [cm]	0
Diameter of coolant channel [cm]	0.1856

Table 4-2 Core design parameters and characteristics (Yoshida *et al.*, 2013)

Reactor thermal power [MW]	1156
Core height [m]	2.0
Core equivalent diameter [m]	4.12
Number of Seed/Blanket assemblies	97/162
Fuel batch (Seed/Blanket)	4/1
Operating cycle length [d]	550
Core operating pressure [MPa]	30
Core pressure drop [MPa]	1.6
Inlet temperature [°C]	385
Average outlet temperature [°C]	440
Average coolant density [kg/m^3]	248
Maximal Cladding Temperature (MCT) [°C]	654
Discharge burnup (Seed) [GWd/t]	48.7
Void reactivity (BOC/EOC) [%Δk/k]	-0.70/-0.37
FPSR	1.026
CSDT [y]	43

Compared with the previous Super FR core designs (Yoo *et al.*, 2006; Liu and Oka, 2013), the current design mainly serves the purpose of high breeding and some parameters are very different such as the inlet and outlet temperatures, the proportion of seed and blanket assemblies and the core pressure. While the coolant flow scheme is similar to other one pass Super LWR core designs (Wu and Oka, 2014) and Super FR core designs (Liu and Oka, 2013), and it is illustrated in Fig. 4-2: the coolant flows through the downcomer and fills the bottom dome, then flows upward via the fuel channels. Then, the coolant is mixed in the upper plenum, and finally comes out from the hot-leg. Compared with Super FRs (Ikejiri *et al.*, 2010; Liu and Oka, 2013), although the coolant channels of tightly packed fuel assembly are designed with smaller cross section and smaller hydraulic diameter, the core is efficiently cooled by increasing the rated coolant flow rate and increasing the heat transfer coefficient. For instance, the average flow rate per given thermal power of "all-upward two-pass flow Super FR" (Liu and Oka, 2013) is 0.5 kg/s/MW, while that of the current study is 1.3kg/s/MW.
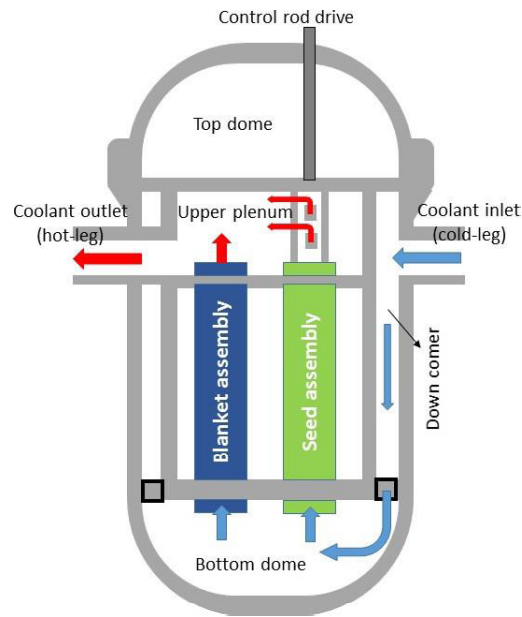
Fig. 4-2 Coolant flow scheme

4.3 Plant and safety system

The plant and safety system of Super FBR are almost the same as those of Super LWRs and Super FRs (Ishiwatari *et al.*, 2003; Ishiwatari *et al.*, 2005a) due to the similar thermal-hydraulic characteristics, as shown in Fig. 4-3. However, it is very different form BWRs mainly because of no separations of water and steam (single phase flow) and no coolant recirculation. As it is single phase flow, the water level does not exist. There is no recirculation of coolant in the core and the entire coolant is fed to the turbine. Hence, as long as the coolant flow in the core is kept, the fuel rods are cooled. Therefore, the safety principle is "to maintain the core coolant flow" rather than "to maintain the water level". The advantage of the "once-through direct cycle" is that the core depressurization can induce the coolant flow and cool the core. Two aspects are essential to sustain the coolant flow rate in the core and described as followings:
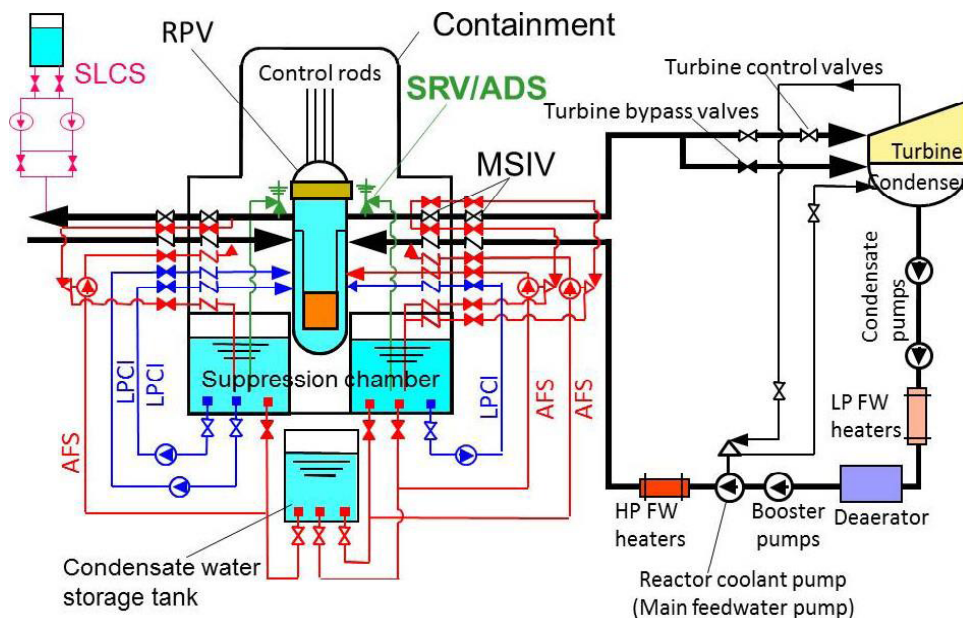
Fig. 4-3 Plant and safety system (Oka *et al.*, 2010)

To maintain the coolant supply from cold-leg

At normal operation conditions, two turbine driven Reactor Coolant Pumps (RCPs) provide the main coolant feedwater flow. When the coolant flow from RCPs is reduced, coolant flow is supplied by high pressure turbine-driven Auxiliary Feedwater System (AFS) and the motor-driven Low Pressure Core Injection system (LPCI) from cold-leg depending on the level of abnormality. Operations of both of them assume a delay time of 30 s from the signal released to reach the full capacity, which is due to the time requirement of actuation of the emergency diesel generators.

To maintain the coolant outlet open at hot-leg

The main steam isolation valves (MSIVs), the main stop valves, the turbine control valves (TCVs) and the turbine bypass valves (TBVs) are designed to guarantee the coolant outlet open at the hot-leg. In order to cope with the closure of these valves, in total of 8 units of Safety Relief Valves (SRVs) are provided to keep the coolant outlet open as well as to prevent the reactor over pressurization. They also function as the Automatic Depressurization System (ADS) to depressurize the reactor under certain reactor conditions. During the depressurization, the coolant flow is induced through the core.

To shut down the reactor, two independent shut down systems are provided in the current design: 1) the reactor can be shut down manually or automatically by insertion of all control rods.

Delay time of 0.55 s is assumed after the scram signal release; 2) In addition, the standby liquid control system (SLCS) is equipped as the backup.

Table 4-3 summarizes the actuations and capacities of the Super FBR safety system which is derived by reference to that of Super FRs, because of the similar coolant flow system and thermal-hydraulic characteristics. To deal with the higher system pressure in Super FBR (30 MPa at normal operating condition) compared with that in Super FRs (25 MPa), auctions related to pressure are proportionally increased with the operating pressure except the ADS auction pressure which is kept the same at 23.5 MPa to prevent unnecessary depressurization.

Table 4-4 shows how the levels of abnormalities correlate with the safety system actuations, which is the same as in Super FRs. The detailed explanations of the design method and logic can be found in the previous work (Ishiwatari *et al.*, 2005a).

Table 4-3 Safety systems and actuation conditions (Oka *et al.*, 2010)

Safety system	Actuation conditions		
Reactor scram system	Pressure high (31.2MPa)		MSIV closure (90%)
	Pressure low (28.8MPa)		Reactor coolant pump trip
	Reactor power high (120%)		Condensate pump failure
	Reactor period short (10s)		ECCS start-up
	Loss of offsite power		Drywell pressure high
	Turbine control valve quickly closed		Earthquake acceleration large
AFS (auxiliary feedwater system) (4% of rated flow×3 units) (turbine-driven)	Main coolant flow rate low (20%)		
	RCP trip or loss of offsite power		
	Condensate pump trip		
	Turbine control valves quickly closed		
	Main stop valves closure		
	MSIV closure (90%)		
SRV (safety relief valve) (20% of rated flow×8 valves)	Open (MPa)	Close (MPa)	Number
	31.44	30.24	1
	31.68	30.48	1
	31.92	30.72	3
	32.16	30.96	3
ADS (automatic depressurization system)	Pressure low (23.5 MPa)		
MSIV (main steam isolation valve)	The same as ADS actuation conditions		
LPCI (low pressure core injection) (12% of rated flow×3 units)	The same as ADS actuation conditions		

Table 4-4 Levels of abnormities and actuations (Oka *et al.*, 2010)

Flow rate low (feedwater or main steam)	
Level 1 (90%)	Reactor scram
Level 2 (20%)	AFS
Level 3 (6%)	ADS/LPCI system
Pressure high	
Level 1 (31.2 MPa)	Reactor scram
Level 2 (31.44 MPa)	SRV
Pressure low	
Level 1 (28.8 MPa)	Reactor scram
Level 2 (23.5 MPa)	ADS/LPCI system

4.4 Analysis methods

4.4.1 Code system

In the past study, the SPRAT and SPRAT-F code systems were developed and validated for the safety analysis of Super LWRs and Super FRs by Okano *et al.* (1996), Ishiwatari *et al.* (2005a, 2005b), Oka *et al.* (2010), Ikejiri *et al.* (2010, 2011) and Li *et al.* (2013). Based on their studies, the current SPRAT code system is developed and modified in order to deal with the higher system pressure and heat transfer in the tightly packed fuel assembly. It incorporates basic models involving mass, energy and momentum conservations, heat transfer and point kinetics model for core power evaluation, as shown in Fig. 4-4.
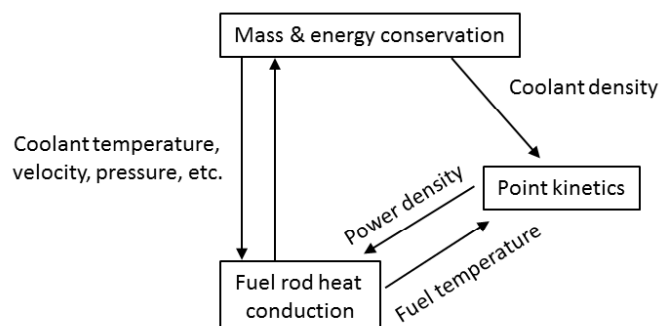
Fig. 4-4 Basic models in SPRAT code system

4.4.1.1 Computational models for supercritical pressure and blowdown phase at subcritical pressure

SPRAT code system is used for accidents and transients analysis at supercritical pressure as well as the blowdown phase of these events. The flow scheme and the system nodalization in the SPRAT code are shown in Fig. 4-5.
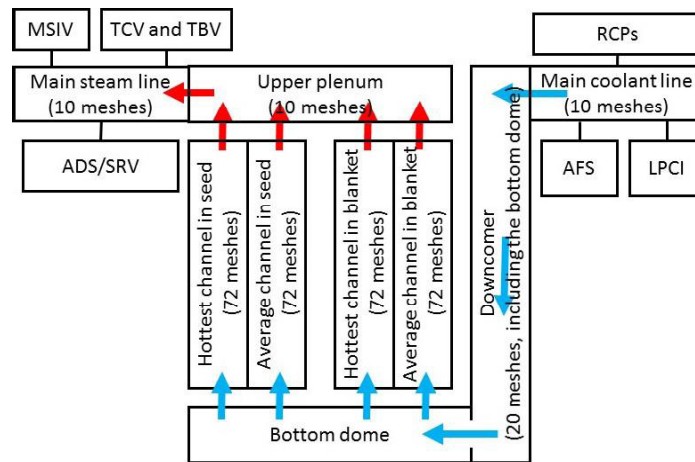
Fig. 4-5 Calculation model and nodalization in SPRAT code

Fuel channels in Super FBR core are modeled by the representative seed and blanket channels. Both fuel channels are further divided into a hot channel and an average channel. The hot channels represent the hottest channels in seed and blanket assemblies, where the Maximum Cladding Temperatures (MCTs) occur. The calculation scheme is the same as the previous study as shown in Fig. 4-6 (Sutanto, 2014).
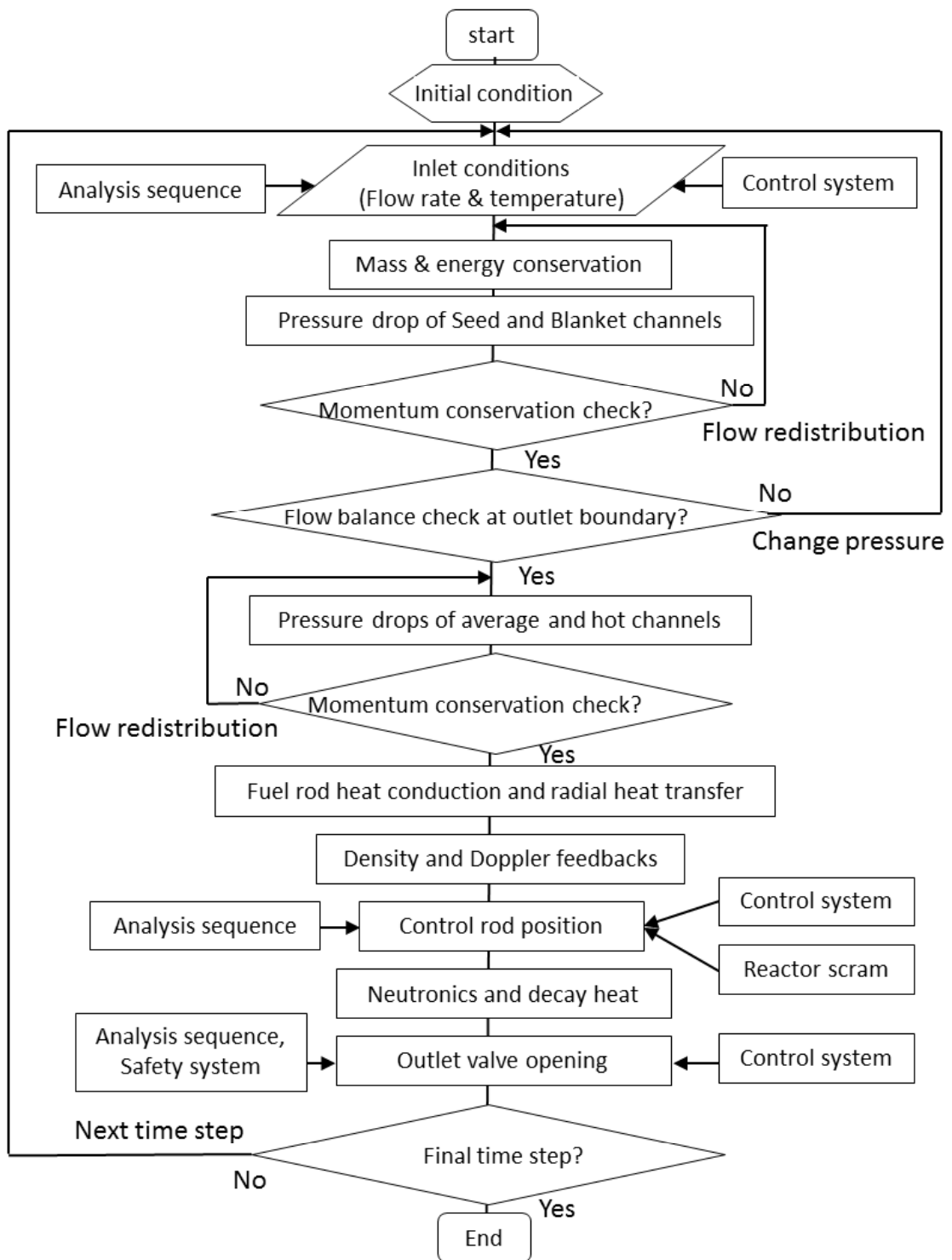
Fig. 4-6 Calculation scheme of SPRAT code (Sutanto, 2014)

4.4.1.2 Computational models for reflooding

Reflooding is the consecutive phase after blowdown during abnormal events. After 30s delay time of the LPCI actuation signal is released, after 30 s delay, coolant is injected in the core from the coolant line. Figure 4-7 is a schematic diagram that indicates the reflooding phase, and its computational scheme is shown in Fig. 4-8. The calculation starts at the time when the downcomer is filled and coolant flow begins to enter the fuel channels. The whole process is performed at the containment pressure. The quench front velocities in the fuel channels are computed by using the Yamanouchi's correlation (Owen and Jones, 1981). The calculation is finished when the water levels in all fuel channels reach to the top.
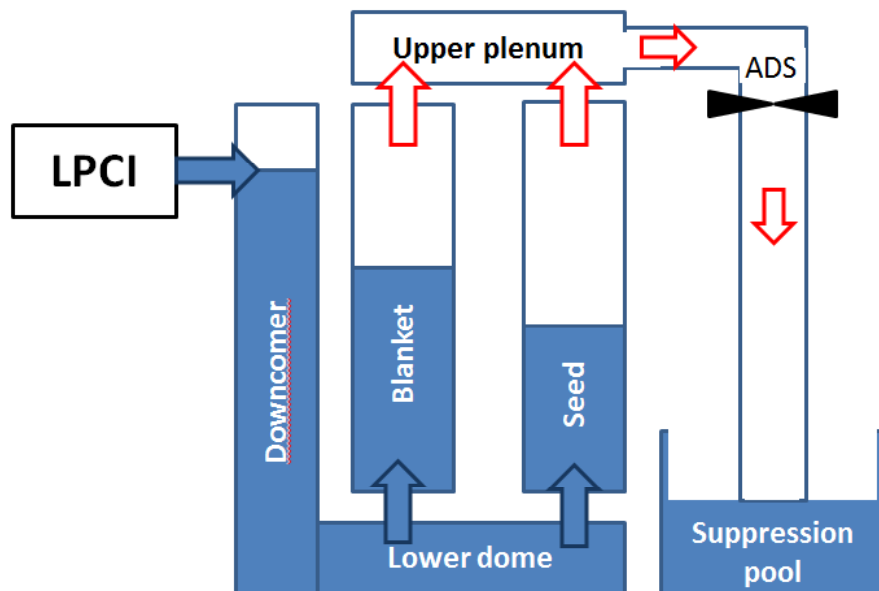
Fig. 4-7 Reflooding model
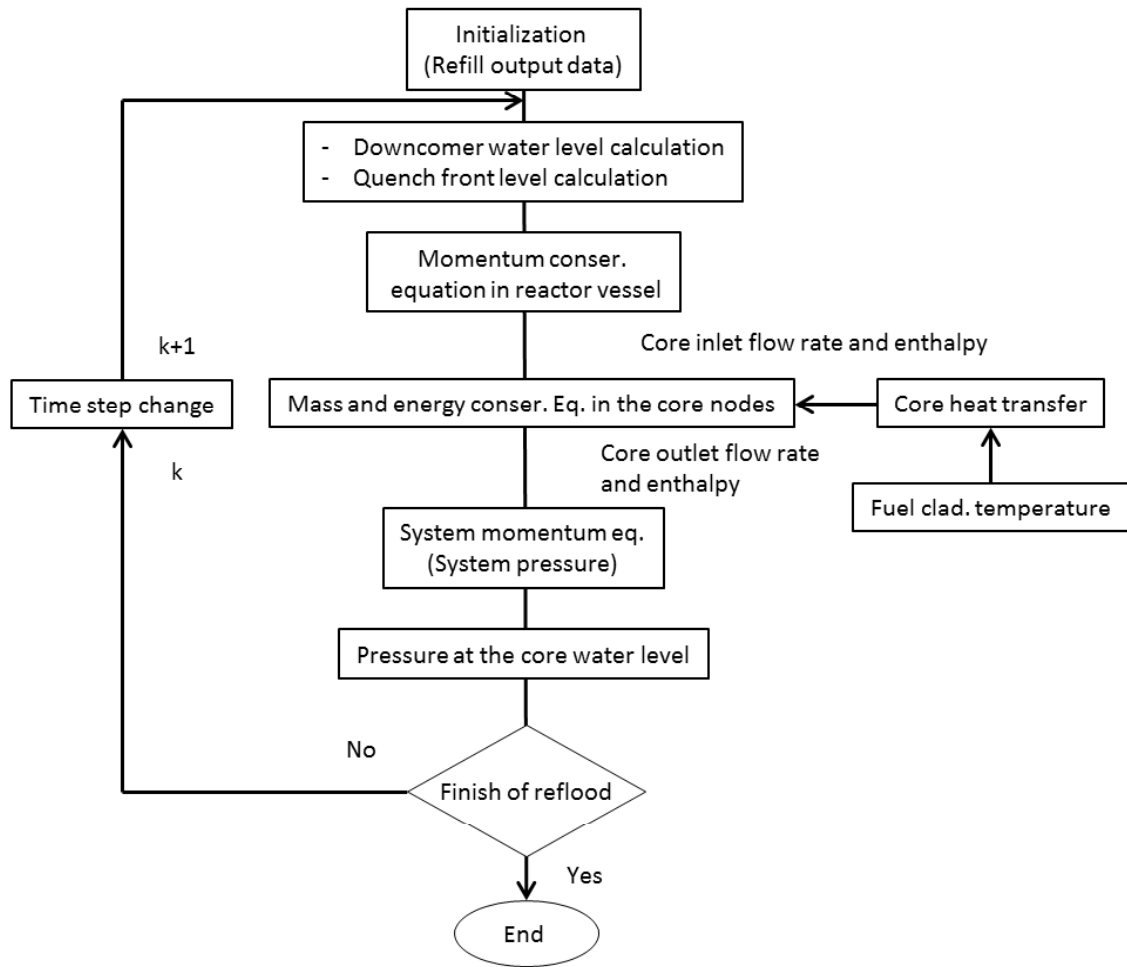
Fig. 4-8 Calculation scheme of reflooding (Sutanto, 2014)

4.4.2 Mass, energy and momentum conservation models

The current code system adopts node junction model for mass and energy conservation calculations. The governing equations for mass conservation is given by:

$$\frac{\partial \rho(z,t)}{\partial t} + \frac{\partial G(z,t)}{\partial z} = 0 \qquad (4\text{-}1)$$

The energy conservation equation is:

$$\frac{\partial \{\rho(z,t)h(z,t)\}}{\partial t} + \frac{\partial \{G(z,t)h(z,t)\}}{\partial z} = \begin{cases} 0 & (channel\ without\ heat\ source) \\ \frac{l_f Q_n''^k(z,t)}{A} & (channel\ with\ heat\ source\ ) \end{cases} \qquad (4\text{-}2)$$

where:

ρ: density (kg/m^3)

G: mass flow (kg/s)

t: time (s)

z: axial position (m)

h: enthalpy (J/kg)

l_f: mesh height (m)

A: surface area of fuel pin (m^2)

Q'': heat flux (W/m^2)

The momentum conservation equation is given for each node k as following:

$$\frac{M^k - M^{k-1}}{\Delta t} = \frac{\Delta P_{seed} - \Delta P_{blanket}}{l} \tag{4-3}$$

where M^k is the momentum for node k, Δt is the time interval, l is the channel length and ΔP is the pressure drop. The total ΔP for seed or blanket channel is comprised of pressure drop due to friction, acceleration, gravity and orifice. The friction pressure drop for supercritical flow has the same form as that of single-phase flow, while Blagius correlation (Blagius, 1913) is used to compute the friction factor, given as:

$$f = 0.0791 Re^{-0.25} \tag{4-4}$$

The calculation of the next two terms (acceleration and gravity) can be referred to section 3.2.2.5, while the only difference is that supercritical flow is regarded as single-phase flow. The pressure drop due to orifice is given by:

$$\Delta P_{ori} = \sum_i K_{ori} \rho_i \frac{v_i^2}{2} \tag{4-5}$$

where K_{ori} is the orifice coefficient, v_i is the fluid velocity.

4.4.3 Heat transfer models

Heat transfer models are mainly account for the heat transfer from fuel to coolant in the radial direction, while in the axial direction because node number is so large that the temperature difference between adjacent nodes in the solid computational domains (fuel and cladding) are relatively small and ignorable, thus the axial heat transfer for these domains are ignored.

In the radial direction, the fuel rod region is resolved by using a 2-D numerical approach in order to accurately represent the characteristics of the heat transfer. Considering the symmetry, 1/12 of one fuel rod and 1/6 of one coolant channel are taken as the computational domain as shown in Fig. 4-9.
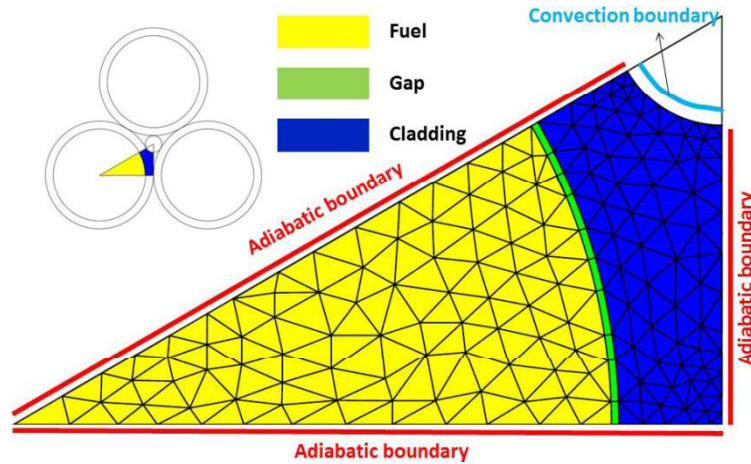
Fig. 4-9 Radial heat transfer model of fuel rod

The heat balance at transient conditions is varying with time, and it is given as:

$$\rho c_p \frac{\partial T}{\partial \tau} = \nabla \cdot \kappa_f \nabla T + q_v(\tau) \qquad \begin{array}{ll} \text{for fuel} & q_v \neq 0 \\ \text{for cladding and gap} & q_v = 0 \end{array} \qquad (4\text{-}6)$$

where q_v is volumetric heat generation rate as a function of time τ, κ_f the thermal conductivity of fuel, ρ is density, c_p is heat capacity and T is temperature. Conductance of the gap and thermal conductivity of the cladding are the same as those described in Section 3.2.4.6, and that of cladding is assumed to be 20 W/m·K for stainless steel.

For adiabatic boundaries, the boundary condition is given by:

$$\nabla T = 0 \qquad (4\text{-}7)$$

while for the convection boundary, the boundary condition is:

$$-\kappa_c \cdot \nabla T = h_f(\tau)(T_c(\tau) - T_{bulk}(\tau)) \qquad (4\text{-}8)$$

where h_f is the heat transfer coefficient on the cladding surface, T_c the cladding surface temperature and T_{bulk} the bulk temperature of coolant.

In the safety analysis, the flow condition is much more complicated than that of core design depending on the abnormal events. First, the pressure condition could change from supercritical pressure to subcritical pressure, therefore, the coolant flow may be more than one physical state, such as liquid single-phase, two-phase and vapor single-phase; second, normally, the flow direction in the core is upward, but in case of some events, such as LOCA, the flow direction may reverse to downward.

For heat transfer of supercritical flow, Watts correlations are used to compute the Nusselt number (*Nu*), which are commonly used for heat transfer calculation in Super FR (Oka *et al.*, 2010), given as:

For upward flow:

Normal heat transfer:

$$Nu = \begin{cases} Nu_v, & \frac{\overline{Gr_b}}{Re_b^{2.7}\overline{Pr_b}^{0.5}} < 10^{-5} \\ Nu_v(1-3000\frac{\overline{Gr_b}}{Re_b^{2.7}\overline{Pr_b}^{0.5}})^{0.295}, & 10^{-5} \leq \frac{\overline{Gr_b}}{Re_b^{2.7}\overline{Pr_b}^{0.5}} \leq 10^{-4} \\ Nu_v(7000Nu_v\frac{\overline{Gr_b}}{Re_b^{2.7}\overline{Pr_b}^{0.5}})^{0.295}, & 10^{-4} \leq \frac{\overline{Gr_b}}{Re_b^{2.7}\overline{Pr_b}^{0.5}} \end{cases} \qquad (4\text{-}9)$$

Deterioration heat transfer:

$$Nu = \begin{cases} Nu_v, & \frac{\overline{Gr_b}}{Re_b^{2.7}\overline{Pr_b}^{0.5}} < 10^{-5} \\ Nu_v(1.27-19500\frac{\overline{Gr_b}}{Re_b^{2.7}\overline{Pr_b}^{0.5}})^{0.7}, & 10^{-5} \leq \frac{\overline{Gr_b}}{Re_b^{2.7}\overline{Pr_b}^{0.5}} \leq 4.5 \times 10^{-5} \\ Nu_v(2600Nu_v\frac{\overline{Gr_b}}{Re_b^{2.7}\overline{Pr_b}^{0.5}})^{0.305}, & 4.5 \times 10^{-4} \leq \frac{\overline{Gr_b}}{Re_b^{2.7}\overline{Pr_b}^{0.5}} \end{cases} \qquad (4\text{-}10)$$

For downward flow:

$$Nu = Nu_v(1-3000\frac{\overline{Gr_b}}{Re_b^{2.7}\overline{Pr_b}^{0.5}})^{0.295} \qquad (4\text{-}11)$$

$$Nu_v = 0.021 \cdot Re_b^{0.8}\overline{Pr_b}^{0.55}\left(\frac{\rho_w}{\rho_b}\right)^{0.35} \qquad (4\text{-}12)$$

$$\overline{Gr_b} = \frac{(\rho_b-\overline{\rho})g \cdot D_h^3}{\rho_b v_b^2} \qquad (4\text{-}13)$$

$$\overline{Pr_b} = \frac{\overline{C_P} \cdot \mu_b}{\lambda_b} \qquad (4\text{-}14)$$

$$\overline{\rho} = \frac{\int_{T_b}^{T_w} \rho dT}{T_w-T_b} \qquad (4\text{-}15)$$

$$\overline{C_P} = \frac{\int_{T_b}^{T_w} C_P dT}{T_w-T_b} = \frac{h_w-h_b}{T_w-T_b} \qquad (4\text{-}16)$$

where Nu_v is the Nusselt number without buoyancy effect, *Pr* the Prandtl number, μ the viscosity (kg/s·m), *C* the specific heat (J/kg·K), λ the thermal conductivity (J/m·K), subscript *w* and *b* indicate the wall and bulk fluid respectively.

For heat transfer at subcritical pressure, the following correlations are used and summarized in Table 4-5. More details can be referred to Yi (2004).

Table 4-5 Heat transfer correlation at subcritical pressure (Yi, 2004)

Mode	Heat transfer regimes	Heat transfer correlation
1.	Subcooled heat transfer	Dittus-Boelter Correlation
2.	Nucleate boiling	Thom Correlation
3.	Forced convective vaporization	Schrock-Grossman Correlation
4.	Forced convection in superheated vapor	Dittus-Boelter Correlation
5.	Transition boiling	McDonough, Milich and King Correlation
6.	Stable film boiling	Groeneveld Correlation
7.	Pool film boiling	Modified Bromley Correlation
8.	Low pressure flow film boiling	Dougall and Rohsenow Correlation

4.4.4 Models for blowdown and reflooding

Blowdown phase may occur at break of inlet or outlet pipes and in case of ADS acuation. The equilibrium critical flow model (Lahey and Moody, 1993) is used to estimate the critical flow at the break or ADS outlet. When the output fluid is superheated vapor, the critical flow rate is estimated by:

$$G = \rho_0 \sqrt{2 C_P T_0 \left\{ \left(\frac{P_{cv}}{P_0} \right)^{\frac{2}{\gamma}} - \left(\frac{P_{cv}}{P_0} \right)^{\frac{1+\gamma}{\gamma}} \right\}} \qquad (4\text{-}17)$$

where:

$$P_{cr} = P_0 \left(\frac{2}{1+\gamma} \right)^{\frac{\gamma}{\gamma-1}} \qquad (4\text{-}18)$$

in case of two-phase flow condition, the critical flow rate is given by Moody (1965):

$$G_{cr} = \frac{1}{\frac{x_e}{\rho_g} + \frac{1-x_e}{\rho_f}} \sqrt{2 \left(h_0 - x_e h_g - (1 - x_e) h_f \right)} \qquad (4\text{-}19)$$

in case of subcooled condition, Zaloudeck's correlation (Bordelon *et al.*, 1974) is used:

$$G = \sqrt{2 \times 1.0133 \times 10^5 \rho_0 \left(P_0 - P_{cv}\right)}, \quad P_{cv} > P_{sat} \tag{4-20}$$

$$G_{cr} = 0.95\sqrt{2 \times 1.0133 \times 10^5 \rho_{sat}\left(P_0 - P_{sat}\right)}, \quad P_{cv} < P_{sat} \tag{4-21}$$

For reflooding calculation, the quench front velocity V_{qf} is computed according to Yamanouchi's correlation (Owen and Jones, 1981):

$$V_{qf} = \rho c \left(\frac{\varepsilon}{h_{qf}}\right)^{1/2} \frac{(T_w - T_b)^{1/2}(T_w - T_L)^{1/2}}{(T_L - T_b)} \tag{4-22}$$

where ε is the cladding thickness, h_{qf} the heat transfer coefficient at quench front taken from Yamanouchi to be a constant value of 5e-4 W/m^{2}K, T_L is the Leidenfrost temperature equal to 100°C.

4.4.5 Neutronic calculation model

The point kinetic model is used for evaluation of core power at transient over short time period, including six groups of delayed neutrons and two group approximation equations for decay heat, conservatively, which gives 20 % higher than that given by the ANS model (ANS, 1971). To obtain the neutron density and delayed precursor concentrations, the following equations are solved:

$$\frac{dn(t)}{dt} = \frac{\rho - \beta}{\Lambda} n(t) + \sum_{i=1}^{6} \lambda_i C_i \tag{4-23}$$

$$\frac{dC_i(t)}{dt} = \frac{\beta_i}{\Lambda} n(t) + \lambda_i C_i(t), i = 1 \dots 6 \tag{4-24}$$

The decay heat is computed based on the two group approximation:

$$\frac{d}{dt} P_{\alpha j}(t) = \lambda_{Pj}(\alpha_j Q(t) - P_{\alpha j}(t)), j = 1, 2 \tag{4-25}$$

The total core power then is given by:

$$Q(t) = Q_0 n(t) + P_{\alpha 1}(t) + P_{\alpha 2}(t) \tag{4-26}$$

where $n(t)$ is the neutron density, Q is the total reactor power, Q_o is the conversion factor for thermal power, C_i is the delayed neutron density for group i, ρ is reactivity, α_j is fraction of decay heat for group j, λ_i is decay constant of delayed neutron for group i, β is delayed neutron fraction, Λ is prompt neutron generation time.

During the core power calculation, two main kinds of feedback reactivity are considered, namely the feedback from the average coolant density change and fuel temperature change (Doppler effect).

4.5 Plant dynamics and control system design for Super FBR

In addition to safety system, control systems with respect to pressure, power, and outlet coolant temperature are also of key elements for both normal operation and transient conditions. The control systems for Super FBR are designed as the same way as Super FRs (Oka *et al.*, 2010) as shown in Fig. 4-10 and the descriptions are given in the following sections.
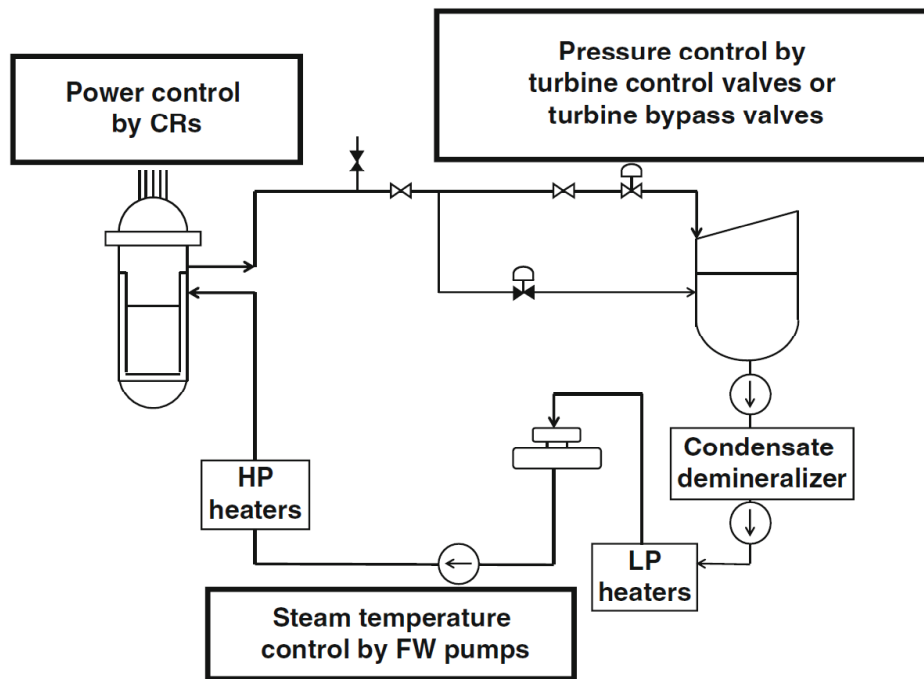
Fig. 4-10 Control system for Super FR (Oka *et al.*, 2010) and Super FBR

4.5.1 Control system of Pressure

The TCVs are used to maintain the turbine inlet pressure by regulating the valve opening. The TCV opening ratio $V(t)$ is proportional to the deviation between the pressure setpoint P_{set} and actual steam pressure $P(t)$ with lead-lag compensation (Oka *et al.*, 2010). The control equations are:

$$V_s(t) = V_0 - \frac{P(t) - P_{set}}{K}$$
$$V(t) = V_s(t) + T_1 \frac{dP}{dt} - T_2 \frac{dV}{dt} \tag{4-27}$$

where V_0 is rated opening of TCVs (100%), $V_s(t)$ is the signal for TCV opening (%), T_1 is the lead time, T_2 is the leg time, and K is the gain (MPa) that connects the pressure deviation with the valves opening. T_1 and T_2 are determined to be 2 s and 5 s, respectively, by referring

to BWRs. K is the main design parameter. Sensitivities related to K and system pressure are analyzed by decreasing the setpoint of steam pressure by 1% (from 30 MPa to 29.7 MPa), as shown in Fig. 4-11 and Fig. 4-12. The results indicate that K range from 0.2 to 0.5 is able to stabilize the pressure. Thus, K is determined to be 0.4MPa.
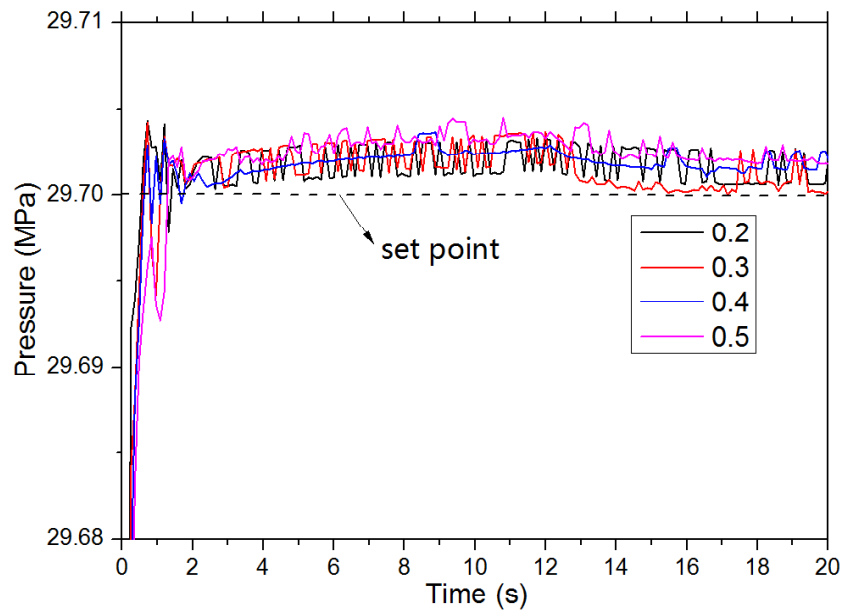
Fig. 4-11 Steam pressure response with different gain (K) ranging from 0.2 to 0.5
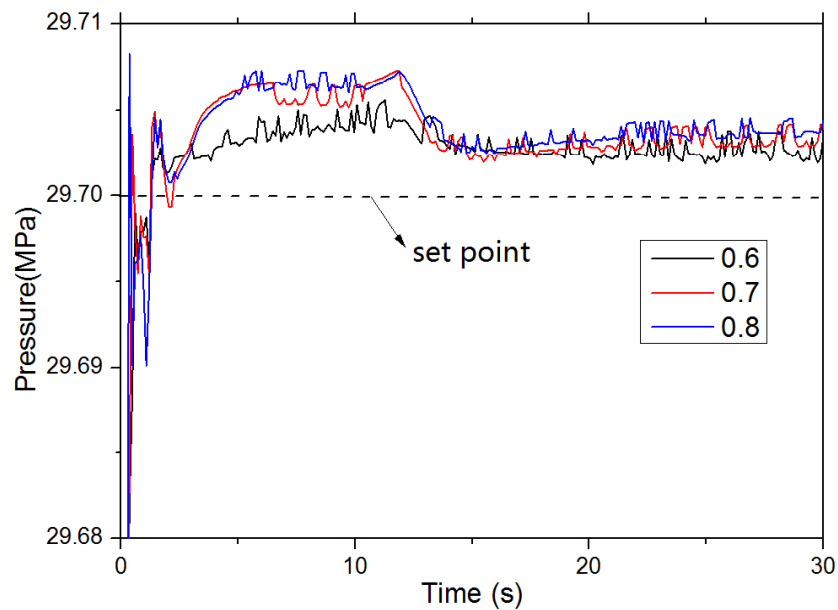
Fig. 4-12 Steam pressure response with different gain (K) ranging from 0.6 to 0.8

4.5.2 Control system of main steam temperature

The main steam temperature is maintained by controlling the feedwater flowrate (Oka *et al.*, 2010). In the system of Super FRs, a Proportional-Integral (PI) controller (Franklin *et al.*, 1994) is applied. For Super FBR, a Proportional-Integral-Derivative (PID) controller is used. The feedwater flowrate is obtained based on the following equations:

$$G_s(t) = K_p \left[e(t) + \frac{1}{T_i} \int_0^t e(t)dt + T_d \frac{de(t)}{dt} \right]$$
$$e(t) = T_{out} - T_{set}$$

$$(4\text{-}28)$$

where $G_s(t)$ is additional amount of flowrate outputted by coolant pumps, K_p, T_i, T_d are the proportional coefficient, integral time and differential time in PID controller respectively, $e(t)$ is the deviation between setpoint and actual values of steam temperature. K_p, T_i and T_d are determined to be 120, 10s and 0.001s respectively. Figure 4-13 shows a comparison between PI controller and PID controller used for the system of Super FBR. The calculation is conducted by increasing the setpoint by 1%(from 445°C to 449.5°C). The result indicates that the PID controller can stabilize the main steam temperature faster than original PI controller.
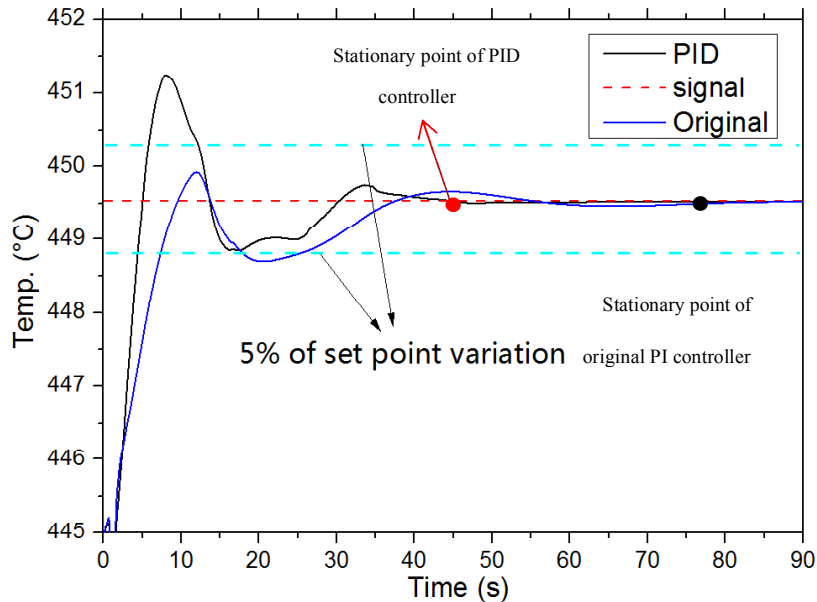
Fig. 4-13 Comparison of PI controller (original) and PID controller for main steam temperature control

4.5.3 Control system of reactor power

Control rods system is used to control the reactor power. By regulating the control rods speed and position, the reactor power can be stabilized. The following equations are used to determine the control rods speed v:

$$v = \begin{cases} v_{max}e/b & (e < b) \\ v_{max} & (e \geq b) \end{cases} \tag{4-29}$$

where v_{max} is the maximum speed determined by driven system, e is the deviation (%) between the actual power and setpoint, and b is the maximum deviation (%) for proportional control. v_{max} is taken from PWRs and is determined to be 1.9 cm/s due to similarity in control rod driven system of Super FBR and PWR. The maximum deviation, b, is determined by sensitivity analysis where the setpoint of power is decreased by 5 % from the rated power (100%). The responses of the core power and main steam temperature are shown in Fig. 4-14 and Fig. 4-15, respectively. By considering overshoot and settling time of these parameters, b is determined to be 40%.
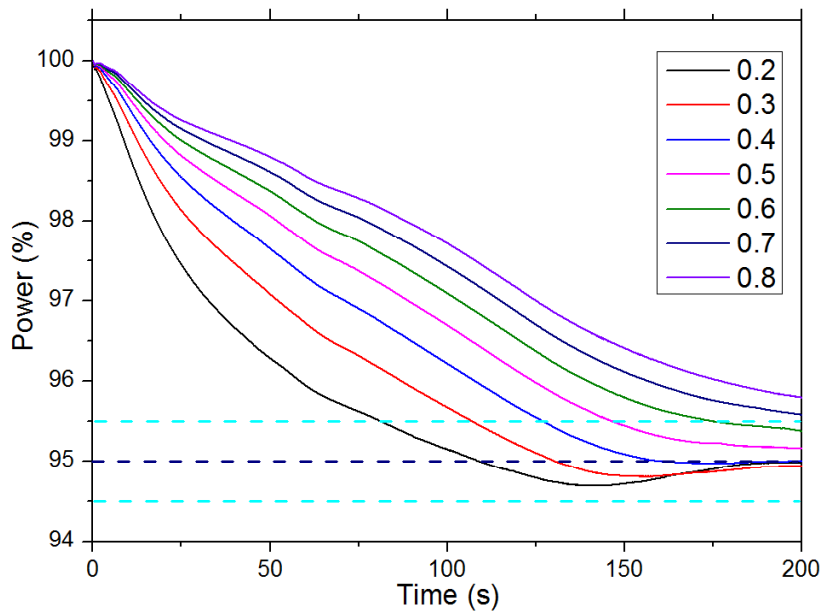
Fig. 4-14 Core power response with different maximum deviation (b)
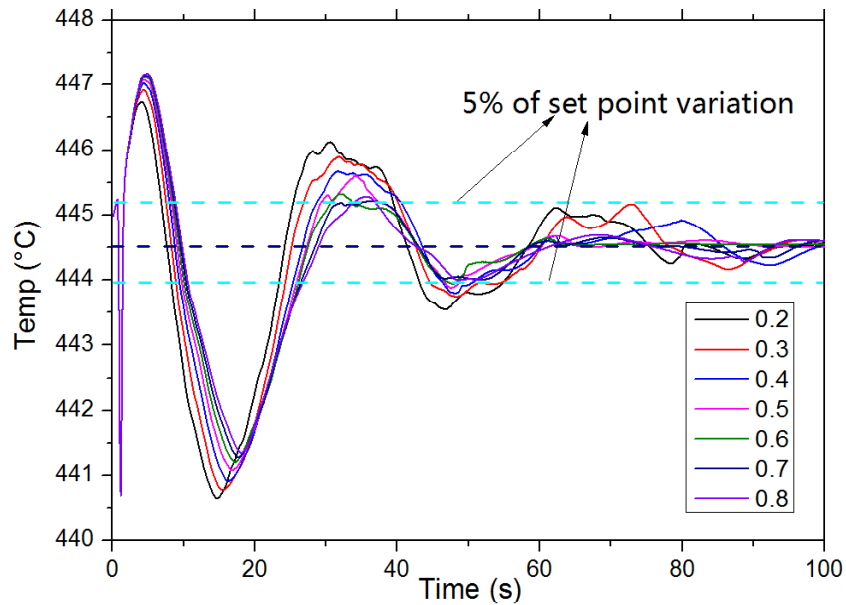
Fig. 4-15 Main steam temperature response with different maximum deviation (*b*)

4.6 Selection of abnormal events and safety criteria

In the past study (Ishiwatari *et al.*, 2005b), the abnormal events selection and classification of Super LWRs and Super FRs were studied in detail by reference to those of LWRs, sodium cooled reactors and gas cooled rectors. The accidents and transients analyzed in the current study are selected from those of Super LWRs and Super FRs and summarized in Table 4-6. They are mainly with respect to the abnormality of reactivity, pressure, coolant flow and inadvertent start or malfunction of core cooling system at supercritical-pressure condition.

The safety criteria in the present study are developed based on the previous study for Super FRs (Ishiwatari *et al.*, 2005b). In order to maintain the integrity of fuel rods and pressure boundary, the limitations for fuel pellet enthalpy increase, Maximal Cladding Temperature (MCT) and maximal core pressure are proposed:

1) The criteria of MCT for stainless steel cladding are 1260°C and 850°C for accidents and transients respectively; during accidents, oxidation of cladding is expected to be the limiting failure mode; 1260°C is used for accidents criterion, which is referred to the criterion temperature for LOCA in the early US PWRs with stainless steel cladding (Oka *et al.*, 2010). 850°C is the transient criterion for Super LWR with cladding (stainless steel) thickness of 0.63mm (Yamaji *et al.*, 2006), considering the buckling collapse as the most limiting failure mode. In the current design, although the cladding thickness is 0.873 mm, but the system pressure is 5MPa higher that of previous reactors (25MPa), thus this criterion

temperature is tentative, and detailed value will be studied in future. It is worth to note that 1260°C and 850°C are the criteria for Maximum Cladding Surface Temperature (MCST) in the past studies, and conservatively, the same values are used for MCT.

2) The maximal allowable pellet enthalpy increase are 230cal/g and 170cal/g for accidents and transients, respectively. Both values are taken from that of LWRs to prevent the melting of pellet centerline and maintain the cladding strain within the elastic region (plastic strain < 1%).

3) The maximal allowable pressure are 36.3MPa for accidents and 34.65MPa for transients, which are 105% and 110% of the maximum pressure of normal operation (33 MPa) respectively, considering using the theology from modern Ultra-Supercritical boilers (Viswanathan, 2006).

Table 4-6 Accidents and transients analyzed in the present study (Ishiwatari *et al.*, 2005b)

Classification	Event number	Initiating events	Sequence of abnormality
Accidents	A1	Total loss of feedwater flow	RCP trip (2/2) at 0s
	A2	Reactor coolant pump seizure	RCP stop (1/2) at 0s
	A3	CR[*] ejection at full power	Ejection of a CR cluster with maximum reactivity
Transients	T1	Loss of feedwater heating	Feedwater heater (1/8) stop at 0s
	T2	Inadvertent start-up of AFS	Auxiliary feedwater system starts at 0 s
	T3	Partial loss of reactor coolant flow	RCP trip (l/2) at 0s
	T4	Loss of offsite power	Turbine trip at 0s, RCP trip (2/2) at 10s
	T5	Loss of turbine load without turbine bypass	Turbine trip at 0s, Bypass failure, RCP trip (2/2) at 10s, turbine bypass valve close
	T6	Loss of turbine load with turbine bypass	Turbine trip at 0s, Bypass failure, RCP trip (2/2) at 10s, turbine bypass valve open
	T7	Uncontroled CR withdrawal at normal operation	Withdrawal of a CR cluster with maximum reactivity
	T8	Main Coolant Flow Control System Failure	Signal of maximum flow rate injection
	T9	Pressure control system failure	Signal of maximum valve opening
	T10	MSIV closure	All MSIV closing in 3s, RCP trip (2/2) at 10s

*CR: Control Rod

4.7 Events analysis

All events at both the beginning of the cycle (BOC) and the end of the cycle (EOC) are analyzed. Qualitatively, for each event, the results of BOC and EOC show the same time-dependent behavior; while quantitatively, there are small differences due to the changes of some core parameters such as power distribution, burnup and coolant temperature distribution. In Sections 4.7.1 and 4.7.2, only the results of BOC are discussed while the results are summarized in Section 4.9 for both BOC and EOC. By referring to the safety analysis of BWR, the control system is assumed to be out of action during the accidents but functional during the abnormal transients.

4.7.1 Analyses of accidents
4.7.1.1 Total loss of feedwater flow

The safety analysis results of the total loss of feedwater flow accident is shown in Fig. 4-16. At the beginning of this accident, all the reactor coolant pumps (RCPs) are tripped. The feedwater flow (main coolant line flow rate) is assumed to be linearly reduced to zero in 5 s. At 0.5 s, by detecting the feedwater flow rate lower than 90% of the rated value, the safety protection system shuts down the reactor, and the power continuously decreases to the decay heat level within 3 s.

Due to the absence of the control system, the core pressure slowly decreases for the first 5 s with the decrease of feedwater flow rate and power. The decrease of core flow rate (seed flow rate and blanket flow rate) is mitigated to some extent by the pressure decrease and the core heat-up that both lead to coolant expansion in the core. Thus, at 5s, the flow rates in both seed and blanket channels are still higher than 50%, although that of the main coolant line is already decreased to 0%.

When the pressure is lower than 23.5MPa, the ADS and LPCI are actuated. By inducing a strong outlet flow via the ADS, the flow rates in fuel channels immediately increase (in order to clearly show the behavior of power and flow rate in the first few seconds, the scale in Fig. 4-16 from 150% to 950% (the y-axis on the left hand side of the figure) are cut off) to about 1200 % of the rated value and MCTs rapidly decrease.
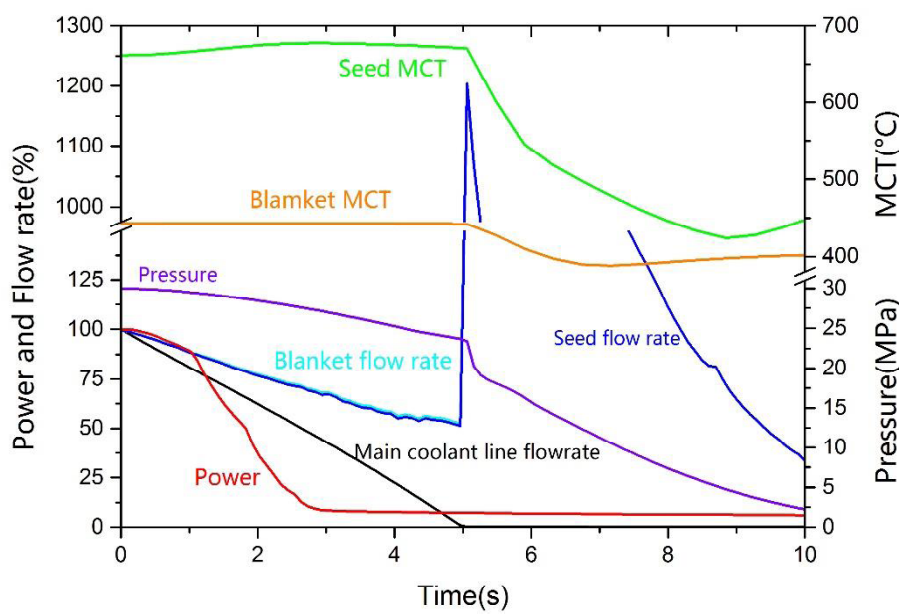
Fig. 4-16 Plant behavior during total loss of feed water flow

Figure 4-17 shows the behavior of MCTs including that of the following reflooding phase. Two units of LPCI start to supply coolant at 42s. The result indicates that in a few seconds from the end of depressurization, the MCTs rapidly increase due to the decrease in coolant flow as well as the release of the stored heat from the fuel pallets. After reflooding for 60s, MCT of seed assembly begins to decrease. The MCT of seed channel is at the peak of 691°C in the reflooding phase, which is well below the criterion (1260°C).
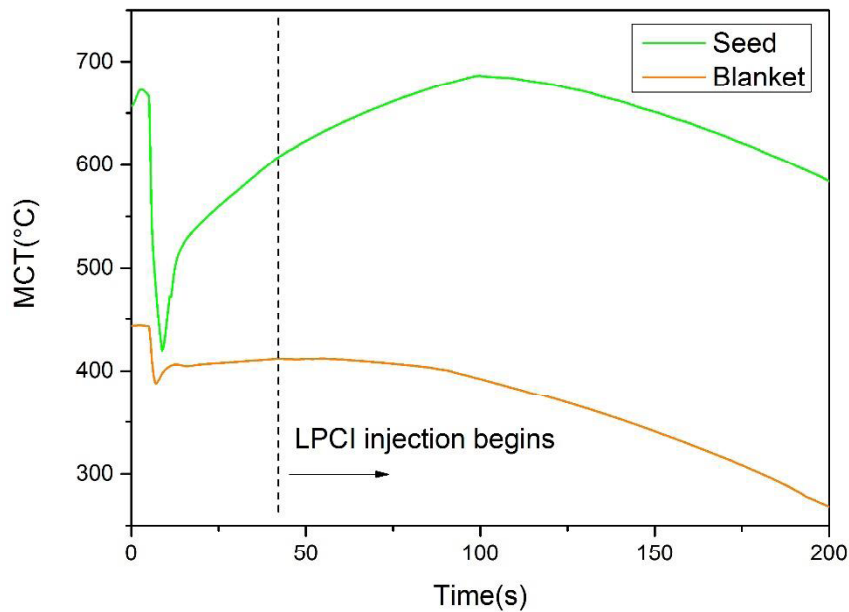
Fig. 4-17 MCTs during total loss of feed water flow

4.7.1.2 Reactor coolant pump seizure

At the beginning of this accident, one of the two RCPs immediately stops. Consequently, the main coolant line flow rate suddenly decreases to 50% of the rated flow. The result is shown in Fig. 4-18. The scram signal is released at 0 s by detecting the "reactor coolant pump trip". At the beginning, core pressure decreases due to the step decrease of flow rate, although the core heat-up slightly mitigates the effect. After scram, as the power rapidly decreases, the decrease of pressure continues due to the mismatch between flow rate and power. Meanwhile, decrease of pressure results in an expansion of coolant which slightly raises the core flow rate. MCTs increase during the first 2 s due to the high power to flow rate ratio, and then they start to decrease when the power is further decreased.

When the core pressure decreases to 23.5MPa (at 7.5s,), the ADS and LPCI signals are released. During the depressurization, large amount of flow rate is induced in the core, thus the MCTs are further decreased along with the rapid drop of pressure. After the depressurization, LPCI provides the coolant supply in the longer term.
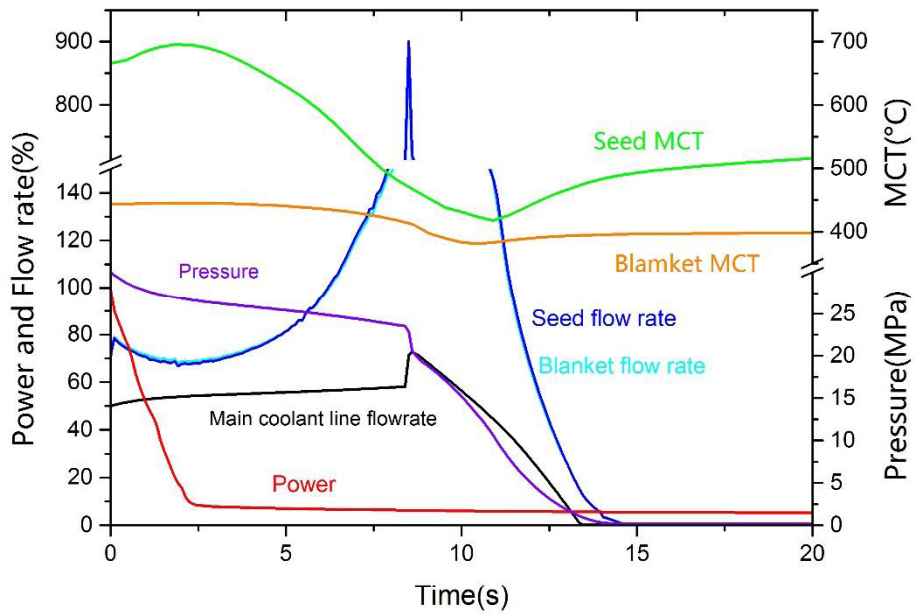
Fig. 4-18 Plant behavior during reactor coolant pump seizure

The MCTs behavior during the reflooding phase is similar to that in "total loss of feedwater flow" (Section 4.6.1.1), as shown in Fig. 4-19. The difference is that the peak of MCT (695.5°C) appears in the blowdown phase.
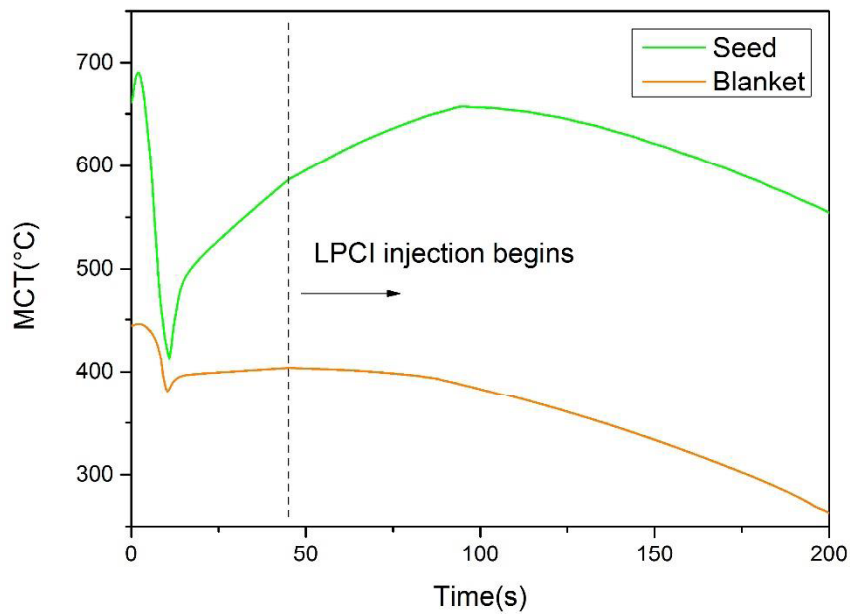
Fig. 4-19 MCTs during reactor coolant pump seizure

4.7.1.3 Control rod ejection

This accident causes the large and fast reactivity insertion. Initially, a control rod cluster with assumed maximum reactivity worth of 1.1 dollars is ejected out of the core with a velocity of 9500 m/s (Ishiwatari, 2005). This assumption comes from that of Super FR and is subject to future studies with control rod design. In this event, the feedback effect of coolant density is conservatively neglected, while the Doppler feedback effect is taken into account. Figure 4-20 shows the simulated plant behavior. The large positive reactivity insertion gives rise to the power soaring up. Scram signal is released with a delay time of 0.55s after the safety system detects the "period short (10s)", but before that, the power already begins to decrease due to the Doppler effect.

Meanwhile, due to small volume fraction of coolant, the core heat-up leads to the rapid increases of the core pressure and MCTs. After scram, along with the core cooling down (which means both the MCTs and the coolant temperature decrease), the core pressure decreases (still higher than the critical pressure of 22.1 MPa) and the core flow rates temporarily exceeds the rated values because of the coolant expansion around the pseudo-critical point (374 °C, 22.1 MPa), where the water density varies greatly with temperature as shown in Fig. 4-21.
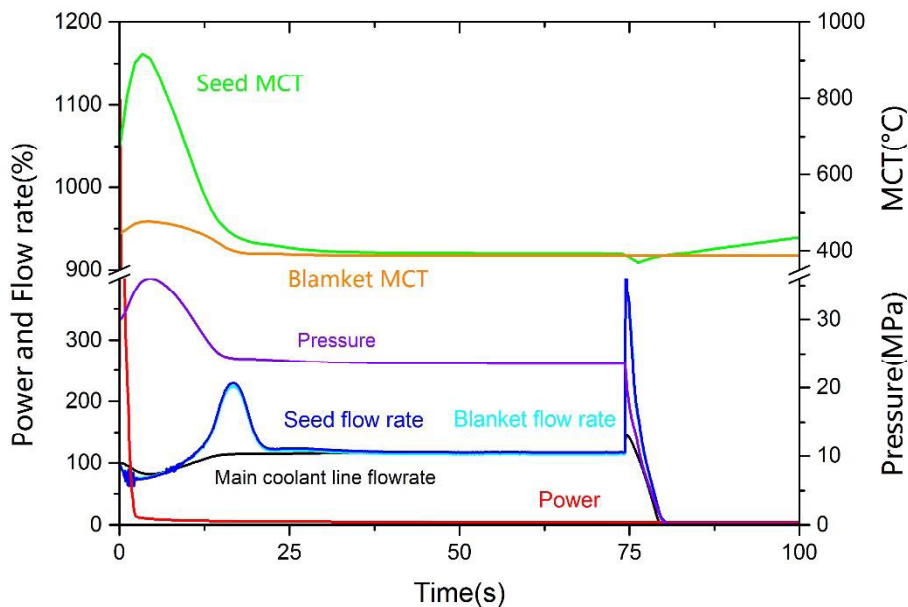
Fig. 4-20 Plant behavior during control rod ejection
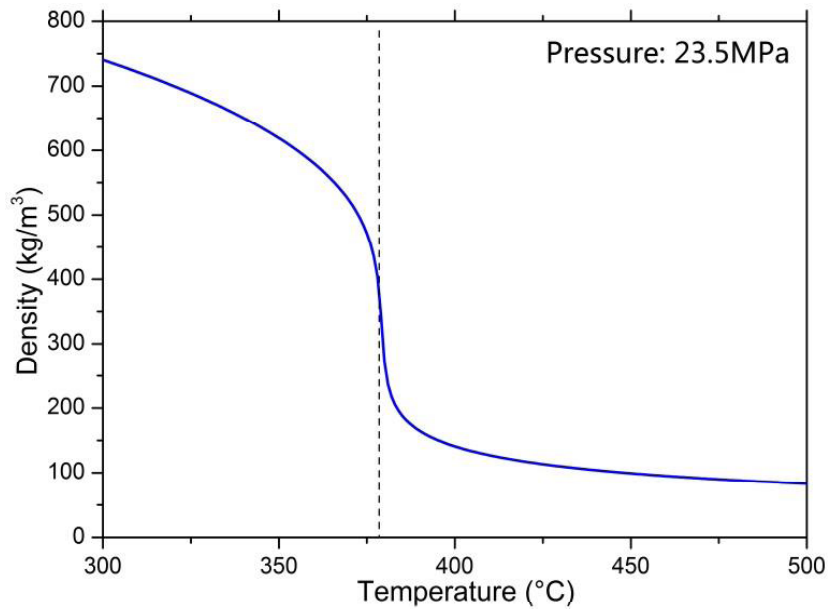
Fig. 4-21 Water density variation with temperature at supercritical pressure

At 75s, ADS and LPCI are actuated when the pressure is lower than 23.5 MPa. Large core flow rate is introduced by actuation of ADS, which rapidly decreases the core pressure. After depressurization, reflooding progresses and MCTs are further decreased after 170s as shown in Fig.4-22. The MCT (917.8°C) appears at the beginning of this event, which is still well below the criterion (1260°C). The peak fuel enthalpy is 137.5 cal/g at 1.5 s, and it is also below the criterion (230 cal/g).
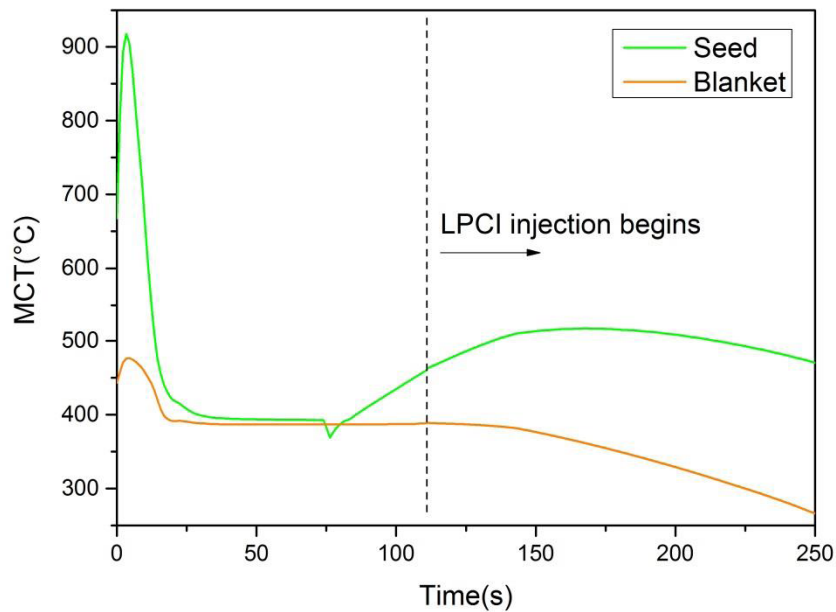
Fig. 4-22 MCTs during control rod ejection

4.7.2 Analysis of transients

4.7.2.1 Loss of feedwater heating

At the beginning of this event, the inlet coolant temperature drops by 55°C due to the loss of one feed water heater. The coolant density increases in the main coolant line which leads to a decrease of the flow rate in fuel channels. This is one of the characteristics of the once-through direct cycle without recirculation. Because of the flow rate decrease, the core experiences a short term heat-up at the beginning, which causes the power to decrease due to the voiding in the core and the MCTs to increase due to the mismatch of power and flowrate. After the high density coolant flows into the fuel channels, the positive reactivity is induced. Therefore, the core power increases again as well as the MCTs. At the same time, in order to mitigate the core heat-up, temperature controller increases the main coolant line flow rate, and then the MCTs begin to decrease. Scram signal is released at 10 s by detecting the "reactor power high (120%)". After that, MCTs are further decreased as shown in Fig. 4-23.
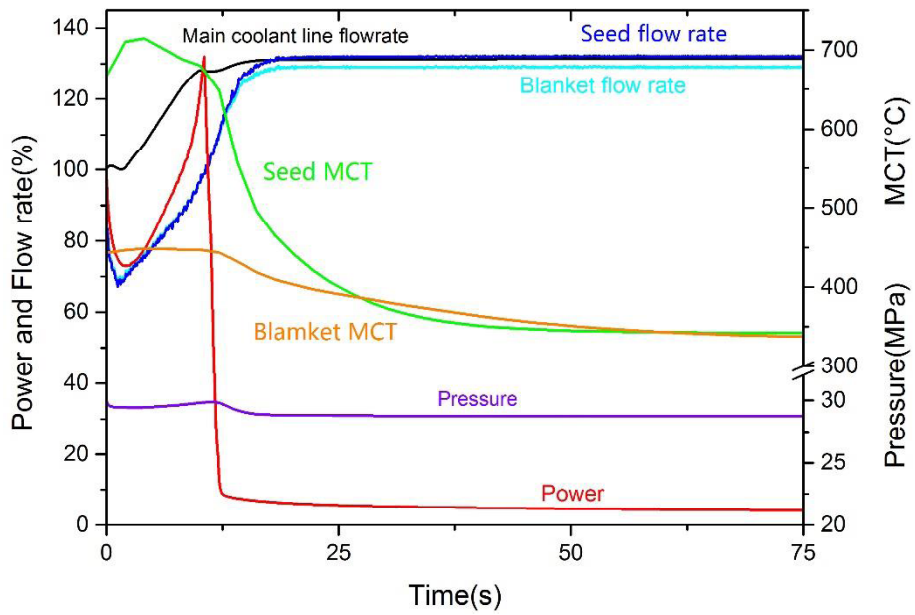
Fig. 4-23 Plant behavior during loss of feedwater heating

4.7.2.2 Inadvertent startup of AFS

This event is similar to the "loss of feedwater heating", since both events lead to positive reactivity insertion at the beginning of the event. Difference is that the reactivity insertion in this event is due to the injection of low temperature (30°C) feed water at 12% of rated flow from AFS. Responses of the safety systems and behaviors of the main parameters are similar to those in "loss of feedwater heating", as shown in Fig. 4-24.
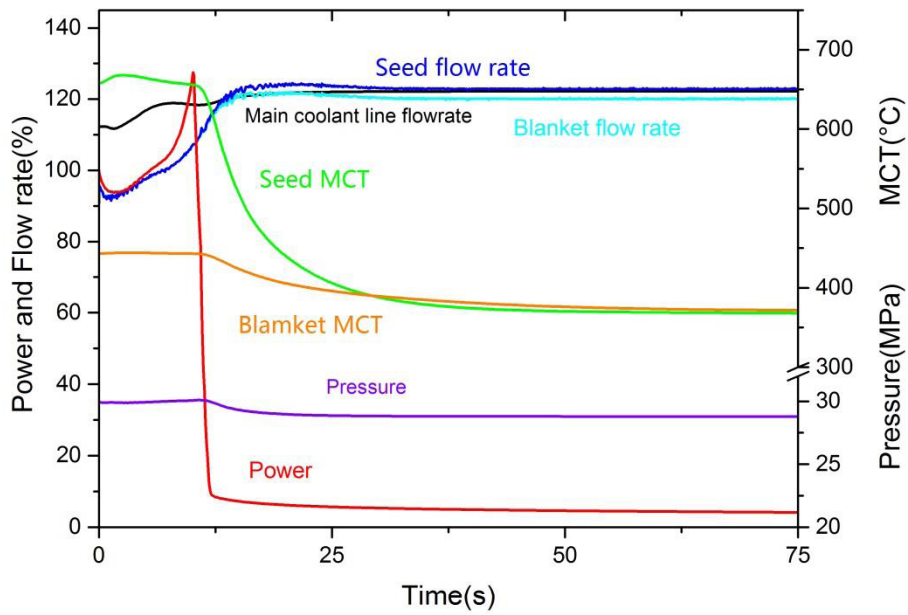
Fig. 4-24 Plant behavior during inadvertent startup of AFS

4.7.2.3 Partial loss of feed water flow

At the beginning of this event, one RCP is tripped with a coast-down time of 5 s, thus the feedwater flow rate linearly decreases to 50 % of the rated flow in 5 s. The scram signal is released when the "flow rate low (90 %)" is detected. At the first few seconds, MCTs increase because of the higher power to flow rate ratio, then the reactor shuts down and they decrease as well. With the decrease of flow rate, pressure deceases at the beginning, and then the pressure controller closes the TCVs to a lower position, thus the pressure remains stable above 27 MPa as shown in Fig. 4-25.
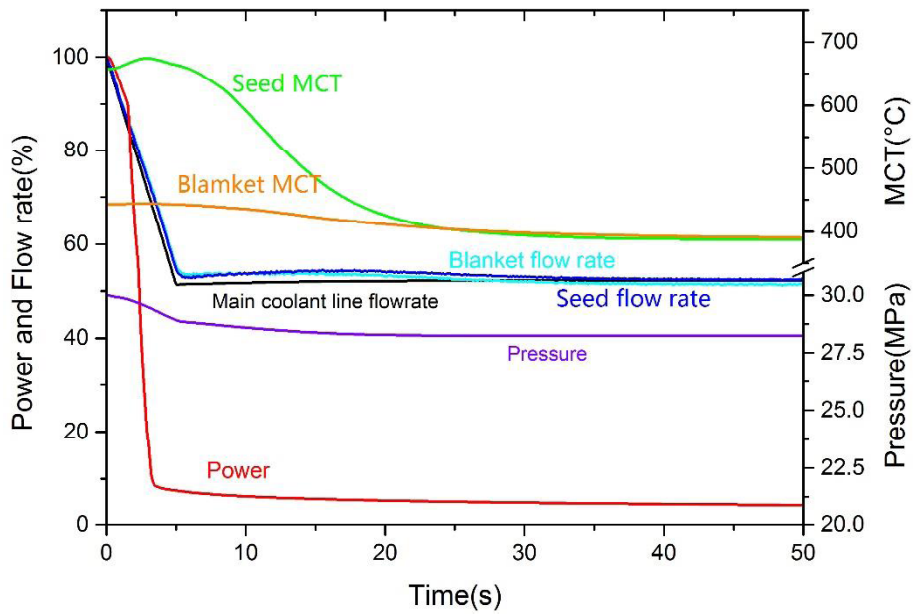
Fig. 4-25 Plant behavior during partial loss of feed water flow

4.7.2.4 Loss of offsite power

At the begining, the motor-driven condensate pumps are tripped and the TCVs are quickly closed with the immediate opening of the TBVs. In the meantime, the reactor is shut down and reactor power quickly decreases at the beginning as shown in Fig. 4-26. AFS signal is released by detecting the "loss of offsite power". Both RCPs are assumed to trip at 10s due to loss of coolant supply to deaerator. The core flow rate oscillates due to the TCVs closeure and action of control systems, and at 10s, it decreases to 0%.

Before 20s, relatively high core flow rate lowers the MCTs down, however, with decrease in flow rate, the MCTs rise again. Over a longer term, they are finally dcreased by coolant supply from AFS. Pressure decreases at the beginning due to reactor scram, then it remains stable by the pressure controller.
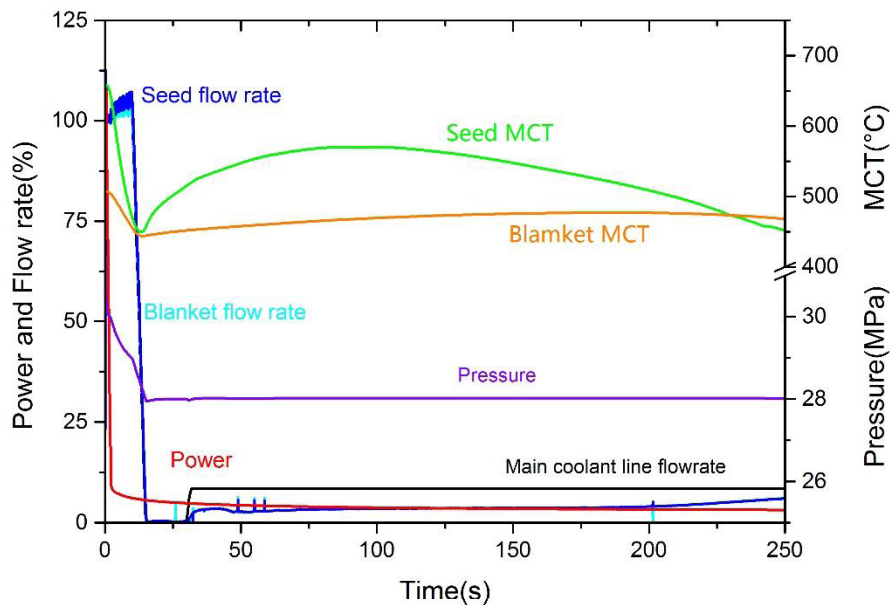
Fig. 4-26 Plant behavior during loss of offsite power

4.7.2.5 Loss of turbine load with bypass valves open

The plant behavior of this event is the same as that of "loss of offsite power", since both events are initiated by instantaneous turbine trip and the reactor isolation (closures of TCVs accompanied by opening of TBVs, reactor scram and actuation of AFS).

4.7.2.6 Loss of turbine load without bypass valves open

Except that the TBVs fail to open, this event is similar to the previous ones (Section 4.6.2.4 and 4.6.2.5). The presssure rises at the beginning due to closure of the outlet of the coolant flow, and then the SRVs open to mitigate the pressure increase and it leads to the oscillation of both the pressure and the flow rates because of the SRVs opening and closing. The behavior of MCTs is similar to that of "Loss of offsite power" and "Loss of turbine load with bypass valves open", because the power to flow ratio behaves similarly to those due to functioning of the reactor scram, SRVs, and AFS. The MCTs are finally decreased by AFS. The result is shown in Fig. 4-27.
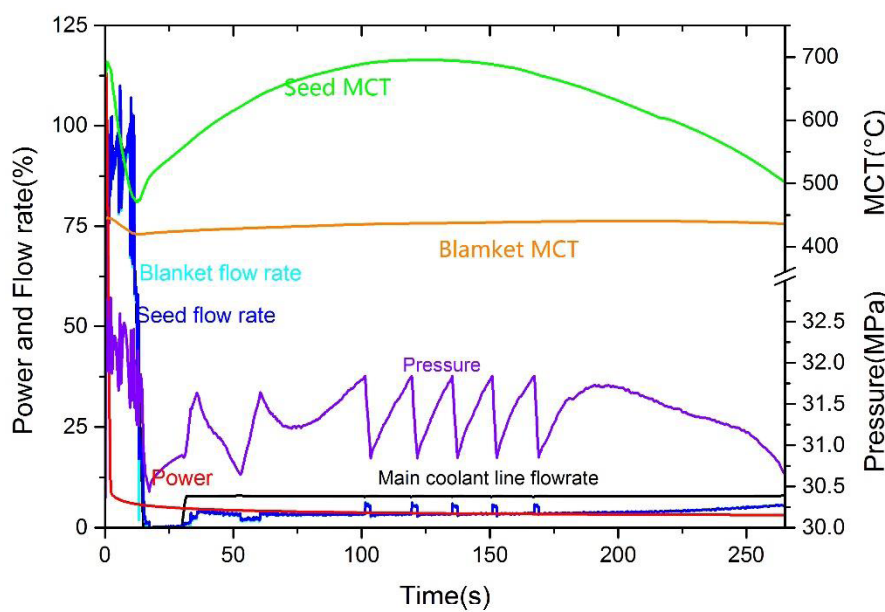
Fig. 4-27 Loss of turbine load without bypass valves open

4.7.2.7 Uncontroled CR withdrawal at normal operation

The control rods cluster with maximum reactivity worth of 1.1 dollars is assumed to be withdrawn at the velocity of 114 cm/min. Unlike the analysis for "control rod ejection" accident, both the doppler and coolant density feedbacks are considered in this event. Result is shown in Fig. 4-28. By contrast, the lower velocity of control rods withdrawal leads to a milder increase of power. The MCTs and pressure rise at the beginning, and then the temperature controller supplies more feedwater flow to mitigate the core heat-up.

By detecting the "power high (120%)", scram signal is released at 25 s followed by the decrease of MCTs and pressure. The peak enthalpy of the fuel pellet is 97.6 cal/g at 23.1s which is much lower than criterion of 170 cal/g.
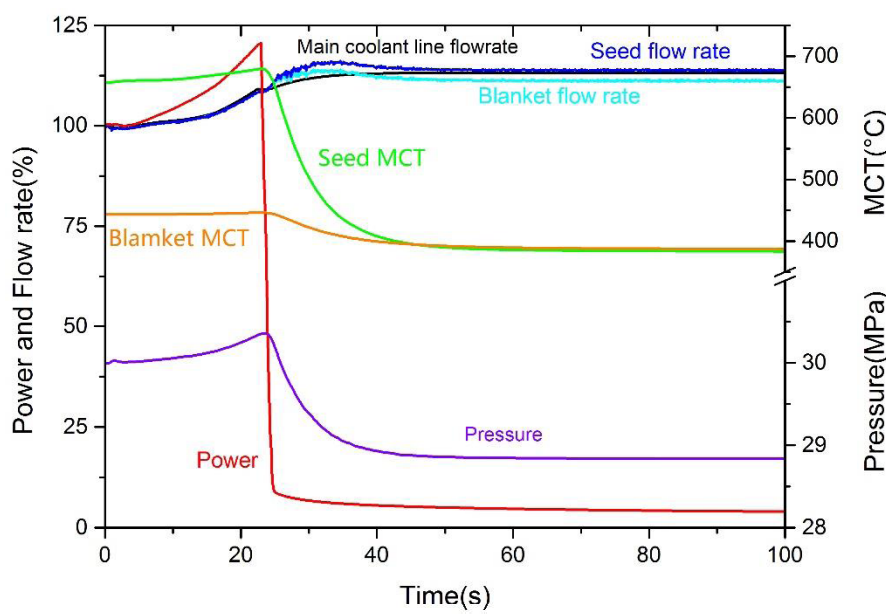
Fig. 4-28 Plant behavior during uncontroled CR withdrawal at normal operation

4.7.2.8 Main Coolant Flow Control System Failure

Due to the malfunction of the feedwater control system, the flow rate in the main coolant line is assumed to gradually increase to 138% of the rated flow at the beginning. The increase of the flow rate gives rise to high average coolant density in the core, which then leads to the power increase. Due to the power control system, the power is finally regulated to as that of the normal operation. The MCTs decrease from the beginning because of the high feedwater flow rate. The result is shown in Fig. 4-29.
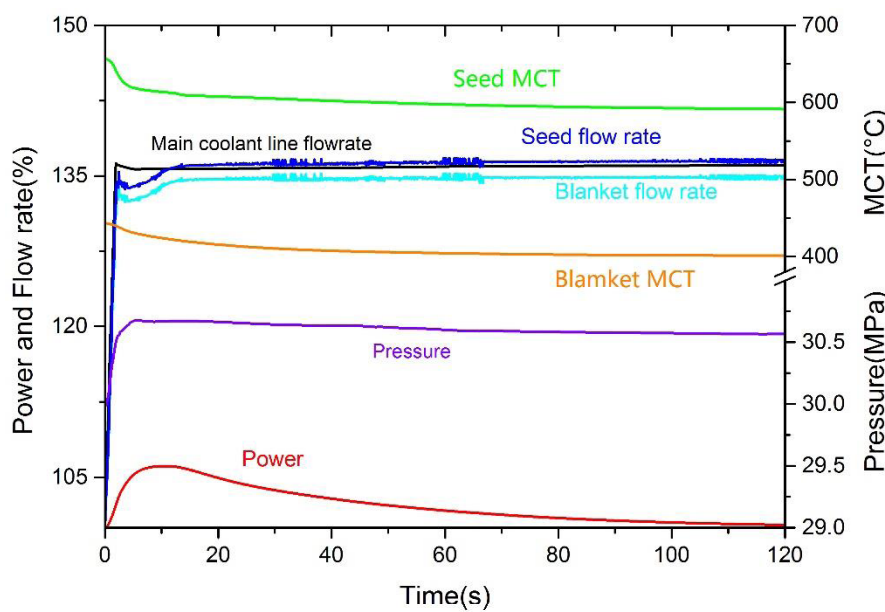
Fig. 4-29 Plant behavior during feed water flow rate control system failure

4.7.2.9 Pressure control system failure

The malfunction of pressure control system assumes that the TCVs progressively open to 130% of the rated opening. As a result, the core pressure slowly decreases. When the pressure is lower than 28.8MPa, the power decreases due to the scram actuation. On the other hand, the pressure decrease in return leads to the increase in the core flow rate by the coolant expansion around the pseudo-critical point. This phenomenon has also been observed in the accident "control rod ejection" and "reactor pump seizure". Therefore, the cladding temperatures are always below the initial values. When the pressure is reduced to 23.5MPa, ADS and LPCI are actuated so as to cool the core over a longer term as shown in Fig. 4-30 and Fig. 4-31.
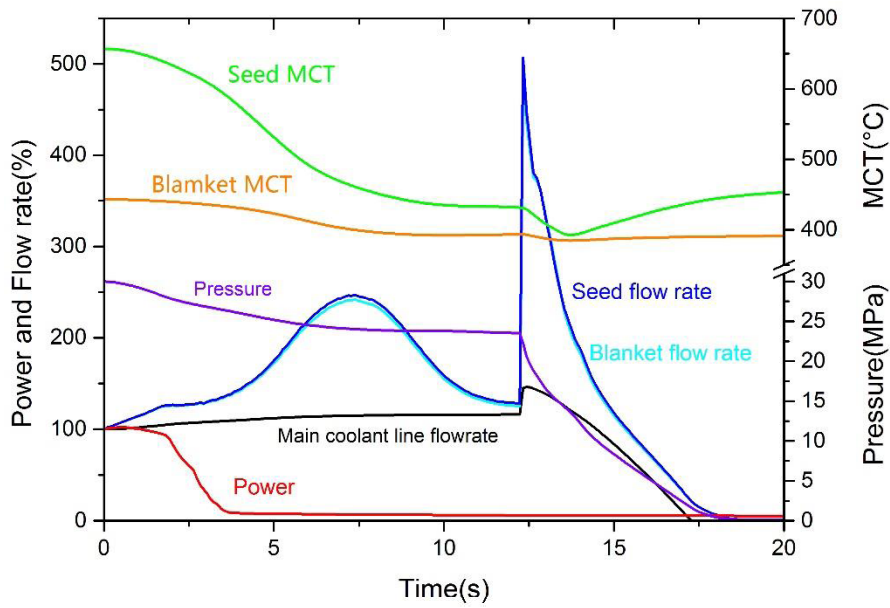
Fig. 4-30 Plant behavior during pressure control system failure
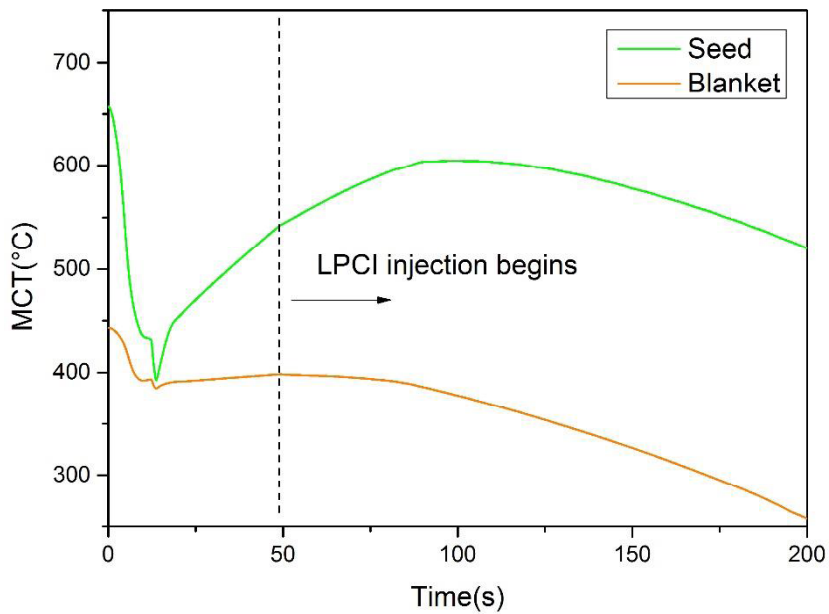
Fig. 4-31 MCTs during pressure control system failure

4.7.2.10 MSIV closure

In this event, all of the MSIVs are assumed to be closed, which makes the core behavior similar to that of "Loss of turbine load without bypass valves open".

4.8 Characteristics of radial temperature distribution

Figure 4-32 shows the steady state radial temperature distribution of the hottest cross-section in which the MCT is located. It can be noted that the MCT appears at the position where it is the furthest from the coolant channel in cladding. Thus, there is the largest heat resistance and it leads to the MCT.
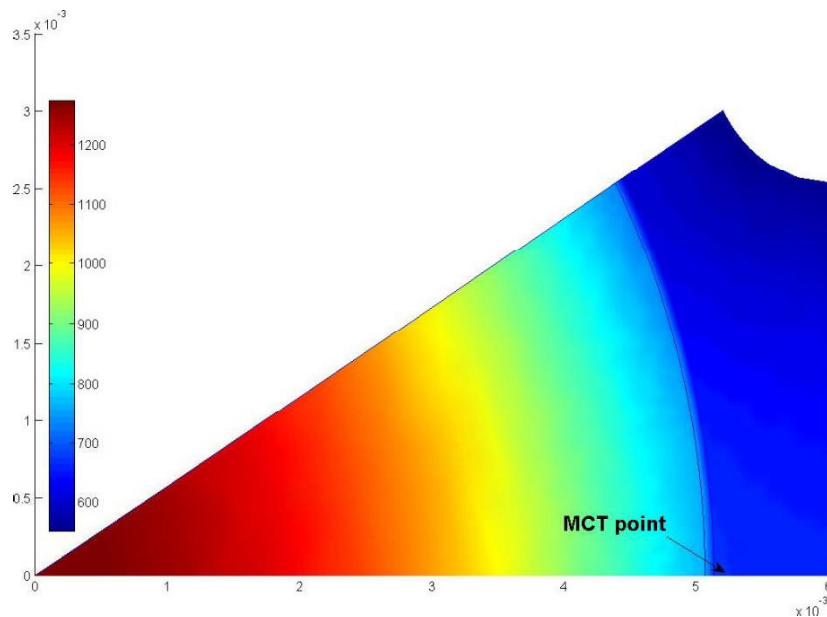
Fig. 4-32 Radial temperature distribution of the hottest cross-section at normal operation

From the above analysis of accidents and trasients, it is seen that the MCT behavior with time can be divided into two phases in these events. The fist phase is characterized by the first sharp decrease of MCTs caused by reactor scram or flow rate increase at the begining of the events; the second phase is from the end of the fist phase and can be identified by two phenomena depended on events: 1) the MCTs rise again and then decrease (such as "total loss of feed water flow"), or 2) slowly and monotonically decrease to be nearly stable (such as "Partial loss of feed water flow").

The radial temperature distribution of fuel rod is much different between the two phases. Figure. 4-33 shows the radial temperature distribution in "total loss of feedwater flow" in the first phase, and Fig. 4-34 shows that in the second phase. By contrast, it is seen that the temperature distribution maintains a larger degree of nonuniformity in the first phase, while in

the second phase (except "Feed water flow rate control system failure") the distribution quickly becomes uniform. At normal operation (or the begining of each event), the cladding temerpature distribution is more uniform than that of fuel, and the nonuniformity in fuel pellet is mainly because of the relatively low thermal conductivity of the fuel pellet. Although the heat conductivity of cladding is much higher, the temperature distribution is still more nonuniform than that of conventional cladding, owing to the special geometry. The temperature distributions in both fuel pellet and cladding become uniform after reactor scram due to the release of heat storage with the decrease of heat flux. In some cases, release of the stored heat from fuel pellet leads to a fast increase of MCT, for instance,as shown in Fig. 4-17 (from 11s to 15s).
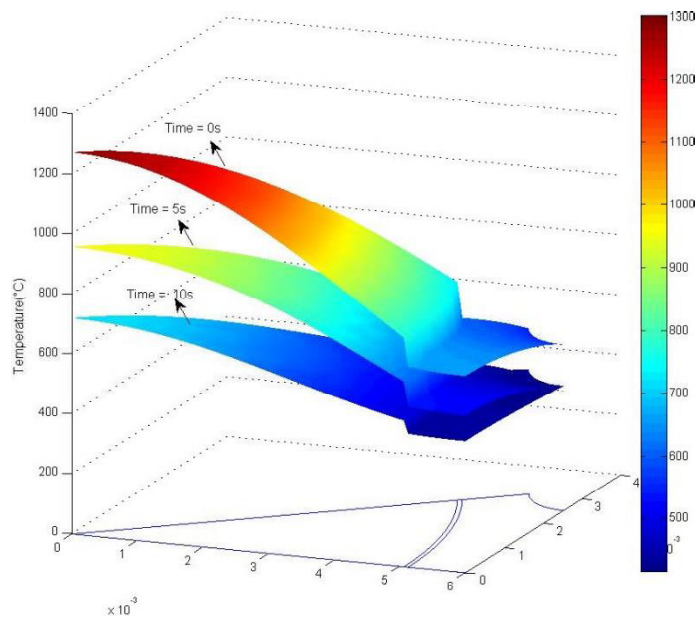
Fig. 4-33 Radial temperature distribution in the first phase of "total loss of feedwater flow"
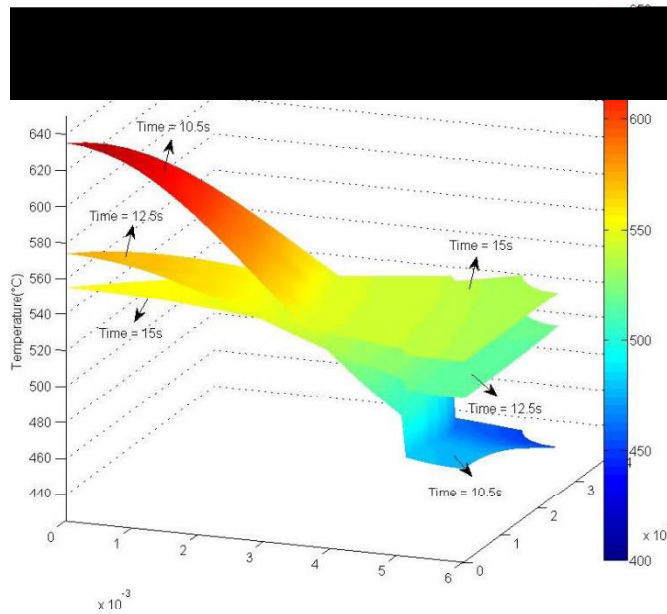
Fig. 4-34 Radial temperature distribution in the second phase of "total loss of feedwater flow"

4.9 Summary

The results of the peak value of MCT and peak pressure for all the selected accidents and transients at both BOC and EOC are illustrated in Fig. 4-35 and Fig. 4-36 respectively. It can be clearly seen that all the criteria for cladding temperature and core pressure are satisfied, which indicates that the current safety system is capable to protect the reactor well . However, it should be noted that further research is necessary regarding design criteria, which have been tentatively adopted from previous works (Ishiwatari, 2005a; Ikejiri, 2010; Li, 2013; Sutanto, 2014) as well as some scenarios and design parameters which may have large sensitivities on fuel integrities. Among these events, the "control rod ejection" (A3) is the most important event, because both the maximal MCT and peak pressure are higher than those of other events. Some parameters, such as control rod worth may have high sensitivity on the plant behavior and its influence should be further studied. By contrast, the "total loss of flow" is the most important event for Super FR (Ikejiri *et al.*, 2010). On account of the small coolant volume, the pressure and MCTs are more sensitive to the change of coolant temperature and flow rate arising from the core heat-up by the large reactivity insertion.
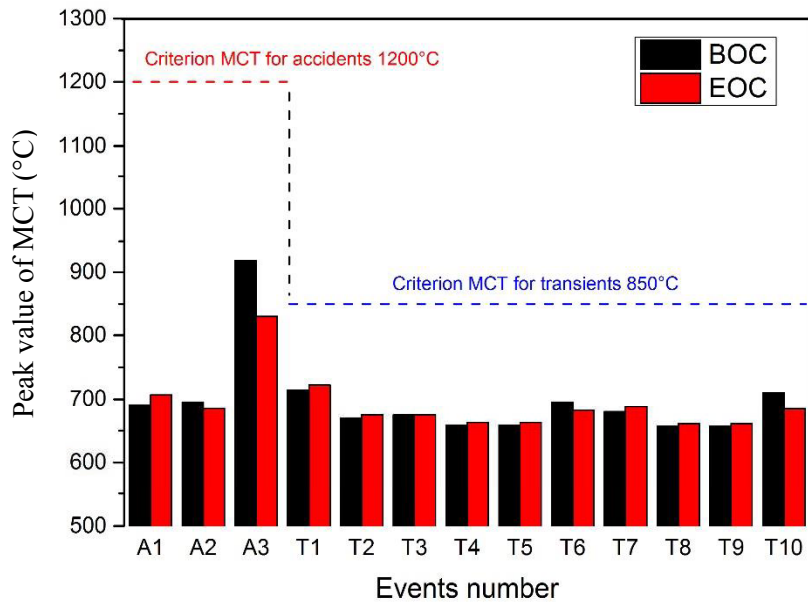
Fig. 4-35 Summary of Peak values of MCT during abnormal events
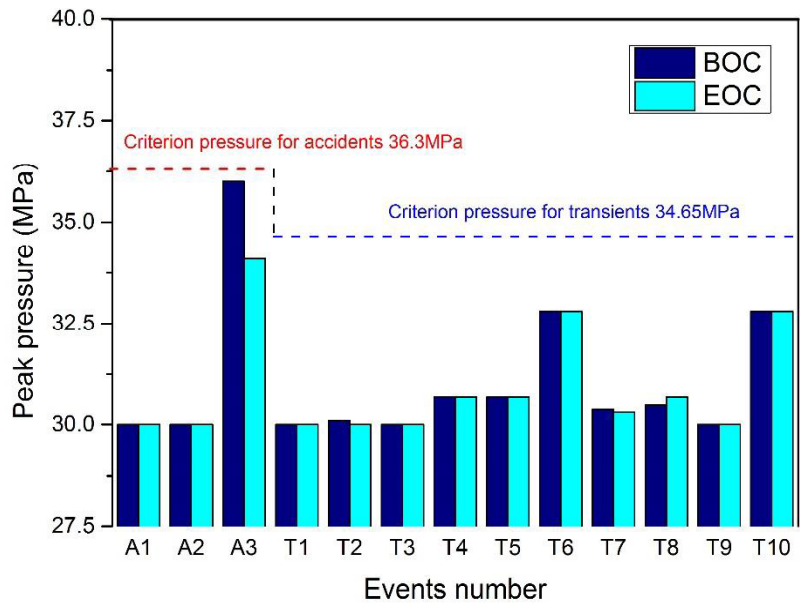
Fig. 4-36 Summary of peak core pressures

It is concluded that the present core and system design of Super FBR satisfy all the safety criteria at the accidents and transients at supercritical pressure at both BOC and EOC. The

analysis of LOCA (loss of coolant accident) and the ATWS (anticipated transient without scram) are remained for further study.

4.10 Reference

ANS Standards Committee, 1971. Decay Energy Release Rates Following Shutdown of Uranium-Fueled Thermal Reactors. American Nuclear Society.

Bordelon F.M., *et al.*, 1974. SATAN VI Program: Comprehensive Space-Time Dependent Analysis of Loss of Coolant, WCAP-8302 (Proprietary), WCAP-8306 (Nonproprietary).

Blagius, P. R. H., 1913. Das Aehnlichkeitsgesetz bei Reibungsvorgangen in Flüssigkeiten. Forschungsheft (131), pp.1-41

Franklin, G., David Powell, F. J., Emami-Naeini, A., 1994. Feedback Control of Dynamic Systems. 3rd edition. USA. Addison-Wesley

Hibi, K., Shimada, S., Okubo, T., Iwamura, T., Wada, S., 2001. Conceptual designing of reduced-moderation water reactor with heavy water coolant. Nuclear Engineering and Design, 210(1–3), pp. 9-19.

Ishiwatari, Y., Oka, Y., Koshizuka, S., 2003. Control of a high temperature supercritical pressure light water cooled and moderated reactor with water rods, Journal of Nuclear Science and Technology, 40(5), pp. 298-306.

Ishiwatari, Y. *et al.*, 2003. ATWS analysis of supercritical pressure light water cooled reactor. Proc. GLOBAL2003, New Orleans, Louisiana, USA, Nov. 16–20, pp. 2335.

Ishiwatari, Y., Oka, Y., Koshizuka, S., Yamaji, A., Liu, J., 2005a, "Safety of super LWR, (I) safety system design," Journal of Nuclear Science and Technology, 42 (11), pp. 927-934.

Ishiwatari, Y., Oka, Y., Koshizuka, S., Yamaji, A., Liu J., 2005b, "Safety of Super LWR, (II) safety analysis at supercritical pressure," Journal of Nuclear Science and Technology, 42 (11), pp. 935-948.

Ikejiri, S., Ishiwatari, Y., Oka, Y., 2010. Safety analysis of supercritical-pressure water-cooled fast reactor under supercritical pressure. Nuclear Engineering and Design, 240, pp. 1218-1228.

Ikejiri, S., Han, C. Y., Ishiwatari, Y., Oka, Y., 2011. LOCA Analysis of Super Fast Reactor. Journal of Nuclear Science and Technology, 48(10), pp. 1289-1299

Lahey R.T., Moody F. J., 1993. The Thermal-Hydraulics of a Boiling Water Nuclear Reactor. American Nuclear Society, La Grange Park, pp. 436-441.

Li, H.P., Oka, Y., Ishiwatari, Y., 2013. Safety analysis of a supercritical water cooled fast reactor with all-upward two-pass flow, Annals of Nuclear Energy, 59, pp. 1-9.

Liu, Q. and Oka, Y., 2013. Core design for super fast reactor with all upward flow core cooling. J. Ann. Nucl. Energy 57, pp. 221-229.

Moody F.J., 1965. Maximum flow rate of a single component, two-phasemixture", J. Heat Transfer, Trans. ASME, Ser. C, 87 [1], pp. 134-142.

Wu, J. and Oka, Y., 2014. Improved single pass core design for high temperature Super LWR. Nuclear Engineering and Design, 267, pp. 100-108.

Owen, C. and Jones, Jr., 1981. Nuclear reactor safety heat transfer. Hemisphere Publishing Corporation.

Okano, Y., Koshizuka, S., Kitoh, K., Oka, Y., 1996. Flow-induced accident and transient analyses of a direct-cycle, light-water-cooled, fast breeder reactor operating at supercritical pressure, Journal of Nuclear Science and Technology, 33, pp. 307-315.

Oka, Y., Koshizuka, S., Ishiwatari, Y., Yamaji, A., 2010, Super Light Water Reactors and Super Fast Reactors. Springer. Chap. 6.

Oka, Y., Inoue, T., Yoshida, T., 2013. Plutonium breeding of light water cooled fast reactors. Journal of Nuclear Science and Technology, 50(1), pp. 15-20.

Yi, T. T., 2004. Startup and Stability of a High-Temperature Supercritical-Pressure Light Water Reactor. Doctoral thesis, The University of Tokyo.

Yamaji, A., Oka, Y., Ishiwatari Y. *et al.*, 2006. Principle of rationalizing the criteria for abnormal transients of the Super LWR with fuel rod analyses. Ann. Nucl. Energy, 33, issue 11-12 (984)

Yoo, J., Ishiwatari, Y., Oka, Y., Liu, J., 2006. Conceptual design of compact supercritical water-cooled fast reactor with thermal hydraulic coupling. Ann. Nucl. Energy, 33, pp. 945–956.

Sutanto, 2014. Start-up and Safety Analyses of Super Fast Reactors. Doctrol thesis, Waseda Univercity.

Viswanathan, R., 2006. U.S. Program on Materials Technology for Ultrasupercritical Coal Power Plants. Electric Power Research Institute, Palo Alto, CA, March 2006.

Chapter 5 Conclusions

Designing the Fast Breeder Reactors (FBRs) cooled by light water is of great advantages over that cooled by liquid metal on account of its reliability and low capital cost, yet it has been challenging for decades. In the earlier studies, the reactors developed with tight fuel rod lattice achieved high conversion ratio of close to 1.0 or slight breeding but still are not able to attain the goal of high breeding that achieves CSDT of less than 50 years. That is, high breeding which enables fast installation of the FBR system at a rate comparable to the growth rate of energy demand in advanced countries such as the G7 members (1.4 % / year). The FBRs cooled by light water that achieved high breeding would greatly enhance the role of LWR in terms of providing reliable, low-cost and sustainable energy for the future. The current study addresses development of concept of the high breeding by light water cooling with tightly packed fuel assemblies, including the analysis of thermal hydraulic characteristics of the narrow coolant channels, the designing of the high breeding core and the safety analysis.

The channel geometry is one of the most important design considerations for the tightly packed fuel assembly concept. By using the CFD analyses, the thermal hydraulic characteristics of three representative channel geometries, which are selected based on the values of ratio of hydraulic diameter to channel area, are understood. Geometry B (triangle with round corner) is demonstrated to be superior to other geometries at all evaluated pressure conditions, owing to its broader thermal-hydraulic design margin in terms of achievable power, cladding temperature and pressure drop. The superiority of geometry B is benefited from its appropriate match between the hydraulic parameter and channel area. Efficiency of the cooling depends both on channel area and hydraulic diameter. The small channel area of geometry A leads to high MCT while the small hydraulic diameter of geometry C leads to high MCST. In contrast, geometry B is moderate with respect to these parameters. Also, pressure drop (which is not a design criterion, but is still an important design parameter) is sensitive to channel area. The design range can only be determined by satisfying both MCT and MCST criteria. Hence, geometry B leads to broader design range in terms of achievable power, cladding temperature and pressure drop. In practical applications, both geometry A and B are applicable for tightly packed fuel assembly in high breeding Super FBR, PWR and BWR, while geometry C is not suitable for PWR and BWR, because its CHF is too small and the required steam quality cannot be attained.

With the new findings from CFD analysis, both geometry A and B are adopted as coolant channels for designing a high breeding BWR core with tightly packed fuel assemblies. Geometry

A is beneficial to breeding form the viewpoint of neutronics and geometry B is favorable with respect to the thermal hydraulic design margins. Hence, geometry A and B are applied as coolant channels in blanket and seed assemblies, respectively. From sensitivity studies, it is found that, lower enrichment is better for achieving both breeding and negative void reactivity, and higher burn up is better for breeding but worsens the negative void reactivity coefficient towards positive. The design area in terms of above factors is clearly understood. Finally, it is found that the Linear Heat Generation Rate (LHGR) is the main limitation to improve the breeding. Application of geometry B and enrichment zoning in both radial and axial directions effectively suppress the power peaking factors and increase the core power. The final core design eventually achieves a CSDT of 41.6 years meanwhile satisfies all the design criteria that include negative void reactivity, MCHFR > 1.9 and MLHGR < 44kW/m. Possibility of high breeding with BWR condition has been shown for the first time

The safety characteristics of Super FBR with tightly packed fuel assemblies are clarified. The safety and plant system is designed in the same way as Super FRs while operated at a higher system pressure of 30 MPa. The actuation pressure for reactor scram is proportionally increased to shut down the reactor duly in abnormalities, while the actuation pressure of ADS is remained slightly above the critical pressure (22.1MPa) to avoid unnecessary system depressurization. Compared with Super FRs, application of tightly packed fuel assembly makes Super FBR more sensitive to "core heat-up" initiation events, and the variation in core pressure and cladding temperature are larger when a positive reactivity is inserted. The most important event is found to be the accident "control rod ejection" rather than "total loss of feedwater flow" which is the one in Super FRs. It is mainly because of the small fraction of coolant volume. With the improved plant and safety system, all the safety criteria are satisfied in the safety analysis of Super FBR for selected accidents and transients.

Thus, the present study has shown the core designs and safety of the high breeding fast reactors cooled by light water. The potential of achieving high breeding with light water cooling has been shown for the first time in the world.

Nomenclature

A	Area (m^2)
A_p	Projected area (m^2)
C	Drag coefficient
c_p	Specific heat (J/g·°C)
d	Diameter(m)
d_{gp}	Gap between pellet and cladding (m)
D_h	Hydraulic diameter (m)
D_{heated}	Heated diameter (m)
f	Volumetric force vector
f_{lo}	Single-phase friction factor
$\vec{F}_{ij}^{D}$	Drag force from cell i to cell j (N)
$\vec{F}_{ij}^{L}$	Lift force from cell i to cell j (N)
$\vec{F}_{ij}^{TD}$	Turbulent dispersion force from cell i to cell j (N)
$\vec{F}_{ij}^{VM}$	Virtual mass force from cell i to cell j (N)
G	Mass flux (kg/m^2·s)
G_{cr}	Mass flux of critical flow (kg/m^2·s)
g	Gravitational acceleration (m/s^2)
h	Enthalpy (J)
h_c	Heat transfer coefficient [W/(m2°C)]
$h_{2\emptyset}$	Heat transfer coefficient for two phase flow [W/(m2°C)]
h_b	Enthalpy with bulk temperature(J)
h_w	Enthalpy with wall temperature(J)
I	Turbulence intensity (%)
K_{dry}	Vapor contact area fraction
K_{ori}	Orifice coefficient
k	Heat conductivity (W/m·K)
k_b	Thermal conductivity with bulk temperature (W/m^2·K)
k_w	Thermal conductivity with wall temperature (W/m^2·K)
k_f	Thermal conductivity of fuel pellet (W/m·K)

k_c	Thermal conductivity of cladding (W/m·K)
k_g	Heat conductivity of gas filled in the gap (W/m·K)
K-EFF	Effective multiplication factors
K-INF	Infinite multiplication factor
L	Length (m)
$\dot{m}$	Mass flowrate(Kg/s)
n	Neutron density
Nu	Nusselt number
Nu_v	Nusselt number without buoyancy effect
P	Pressure (MPa)
P_c	Critical pressure (MPa)
P_{set}	Setpoint of pressure
Pe	Péclet number
Pr	Prandtl number
Q_{fuel}	Total heat generated by the fuel pellet (J)
q	Linear heat rate of fuel (kW/m)
q''	Heat flux (kW/m^2)
q'''	Heat density(J/m^3)
r	Radius (m)
Re	Reynolds number
S	Slip ratio
t	Time (s)
T	Temperature (ºC)
T_{bulk}	Bulk temperature (ºC)
T_w	Wall temperature (ºC)
T_c	Fuel cladding temperature (ºC)
T_{fuel}	Fuel pellet temperature (ºC)
$\boldsymbol{u}$	Velocity (m/s)
$\boldsymbol{u}_*$	Friction velocity (m/s)
V_{gi}	Drift velocity (m/s)
x	True quality
x_e	Equilibrium quality
x_d	Bubble departure quality

Greek letters:

α	Void fraction
α_δ	Layer averaged vapor volume fraction
α_g	Bubble volume fraction
α_{dry}	Critical vapor volume fraction
δ	Near wall layer thickness (m)
ε	Cladding thickness (m)
θ	Angle (°)
$\emptyset^2$	Two-phase multiplier
μ	Viscosity (Pa·s)
ρ	Density (kg/m^3)
ρ_b	Coolant density with wall temperature (kg/m^3)
ρ_w	Coolant density with bulk temperature (kg/m^3)
λ_i	Decay constant of delayed neutron for group i
$y+$	Non-dimensional wall distance
Δz	Axial calculation mesh height (m)
ΔP	Pressure drop
AAP	Average assembly power (W)

Abbreviation

ABWR	Advanced Boiling Water Reactor
ADS	Automatic Depressurization System
AFS	Auxiliary Feedwater System
ATWS	Anticipated Transient Without Scram
BOC	Beginning of Cycle
BOEC	Beginning of Fuel Equilibrium Cycle
BOL	Beginning of Life
BWR	Boiling Water Reactor
CFD	Computational Fluid Dynamics
CHF	Critical Heat Flux
CHFR	Critical Heat Flux Ratio
CPM	Collision Probability Method
CR	Control Rod
CST	Cladding Surface Temperature
CSDT	Compound System Doubling Time
DBA	Design Basis Accident
DNB	Departure from Nucleate Boiling
ECCS	Emergency Core Cooling System
EF	Ex-Core Factor
EOC	End of Cycle
EOEC	End of Equilibrium Cycle
FA	Fuel Assembly
FDM	Finite Difference Method
FP	Fission Plutonium
FPP	Fossil-Fuel Fired Power Plant
FPSR	Fissile Plutonium Surviving Ratio
GFR	Gas-Cooled Fast Reactor
GIF	Generation International Forum
HEM	Homogeneous Equilibrium Model
HD	Hydraulic Diameter
HFF	Heterogeneous Form Factor

HPD	Homogeneous Power Distribution
HPLWR	High Performance Light Water Reactor
HPP	Homogeneous Pin Power
JAEA	Japan Atomic Energy Agency
LFR	Lead Cooled Fast Reactor System
LHGR	Linear Heat Generation Rate
LOCA	Loss of Coolant Accident
LMFBR	Liquid Metal Cooled Fast Breeder Reactors
LPCI	Low Pressure Coolant Injection
LWR	Light Water Reactor
MCHFR	Minimum Critical Heat Flux Ratio
MCST	Maximum Cladding Surface Temperature
MDHFR	Minimum Deterioration Heat Flux Ratio
MDNBR	Departure from Nucleate Boiling Ratio
MLHGR	Maximum Linear Heat Generation Rate
MOEC	Middle of Equilibrium Cycle
MOX	Mixed Oxide Fuel
MSIV	Main Steam Isolation Valve
MSR	Molten salt reactor system
PCMI	Pellet-cladding mechanical interaction
PI	Proportional-Integral controller
PID	Proportional-integral-derivative controller
PIJ	Collision probability calculation module
PWR	Pressurized water reactor
RCP	Reactor Coolant Pump
RDT	Reactor Doubling Time
RMWR	Reduced-Moderation Water Reactor
RPV	Reactor pressure vessel
SCWR	Supercritical water cooled reactor
SCRELA	Supercritical-pressure Light Water Reactor LOCA analysis
SFR	Sodium-cooled fast reactor
SRV	Safety Relief Valve
SS	Stainless steel

SLCS	Standby Liquid Control System
SPRAT	Supercritical Pressure Reactor Accident and Transient
Super LWR	Super light water reactor
Super FR	Super fast reactor

研究業績書

種 類 別	題名、　　発表・発行掲載誌名、　　発表・発行年月、　　連名者（申請者含む）
(1) Paper	1.　**R. Guo**, Y. Oka. CFD analysis of coolant channel geometries for a tightly packed fuel rods assembly at subcritical pressure. Nuclear Engineering and Design, Vol. 284, pp. 115-129. 2.　**R. Guo**, Y. Oka. CFD analysis of coolant channel geometries for a tightly packed fuel rods assembly of Super FBR. Nuclear Engineering and Design. Nuclear Engineering and Design, Vol. 288, pp. 119-129.
(2) Presentation	1.　**R. Guo**, Y. Oka. Safety characteristics of a high breeding reactor cooled by supercritical water. AESJ Spring Meeting, March 26-28, Tokyo, Japan. (2014) 2.　**R. Guo**, Y. Oka. Safety analysis of Breeding Super FR. ICONE-22, July 7-11, Prague, Czech Republics. (2014) 3.　**R. Guo**, A. Yamaji, Y. Oka. CFD analysis of coolant channel geometries in a tightly packed fuel rods assembly. ICONE-23, May 17-21, Chiba, Japan. (2015)